

Materials and Device Design for MEMS Piezoelectric Mechanical Vibration Energy Harvesters

by
Miso Kim

Submitted to the Department of Materials Science and Engineering
In Partial Fulfillment of the Requirements for the Degree of

Doctor of Philosophy

at the

MASSACHUSETTS INSTITUTE OF TECHNOLOGY

February 2012

© 2012 Massachusetts Institute of Technology. All rights reserved.

Author.....
Department of Materials Science and Engineering
September 06, 2011

Certified by.....
Brian L. Wardle
Associate Professor of Aeronautics and Astronautics
Thesis Supervisor

Certified by.....
Harry L. Tuller
Professor of Materials Science and Engineering
Thesis Reader

Accepted by.....
Christopher A. Schuh
Professor of Materials Science and Engineering
Chair, Departmental Committee on Graduate Students

Materials and Device Design for MEMS Piezoelectric Mechanical Vibration Energy Harvesters

by

Miso Kim

Submitted to the Department of Materials Science and Engineering
on September 6, 2011 in partial fulfillment of
the requirements for the degree of
Doctor of Philosophy in Materials Science and Engineering

Abstract

Piezoelectric vibration energy harvesters (PVEHs) for microelectromechanical systems (MEMS) have received considerable attention as an enabling technology for self-powered wireless sensor networks. MEMS-PVEHs are particularly attractive because of the potential to deliver power indefinitely and their ability to be integrated concurrently with microfabrication of sensor nodes. A key challenge has been insufficient power and voltage generation for practical applications. Along with research efforts on improved materials, efficient electronics, and fabrication of devices, modeling is an indispensable element in predicting and designing PVEHs. Here, an improved electromechanically-coupled model is developed including the ability to analyze proof mass effects and different electrode configurations. Although essential in microscale devices to move device resonances towards optimal frequency points for harvesting, proof masses have not been treated rigorously in extant work. An improved treatment of a rigid proof mass with rotation, and an exact treatment (two-beam model) of a flexible proof mass, are presented and experimentally verified using a macroscale, symmetric, bimorph, cantilevered PVEH device operating in {3-1} mode with a rigid proof mass, and a micron-scale Si cantilever with a flexible proof mass, respectively. Focused ion beam milling is used to create different flexible proof masses, and atomic force microscopy is used to study the mechanical behavior of micron-scale, single-crystal Si cantilevers. It is found that the two-beam model is necessary for the majority of

the proof mass cases considered, especially when considering key power-generation characteristics such as strain developed in the piezoelectric layers. The effects of piezoelectric material properties on device performance are studied via model-based sensitivity analyses to gain insight into the design and selection of optimal piezoelectric materials for power and voltage generation. Notably, and non-intuitively, optimum power either at resonance or anti-resonance is independent of the piezoelectric coupling constant of the piezoelectric material, obviating the oft-cited rationale for materials research to increase piezoelectric coupling coefficients. For example, in an exemplary PVEH optimization, maximum power and voltage are obtained at relatively low values (30~40 % of bulk PZT, near AlN and ZnO film values) of piezoelectric coupling coefficients. The improved model is used as a multi-variable design tool for designing a novel piezoelectric/ultrananocrystalline diamond (UNCD) heterostructure MEMS-PVEH device. This thesis contributes to the development of MEMS- PVEHs by offering new insights at both the materials and system levels, including optimization findings using different objective functions, such as efficiency. Future work includes application of the model-derived piezoelectric materials design guidelines to aid in the design of optimal MEMS-PVEH systems, fabrication of designed UNCD/piezoelectric-based MEMS-PVEHs, and analytical and experimental studies of both structural and piezoelectric fatigue phenomena for enhanced reliability of PVEHs.

Thesis Supervisor: Brian L. Wardle

Title: Associate Professor of Aeronautics and Astronautics

Acknowledgements

My years at MIT could be one of the most precious and grateful experience in my life – thanks to so many wonderful people around me. I am such a blessed person. I don't think it would be even possible to list all those people's names that I want to and should thank for being there as companions and helping me with walking all the way through.

First, I would like to express my deepest gratitude to my advisor, Prof. Brian L. Wardle. Thanks to him, I was able to start working on my beloved thesis topic, “piezoelectric energy harvesting”. It was a great pleasure to work with him as I could learn how to approach and tackle problems with creativity and broader perspectives from him. His keen insight always impresses me. Without his persistent and kind guidance and encouragement, I could not have had completed my thesis. I also owe considerable gratitude to Prof. John Dugundji for not only providing his invaluable and extensive knowledge of structural dynamics but also being a caring and thoughtful mentor.

I feel extremely lucky and honored to have Prof. Harry L. Tuller (DMSE, MIT), Prof. Lorna Gibson (DMSE, MIT), and Prof. Seung-Hyun Kim (Brown University) on my thesis committee as each of them is the influential figure in his/her field and I sincerely admire them all a great deal. Along with Prof. Brian L. Wardle and Prof. John Dugundji, each of my thesis committee members will be my role models in my lifetime.

This thesis contains several chapters that are based on the extensive collaboration with prominent researchers in various fields. I spent my last year of Ph.D. program at Argonne National Laboratory (ANL) as a guest graduate student. Chapter 5 is the product of systematic experiments and in-depth discussion with Dr. Seungbum Hong (MSD, ANL) and Dr. Dean J. Miller (EMC, ANL) during my stay at ANL. Dr. Orlando Auciello (MSD, ANL) kindly guided me to take interest in potential use of UNCD as a novel structural layer, which motivated the work presented in Chapter 9. Prof. Dong-Joo Daniel Kim and Dr. Jung-Hyun Park at Auburn University provided experimental data of MEMS-PVEH device performance, based on which model-experiment comparison study was performed and presented in Chapter 8.

I would like to thank all those people who made my life at MIT significantly abundant. I

am extremely lucky to have TELAMS as my labmates and friends. Every single of them is a wonderful and amazing person. Because of them, I enjoyed going to the office even when I underwent hardship during my graduate study. I will miss them so much. I can't forget my beloved trillium trio members, Aaron and Debbie (and Debbie's family). The time we spent together in playing music and chatting with homemade sweets was one of my best favorite moments and made me breathe and laugh. I would also like to appreciate Prof. David Paul for being a kind and loving friend as well as teacher. I would like to express my gratitude to the friends I have met at MIT. There are numerous people I want to remember and thank at MIT but due to the limit in space, I will just name a few: Yeryoung, Bobae, Tairyn, Hyemin, Jerin, Jhongwoo, and Kitae.

While I was in Boston, I met so many wonderful people in church and other places. I was always touched by the warmth and comfort of Haewon, Seyeon, Taeseok, Kelly, Zach, Sunhae, Yonghee, and Sunhae's parents. Without their prayer, I couldn't have stood where I am now. I also would like to thank all those incredible people I met in Chicago: my dear friend, Seoyoung, and every single people I met at ANL (especially our lunch crew in building 212 and Amanda's group members).

Prof. Han-il Yoo at Seoul National University motivated and helped me to come to MIT and pursue my Ph.D. degree. I am deeply thankful to him for leading me to here in the first place.

Last but not least at all, I want to thank my family. My parents have always been there for me and provided infinite love and support. I am really lucky that I was born as their daughter. I thank my sister and her husband who are the ones that can make me laugh especially when I am down. I would like appreciate my mom-in law and sister-in-law for being my family. I really do not know how to express my gratitude to my husband, Jongchul. His love, passion, and belief are the driving force to lift me up and make me a strong and confident person. He is just beyond description. Thank you, my love.

I give thanks to my shepherd, the LORD. I shall not be in want. ☺

Table of Contents

Abstract	3
Acknowledgements	5
Table of Contents	7
List of Figures	12
List of Tables	20
Nomenclature	22
1. Introduction.....	27
1.1 Energy Harvesting for Mobile and Wireless Electronics	28
1.1.1 Solar Cells	29
1.1.2 Thermoelectric Generators	30
1.1.3 Vibration-based Generators	31
1.1.4 Bio-Energy Harvesting	31
1.1.5 Other Energy Harvesting Technologies.....	32
1.2 Mechanical Vibration Energy Harvesting	34
1.2.1 Electromagnetic and Electrostatic Vibration Energy Harvesting	37
1.2.2 Piezoelectric Vibration Energy Harvesting	38
1.2.2.1 Piezoelectric Effect	39
1.2.2.2 Piezoelectric Materials	40
1.2.2.3 Configurations of Piezoelectric Energy Harvesting Devices and Systems.....	42
1.2.2.4 Recent Advances and Future Trends.....	45
2. Prior Work on Piezoelectric Vibration Energy Harvesters	49
2.1 Review of Existing Work	49
2.2 Modeling of Cantilevered Piezoelectric Vibration Energy Harvesters	52

2.2.1	Beams and Plates with Piezoelectric Elements	53
2.2.2	Electromechanical Model for Single Beam Mode and Power Optimization.....	58
2.3	Issues and Unsolved Problems in Current Understanding of Piezoelectric Energy Harvesters.....	62
2.4	Overview of This Thesis	65
3.	Modeling of Proof Mass Effects on Vibration Energy Harvester Performance.....	67
3.1	Simple Approximation for Concentrated Proof Mass	68
3.2	Improved Treatment of Rigid Proof Mass with Rotation.....	71
3.3	Exact Treatment of Flexible Proof Mass Using Two-beam Method.....	77
3.4	Summary of Key Effects of Proof Mass Modeling Treatments	81
4.	Experiment-Model Correlation for Macro-scale PVEHs with a Proof Mass	85
4.1	Model Implementation for Cantilevered Bimorph Piezoelectric Energy Harvesters.....	86
4.2	Experimental Procedures for Device Characterization of Macro-scale Energy Harvesters.....	89
4.2.1	Experimental Setup and Device Performance Measurements	89
4.2.2	Test-device Dimensions and Material Properties.....	90
4.3	Experiment-Model Correlation and Discussion of Proof Mass Effects on Harvesting Performance	94
4.3.1	Model Implementation	94
4.3.2	Mechanical Mode Shapes for the Proof Masses	96
4.3.3	Performance of Piezoelectric Vibration Energy Harvesters	97
4.3.3.1	Resonant and Anti-resonant Frequencies	97
4.3.3.2	Model-Experiment Comparison of Overall Energy Harvester Response.....	98

4.3.3.3 System Behavior under Various Operating Conditions 115

5. Experiment-Model Correlation for MEMS-scale Cantilevers with a Flexible Proof Mass119

5.1 Fabrication of Proof Masses Using Focused Ion Beam 122
5.2 Characterization of MEMS-scale Cantilevers Using Atomic Force Microscopy 124
5.3 Mechanical Behavior of Micron-scale Cantilevers With a Proof Mass 127
5.4 Implications for Performance of Piezoelectric Energy Harvesters 131

6. Model-derived Piezoelectric Materials Design in Energy Harvesting...133

6.1 Piezoelectric Materials and Material Constants 134
6.2 Sensitivity Analysis of Device Performance to Material Properties 136
6.3 Damping Analysis and Its Relation to Piezoelectric Coupling in Energy Harvesting 141
6.4 Energy Harvesting Device Implications..... 146

7. Model-based Optimization Framework and Performance Quantification of Piezoelectric Energy Harvesting Devices.....153

7.1 Standardization of Key Performance Metrics for Energy Harvesters 153
7.1.1 Identification of Key Performance Parameters 154
7.1.2 Definition and Exploration of Harvesting Efficiency 158
7.1.3 Optimal Design for Different Key Performance Metrics 165
7.2 Direct Estimation of Materials and System Properties 170
7.2.1 Bottom-up Approach 170
7.2.2 Top-down Approach..... 171

8. Design of Unimorph MEMS Piezoelectric Energy Harvesters in {3-1} and {3-3} Modes of Operation.....175

8.1 Analytical Modeling for Microfabricated Unimorph Piezoelectric Cantilever with Different Electrode Configurations 175

8.2	Experimental Evaluation and Correlation with Modeling	183
8.3	Design of MEMS Piezoelectric Energy Vibration Energy Harvesters for Different Objectives	194
8.3.1	Design Constraints for Aerostructural Sensor Applications.....	194
8.3.2	Multi-variable Design Optimization for Various Performance Metrics	195
8.3.3	Optimization Results for an Example Prototype MEMS Harvesting Device.....	197
9.	Device Design Study: MEMS Piezoelectric Energy Harvesters with Novel Structural Layer Materials.....	203
9.1	Introduction & Motivation	203
9.2	Modeling and Prototype Design of Power-optimized PZT/Ultrananocrystalline Diamond (UNCD) Energy Harvesting Cantilevers.....	205
9.3	Processing Design of Piezoelectric MEMS Energy Harvesters based on Piezoelectric/Ultrananocrystalline Diamond Thin Film Heterostructures	209
10.	Application of Electromechanical Modeling to Other Systems.....	211
10.1	Modeling of Piezoelectric Actuator System.....	211
10.2	Design of High-Frequency Si-based MEMS Resonators.....	213
10.2.1	Device Design Considerations	214
10.2.2	Modeling of Electrostatically-driven Beam Resonators	216
10.2.3	Results of Model-based Device Design for Si MEMS Resonators..	221
10.2.4	Proposed MEMS Fabrication Sequence for Si Resonators	224
11.	Conclusions and Recommendations.....	227
11.1	Contributions of This Work.....	227
11.2	Recommendations for Future Work	230

References234

Appendix246

 Appendix A. Effective Piezoelectric Materials Constants for Beams, Plates and Thin
 Films in {3-1} and {3-3} Modes of Operation 247

 Appendix B. Supplement for Chapter 5..... 255

 B.1 SEM Images of MEMS-scale Cantilever with Proof Masses of Different
 Lengths Fabricated Using FIB 255

 B.2 Experimental Sequence and Detailed Manual for Characterization Using
 AFM (MFP-3D, Asylum Research) 258

List of Figures

Figure 1.1 Comparison of static power density and lifetime from vibration, solar, and various battery chemistries [11].....33

Figure 1.2 Plot of static power density versus voltage for common regenerative and lithium/lithium-ion power supply strategies [1].34

Figure 1.3 Power spectral density (PSD) vs. frequency of a microwave oven (a) top and (b) side [30].36

Figure 1.4 Unimorph cantilevered piezoelectric energy harvester device in {3-1} mode of operation with standard electrode configuration. Note asymmetric layers and the need for a “structural” layer.44

Figure 1.5 Interdigitated electrode (IDTE) configuration in cantilevered piezoelectric energy harvesting {3-3} mode devices: (a) top-view and (b) side-view.44

Figure 1.6 Schematic of a cantilevered piezoelectric energy harvesting system with simple electrical resistance loading, R_l45

Figure 2.1 Schematic of a base-excited cantilevered PVEH. Here, v is the voltage developed across electrical resistance, R_l . w_{tip} and \ddot{w}_B represent tip displacement and base acceleration, respectively while L_T indicates the total length of the cantilever. x_t denotes the transverse beam/plate coordinate while x_a is the axial beam/plate coordinate.....53

Figure 3.1 Conceptual schematic of a concentrated-mass assumption in a cantilevered system.....	69
Figure 3.2 Schematic of base-excited cantilevered beam/plate with a proof mass at the tip.....	72
Figure 3.3 Schematic of a cantilever with a long, flexible proof mass. Notations ‘beam 1’ and ‘beam 2’ are used to demonstrate the concept of ‘two-beam method’.....	78
Figure 4.1 Illustration of symmetric, bimorph energy harvester with a tip proof mass. The active elements are electrically connected in series.....	86
Figure 4.2 Connection between the electrostatic shaker (as the part that moves the system), the clamping device, and the energy harvester device with Proof Mass I. Energy harvester device is electrically wired through electrical leads in order to obtain electrical data as shown in the left image.....	92
Figure 4.3 Variation of mechanical mode shapes and second derivatives (strain is proportional to the second derivative) in the axial direction from the clamp ($x=0$) to the proof mass junction ($x=1$). Here, x represents an axial position of normalized length of the device plate.....	96
Figure 4.4 No Proof Mass (No PM): predicted vs. measured response: tip displacement plotted against the electrical load at various input frequencies. Base acceleration is held constant at 2.5 m/s^2 . Empty squares in red color indicate the tip displacements measured at open-circuit condition ($R_l \rightarrow \infty$).....	105
Figure 4.5 No Proof Mass (No PM): predicted vs. measured response: voltage developed, plotted against the electrical load at various input frequencies. Base acceleration is held constant at 2.5 m/s^2 . Empty squares in red color indicate the voltages measured at open-circuit condition ($R_l \rightarrow \infty$).	106

Figure 4.6 No Proof Mass (No PM): predicted vs. measured response: extracted power plotted against the electrical load at various input frequencies. Base acceleration is held constant at 2.5 m/s².107

Figure 4.7 Proof Mass I (PM I): predicted vs. measured response: tip displacement plotted against the electrical load at various input frequencies. Base acceleration is held constant at 0.5 m/s². Empty squares in red color indicate the tip displacements measured at open-circuit condition ($R_l \rightarrow \infty$).108

Figure 4.8 Proof Mass I (PM I): predicted vs. measured response: voltage developed, plotted against the electrical load at various input frequencies. Base acceleration is held constant at 0.5 m/s². Empty squares in red color indicate the voltages measured at open-circuit condition ($R_l \rightarrow \infty$).109

Figure 4.9 Proof Mass I (PM I): predicted vs. measured response: extracted power plotted against the electrical load at various input frequencies. Base acceleration is held constant at 0.5 m/s².110

Figure 4.10 Proof Mass II (PM II): predicted vs. measured response: tip displacement plotted against the electrical load at various input frequencies. Base acceleration is held constant at 0.2 m/s². Empty squares in red color indicate the tip displacements measured at open-circuit condition ($R_l \rightarrow \infty$).111

Figure 4.11 Proof Mass II (PM II): predicted vs. measured response: voltage developed, plotted against the electrical load at various input frequencies. Base acceleration is held constant at 0.2 m/s². Empty squares in red color indicate the voltages measured at open-circuit condition ($R_l \rightarrow \infty$).112

Figure 4.12 Proof Mass II (PM II): predicted vs. measured response: extracted power plotted against the electrical load at various input frequencies. Base acceleration is held constant at 0.2

m/s².....113

Figure 4.13 Dual-power optimization at resonance and anti-resonance for each proof mass case.....114

Figure 4.14 3-D plot (2 views) of output power against normalized frequency and electrical resistance. The model simulation is run on the experimentally verified macroscopic energy harvester with PM I.....117

Figure 4.15 Power versus electrical resistance at various damping conditions. The model simulation is run on the experimentally verified macroscopic energy harvester with PM I.....118

Figure 5.1 Schematic of AFM equipped with a cantilever (with a proof mass).....121

Figure 5.2 SEM images of the as-purchased tip-less single-crystal silicon cantilever probe (Source: <http://www.asylumresearch.com/Probe/TL-FM,Nanosensors>).....122

Figure 5.3 Schematic of dual-beam FIB apparatus and sample configuration for edge-on milling.....123

Figure 5.4 3-D schematic and SEM images of a single-crystal silicon cantilever with a flexible, distributed, thin proof mass fabricated by FIB lithography. Inset shows 2-D schematic of base-excited cantilevered beam with a proof mass at the tip with model parameters.....124

Figure 5.5 Resonant frequency vs. normalized proof mass length (simulated vs. experiments).....128

Figure 5.6 Normalized mechanical mode shape along the beam length (x) for various sizes of proof mass.....130

Figure 5.7 Curvature of normalized mode shape along the beam length (x) for various sizes of proof mass.....130

Figure 6.1 Sensitivity of output power of a PVEH device to materials properties: (a) output power versus piezoelectric constant, e_{31}^* , and (b) output power versus dielectric constant, ϵ_{33}^S , at resonance and 20 k Ω for the device (PM I) of Chapter 4.....138

Figure 6.2 Device performance trends with e_{31}^* : (a) Output power versus normalized frequency (Ω) at various piezoelectric constants, e_{31}^* , under given operating conditions (at resonance and at 20 k Ω), (b) maximum output power vs. piezoelectric constant, (c) peak-power frequency ratio vs. piezoelectric constant, e_{31}^* 140

Figure 6.3 Power output versus normalized frequency at various electrical resistances for macroscopic energy harvester with PM I. Base acceleration is held at 0.5 m/s². R_l is the electrical load resistance, $R_{l,r}$ and $R_{l,ar}$ are the power optimized electrical loads at resonance and anti-resonance, respectively. The solid line in red color is the optimized power (optimal electrical load, $R_{l,opt}$, at all frequencies).....150

Figure 6.4 Voltage versus normalized frequency at various electrical resistances for macroscopic energy harvester with PM I. Base acceleration is held at 0.5 m/s². R_l is the electrical load resistance, $R_{l,r}$ and $R_{l,ar}$ are the power-optimized electrical loads at resonance and anti-resonance, respectively. The solid line in red color is the optimized power (optimal electrical load, $R_{l,opt}$, at all frequencies).....151

Figure 6.5 Power-optimized voltage (solid line in red color) and electrical resistance (dotted line in blue color) at resonance versus piezoelectric constant, e_{31}^* , with indication of commonly used piezoelectric materials: $e_{31}^* = -1.0$ for AlN and PVDF, -8.5 for PZT(111) [Zr/Ti =45/55] film, -12 for PZT(100) [Zr/Ti =53/47] film, and -14.7 for bulk-PZT. At all piezoelectric constants (*i.e.*, regardless of the choice of piezoelectric materials), a given PVEH system is predicted to

generate equal power, $167 \mu\text{W}$152

Figure 7.1 Schematic of a simple, 1-dimensional piezoelectric energy conversion device modeled by Richards *et al.* [102].....158

Figure 7.2 Schematic of a base-excited cantilevered beam/plate with indication of parameters defined for efficiency.....160

Figure 7.3 Mechanical input power vs. electrical resistance at various operating frequencies for a macroscopic, bimorph energy harvester in {3-1} mode of operation with no proof mass (No PM).....168

Figure 7.4 Electrical output power vs. electrical resistance at various operating frequencies for a macroscopic, bimorph energy harvester in {3-1} mode of operation with no proof mass (No PM).....168

Figure 7.5 Harvesting efficiency vs. electrical resistance at various operating frequencies for a macroscopic, bimorph energy harvester in {3-1} mode of operation with no proof mass (No PM).....169

Figure 7.6 Harvesting efficiency at resonance (109.5 Hz) vs. electrical resistance at various damping conditions for a macroscopic, bimorph energy harvester in {3-1} mode of operation with no proof mass (No PM).....169

Figure 8.1 {3-1} and {3-3} mode unimorph PVEH configurations: side-view elements of (top) a cantilevered PVEH in {3-1} mode of operation with standard electrodes, and (bottom) a cantilevered PVEH in {3-3} mode of operation with IDTEs.....177

Figure 8.2 Side-view of piezoelectric layer in a unimorph, cantilevered PVEH in {3-3} mode of operation: {3-3} mode of operation (left) and approximate model (right) of electric field (E)

between interdigitated electrodes. p is the pitch of the electrodes and a is the width of the electrodes. x_1^* and x_3^* are the element local coordinates. P denotes polarization.....178

Figure 8.3 A unimorph, MEMS-scale PVEH: (a) schematic of the side view of piezoelectric energy harvesting cantilever based on SOI wafer, (b) cantilever structure with indication of dimension parameters. Reprinted with permission from [105, 106].....185

Figure 8.4 Fabricated, unimorph, MEMS-scale PVEH: (a) SEM image and (b) optical image of a MEMS-scale PZT cantilever in {3-1} mode with a proof mass, (c) optical image of a MEMS-scale PZT cantilever with a proof mass in {3-3} mode with IDTEs. (a) Reprinted with permission from [106]. (b), (c) courtesy of Dr. Jung-Hyun Park.....185

Figure 8.5 Characteristics of fabricated PZT thin films: (a) X-Ray Diffraction and (b) polarization-voltage hysteresis loop for polycrystalline PZT thin films.....188

Figure 8.6 Dielectric constant-voltage curves.....189

Figure 8.7 Model-experiment comparisons for a MEMS-scale unimorph energy harvesting PZT cantilever with a proof mass in {3-1} mode: (a) voltage versus electrical resistance and (b) power versus electrical resistance at resonances and various damping conditions. Q indicates the quality factor.....193

Figure 8.8 MEMS-scale unimorph energy harvesting PZT cantilever with a proof mass in {3-3} mode with IDTEs: predicted (a) voltage versus electrical resistance and (b) power versus electrical resistance at resonances and $Q = 250$. No measured data available.....194

Figure 8.9 3-D plots of two-variable optimal design exercise for {3-3} SHM MEMS-PVEHs: (a) operating power density optimal designs and (b) power output optimal designs, both as a function of active beam length (L) and proof mass (L_{PM}). Both are at $Q = 100$ ($\zeta_m = 0.005$). Sharp peaks in the above plots are due to the collection of discrete data points during simulation and do

not represent the real phenomenon.....	200
Figure 8.10 1-D plot of operating power density as a function of proof mass length (L_{PM}) when the active beam length (L) is fixed at 100 μm and P_{op} is optimized.....	201
Figure 9.1 PZT/UNCD characteristics for MEMS-PVEHs: (a) TEM image of nano-size grains in UNCD, and (b) SEM image of PZT/UNCD cantilever [117].....	204
Figure 10.1 Schematics of beam resonators driven by electrostatic actuation with indication of dimensions, drive and sense electrodes, and the vibration direction: (a) top-view of singly-clamped beam, (b) side-view of singly-clamped beam, (c) top-view of doubly-clamped beam, and (d) side-view of doubly-clamped beam.....	216
Figure 10.2 A parallel-plate electrostatic actuator: (a) schematic of the basic electrostatic actuator with the movable plate attached to a spring, and (b) electrical (electrostatic) force and spring forces for voltage controlled parallel-plate electrostatic actuators [121].....	217
Figure 10.3 Schematic and measured data for a single-crystal silicon capacitive resonator from [123]: (a) doubly-clamped beam single crystal silicon resonator and (b) plot of the resonance frequency vs. polarization voltage for a 300 μm long, 6.5 μm wide beam resonator.....	222
Figure 10.4 Model-derived design space for (a) singly-clamped beam resonators and (b) doubly-clamped beam resonators. Both are targeted to operate at 10 MHz and 25 MHz.....	222
Figure 10.5 Fabrication process for silicon beam resonators – side view.....	226
Figure A.1 Schematic of piezoelectric effect for beams and plates in (a) {3-1} mode of operation and (b) {3-3} mode of operation.....	248

List of Tables

Table 1.1 Acceleration magnitude and frequency of peak for various sources [11].....	36
Table 4.1 Geometric and material properties of the tested macroscale bimorph energy harvesters.....	93
Table 4.2 Geometric dimensions of device proof masses and input base accelerations.....	94
Table 4.3 Key device parameters for model implementation.....	95
Table 4.4 Summary of frequencies, dimensionless time constants and electrical load at short-circuit and open-circuit conditions.....	98
Table 6.1 Comparison of material properties of commonly used piezoelectric materials.....	136
Table 7.1 Key metrics for energy harvesting device comparison.....	156
Table 8.1 Dimension for a unimorph thin film PZT cantilever.....	185
Table 8.2 Layers in micro-scale, unimorph, PZT-based energy harvester devices in {3-1} and {3-3} modes of operation.....	186
Table 8.3 Material properties of layers in MEMS unimorph energy harvester device [30, 79]..	192
Table 8.4 Key device parameters for model implementation on MEMS unimorph energy	

harvester devices in {3-1} and {3-3} modes (see Tables 8.1-8.3).....	190
Table 8.5 Example device dimensions for a unimorph, {3-3} mode energy harvester, given microfabrication constraints.....	197
Table 9.1 Material properties of layers in UNCD/PZT-based MEMS energy harvester device [30, 79, 124, 125].....	207
Table 9.2 Layers and each thickness of PZT/UNCD based energy harvester and Si-based energy harvester in {3-1} mode of operation.....	208
Table 9.3 Predicted results of device performance for the PZT/UNCD and Si-based energy harvesters.....	209
Table 10.1 Beam dimensions for the fabrication of high-frequency Si beam resonators.....	223
Table 10.2 Predicted key parameters from modeling of singly-clamped, 25 MHz (S. 25 MHz), singly-clamped, 10 MHz (S. 10 MHz), doubly-clamped, 25 MHz (D. 25 MHz), doubly-clamped, 10 MHz (D. 10 MHz) beam resonators.....	223
Table 10.3 Maximum dynamic deflection and dynamic pull-in conditions of a singly-clamped, 10 MHz beam at various damping conditions.....	224
Table 10.4 Maximum stress and strain at quality factor, $Q = 1000$	224
Table B.1 Under-, Front-, and Side-view SEM images of tip-less cantilever in the state of as-received, after front trim and after side trim.	255
Table B.2 Under- and side-view SEM images of MEMS-scale cantilever with proof masses of different lengths fabricated using FIB.....	256

Nomenclature

Symbol	Description
a	width of interdigitated electrode (IDTE)
A	area
A_{el}	area of electrodes in IDTE modeling
A_p	area of a piezoelectric layer cross-section in IDTE modeling
subscript, ar	anti-resonance
B_f	modal forcing matrix with elements $B_{f,ij}$
B_f	scalar forcing function
b	width of structure
C	damping matrix with elements C_{ij}
C	scalar damping constant
C_m	mechanical damping constant
C_e	electrical damping constant
c^E	piezoelectric material elastic stiffness matrix at constant electric field ($E = 0$) with elements c_{ij}^E
c	length of the electrode in Si-based resonators
C_p	capacitance coefficient matrix with elements $C_{p,ij}$
C_p	scalar capacitive coefficient
D	electric displacement vector with elements D_i
d	piezoelectric constant matrix with elements d_{ij}
E	electric field vector with elements E_j

E	scalar electrical field, or Young's modulus
\overline{EI}	effective bending stiffness
e	piezoelectric constant matrix with elements e_{ij}
F_B	base excitation force
F_{EP}	dimensionless forcing term for electrical output power
F_{MP}	dimensionless forcing term for mechanical input power
F_{spring}	spring force in electrostatic resonator analysis
$F_{electrostatic}$	electrostatic force in electrostatic resonator analysis
F_{net}	net force in electrostatic resonator analysis
f_r	resonant frequency in [Hz]
f_{ar}	anti-resonant frequency in [Hz]
$f(x,t)$	external force
subscript, f	thin films
g	gap size or, unit of gravitational acceleration, 9.8 m/s^2
g_0	initial gap size
g_{pi}	gap size at pull-in
h	height or thickness in vibration direction
h_{PM}	proof mass height
$I(x)$	cross-sectional area moment of inertia
I_0	moment of inertia at the beam junction to the proof mass
I_{out}	current
\mathbf{K}	modal stiffness matrix with elements K_{ij}
K or k	stiffness or spring constant
L	beam length or active (piezoelectric) beam length
L_{PM}	proof mass length
L_T	total length of the beam/plate
L_E	length of electrode in IDTE
L_e	effective length in concentrated proof mass analysis
L_p	the length of piezoelectric layer not under the IDTEs
\mathbf{M}	modal mass matrix with elements M_{ij}

M	scalar mass
M_B	mass of base accelerating the cantilever in efficiency (η) analysis
M_{EH}	energy harvester total mass
M_0	mass of overhang in rigid proof mass modeling (= mass of proof mass + mass of the beam under the proof mass in Figure 3.2)
M_{PM}	mass of proof mass
M_T	total mass of beam/plate and proof mass
m	mass per length
subscript, opt	(power) optimum
\mathbf{P}	piezoelectric poling vector or polarization with elements P_i
P_{in}	mechanical input power
P_{op}	operating power density
P_{out}	electrical output power
P_{st}	static power density
p	spacing between the center of IDTEs (or called pitch)
subscript, p	piezoelectric layer
Q	charge or quality factor
q	charge
R_l	electrical load resistance
$r(t)$	general mechanical coordinate
subscript, r	resonance
\mathbf{S}	strain vector with elements S_j
S_0	static moment at the beam junction to the proof mass
S_p	the moment of area, A_p , in IDTE modeling
\mathbf{T}	stress vector with elements T_i
T_k	kinetic energy
subscript, s	structural layer
t_p	thickness of the piezoelectric layer
t	thickness of each layer, or time
superscript, t	transpose of matrix

U	internal potential energy
\mathbf{u}	mechanical relative displacement vector with elements u_i
V	volume
V_{op}	operating volume
V_{st}	static volume
\mathbf{v}	voltage vector with elements v_i
v	scalar voltage
v_{app}	applied voltage
v_{pi}	pull-in voltage
W	external work
W_e	electrical energy or work
w or $w(x, t)$	beam deflection
w_B	absolute base displacement
w_{tip}	beam tip displacement
x_a	general beam structure axial coordinate
x_t	general beam structure transverse coordinate
W	external work
W_e	electrical energy
z	distance measured from neutral axis in beam/plate or, relative displacement in electrostatic resonator analysis
z_N	distance between the centroid of area, A_p , and the neutral axis of the combined beam in IDTE modeling
z_{NA}	neutral axis distance
α	dimensionless time constant
δ_{ij}	Kronecker delta
η	power efficiency
$\boldsymbol{\varepsilon}$	piezoelectric material permittivity matrix with elements ε_{ij}
φ	scalar electrical potential
ψ_r	mechanical mode shape
ρ	density

Θ	coupling coefficient matrix with elements θ_{ij}
ζ_m	mechanical damping ratio
ζ_e	electrical damping ratio
κ^2	system coupling factor
λ_N	convenient modal analysis constant
ν	Poisson's ratio
Ω	normalized frequency ratio
ω	input driving frequency in [rad/s]
ω_I	first mode resonant frequency in [rad/s]
ω_N	N^{th} mode resonant frequency in [rad/s]
ω_r	resonant frequency in [rad/s]
ω_{ar}	anti-resonant frequency in [rad/s]
superscript, *	effective piezoelectric constants for beam or plate in {3-1} or {3-3} mode of operation (see Appendix A)

Chapter 1

Introduction

In recent years, harvesting ambient energy from the environment has been a growing interest area and major focus of many research groups [1]. Many ambient power sources such as thermal gradients, mechanical vibrations, fluid flow, solar, human-driven sources [2, 3] etc. have been actively investigated in order to realize alternative power supplies. Ambient sources are potential candidates to replace existing power sources such as batteries that have a limited energy storage capacity and lifetime for some applications [4]. In particular, mechanical vibration energy harvesting has drawn much attention as substantial advances have been achieved in integrated circuit technology, particularly in low power digital signal processors, reducing power requirements for wireless sensor nodes [5, 6]. Energy harvesting from external mechanical excitation is made through conversion of nearly ubiquitous, ambient mechanical vibration energy using one of three transduction mechanisms: electrostatic, electromagnetic, or piezoelectric effects [1, 7]. Although each transduction mechanism and corresponding application has advantages in different areas, energy conversion using piezoelectricity is regarded as one of the most promising technologies for MEMS devices. Piezoelectric materials [8] produce an electrical charge or voltage when subjected to a mechanical stress or strain, or vice versa. Vibrational energy is directly converted to voltage with no need for complex geometries or additional components. This is in contrast with electrostatic devices where an input voltage is required. Perhaps most importantly, piezoelectric vibration energy harvesters (PVEHs) can generate high

output voltages with enhanced efficiency [7]. In this chapter, an overview of various energy harvesting technologies for mobile and wireless electronics is presented, followed by an introduction of piezoelectric mechanical vibration energy harvesting in order to set the context for the research work in this thesis.

1.1 Energy Harvesting for Mobile and Wireless Electronics

Energy harvesting, power harvesting, or energy scavenging is the process of acquiring the energy surrounding a system and converting it into usable electrical energy. One driving force behind the search for new energy harvesting devices is the desire to power sensor networks and mobile devices without batteries. Many electronics have heavily relied on the use of electrochemical batteries for providing electrical energy to the device. Batteries, however, lag today's rapid development of wireless and mobile applications due to their finite lifespan and limited energy storage capacity, generating issues of replacement and disposal. In addition to these inherent limitations, batteries have shown relatively stagnant growth in technology over the past decade, while the performance of computing systems has grown steadily [9]. For portable electronics, replacing the battery is problematic. In the case of wireless sensors, these devices can be placed in very remote locations such as structural sensors on a bridge or global positioning system (GPS) tracking devices on animals in the wild. Simple replacement of the battery can become a very expensive task or even impossible. For embedded sensors for structural health monitoring of vehicles or aircraft bodies, in particular, it is not feasible to replace batteries. The concept of energy harvesting works towards developing self-powered devices that do not require replaceable power supplies. From external sources such as light, thermal gradients, wind, water flow, mechanical vibration, and human/animal activities, ambient energy in the surrounding medium can be obtained and used to replace or charge batteries. This captured energy can then be used to prolong the life of the power supply or in the ideal case provide endless energy for portable and/or wearable electronics (*e.g.*, cellular phones, mobile computers, radio communication equipment, etc.) and wireless sensor networks. Recent advances in wireless technology and low-power electronics as MEMS systems enable achievement of rapidly decreasing size, cost, and power consumption of sensors and electronics,

resulting in a surge of research in energy harvesting for practical real-world applications.

The history of energy harvesting dates back to the windmill and the waterwheel. Today, more power-generating options are available for harnessing ambient environmental energy, including solar energy, thermal energy, vibration-based devices, human power and so on derived from vehicles, structures, industrial equipment, environment, and the human body (Refer to Table 1 in [10]). Following is a brief review of solar cells, thermoelectric, vibration-based energy harvesting, bio-energy harvesting and other harvesting methods that have been investigated in the extant literature.

1.1.1 Solar Cells

Solar cells are one of the most commonly considered strategies of ‘energy harvesting’ that harnesses ambient light. These systems consist of solar arrays and signal processing circuitry. Power from solar cells results from the photovoltaic effect, which is the direct conversion of incident light into electricity. In direct sunlight, solar cells provide excellent power density of $15,000 \mu\text{W}/\text{cm}^3$ which is about two orders of magnitudes higher than other sources [10, 11]. In addition, ease of integration, modularity, lack of emission or noise, lack of moving parts, and use of a readily available source are advantageous aspects of solar power systems [1]. However, solar cells are limited in dim office lighting, or areas with no light. On cloudy days, power density is only around $150 \mu\text{W}/\text{cm}^3$ [11]. Thus, in embedded applications, in particular, solar cells would not be suitable because there may be no light present, or the cells can be obscured by contamination [7]. In addition to the issue of variation in light intensity, bulky electronics required for the additional signal processing circuitry, relatively large surface area required for arrays of cells, low conversion efficiencies, and high cost are the major challenges in the implementation of solar technology. Most commercially manufactured solar cells are based on relatively inexpensive crystalline silicon modules or flexible amorphous silicon panels with energy efficiency of 10-20 %. Higher efficiencies have been achieved using novel fabrication techniques using III-V compounds (GaAs, InP, and GaSb) but these are costly and contain either toxic or rare elements [1]. Detailed performance characteristics of both commercial and novel solar-power systems are summarized in tables and found in Reference [1]. Established products

that harvest light as an energy source range from solar homes producing kilowatts on a bright day to solar chargers for cell phones reported to produce up to 2 W of power in direct sunlight. Researchers continually strive to refine solar cell materials and technologies to increase efficiency [9].

1.1.2 Thermoelectric Generators

Generation of electricity via thermal gradients is another form of energy harvesting for powering portable devices. Thermoelectric generators are devices which convert heat (temperature differences) directly into electrical energy, using a phenomenon called the "Seebeck effect" (or "thermoelectric effect") [12-15]. A thermoelectric device creates a voltage when there is a different temperature. Conversely when a voltage is applied to it, it creates a temperature difference (known as the Peltier effect) [12]. This effect can be used to generate electricity, to measure temperature, or to heat or cool objects. Power scavenged from thermal gradients is substantial enough to be of interest if the necessary thermal gradients are available. A typical thermoelectric module consists of p- and n-doped semiconductors of Bi_2Te_3 , sandwiched between two metallized ceramic plates [13]. Thermoelectric converters are solid-state devices and have no moving parts, allowing long hours of steady-state operation without a need to replenish materials. It is also advantageous that heating and cooling can be reversed [13]. One downside to thermoelectric energy conversion is low efficiency, currently less than 10 %. In addition to low efficiency, difficulty in finding large temperature gradients ($> 10\text{ }^\circ\text{C}$) in small volumes ($< 1\text{cm}^3$) restricts realization of power-generating thermoelectric devices for MEMS applications [14]. Commercial realization of thermoelectric generators has also been delayed due to materials problems associated with thermocouple modules. These modules are fabricated from intermetallic compounds such as Bi_2Te_3 , Pb-Te, and Si-Ge, which have intrinsically low melting and/or decomposition temperatures, low energy conversion efficiency and toxic content, and are presently scarce [1]. Ideal thermoelectric materials have a high Seebeck coefficient, high electrical conductivity, and low thermal conductivity. Thus, in order to increase efficiency, development of materials is essential that are able to operate in higher temperature gradients, and that can conduct electricity well without also conducting heat. In this regard, most research has

focused on optimization of thermoelectric materials and module geometry. Early thermoelectric microgenerators produced only a few nW, but more recently, this approach has been combined with micro-combustion chambers to improve output power to $\sim 1 \mu\text{W}/\text{thermocouple}$ [7]. From industrial equipment, structures, and even the human body, we can capture mWs of energy with voltage generation of 100-200 $\mu\text{V}/\text{K}$. Practical examples are the wearable thermoelectric products developed over the last years such as the Seiko Thermic wristwatch [9] that uses 10 thermoelectric modules to generate sufficient energy (orders of μW) to run its mechanical clock movement from the small thermal gradient provided by body heat over ambient temperature. Radioisotope thermoelectric generators are used to provide electric power for spacecraft and automotive thermoelectric generators are proposed to convert waste heat, such as in automobile engine combustion, into electricity [15].

1.1.3 Vibration-based Generators

Vibrations are the most pervasive source in the environment and enable many applications such as sensors embedded in advanced structures where solar or other ambient energy does not exist. Suitable vibrations can be found in numerous applications including common household goods (refrigerators, washing machines, microwave ovens etc.), industrial plant equipment, moving structures such as automobiles and aircraft and infrastructure such as buildings and bridges. There are three main transduction mechanisms that can be used to extract mechanical energy and convert it into electricity: piezoelectric, electromagnetic, and electrostatic mechanisms. Each approach has its own advantages and disadvantages and these are described in more detail in Section 1.2, together with an in-depth discussion on piezoelectric vibration energy harvesting, which is the main interest and focus of this thesis.

1.1.4 Bio-Energy Harvesting

There is ample power to scavenge from biological systems. As the human body is a tremendous storehouse of energy, the use of power harvesting devices to capture the energy lost during everyday human life is a captivating idea and has been one of the main topics facilitating

the rapid growth of the power harvesting field. Starner [16] has presented an overview of the amount of power expended for various human activities such as power from body heat, breathing, blood pressure, keyboard typing, arm motion, and walking [16, 17]. Inventions based on human-powered devices range from wind-up magnetic generator-powered flashlights, to wind-up cell phone chargers and radios, to self-powered piezoelectric radio buttons, self-powered radio transmitters, and self-powered wireless push button remote controls for television [9]. Generating electricity during human walking has attracted the attention of many researchers. Humans typically exert up to 130 percent of their weight across their shoes at heel strike and toe-off, and standard jogging sneakers' cushioned soles can compress by up to a centimeter during a normal walk. For a 154-pound person, this indicates that about 7 W of power could be available per foot at 1-Hz stride from heel strike alone [9]. Piezoelectric elements such as PZT and PVDF have been integrated beneath a standard running sneaker's removable insole to scavenge energy during human walking [1, 7, 9, 18-21]. Research has also been carried out to investigate the possibility and practicality of implantable and wearable power supplies from both human and animal activity. Reviews on human-powered generation with special focus on piezoelectric energy harvesting systems are available [1, 7, 21]. Besides the human body, we can find abundant possibilities to scavenge energy in nature. Voltree Power has developed bio-energy harvesters that can power remote sensors and mesh networks that can monitor forest fires and weather in the forest by converting living plant metabolic energy to usable electricity [22].

1.1.5 Other Energy Harvesting Technologies

Other opportunities to harness energy from the environment lie in ambient fluid flows. Ocean waves are converted into useful electricity and can be used to power oceanographic monitoring sensors for autonomous operation [9]. The concept of so-called energy harvesting eels has been proposed and implemented into devices using thin flexible piezoelectric membranes for energy harvesting in the ocean [23, 24]. Windmills [25, 26] and micro-wind turbines [1] are devices to harvest energy from wind currents readily available in the environment. Radio waves are now commonplace energy sources used in passive Radio Frequency Identification (RFID) tags to power remote devices.

In [11], Roundy *et al.* classified power sources into two categories: fixed-energy sources and fixed power sources. The latter are power scavenging sources as reviewed here in the above and their lifetime is potentially infinite. In contrast, fixed energy sources such as batteries, hydrocarbon fuel, or fuel cells contain a fixed amount of energy, and therefore the average power generation is a function of lifetime (see Figure 1.1). Priya also compared various potential power sources for the sensor networks in [10]. Readers also can find a detailed review on power supplies for MEMS devices in [1]. In that paper, the authors summarize fundamentals, recent advances, applications and future trends of both non-regenerative power supplies (*e.g.*, batteries, microcombustors, turbine and heat engines, and microfuel cells) and regenerative power supplies (solar cells, thermoelectric power, vibration energy harvesting systems). A plot that shows power density and voltage of various power supplies mentioned above is reproduced from [1] for comparison in Figure 1.2.

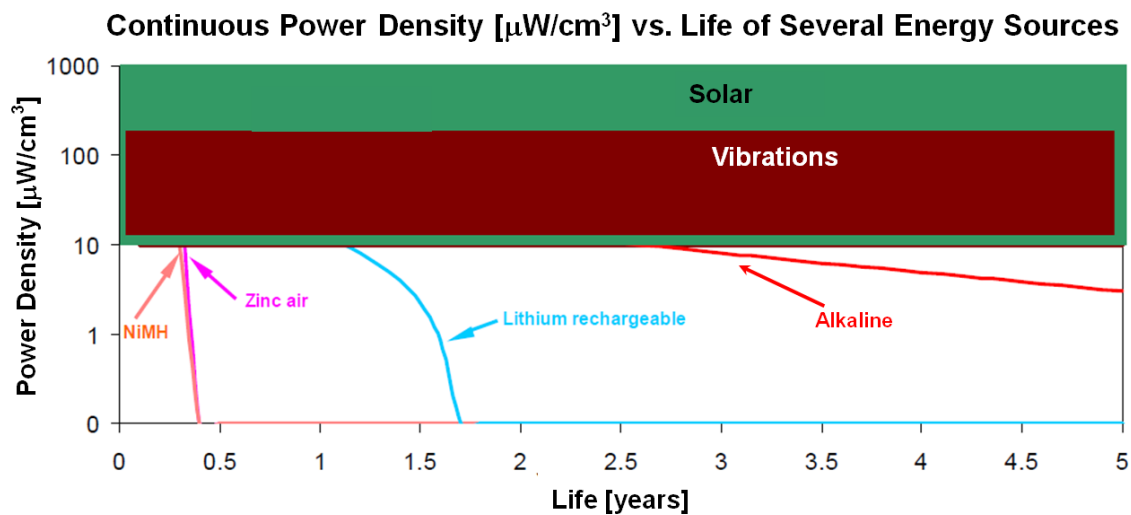


Figure 1.1 Comparison of static power density and lifetime from vibration, solar, and various battery chemistries [11].

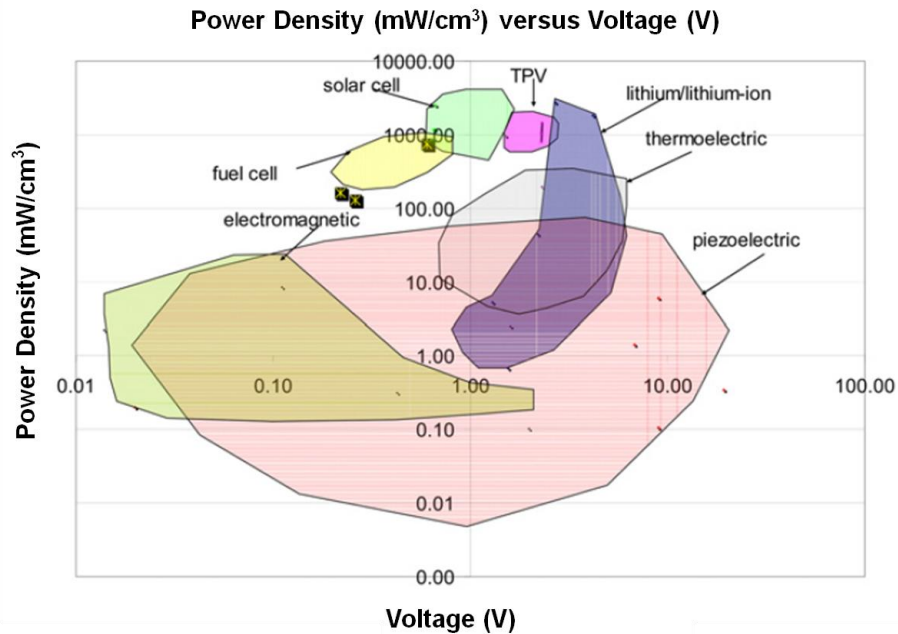


Figure 1.2 Plot of static power density versus voltage for common regenerative and lithium/lithium-ion power supply strategies [1].

Note that the concept of harvesting renewable, otherwise wasted energy from the environment, can also be an attractive solution to environmental problems as it is based on a clean source of electricity. We can mitigate the environmental impact caused by issues related to the disposal of batteries by harnessing these renewable sources. Also, it can bring tremendous economic impact into society as the input energy sources for energy harvesters are free.

1.2 Mechanical Vibration Energy Harvesting

Energy harvesting is the enabling technology for numerous distributed devices such as wireless sensor nodes, having application in diverse areas such vehicle health monitoring, smart cities/infrastructure, condition-based monitoring of manufacturing equipment, and threat detection. Among diverse sources, mechanical vibrations are the most pervasive form of ambient energy and such vibrations are the only ambient energy to harvest in many cases such as wireless sensors for embedded structural monitoring, negating possible alternative sources such as solar. The main techniques of harvesting energy from ambient vibrations have been shown to be

capable of generating output power levels in the range of μW to mW [1], depending on the source and transduction mechanism. Although such energy levels would have been considered as ‘unusable’ a few years ago, advances in modern-day VLSI circuit designs permit low-power operation and utilization of energy harvesting devices as a power solution. Current laboratory-based wireless sensors have reported operating power requirements of 100s-1000s of μWs with projections into the 10s of μWs [27], leading to the conclusion that vibrations can provide useful amounts of net power for small, low-drain devices such as distributed sensors. Devices of small volume would be desirable in applications like embedded sensors [28], spurring the development of MEMS-scale energy harvesting devices.

Vibrations that occur in common household and office environments are classified as ‘low-level’ vibrations, compared to more energetic vibrations that can be found, for example, in large industrial equipment. Low-level vibrations are of main interest and targeted in device design because of a wide range of potential applications that can be powered by harvesting vibrations at this level. Roundy *et al.* [11] investigated the nature of various sources of vibrations available and summarized it as reproduced in Table 1.1 that includes the peak acceleration (m/s^2) and peak frequency (Hz) values of a number of low-level vibrating structures. du Toit *et al.* [29, 30] also performed a quantitative comparison of ambient vibration sources, particularly for MEMS piezoelectric vibration energy harvesters in both vacuum and atmospheric conditions, suggesting that significant power is present in the range from 100-300 Hz for a number of ambient sources. du Toit presented the graphical demonstration of the power spectral density (PSD) in frequency domain ranging from 0 to 1 kHz for several sources of ambient vibration [30]. Among them, a plot of PSD vs. frequency for a microwave top and side is reproduced in Figure 1.3. The information about the potential vibration sources is very important in both design and operation of vibration energy harvesters. As most vibration-based generators are spring-mass-damper systems, they generate maximum power at resonance when the natural frequency of the system matches the frequency of the input vibration. Thus, it is essential to design devices with appropriate geometric configuration and materials properties that are matched to the targeted available PSD.

Table 1.1 Acceleration magnitude and frequency of peak for various sources [11].

Vibration Source	Acceleration [m/s^2]	Frequency at the peak [Hz]
Car engine compartment	12	200
Base of 3-axis machine tool	10	70
Blender casing	6.4	121
Clothes dryer	3.5	121
Person nervously tapping their wheel	3	1
Car instrument panel	3	13
Door frame just after door closes	3	125
Small microwave oven	2.5	121
HVAC vents in office building	0.2-1.5	60
Windows next to a busy road	0.7	100
CD on notebook computer	0.6	75
Second story floor of busy office	0.2	100

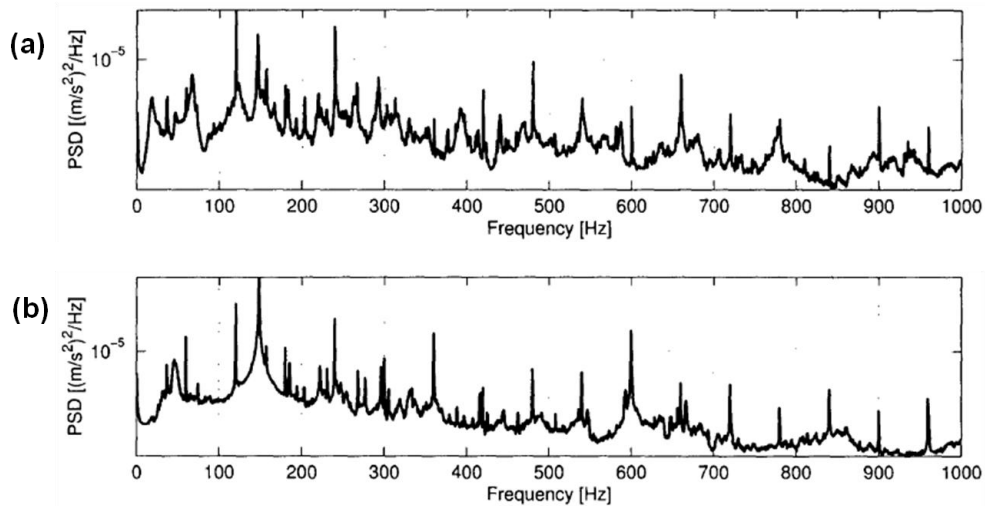


Figure 1.3 Power spectral density (PSD) vs. frequency of a microwave oven (a) top and (b) side [30].

1.2.1 Electromagnetic and Electrostatic Vibration Energy Harvesting

Vibration energy harvesting requires a transduction mechanism to generate electrical energy and several approaches exist to convert vibrations to electrical power including electromagnetic, electrostatic, and piezoelectric conversion. In the following, basic operating principles, advantages and disadvantages of electromagnetic and electrostatic vibration energy harvesters are briefly reviewed before moving on to the main topic in this thesis, piezoelectric energy harvesting.

Electromagnetic induction, first discovered by Faraday in 1831, is the generation of electric current in a conductive coil within a magnetic field from the relative motion between a coil and the magnetic field. The amount of electricity generated is a function of strength of the magnetic field, the velocity of the relative motion, and the number of turns of the coil. Electromagnetic energy harvesters basically consist of permanent magnets (*e.g.*, NdFeB magnet), a coil, and a resonating cantilever beam. It is generally preferable that the magnets are attached to the cantilever structure as they can act as inertial masses [1, 7]. Electromagnetic converters offer a well-established technique of electrical power generation and the effect has been used for many years in a variety of electrical generators [6, 7, 9, 31]. Primary disadvantages of electromagnetic energy harvesters are their low output voltages, typically well below 1 V in magnitude, and the difficulties in reducing down to the micron-scale. While high-performance bulk magnets and multi-turn, macro-scale coils are readily available [7, 9], it is quite difficult to realize MEMS-scale electromagnetic harvesters due to the relatively poor properties of planar magnets in thin film structures, the limitations on the number of turns achievable with planar coils and the restricted amplitude of vibration. Problems associated with the assembly and alignment of sub-millimeter scale electromagnetic systems are also significant.

The basic concept of electrostatic energy harvesters is a variable capacitor that consists of a charged capacitor with moving plates. The relative movement between electrically isolated charged capacitor plates requires work against the electrostatic force between the plates, thus providing the harvester energy. Electrostatic generators are generally classified into three types: in-plane overlap varying, in-plane gap closing, and out-of-plane gap closing. Details on these can be found [7, 11]. Electrostatic energy harvesters are attractive in that their fabrication process is

well-established in silicon micromachining (compatible with CMOS), thereby enabling miniaturization of devices. MEMS-scale electrostatic energy harvesters can benefit from being able to increase energy density with applied voltage by decreasing capacitor spacing. However, it should be noted that reduction in capacitor surface area for miniaturization decreases energy density. Unfortunately, electrostatic generators require an initial polarizing voltage or charge to start unless they utilize an electret layer [32]. The output impedance of the electrostatic harvesting devices is often very high and this makes them less suitable as a power supply. The output voltage produced by the devices is relatively high (> 100 V) but often results in a limited current-supplying capability. Accordingly, they are intended to support extremely low-power applications. At MEMS-scale implementations, there is also the risk of capacitor electrodes shorting and of 'stiction' [7].

1.2.2 Piezoelectric Vibration Energy Harvesting

Piezoelectric materials produce electrical charge or voltage across them when a mechanical stress or strain is applied, or vice versa [8]. When subjected to mechanical strain, piezoelectric materials become electrically polarized and the degree of polarization is proportional to the applied strain. Conversely, these materials deform when exposed to an electrical field. This functionality enables the use of piezoelectric materials to convert mechanical energy into electrical energy. As previously reviewed, several methods exist for obtaining electrical energy from vibration sources including the use of electromagnetic induction, electrostatic conversion, and piezoelectric materials. Of these three vibration-based devices, PVEH devices have received the most attention because piezoelectric devices convert applied strain energy from vibration into usable electrical energy directly. There is no requirement for having complex geometries and numerous additional components and thus, PVEHs are the simplest type of generator to fabricate. Another major advantage is that piezoelectric generators are well suited for application not only to macroscopic but also micro-scale devices since several processes exist for depositing piezoelectric films (thin and thick) [9]. Piezoelectric based harvesters are also capable of delivering relatively high output voltage (but only at low electrical current), providing the needed voltage level (0.3-4 Volts) to charge a secondary battery or run a

sensor directly. This is in contrast with electromagnetic generators that may require transformers to meet applications with required voltage higher than ~ 2 V [1, 7, 21].

1.2.2.1 Piezoelectric Effect

Piezoelectric materials consist of ferroelectric materials, such as $\text{Pb}(\text{Zr,Ti})\text{O}_3$, BaTiO_3 , and LiNbO_3 , and non-ferroelectric materials, such as AlN and ZnO [33, 34]. One of the defining traits of a piezoelectric material is that the molecular structure is oriented such that the material exhibits a local charge separation, known as an electric dipole. Throughout the material composition, the electric dipoles are oriented randomly, and for ferroelectrics, the dipoles can be oriented such as when the material is heated slightly below the Curie temperature and/or a very strong field is applied, the electric dipoles reorient themselves relative to the electric field; this process is termed poling. Once the material is cooled, the dipoles maintain their orientation and the material is then said to be poled. After the poling process is completed, the material will exhibit a relatively high piezoelectric effect. Thus, poled ferroelectrics are very effective and attractive piezoelectrics. Energy conversion using piezoelectric materials is possible because mechanical strain in a piezoelectric material induces deformation of electric dipoles, forming electrical charges that can be removed from the material and used to power various devices. Such mechanical and electrical behavior of piezoelectric materials can be described using linear piezoelectric constitutive equations that contain relevant material property constants, one type of which expression is as follows:

$$T_i = c_{ij}^E S_j - e_{ij} E_j \quad (1.1)$$

$$D_i = e_{ij} S_j + \varepsilon_{ij}^S E_j \quad (1.2)$$

S_j and T_i are the mechanical strain and stress, while E_j and D_i are the electric field and the electrical displacement. c_{ij}^E represents the elastic stiffness coefficient and ε_{ij} is the permittivity values. When there is a superscript like S in ε_{ij}^S , it is such that the permittivity is evaluated at a

constant strain. Piezoelectric coefficient, e_{ij} , is the measure of piezoelectric coupling of the given active materials. Piezoelectric materials typically exhibit anisotropic characteristics, thus, the properties of the material differ depending upon the direction of forces and orientation of the polarization and electrodes. Subscripts in the equations above denote such directions. For a more complete description of the constants the reader is referred to the IEEE standards [35]. These constitutive equations are the basis to derive the governing equations of electromechanical modeling for PVEH systems, which will be used throughout this thesis. Since the piezoelectric materials are required to be strained directly, the performance, lifetime and transduction efficiency are dependent upon the materials properties. A rigorous model-based analysis and important findings on the relation of material properties and PVEH device performance are presented in Chapter 6.

1.2.2.2 Piezoelectric Materials

There is a wide range of piezoelectric materials available for different application environments [1, 33, 34, 36, 37]: single crystals, polycrystalline ceramics, polymers, composites, relaxor-type ferroelectrics, etc. Single crystal materials including quartz, lithium niobate (LiNbO_3) and lithium tantalate (LiTaO_3) are important functional materials in surface acoustic wave (SAW) devices and high-frequency filter applications [36]. However, little has been investigated on their use in energy harvesting. They have relatively high electromechanical coupling coefficients but small dielectric constant, generating less electricity than the ceramic material, PZT [38]. These materials are only available in bulk single crystals.

Polycrystalline ceramics are the most extensively explored as piezoelectric energy harvesting materials along with polymers [1, 33, 34]. Piezoelectric ceramic materials include ferroelectric materials with perovskite crystal structures such as barium titanate (BaTiO_3), lead titanate (PbTiO_3 , PCT), lead zirconate titanate ($\text{PbZr}_x\text{Ti}_{1-x}\text{O}_3$, PZT) and non-ferroelectric materials with wurtzite crystal structures such as ZnO and AlN. Among all, lead zirconate titanate (PZT), a solid solution of ferroelectric PbTiO_3 and antiferroelectric PbZrO_3 , is the most common type of piezoelectric used in energy harvesting applications due to its high piezoelectric coupling. The dielectric and piezoelectric constants of PZT depend strongly on materials

composition and doping. In terms of composition, PZT films at the morphotropic phase boundary (MPB) with a Zr/Ti ratio of 52/48 have been shown to exhibit a maximum in the piezoelectric response and are typically used in MEMS device applications. Doping effects on PZT material properties of various dopant elements such as Nb, Ta, and Mn have been many researchers' focus. Bulk poled PZT as a piezoelectric ceramic material is used widely in sensor, actuator, and transducer applications. PZT thin films are very competitive for power generation due to their higher piezoelectric coefficients than bulk PZT, and suitable for MEMS applications [37, 39]. Although PZT thin films have served successfully in numerous devices thanks to the advances of integration techniques, the growth of high-quality PZT thin films still needs some effort [33].

There has also been considerable interest in non-ferroelectric piezoelectric semiconductors such ZnO and AlN as harvesting materials. Their compatibility with conventional processing technologies for integrated circuit technology offer advantages to their development for MEMS-PVEHs. Thin films that are epitaxially grown on a substrate are the typical form because these materials are not ferroelectric and thus cannot be poled like perovskite materials. Although their piezoelectric coefficients are considerably lower than those of ferroelectric ceramics such as PZT, their semiconducting characteristics and potential application in bio-chemical sensors with improved sensitivity and selectivity (*e.g.*, ZnO nanorods) have brought a great deal of research into these materials [36]. In 2000, Wang and Song [40] at Georgia Institute of Technology demonstrated piezoelectric nanogenerators based on zinc oxide nanowire arrays, which can convert nanoscale mechanical energy into electrical energy with an efficiency of 17-30 %, attracting considerable attention in this area of research. Later, using semiconducting properties of ZnO, the same group developed a nanowire structured hybrid cell that can scavenge solar and mechanical vibration energies simultaneously [41]. Recently, Imec created an energy harvesting wireless sensor by employing AlN that can generate 85 μW of power, a record-setting amount for MEMS energy harvesters before packaging, but 10 μW of power after packaging to protect the device due to air-damping effects. This energy harvester was connected and operated to a power wireless temperature sensor that requires 10 μW ~1.5 mW upon optimization at the target vibration frequency, 353 Hz and at 0.64 g, making one step forward to commercialization of AlN-based energy harvesters [42].

There has been a growing interest in polymer piezoelectric materials [43] and poly(vinylidene fluoride) (PVDF) is the representative flexible piezoelectric material to serve in a number of energy harvesting prototype devices reported, such as “energy harvesting eels” described in the previous section [37]. Unlike brittle piezoelectric ceramic materials, polymer piezoelectric materials such as PVDF (PVF₂), or PVDF-TrFE offer considerable flexibility and thus can sustain large amounts of strain. In the development of polymer-based energy harvesters, durable and strong electrode layers are required to operate piezoelectric devices over time. To date, study on electrode materials for PVDF has been performed using not only inorganic materials such as platinum (Pt) and indium tin oxides (ITO), but also poly(3,4-ethylenedioxythiophene)/poly(4-styrenesulfonate) (PEDOT/PSS) electrodes in the form of coating onto PVDF.

Composite materials that typically consist of piezoelectric ceramic materials and polymers, mostly PZT rod and fibers embedded in a polymer matrix, have also been used for energy harvesting [10]. Sodano *et al.* performed several studies to compare harvesting ability and efficiency of macro-fiber composite (MFC) and quick-pack (QP) actuators with commercially available PZT ceramics [21, 44, 45].

Despite their extremely high electromechanical coupling coefficients, little research has been undertaken on energy harvesting devices based on relaxor-type ferroelectrics, suggesting more room for PVEH devices with enhanced performance [1, 36, 46]. There are (Mg_{1/3}Nb_{2/3})O₃ (PMN), Pb(Zn_{1/3}Nb_{2/3})O₃ (PZN), and binary forms of these systems coupled with PbTiO₃, PMN-PT and PZN-PT, respectively. Last but not least, it should be noted that material properties of thin films differ from those of bulk even for the same materials and thus, they should be evaluated differently [33, 34, 39]. Comprehensive reviews on piezoelectric materials’ history and properties in bulk form and progress to date in piezoelectric thin film materials and devices are available in numerous books [8, 48-51] and articles [33, 34, 36, 39].

1.2.2.3 Configurations of Piezoelectric Energy Harvesting Devices and Systems

A single PVEH device typically consists of piezoelectric layers, structural layers, electrode layers, and a proof mass. The most common geometric configuration is cantilever beams or

plates because it is geometrically compatible with MEMS fabrication processes and has proven to be easy to implement and effective for harvesting energy from ambient vibrations [37]. A cantilever is a compliant structure that can not only provide low resonant frequencies, reduced further by the addition of a mass on the end of the beam/plate, but also produce high strain, and thus more power generation, in comparison with other structural configurations [7]. There have been other efforts to enhance power performance of PVEH devices by modifying geometric configurations [1, 37]. Trapezoidal shapes by tapering or initially curved cantilevers were studied in order to improve conventional cantilever designs and to better suit other harvesting applications. Besides, triangular or clamped circular plates, known as ‘cymbal’, transducers have been of interest. S-, or T-shaped or modified membrane configurations are chosen to explore a wide range of vibrations using their nonlinear characteristics [1, 7]. Depending on the number of piezoelectric element layers, the structure can be categorized as unimorph, bimorph, or multi-layered (stack) configurations [1]. A unimorph configuration comprises one piezoelectric layer sandwiched between two electrodes along with structural layers. Two piezoelectric layers are involved in bimorph configurations and these two layers are interconnected electrically either in series or in parallel. There are two practical modes of transduction according to the direction of electrical field and applied strain: {3-1} and {3-3} modes of operation [52]. Conventionally, the poling direction is always in the “3” direction and thus this coincides with the direction of electric field induced upon applied mechanical strain. In {3-1} mode, the voltage (and therefore, electric field) act perpendicular to the “3” direction as the mechanical strain is applied in the “1” direction. In “3-3” mode, both strain and voltage occur in the same direction, “3”. Choice of electrode configuration is dependent upon the mode of operation. Standard capacitor type electrodes are employed for {3-1} modes of operation while interdigitated electrodes (IDTEs) are commonly used to implement {3-3} modes of operation, each of which is illustrated in Figures 1.4 and 1.5, respectively for cantilevered PVEH systems [1, 21, 53, 54]. Chapter 8 covers detailed modeling of these two different modes of operation and corresponding electrode configurations with associated schematics. Individual or arrays of energy harvester devices are wired to the appropriate electrical circuit to extract the electrical properties such as voltage and power. The input power source comes from base-excited mechanical vibrations. A general architecture of piezoelectric energy harvesting is illustrated in Figure 1.6.

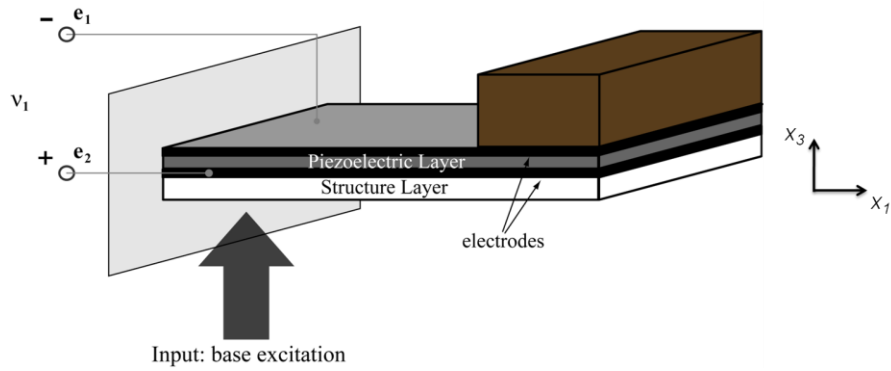


Figure 1.4 Unimorph cantilevered piezoelectric energy harvester device in {3-1} mode of operation with standard electrode configuration. Note asymmetric layers and the need for a “structural” layer.

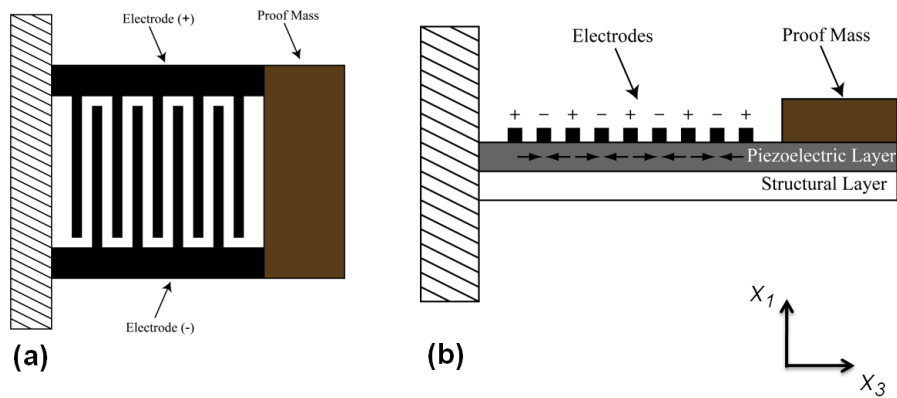


Figure 1.5 Interdigitated electrode (IDTE) configuration in cantilevered piezoelectric energy harvesting {3-3} mode devices: (a) top-view and (b) side-view.

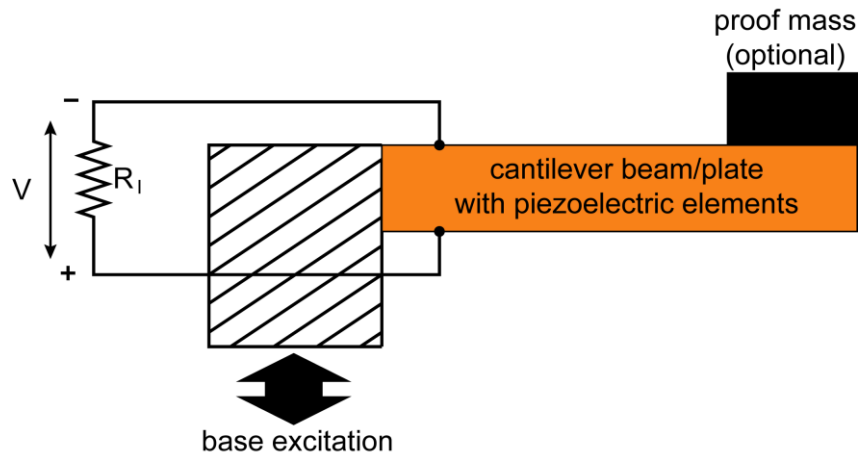


Figure 1.6 Schematic of a cantilevered piezoelectric energy harvesting system with simple electrical resistance loading, R_l .

1.2.2.4 Recent Advances and Future Trends

In 1967, a small, tip-loaded piezoelectric cantilever for powering bioelectric implants was proposed in the US patent [55] and shown to produce $150 \mu\text{W}$ when mechanically coupled to 80 Hz heartbeats. It is, however, the late 90's that active investigation on piezoelectric energy harvesting began in earnest. Due to the ever-increasing desire to produce portable and wireless electronics with extended lifespan, the use of piezoelectric materials to capitalize on ubiquitous ambient vibrations is one method that has seen dramatic growth both in research and use. Nonetheless, generation of sufficient amounts of power still remains a primary issue in practical applications. Accordingly, a majority of the latest research has focused on improving the efficiency of piezoelectric power harvesting devices through various ways: i) modification of device configurations such as bending modes and device geometries, ii) design and development of piezoelectric materials with enhanced properties, and iii) alteration of electrical circuits for power harvesting and storage. Recent advances PVEH devices are well summarized and available in several publications, some of which are briefly introduced in the following in chronological order. In 2004, Sodano *et al.* [21] reviewed the research that had been performed

in the field of piezoelectric vibration energy harvesting until 2003 with special focus on the development of power storage and circuitry, implantable and wearable power supplies based on piezoelectric energy harvesting reported by then, and also the damping effect on power harvesting. Beeby *et al.* [7] categorized the reported devices into impact coupled, human powered, cantilever-based and other PVEHs in their review in 2006 on vibration energy harvesting for wireless-self powered microsystems. As a follow-up of Sodano *et al.*'s paper, Anton *et al.* [37] published a review paper in 2007 that summarized the published harvesting devices and techniques using piezoelectric materials between 2003 and 2006. They discussed the reported devices according to the methods of improving power efficiency (*e.g.*, through piezoelectric configurations, through circuitry and method of power storage) and area of application (*e.g.*, implantable and wearable power supplies, harvesting ambient fluid flows, power harvesting in MEMS systems, and self-powered sensors). Cook-Chennault *et al.* [1] performed an extensive review on power supply systems for MEMS portable devices, where readers can find a useful list of proof-of-concept devices and fabrication techniques for piezoelectric energy harvesting under the categories of windmills, shoe inserts, implantable devices, wave energy, and pulse generators. Besides, readers can benefit from general reviews on the previous research on piezoelectric energy harvesting [9, 10, 28, 46].

One last note is on vibration energy harvesters operating in a wide range of frequencies. At resonance (and anti-resonance), vibration-based energy harvesting devices can produce maximum output power [29]. However, it is not easy to make the resonant frequency of the devices align with the frequencies available from the vibrations in the surroundings. Thus, other methods to extract more power from a given vibration source is designing vibration-based energy harvesting devices and systems that can be either tuned or operated over a wide range of frequencies instead of being operated only at resonances. Either intermittent or continuous tuning of the devices necessitates periodic change in dimensions or stiffness of the systems, or adjustment of capacitive loads in electrical circuits. In order to operate the devices at various frequencies, widening the bandwidth of device frequencies is a passive solution and this can be achieved by using arrays of energy harvesting devices or employing nonlinear or bi-stable structures. In addition to the efforts designing circuits that can optimize power flow from the piezoelectric energy harvesters and minimize circuit losses, development of strategies to increase

the operating frequency range is a key interest in current research of piezoelectric energy harvesting [57].

Chapter 2

Prior Work on Piezoelectric Vibration Energy Harvesters

2.1 Review of Existing Work

In order to harvest mechanical vibration energy utilizing the piezoelectric effect, researchers have developed devices for various applications including windmills, shoe inserts, implantable devices, etc. [1]. Especially, for applications in microsystems, several studies have focused on developing MEMS piezoelectric vibration energy harvesters (PVEHs) using established piezoelectric film processing [53, 54, 58-60] as described in Chapter 1. Along with research on fabrication of devices, researchers have also put considerable amount of effort in developing analytical models for PVEHs to study the dynamic characteristics of these structures. Several models have been proposed and applied not only to predict and analyze the devices but also to optimize the design for future applications.

Early modeling attempts include Smits and Chio's study [61] on the electromechanical characteristics of piezoelectric benders under various electrical and mechanical boundary conditions, which is based on internal energy conservation. However, no expression for voltage generation is provided in their model. Hwang *et al.* analyzed the static responses of a

piezoelectric bimorph beam based on finite element method but didn't perform model-experiment comparison study [62]. Umeda *et al.*[63] used mechanical lumped models of a mass, a spring, and a damper to derive equivalent circuit model that is capable of calculating the amount of electrical energy converted from impact energy. A simple, general model for the conversion of the kinetic energy of a vibrating mass to electrical power was proposed by Williams and Yates in 1996 [31]. This model is based on an assumed linear harmonic oscillator (mass-damper-spring) system without specifying conversion mechanisms and thus a number of researchers have adopted this model [1, 7, 10], particularly when there is a need to compare different vibration-based energy harvesting mechanisms. In this model, the effect of electromechanical coupling is represented by a viscous damping coefficient in the mechanical domain equation. This approach gives initial insight in performance from vibration conversion and is quite reasonable for a certain type of electromagnetic energy harvesters as Williams and Yates showed in their device evaluation [31]. Yet, it is not capable of incorporating the specific effect of piezoelectric coupling in the mechanical domain, which is more sophisticated than just viscous damping [64].

Roundy *et al.* formulated an equivalent electrical circuit model for PVEHs operated under low-g vibration conditions where they describe the mechanical components of the mechanical elements to represent the system purely in the electrical domain [65]. This is a convenient modeling approach since lumped parameters are easily expressed in the mechanical equilibrium and electrical loop equations, which can be directly coupled through the piezoelectric constitutive relations. While this analysis could highlight a key effect of the piezoelectric materials' electromechanical coupling behavior, it lacks mechanical dynamics of the structure such as the dynamic mode shape and the accurate strain distribution along the cantilevers. Furthermore, their assumption that the operating frequency is constant at the natural frequency of the structure results in neglecting a second higher frequency (optimal power) operating point, known as anti-resonance [29]. Lu *et al.* [66], Chen *et al.* [67], and Lin *et al.* [68] have also presented analytical modeling to evaluate the performance of piezoelectric power generators for MEMS applications, particularly in terms of power and conversion efficiencies, where they oversimplified the piezoelectric coupling in the beam equations as viscous damping and didn't consider the resonances phenomenon.

As an alternative modeling approach, Euler-Bernoulli beam theory [69] has also been applied to study the dynamics of PVEHs in combination with either force equilibrium analysis [70] or via energy methods [71]. Using the conventional combination of the variational principle (also known as the Hamilton's principle) and the Euler-Bernoulli beam assumptions, Sodano *et al.* [72] developed an analytical model for a cantilevered PVEH, which allows prediction of the electromechanical responses in higher vibration modes but misses some key points (*e.g.*, resonance and anti-resonance operating points of interest). As an improved modeling approach, a coupled electromechanical model, based on a structural modal analysis for a base-excited cantilever, was developed by du Toit *et al.* [73, 74]. In these studies, useful closed-form analytic expressions for key device performance characteristics were presented using the energy method approach focusing on a single vibrational mode [29, 30], from which both electrical and mechanical performance could be predicted and optimized across electrical loading conditions and frequencies. This power-optimized electromechanically coupled model was experimentally verified using a macroscopic, symmetric bimorph, piezoelectric {3-1} device. The verified model, in a convenient normalized form that allows clear interpretation of the device performance, may also be used for proper experimental design as in the current work. Other investigations of similar PVEH configurations are given by [75, 76]. Erturk and Inman [77, 78] derived a distributed parameter electromechanical model for cantilevered PVEHs, based on Euler-Bernoulli theory. In their analysis, base motion is not restricted to harmonic oscillation widely used and is described using not only transverse displacement but also small rotation. Experimental verification of this model is available in [76] where the model was applied to bimorph cantilever configurations both with series and parallel connections of piezoelectric layers. Their analysis provides similar results to du Toit *et al.*'s modeling approach but omits the normalization and many key trends (*e.g.*, resonance and anti-resonance operating points of interest). Ajitsaria *et al.* [75] also presented a bimorph cantilever model which combines Euler-Bernoulli beam theory and Timoshenko beam equations. The issue here is that they combined the static piezoelectric actuation equations where radius of curvature and a static tip force exist with the dynamic Euler-Bernoulli beam equations where the radius of curvature clearly varies spatially along the beam.

In many analyses, cantilever beam and plate configurations were chosen not only because

they are geometrically compatible with MEMS fabrication processes, but also because such a compliant structure can produce high strain, and thus more power generation, in comparison with other structural configurations.

Various modeling approaches have appeared in the literature and are briefly described as above. Some of them might be misleading due to weak mathematical assumptions involved or oversimplifications. The work in this thesis mainly follows the electromechanically coupled modal model for cantilevered PVEHs presented by du Toit *et al.* [29, 30, 73, 74] to develop more accurate analytical model for PVEH devices with a proof mass. It entails correction of key parameters in the governing equations, a more detailed damping ratio analysis, and implementation of the model on specific test-device configurations (*e.g.*, unimorph and bimorph, modes of operation with different electrode configurations).

2.2 Modeling of Cantilevered Piezoelectric Vibration Energy Harvesters

In this section, a coupled electromechanical modal model [30, 74] is briefly reviewed before a detailed derivation to incorporate the proof mass is undertaken in Chapter 3. The derivation is based on Euler-Bernoulli theory and an energy method approach. Then, key mechanical and electrical device characteristics are extracted. While modeling begins with treatment of the general multi-degree-of-freedom system, the closed-form analytic solution in a single mode model is of focus that has been shown to be adequate to predict device performance in past work [29, 30, 73, 74]. The model is implemented for the case of various energy harvesters built and tested for model verification [30, 74]. Each energy harvester is composed of piezoelectric elements, structural layers, and electrodes and the device is wired to the appropriate electrical circuit to extract voltage and power. The input power source comes from base-excited mechanical vibrations (see Figures 1.6 and 2.1).

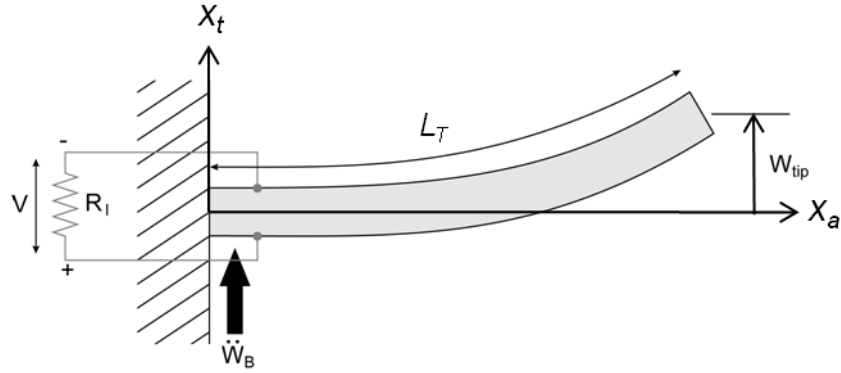


Figure 2.1 Schematic of a base-excited cantilevered PVEH. Here, v is the voltage developed across electrical resistance, R_l . w_{tip} and \ddot{w}_B represent tip displacement and base acceleration, respectively while L_T indicates the total length of the cantilever. x_t denotes the transverse beam/plate coordinate while x_a is the axial beam/plate coordinate.

2.2.1 Beams and Plates with Piezoelectric Elements

There are two methods to obtain the model for a cantilever beam/plate with piezoelectric elements: an energy method approach and a force equilibrium analysis [70]. Our study is based on the energy method approach, following the energy formulation for actuators by Hagood *et al.* [71] and developed by du Toit *et al.* [74] for energy harvesting. According to the energy conservation law, an electromechanical system can be modeled in terms of the sum of kinetic energy (T_k), internal potential energy (U), electrical energy (W_e) and external work (W) as follows:

$$\int_{t_1}^{t_2} [\delta(T_k - U + W_e) + \delta W] dt = 0 \quad (2.1)$$

Individual energy terms and external work term are defined as:

$$T_k = \frac{1}{2} \int_{V_s} \rho_s \dot{\mathbf{u}}^t \dot{\mathbf{u}} dV_s + \frac{1}{2} \int_{V_p} \rho_p \dot{\mathbf{u}}^t \dot{\mathbf{u}} dV_p \quad (2.2)$$

$$U = \frac{1}{2} \int_{V_s} \mathbf{S}^t \mathbf{T} dV_s + \frac{1}{2} \int_{V_p} \mathbf{S}^t \mathbf{T} dV_p \quad (2.3)$$

$$W_e = \frac{1}{2} \int_{V_p} \mathbf{E}^t \mathbf{D} dV_p \quad (2.4)$$

$$\delta W = \sum_{k=1}^{nr} \delta \mathbf{u}_k \mathbf{f}_k(t) + \sum_{j=1}^{nq} \delta \varphi_j \mathbf{q}_j \quad (2.5)$$

V_p and V_s are volumes of piezoelectric element section and of the structural (inactive) section of the beam, respectively. Likewise, ρ_p and ρ_s denote densities of each section. Dots indicate the time derivatives and $\mathbf{u}(\mathbf{x}, t)$ is the relative displacement matrix, and $\dot{\mathbf{u}}$ represents the velocity. It should be noted that the relative displacement of the structure, $\mathbf{u}(\mathbf{x}, t)$ can be written as the sum of nr individual modes shapes, $\psi_{ri}(\mathbf{x})$, multiplied by a generalized mechanical coordinate, $r_i(t)$, using the Raleigh-Ritz approach [69, 71]. The mode shape is a function only of the axial position because only the transverse displacement (x_t direction) is considered in bending of a beam/plate. Thus, $\mathbf{u}(\mathbf{x}, t)$ can be expressed as $w(x_a, t)$, which is the beam displacement relative to the base of the beam/plate, where x_a is the axial beam/plate coordinate. The relative displacement above is given in equation (2.6):

$$\mathbf{u}(\mathbf{x}, t) = w(x_a, t) = \sum_{i=1}^{nr} \psi_{ri}(x_a) r_i(t) = \boldsymbol{\psi}_r(x_a) \mathbf{r}(t) \quad (2.6)$$

where $\boldsymbol{\psi}_r(x_a)$ represents the row matrix, $[\psi_{r1}(x_a), \psi_{r2}(x_a), \dots]$ of mode shapes.

Equations (2.3) and (2.4) represent the internal potential and electrical energies in terms of the \mathbf{S} , \mathbf{T} , \mathbf{E} , and \mathbf{D} matrices. The \mathbf{S} , \mathbf{T} , \mathbf{E} , and \mathbf{D} matrices are defined as applied strain, developed stress, applied electric field, and developed electric displacement, respectively and the

superscript, \mathbf{t} , here indicates the transpose of the matrix. According to 3-D linear elastic (small-strain) constitutive relations, these matrices are related through electrical parameters such as the permittivity of the piezoelectric element, $\boldsymbol{\varepsilon}$, the piezoelectric constant relating charge density and strain, \mathbf{e} , and the mechanical parameter, \mathbf{c}^E , the stiffness matrix. These physical parameters are obtained differently depending on whether the structure is a beam or a plate (see discussion in [29, 73]). Equation (2.7) is the representative expression for three-dimensional linear elastic constitutive relations where a range of small-signal piezoelectric motion is assumed:

$$\begin{Bmatrix} \mathbf{T} \\ \mathbf{D} \end{Bmatrix} = \begin{bmatrix} \mathbf{c}^E & -\mathbf{e}^t \\ \mathbf{e} & \boldsymbol{\varepsilon}^S \end{bmatrix} \begin{Bmatrix} \mathbf{S} \\ \mathbf{E} \end{Bmatrix} \quad (2.7)$$

Superscripts E , S indicate parameters at constant electric field and constant strain. The three-dimensional linear elastic constitutive relations in equation (2.7) can be easily reduced for simple beam theory and {3-1} and {3-3} modes of operation [29, 30]. For {3-1} mode of operations, for instance, equation (2.7) is reduced to:

$$\begin{Bmatrix} T_1 \\ D_3 \end{Bmatrix} = \begin{bmatrix} c_{11}^E * & -e_{31} * \\ e_{31} * & \varepsilon_{33}^S * \end{bmatrix} \begin{Bmatrix} S_1 \\ E_3 \end{Bmatrix} \quad (2.7a)$$

where analytical expressions of material property constants depending on beam or plate configurations can be found in Appendix A in detail. Appendix A includes the reductions not only for simple beam/plate theory but also for {3-3} mode of operation.

Strain is expressed with respect to mechanical mode shapes. The Euler-Bernoulli beam theory allows the axial strain, S_1 , in the beam to be written in terms of the beam neutral axis displacement and the distance from the neutral axis (x_t : transverse direction, see Figure 2.1), as given by equation (2.8):

$$S_1 = -x_t \frac{\partial^2 w(x_a, t)}{\partial x_a^2} = -x_t \psi_r'' r(t) \quad (2.8)$$

Primes represent spatial derivatives throughout this thesis. Lastly, in order to define the external work term in equation (2.5), nf discretely applied external point forces, $\mathbf{f}_k(t)$ at positions \mathbf{x}_k , and nq charges, q_j , extracted at discrete electrodes with positions \mathbf{x}_j are introduced. In this same equation for the external work term, the quantity $\varphi_j = \varphi(\mathbf{x}_j, t)$ is the scalar electrical potential for each of the nq electrode pairs. For {3-1} mode devices, there is only one electrode pair on either surface of the piezoelectric element, while for a {3-3} mode test device, there may be a large number of electrode pairs distributed over one surface of the piezoelectric layer. This scalar electrical potential term, $\varphi_j = \varphi(\mathbf{x}_j, t)$ can be expressed via a potential distribution, $\psi_{vj}(\mathbf{x})$, and the generalized electrical voltage coordinate, $v_j(t)$ as in equation (2.9):

$$\varphi(\mathbf{x}, t) = \sum_{j=1}^{nq} \psi_{vj}(\mathbf{x}) v_j(t) = \boldsymbol{\psi}_v(\mathbf{x}) \mathbf{v}(t) \quad (2.9)$$

It is important to differentiate the electrical mode shape vector, $\boldsymbol{\psi}_v(\mathbf{x})$ from the mechanical mode shape vector, $\boldsymbol{\psi}_r(\mathbf{x})$. The form of electrical mode shapes varies according to the specifics of test-devices, and will be detailed in later sections.

When one substitutes equations (2.6) to (2.9) into equations (2.2) to (2.5), the energy and external work expressions in equations (2.2) to (2.5) can be rewritten in terms of mechanical or electrical mode shapes and material parameters. These rewritten equations (2.2) to (2.5) are then inserted back into the energy conservation equation (2.1). Finally, rearrangement of equation (2.1) allows us to obtain two governing equations of motion as below:

$$\mathbf{M}\ddot{\mathbf{r}} + \mathbf{C}\dot{\mathbf{r}} + \mathbf{K}\mathbf{r} - \boldsymbol{\Theta}\mathbf{v} = -\mathbf{B}_f\ddot{w}_B \quad (2.10)$$

$$\boldsymbol{\Theta}^t \mathbf{r} + \mathbf{C}_p \mathbf{v} + \mathbf{q} = 0 \quad (2.11)$$

As defined in equation (2.6), \mathbf{r} denotes the generalized relative displacement vector. As shown in equation (2.6), in order to convert it to actual displacements, it is necessary to multiply it with the mechanical mode shapes. Exact modal analysis will be followed in the next section. \mathbf{v} is the developed voltage across the piezoelectric element and \mathbf{q} is the charge. Base acceleration, \ddot{w}_B , is

the input to the cantilevered system (see Figure 2.1). Several effective terms, including the mass (\mathbf{M}), the stiffness (\mathbf{K}), coupling ($\mathbf{\Theta}$), and capacitive matrices (\mathbf{C}_p), are defined below. The forcing vector, \mathbf{B}_f , accounts for inertial loading on the beam/plate structure due to the base excitations:

$$\mathbf{M} = \int_{V_s} \boldsymbol{\psi}_r^t \rho_s \boldsymbol{\psi}_r dV_s + \int_{V_p} \boldsymbol{\psi}_r^t \rho_p \boldsymbol{\psi}_r dV_p \quad (2.12)$$

$$\mathbf{K} = \int_{V_s} (-x_t \boldsymbol{\psi}_r'')^t \mathbf{c}_s (-x_t \boldsymbol{\psi}_r'') dV_s + \int_{V_p} (-x_t \boldsymbol{\psi}_r'')^t \mathbf{c}^E (-x_t \boldsymbol{\psi}_r'') dV_p \quad (2.13)$$

$$\mathbf{\Theta} = \int_{V_p} (-x_t \boldsymbol{\psi}_r'')^t \mathbf{e}^t (-\nabla \boldsymbol{\psi}_v) dV_p \quad (2.14)$$

$$\mathbf{C}_p = \int_{V_p} (-\nabla \boldsymbol{\psi}_v)^t \boldsymbol{\varepsilon}^S (-\nabla \boldsymbol{\psi}_v) dV_p \quad (2.15)$$

$$\mathbf{B}_f = \int_0^L m(x_a) \boldsymbol{\psi}_r^t dx_a \quad (2.16)$$

Mechanical mode shapes, electrical mode shapes, and their derivatives mainly comprise these terms. Details on conventions of materials properties used here can be found elsewhere [8, 30, 74]. It should be noted that mechanical damping is included by adding a viscous damping term, \mathbf{C} . As it is assumed that the damping has little dependence on the device natural frequency, damping is typically measured at the device natural frequency, which will be covered in detail in Section 3.4. In the general multi-degree-of-freedom (MDOF) governing equations obtained above, the mechanical domain represented by the actuation equation (2.10) is electromechanically coupled to the electrical domain expressed by the sensing equation (2.11) via the coupling term ($\mathbf{\Theta}$). As the electromechanical coupling stems from the piezoelectric element, the coupling term ($\mathbf{\Theta}$) is directly related to the piezoelectric constants (\mathbf{e}) as shown in equation (2.14). Evaluation of the above coefficients from equations (2.12) to (2.16) for practical applications will be presented in later sections, using a single beam mode ($\boldsymbol{\psi}_{r1}$).

2.2.2 Electromechanical Model for Single Beam Mode and Power Optimization

Expressions for a single beam/plate mode can be obtained if one approximates the infinite degree-of-freedom mechanical system as a single-degree-of-freedom (SDOF) system, where the multi-degree-of-freedom (MDOF) governing equations of motion are reduced to scalar forms. In order to apply the coupled model presented, it is more practical to have scalar equations, which allow simple optimization in terms of maximum power extraction. Single-mode solutions have been shown to be in excellent agreement with results for devices without a proof mass [74]. In a single beam mode for base-excited PVEH structures, scalar expressions in equations (2.17) and (2.18) replace previously presented multi-degree-of-freedom (MDOF) equations (2.10) and (2.11):

$$M\ddot{r} + C\dot{r} + Kr - \theta v = -B_f \ddot{w}_B \quad (2.17)$$

$$\theta \dot{r} + C_p \dot{v} + \frac{1}{R_l} v = 0 \quad (2.18)$$

Note that the sensing equation (2.18) is modified from equation (2.11) by time differentiation, and by using Ohm's law, $v = R_l \frac{dq}{dt}$, for a purely resistive electrical load, R_l . Each coefficient in the single-mode governing equations above can be expressed as below:

$$M = \int_0^L m \psi_r^2 dx_a \quad (2.19)$$

$$K = \int (-x_t \psi_r'') (c_s + c_{11}^{E*}) (-x_t \psi_r'') dV \quad (2.20)$$

$$\theta = \int (-x_t \psi_r'') (e_{31}^*) (-\nabla \psi_v) dV \quad (2.21)$$

$$C_p = \int (-\nabla \psi_v)(\varepsilon_{33}^{S*})(-\nabla \psi_v) dV \quad (2.22)$$

$$B_f = \int_0^L m \psi_r dx_a \quad (2.23)$$

The dV above implies integration over the entire assembly both dV_s and dV_p . The location of the neutral axis, $(x_t)_{NA}$, is found in the usual way for elastic modulus-weighted beams [69]. In equation (2.20), c_s represents the stiffness of structural layers in the axial beam direction and c_{11}^{E*} denotes the effective piezoelectric material elastic stiffness for beam or plate in {3-1} mode of operation (see Appendix A). Note that c_{11}^{E*} , e_{31}^* , and ε_{33}^{S*} are written in equations (2.20) to (2.22) and these expressions can be used for a {3-1} mode PVEH device while c_{33}^{E*} , e_{33}^* , and ε_{33}^{S*} should be used for modeling of {3-3} mode PVEH (see Section 8.1 and Appendix A). In the above, ψ_r and ψ_v will from now on refer to the first mode, ψ_{r1} and ψ_{v1} . As electrical mode shape, ψ_v , highly depends on device specifics including electrical connections between piezoelectric layers and mode operations, coupling term, θ , and capacitance term, C_p , will also vary depending on test-device setups. Geometric configurations of energy harvesters, such as uni-morph or bi-morph structures as well as inter-element connection also affect the effective representations for coupling and capacitive terms. Therefore, suitable equations for coupling and capacitance that correspond to our test-device specifics will be given in the next section.

From the governing equations (2.17) and (2.18), convenient closed form solutions of the relative displacement, voltage developed and power extracted can be obtained, by assuming harmonic oscillation, $r = r_0 e^{i\omega t}$, $v = v_0 e^{i\omega t}$, and $\ddot{w}_B = w_B e^{i\omega t}$ in these equations. The magnitude of the power is calculated as $P_{out} = v^2 / R_l$. These solutions for the mechanical and electrical performance of the PVEHs are [74]:

$$\left| \frac{r}{B_f \ddot{w}_B} \right| = \frac{1}{K} \frac{\sqrt{1 + (\alpha\Omega)^2}}{\sqrt{[(1 - \Omega^2) - 2\zeta_m \alpha\Omega^2]^2 + [(\{1 + \kappa^2\} - \Omega^2)\alpha\Omega + 2\zeta_m \Omega]^2}} \quad (2.24)$$

$$\left| \frac{v}{B_f \ddot{w}_B} \right| = \frac{1}{|\theta|} \frac{\alpha\kappa^2\Omega}{\sqrt{[(1 - \Omega^2) - 2\zeta_m \alpha\Omega^2]^2 + [(\{1 + \kappa^2\} - \Omega^2)\alpha\Omega + 2\zeta_m \Omega]^2}} \quad (2.25)$$

$$\left| \frac{P_{out}}{(B_f \ddot{w}_B)^2} \right| = \frac{\omega_1}{K} \frac{\alpha\kappa^2\Omega^2}{[(1 - \Omega^2) - 2\zeta_m \alpha\Omega^2]^2 + [(\{1 + \kappa^2\} - \Omega^2)\alpha\Omega + 2\zeta_m \Omega]^2} \quad (2.26)$$

In the above expressions, ω_1 denotes the first resonant frequency of a cantilever structure and dimensionless factors are defined such that $\alpha = \omega_1 R_l C_p$ for dimensionless time constant, $\kappa^2 = \frac{\theta^2}{K C_p}$ for system coupling, and $\Omega = \frac{\omega}{\omega_1}$ for the dimensionless frequency ratio. Also, mechanical damping ratio, ζ_m appears and it is related to the damping constant, C via $\zeta_m = \frac{C}{2M\omega_1}$. Mechanical response is calculated using the generalized mechanical displacement, r , which should be multiplied by the normalized mode shape to yield relative displacements, w , that is, $w = \psi_r(x)r$. Note that all these equations for system response are non-dimensionalized with an inertia force represented either by $B_f \ddot{w}_B$ or $(B_f \ddot{w}_B)^2$. It is quite beneficial to be able to use solutions that are properly normalized as one can avoid complications generated from the calculations of complex numbers [76] in order to obtain the results. Also, the way the denominator appears in all three expressions is also noteworthy. As presented previously by du Toit *et al* [29, 30, 73, 74], two optimal frequency ratios for *equal* maximum power generation are gained at resonance and anti-resonance ($\Omega_r = 1$ and $\Omega_{ar} = \sqrt{1 + \kappa^2}$, respectively). The natural frequency will correspond to either the resonance or anti-resonance frequency, depending on the electrical loading for a piezoelectric structure. These two frequency ratios are obtained from the analysis of the system at short-circuit condition ($R_l, \alpha \rightarrow 0$) and open-circuit condition ($R_l, \alpha \rightarrow \infty$). As natural frequencies are generally defined by the ratio of stiffness to mass of the system as in

$\omega = \sqrt{K_{eff} / M}$, the origin of these two natural frequencies for an electromechanically coupled system can be explained from the perspective of stiffness, K_{eff} . If one sets $\Omega = 0$ in equation (2.24), two different effective static stiffnesses, K_{eff} , are obtained by short-circuit condition ($\alpha \rightarrow 0$) and open-circuit condition ($\alpha \rightarrow \infty$), which are K and $K(1+\kappa^2)$, respectively. These stiffnesses stem directly from the piezoelectric constitutive relations that always specify the electrical or stress boundary condition at which the piezoelectric constant is measured [31]. Since the terms inside the denominator of equations (2.24)-(2.26) are succinctly arranged focusing on these two optimal frequency ratio expressions, it is readily possible to analyze the system responses at optimal points for maximum power extraction from the equations (2.24)-(2.26). In order to derive the maximum power value, it is necessary to optimize the power equation (2.26) with respect to load resistance (R_l), which yields a power-optimal electrical load in terms of dimensionless time constant, α_{opt} :

$$\alpha_{opt}^2 = \frac{1}{\Omega^2} \frac{(1-\Omega^2)^2 + (2\zeta_m \Omega)^2}{([1+\kappa^2]-\Omega^2)^2 + (2\zeta_m \Omega)^2} \quad (2.27)$$

Substitution of suitable frequency ratios at both resonance ($\Omega_r = 1$) and anti-resonance ($\Omega_{ar} = \sqrt{1+\kappa^2}$) into equation (2.27) yields two optimal electrical loadings, $\alpha_{opt,r}$ at resonance and $\alpha_{opt,ar}$ at anti-resonance:

$$\alpha_{opt,r}^2 = \frac{4\zeta_m^2}{4\zeta_m^2 + \kappa^4} \quad (2.28)$$

$$\alpha_{opt,ar}^2 = \frac{\kappa^4 + 4\zeta_m^2(1+\kappa^2)}{4\zeta_m^2(1+\kappa^2)^2} \quad (2.29)$$

Note that both optimal electrical loading conditions are dependent on mechanical damping as well as system coupling, and are roughly reciprocals of one another in α_{opt}^2 . Once these values are substituted back into the power equation (2.26), optimal power expressions at resonance and

anti-resonance are gained. In general, mechanical damping ratio, ζ_m , is at least an order of magnitude smaller than square of system coupling, κ^2 , which allows us to approximate equations (2.28) and (2.29) to give simpler expressions for power as well. Using the approximation, $2\zeta_m/\kappa^2 \ll 1$, equations (2.28) and (2.29) may be simplified to produce optimized power both at resonance and anti-resonance as follows:

$$\left| \frac{P_{out}}{(B_f \ddot{w}_B)^2} \right|_{opt,r} = \frac{\omega_1}{K} \frac{1}{8\zeta_m} \quad (2.30)$$

$$\left| \frac{P_{out}}{(B_f \ddot{w}_B)^2} \right|_{opt,ar} = \frac{\omega_1}{K} \frac{\frac{1}{2\zeta_m} \kappa^4}{4\kappa^4 + 4\zeta_m^2(1 + \kappa^2)} \approx \frac{\omega_1}{K} \frac{1}{8\zeta_m} \quad (2.31)$$

As pointed out previously by du Toit *et al* [29], the values of optimal power generated at resonance and anti-resonance have equal magnitude within the given assumptions. It has been shown that for extremely high values of damping (perhaps when the harvester is used as a damper) not seen in typical macro-scale harvesting devices, and certainly not in MEMS devices that have high quality factors, that the approximation above does not hold [76].

2.3 Issues and Unsolved Problems in Current Understanding of Piezoelectric Energy Harvesters

The ultimate goal in research of PVEHs is to realize a powering device that can provide sufficient power for practical applications such that operation of wireless electronics in a self-powered manner is possible. A great deal of the latest research has focused on improving the efficiency of PVEH devices through exploration of various piezoelectric materials, device configurations, and optimization of circuit designs, as summarized in Section 1.2. Thus, it is quite essential to identify and understand the relevant variables and factors that influence the output performance of such harvesting devices in finding innovative ways to develop devices

with enhanced performance. A number of factors have been detailed in the literature based on modeling studies, giving a starting point for device designs. In various modeling approaches proposed, the basic objective of modeling PVEHs is to estimate the amount of voltage developed across electrical resistances in PVEH devices during vibrating operation and then calculate power.

The simplest way to model the piezoelectric harvesting system is to consider the harvesting structure as a mass-spring-damper system and couple it with a simple electrical circuit [31]. Although simple closed-form expressions from this lumped-parameter modeling provide general insight into the problem, it is not capable of fully capturing the piezoelectric coupling effect on system behavior. While many review papers [1, 7, 10] introduce either general kinetic conversion model or electrical equivalent model as representative analysis method for piezoelectric energy harvesting systems, both analyses permit prediction of system responses only at resonance and lack structural dynamics and design and optimization capabilities.

Extensive theoretical analysis of cantilevered PVEHs is possible based on Euler-Bernoulli theory in conjunction with constitutive piezoelectric relations, as du Toit *et al.* presented [73, 74]. This modeling approach can not only predict power harvesting performance, but also capture important aspects of the harvesting systems such as the dynamic mode shape and strain distribution along the cantilever. However, such studies [72-74, 77, 78] have not given much attention to accurate treatment of proof mass effects on PVEH performance, while it is very common to attach or integrate a proof mass at the end of the MEMS-scale cantilevers to obtain the target frequency of interest. As discussed in the following chapters of this thesis, it is observed that even a small change in proof mass geometry results in a substantial change in device performance. This suggests the importance of appropriate treatment of proof mass configuration in device design. Particularly, long, thin, distributed proof masses that are quite common in MEMS-scale devices due to the constraints of thin film processing necessitate more rigorous analysis for such configuration along with experimental verification of such new-developed models.

Besides investigation on the proof mass effects, there are a number of unsolved but important problems that can be answered through proper utilization of models. The first example can be model-derived piezoelectric materials design studies (Chapter 6). To date, analytical

modeling serves in predicting and analyzing the characteristics of PVEHs mainly at the system levels. This enables development of more power -efficient devices through system optimization both at the design level and fabrication. In terms of piezoelectric materials, the primary focus of materials scientists has been on the achievement of materials with the highest piezoelectric coupling coefficients in order to extract more power from a given structure. In that regard, tremendous effort has been put to obtain lead zirconate titanate (PZT) with composition (Zr:Ti = 53:47) near the morphotropic phase boundary [33, 39]. However, the aforementioned depends simply on intuitive consideration and little study has been performed to reveal the detailed relation of piezoelectric materials properties to harvesting device performance.

In addition, a full set of key performance metrics for comparing different PVEH devices have not been clearly defined and standardized, presenting a need for better figures of merit of device performance (Chapter 7). In a majority of analyses, calculation of output electrical power extracted from piezoelectric vibration harvesting has been of primary interest and not much attention has been paid to analytical description of mechanical input power. In order to evaluate harvesting efficiency, defined as the ratio of electrical output power to mechanical input power, it is required to quantify the mechanical input power that the harvesting system can absorb from surrounding vibrations in terms of key system parameters as in the analytical expression for electrical power output. This will help identifying and optimizing system parameters that can be manipulated to gain more mechanical power from given vibration sources and convert it into electrical power with greater efficiency.

Another way of utilizing a model is to develop a multi-variable design tool for performance optimized PVEHs (Chapters 8 and 9) as attempted by Mracek [79]. Hence, design optimization studies based on a verified analytical electromechanical model are suggested, where the final goal is to propose an optimized design for MEMS harvesting devices that is suitable for specific applications of interest.

All these issues and unsolved problems in the current PVEH research have provided the main impetus to the research work in this thesis.

2.4 Overview of This Thesis

The primary goal of this thesis is to make steps forward to realizing pervasive use of wireless, battery-less small electronics powered by MEMS-PVEHs. With this purpose in mind, this thesis contributes new knowledge for better understanding of PVEHs both at materials- and systems-levels. Furthermore, it provides thorough, systematic model-based design guidelines for both optimum piezoelectric material and energy harvesting devices along with the demonstration of a design for a MEMS-PVEH with novel structural layers.

This thesis consists of eleven chapters, starting with Chapter 1 where general concepts of energy harvesting and overview of piezoelectric energy harvesting research are introduced. Chapter 2 follows with a review of existing modeling work for PVEHs while raising concerns and problems that have not been dealt with yet to date. Some of the analysis is extended from the analytical modeling previously developed by du Toit *et al.* [74] and reviewed in detail in Section 2.2.

Chapter 3 contains three levels of modeling of proof mass effects on piezoelectric energy harvesting performance in order to highlight the significance of appropriate treatment of the proof mass in device design. Those include a simple approximation for concentrated proof mass (Section 3.1), improved treatment of rigid proof mass with rotation (Section 3.2), and exact treatment of a flexible proof mass using a two-beam method (Section 3.3).

Chapter 4 and Chapter 5 include experimental verification of the model developed in Chapter 3. Detailed discussion of both mechanical and electrical performance of macroscopic PVEH devices is made in addition to test device specific model implementation and model-experiment comparison study (Chapter 4). Chapter 5 includes experiment-model correlation of mechanical behavior of distributed flexible proof mass of micron-scale cantilevers and its implications for performance of piezoelectric energy harvesting.

Chapter 6 contains an assessment of which, and how relevant, different piezoelectric material properties affect the PVEH device performance, followed by the discussion on how one can apply this knowledge to material and device design for better performance.

Chapter 7 contains standardized key performance metrics for PVEHs and offers ways to utilize the developed model for estimation of materials and system properties in two different

ways: bottom-up and top-down approaches. This helps construction of test methods for full characterization of PVEH performance for a given system, as presented in Chapter 8. Chapter 7 also contains analytical expressions and explains system behavior of device performance such as voltage and power when they are optimized under various operating conditions including input operating frequencies and mechanical damping.

Chapter 8 begins with model implementation and its comparison with experimental test results of MEMS-PVEH devices fabricated by collaborators. Particular attention is given to modeling of a unimorph PVEH with interdigitated electrode (IDTE) configurations. A multi-variable design tool for performance-optimized PVEHs is proposed with a case study (Section 8.3).

In Chapter 9, the tool developed in Chapter 8 is also applied to novel structural layer materials (heterostructure piezoelectric/ultrananocrystalline diamond thin films). This work yields a power-optimized device design for MEMS-PVEHs that will be fabricated and characterized at Argonne National Laboratory.

Chapter 10 contains other possible uses of the developed analytical model. Those include modeling of piezoelectric actuator systems (Section 10.1) and design of low-strain fatigue-resistant MEMS resonators (Section 10.2).

In Chapter 11, the author summarizes the conclusions of this thesis with emphasis on the impact of each part of this work to the research community, followed by a list of ongoing and future work.

Chapter 3

Modeling of Proof Mass Effects on Vibration Energy Harvester Performance

In MEMS applications, as the device dimensions scale down, the natural frequencies of these devices increase and can approach the GHz range. In order to use MEMS-scale energy harvester devices for practical applications, it is desirable to adjust the natural frequencies to lower levels where more significant energy is found in typical spectra [29]. A beam end mass, so called a proof mass, is integral to tune device resonances towards target frequency points in order to use these devices for practical applications in resonant operation. The role of the proof mass becomes significant particularly in realizing MEMS-PVEHs since it enables not only harvesting of low-level vibrations by serving to decrease the resonant frequency of a device, but also generation of increased power by raising the average level of stress and strain in the piezoelectric layer along the beam length that is converted to electrical energy. While it is common to attach or integrate a proof mass at the end of MEMS-scale cantilevers to obtain the target frequency of interest [53, 54], insufficient attention has been paid to a rigorous analytical treatment of a proof mass. In this chapter, an electromechanically coupled model for a cantilevered PVEH with a proof mass is presented.

The most common way to calculate the resonant frequency of a cantilever with a proof mass that is found in the literature is to simply approximate a concentrated proof mass at an

arbitrary point on the beam and to consider the effective mass of the system [75, 80-82]. Such a concentrated mass (or center-of-mass) model is not capable of capturing the structural dynamics that result from geometric properties of a distributed proof mass. Following a brief review on this concentrated proof mass modeling approach in Section 3.1, a more sophisticated approach is presented in Section 3.2. There, a proof mass is considered rigid and contains rotational terms, based on the assumption that the stiffness of a proof mass is much higher than that of the cantilever beam itself, so that the proof mass contributes to the entire system with regard to mass increase. This analysis eliminates the necessity of choosing an arbitrary point for a center-of-mass calculation and thus provides a more accurate prediction for both resonant frequencies and device performance. A model for a flexible, distributed proof mass of MEMS-scale cantilevers follows in Section 3.3. Long, thin, distributed proof masses are quite common in MEMS devices due to the constraints of thin-film processing (*e.g.*, deposition height of proof mass, resolution of lithography, *etc.*). Thus, a flexible proof mass analysis is useful when the proof mass makes contributions not only to the mass but also to the bending stiffness of the system. Both the rigid proof mass and flexible proof mass models are based on a detailed modal analysis.

3.1 Simple Approximation for Concentrated Proof Mass

Many researchers apply a point-mass assumption or concentrated mass assumption when they need to estimate natural frequency of a given structure for design purposes of devices operated at resonance. It is a convenient way to calculate resonant frequencies relatively easily but even this concentrated proof mass assumption is sometimes misapplied, presenting a need for refinement.

In this scheme, a proof mass is assumed to be concentrated at a certain point (mostly located at the half of proof mass length), which means neither geometric dimension nor structural dynamics of a proof mass added to the cantilever contributes to the proof mass modeling. The basic concept of the concentrated proof mass assumption along with relevant dimensions is shown in Figure 3.1. Total length, L_T is the sum of active beam length, L , and the proof mass length, L_{PM} . It is convenient to introduce a parameter, “effective length”, L_e ($= L + 1/2L_{PM}$), which is a distance from the anchor of the cantilever to the point where mass is assumed

to concentrate. Concentrated mass of a proof mass added at the tip is denoted as M_{PM} while m is used for beam mass per length and thus the total mass, $M_T = mL_T + M_{PM}$.

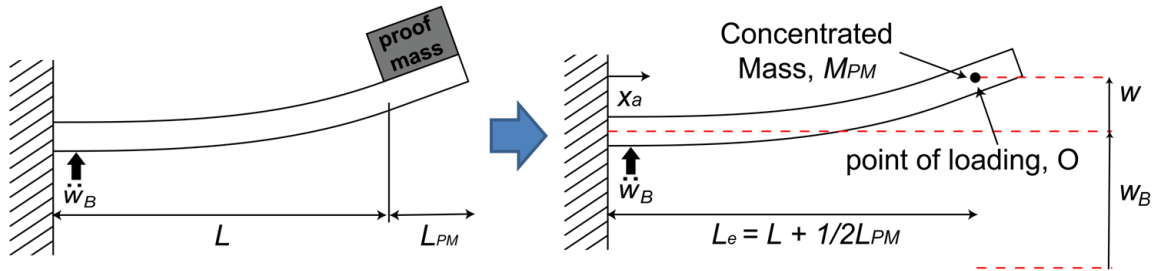


Figure 3.1 Conceptual schematic of a concentrated-mass assumption in a cantilevered system.

The cantilevered structure with given dimensions and mass parameters as indicated in Figure 3.1 can be modeled in terms of the sum of kinetic energy and potential energy and then integrated into the energy methods approach as before (see Chapter 2). Although mechanical elements of cantilevered system are considered here for simplicity of analysis, the same results will hold even when piezoelectric or electrical elements of PVEH devices are included in the analysis. In Section 2.2, displacement along the beam axis of the cantilever under base excitation is written in terms of the mechanical mode shape (ψ_r) and relative displacement, as repeated here:

$$w = \psi_r(x)r(t) \quad (3.1)$$

Total displacement, w_T , is the displacement with respect to the ground (fixed frame) and can thus be obtained from the sum of base displacement, w_B , and displacement $w(x_a)$:

$$w_T = w + w_B \quad (3.2)$$

Using these displacement parameters, kinetic energy (T_k) and potential energy (U) can be written as in equations (3.3) and (3.4):

$$\begin{aligned}
T_k &= \frac{1}{2} \int_0^{L_r} m(\dot{w}_{TOT})^2 dx + \frac{1}{2} M_{PM} [\dot{w}(L_e) + \dot{w}_B]^2 \\
&= \frac{1}{2} \int_0^{L_r} m(\dot{w} + \dot{w}_B)^2 dx + \frac{1}{2} M_{PM} [\dot{w}(L_e) + \dot{w}_B]^2
\end{aligned} \tag{3.3}$$

$$U = \frac{1}{2} \int_0^{L_r} EI \left(\frac{d^2 w}{dx^2} \right)^2 dx \tag{3.4}$$

Substitution of equations (3.3) and (3.4) above into Lagrange's equations gives actuation governing equation (3.5) that includes mechanical key parameters of the vibrating cantilever with a concentrated proof mass:

$$M\ddot{r} + Kr = -B_f \ddot{w}_B \tag{3.5}$$

$$\text{where } M = \int_0^{L_r} m \psi_r^2 dx + M_{PM} \psi_r^2(L_e) \tag{3.6}$$

$$B = \int_0^{L_r} m \psi_r dx + M_{PM} \psi_r(L_e) \tag{3.7}$$

$$K = \int_0^{L_r} EI \left(\frac{d^2 \psi_r}{dx^2} \right)^2 dx \tag{3.8}$$

Then, the first resonant frequency of a cantilever with a concentrated proof mass can be calculated using the relation, $\omega_1 = \sqrt{\frac{K}{M}}$. Although only mechanical elements are considered in the above derivation, the same results will hold even when cantilevered system includes piezoelectric elements, and thus electrical coupling. The same expressions derived in Section 2.2 for piezoelectric cantilevered system with a concentrated proof mass can be used for capacitance

(C_p), coupling (θ), and mechanical damping constant (C), enabling the performance prediction of PVEH devices with the concentrated proof mass approach. This simple approximation for a concentrated proof mass allows relatively easy calculation of resonant frequencies. However, it has a limitation in predicting accurate structural dynamics that offers useful information of electromechanically coupled energy harvesters. Mechanical mode shape defines key parameters for not only mechanical but also electrical behavior of piezoelectric cantilevered systems. When the proof mass is assumed to be concentrated at one point, the entire cantilever system can be regarded as a cantilever without a proof mass from a dimensional perspective, as illustrated in Figure 3.1. Hence, in structural modal analysis, the same mechanical mode shapes will be obtained as those of a free-clamped cantilever without a proof mass when one uses the simple concentrated proof mass analysis. This would result in failure to capture accurately the effect of detailed proof mass properties (*e.g.*, dimensions and materials) on structural modal analysis and subsequently, on device performance, such as strain and power. Improved approaches to encompass the effect of proof mass on PVEH device performance are presented in the next two sections.

3.2 Improved Treatment of Rigid Proof Mass with Rotation

The proof mass is considered rigid and contains rotational terms (due to offset center of gravity and attachment point, see Figure 3.2), instead of a lumped mass or concentrated point mass at a certain point. Effective terms in the governing equations (2.10) and (2.11) are generally expressed in terms of mechanical mode shapes and thus, it is enough to say that the extent of prediction capability of the model depends significantly on the mode shapes. Altering the mode shape via the addition of a proof mass will strongly affect all the effective constants in equations (2.10) and (2.11). While modal analysis and natural frequency calculations of clamped-free cantilevered structures appear in the literature (*e.g.*, [83]), vibration analysis of simple beams with the addition of a proof mass is less common. In this section, it will be shown how much the material and geometric properties of a proof mass and the location where it is placed in the system affect the modal analysis and therefore, the performance of the entire harvesting system.

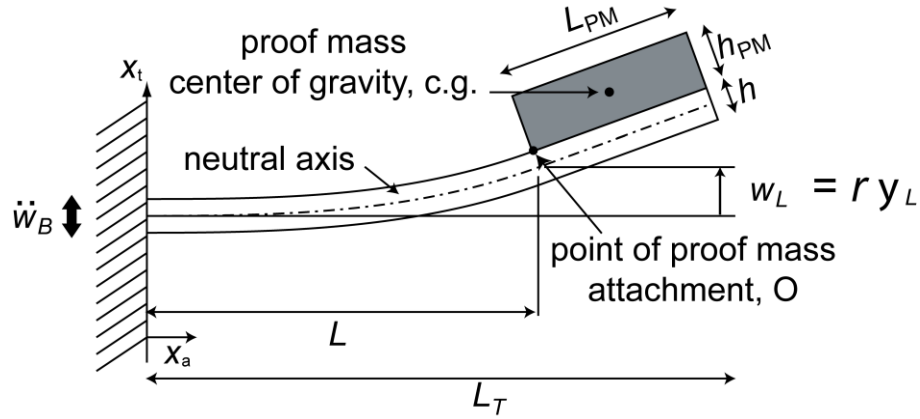


Figure 3.2 Schematic of base-excited cantilevered beam/plate with a proof mass at the tip.

First of all, it is assumed that the stiffness of the proof mass is much larger than that of the beam/plate itself so that proof mass contributes to the entire system with regard to the mass increase, and makes the beam/plate effectively rigid in the outer portion from L to L_{PM} . (Work in Section 3.3 deals with non-rigid mass case when a proof mass also makes contributions to the bending stiffness of the system.) In order to treat more general cases, it is not assumed that the proof mass center of gravity corresponds to the point of loading on the beam/plate. Also, for simplicity, the proof mass is assumed to be uniform in the axial direction with mass per length, equal to m_{PM} , like the beam/plate where the cross-section is considered to be uniform with mass per length, equal to m (see Figure 3.2). It should be emphasized that in this scheme, the part of the beam/plate under the area of proof mass is considered part of the total proof mass for this beam/plate system for calculation ease. Now, we begin with the introduction of mass of overhang, M_0 , static moment, S_0 , at the junction $x=L$, and moment of inertia at the junction, I_0 , to account for the properties of the total proof mass. We can express these terms as follows:

$$M_0 = M_{PM} + mL_{PM} \quad (3.9)$$

$$S_0 = M_0 \cdot \frac{L_{PM}}{2} \quad (3.10)$$

$$I_0 = \frac{m_{PM} L_{PM}}{3} (L_{PM}^2 + h_{PM}^2) + \frac{m L_{PM}}{3} (L_{PM}^2 + h^2) \quad (3.11)$$

where subscript PM indicates the part of a proof mass, and h , L , b and ρ denote height, length, width and density of the beam/plate and the proof mass, respectively in order. It is significant to note that the moment of inertia (I_0) at the junction ($x_a=L$) between the beam/plate and the proof mass, incorporates the rotational inertia of the proof mass.

As adopted from [84, 85], the governing equations in terms of mechanical displacement or mode shape can be determined, using Euler-Bernoulli beam theory, as given by equation (3.12). The N th mode of the mechanical mode shape is represented by $\psi_N(x_a)$, which can be expressed via equation (3.13) where constants (c , d , e , and f) will be solved using the boundary conditions:

$$\overline{EI}\psi_N^{IV} - m\omega_N^2\psi_N = 0 \quad (3.12)$$

$$\psi_N = c \sinh \lambda_N x_a + d \cosh \lambda_N x_a + e \sin \lambda_N x_a + f \cos \lambda_N x_a \quad (3.13)$$

\overline{EI} is the effective bending stiffness, which is obtained considering the neutral axis and the properties of the beam multi-layers, while ω_N represents the mode resonance frequencies. It is convenient to define the parameter, $\lambda_N^4 = \frac{m\omega_N^2}{\overline{EI}}$. Boundary conditions at the fixed end and at the junction point ($x_a = L$) where the beam/plate and the proof mass are connected are given by:

$$\text{At } x_a = 0, \psi_N = 0 \quad (3.14)$$

$$\psi_N' = 0 \quad (3.15)$$

$$\text{At } x_a = L, \overline{EI}\psi_N'' = \omega_N^2 I_0 \psi_N' + \omega_N^2 S_0 \psi_N \quad (3.16)$$

$$\overline{EI}\psi_N''' = -\omega_N^2 M_0 \psi_N - \omega_N^2 S_0 \psi_N' \quad (3.17)$$

where $(\quad)' = \partial/\partial x_a$. Equations (3.14) and (3.15) simply represent a clamped cantilever, whereas equation (3.16) represents bending moment and equation (3.17) represents shear force at the junction between the beam/plate and the proof mass. Upon introducing ψ_N from equation (3.13) into these boundary conditions, one obtains four equations which can be reduced to the 2×2 matrix equation (3.18) along with the expressions of matrix elements, equations (3.19)-(3.22):

$$\begin{bmatrix} A_{11} & A_{12} \\ A_{21} & A_{22} \end{bmatrix} \begin{bmatrix} c \\ d \end{bmatrix} = 0 \quad (3.18)$$

$$A_{11} = (\sinh \bar{\lambda}_N + \sin \bar{\lambda}_N) + \bar{\lambda}_N^3 \bar{I}_0 (-\cosh \bar{\lambda}_N + \cos \bar{\lambda}_N) + \bar{\lambda}_N^2 \bar{S}_0 (-\sinh \bar{\lambda}_N + \sin \bar{\lambda}_N) \quad (3.19)$$

$$A_{12} = (\cosh \bar{\lambda}_N + \cos \bar{\lambda}_N) + \bar{\lambda}_N^3 \bar{I}_0 (-\sinh \bar{\lambda}_N - \sin \bar{\lambda}_N) + \bar{\lambda}_N^2 \bar{S}_0 (-\cosh \bar{\lambda}_N + \cos \bar{\lambda}_N) \quad (3.20)$$

$$A_{21} = (\cosh \bar{\lambda}_N + \cos \bar{\lambda}_N) + \bar{\lambda}_N \bar{M}_0 (\sinh \bar{\lambda}_N - \sin \bar{\lambda}_N) + \bar{\lambda}_N^2 \bar{S}_0 (\cosh \bar{\lambda}_N - \cos \bar{\lambda}_N) \quad (3.21)$$

$$A_{22} = (\sinh \bar{\lambda}_N - \sin \bar{\lambda}_N) + \bar{\lambda}_N \bar{M}_0 (\cosh \bar{\lambda}_N - \cos \bar{\lambda}_N) + \bar{\lambda}_N^2 \bar{S}_0 (\sinh \bar{\lambda}_N + \sin \bar{\lambda}_N) \quad (3.22)$$

For convenience, all terms above are nondimensionalized such that $\bar{\lambda}_N = \lambda_N L$, $\bar{M}_0 = \frac{M_{PM}}{mL}$,

$\bar{S}_0 = \frac{S_0}{mL^2}$, and $\bar{I}_0 = \frac{I_0}{mL^3}$. We solve for $\bar{\lambda}_N$ which makes the determinant $\begin{vmatrix} A_{11} & A_{12} \\ A_{21} & A_{22} \end{vmatrix} = 0$ and

thus obtain successive values of $\bar{\lambda}_N$, from which the resonance frequencies associated with each N th mode, ω_N can be calculated through the relation, $\bar{\lambda}_N^4 = \lambda_N^4 L^4$. The first resonance frequency, ω_1 , for example, is given by equations (3.23) and (3.24), in units of [rad/s] and [Hz], respectively:

$$\omega_1 = (\bar{\lambda}_1)^2 \sqrt{\frac{EI}{mL^4}} \quad [\text{rad/s}] \quad (3.23)$$

$$f_1 = \frac{1}{2\pi} \omega_1 \quad [\text{Hz}] \quad (3.24)$$

It should be noted that ω_1 is also related to mass and stiffness through $\omega_1 = \sqrt{K/M}$. Then, the general bending mode shape of a clamped-free (simple cantilever) beam/plate with a proof mass is:

$$\psi_N = d[(\cosh \lambda_N x_a - \cos \lambda_N x_a) - \frac{A_{12}}{A_{11}} (\sinh \lambda_N x_a - \sin \lambda_N x_a)] \quad (3.25)$$

This is a rewritten form of equation (3.13) only in terms of a single arbitrary scaling constant, (here, d is used.), and it is noted that $\lambda_N x_a = \bar{\lambda}_N \frac{x_a}{L}$. Once the parameter, $\bar{\lambda}_N$ or λ_N is known from the zero determinant, both mode shape and the resonance frequency for the N th mode are determined. For practical use, we normalize the mode shape to $\psi_N(L) = 2$ at the junction, which gives $d = 2/[(\cosh \lambda_N x_a - \cos \lambda_N x_a) - \frac{A_{12}}{A_{11}} (\sinh \lambda_N x_a - \sin \lambda_N x_a)]$. The actual beam/plate tip deflection at $x = L + L_{PM}$, is then given by $w_{tip} = [2 + L_{PM} \psi'_N(L)]r$, rather than simply $w_{ip} = 2r$ as used in the no proof mass case in Chapter 2.

Addition of a proof mass will cause the effective mass of the structure, previously given by equation (2.12), to have a different form as shown in equation (3.26), which is obtained from the Lagrange's equations of motion [71, 83]:

$$\mathbf{M} = \int_{V_s} \psi_r^t \rho_s \psi_r dV_s + \int_{V_p} \psi_r^t \rho_p \psi_r dV_p + M_0 (\psi_r(L))^t \psi_r(L) + 2S_0 (\psi_r(L))^t \psi'_r(L) + I_0 (\psi'_r(L))^t \psi'_r(L) \quad (3.26)$$

The last three terms in equation (3.26) incorporate the properties of the proof mass. Although the first two terms are present as in equation (2.12) when a proof mass is not considered, the resulting values of these terms will be quite different when a proof mass is added to the

cantilevered structure. This is because the mode shapes vary due to material and geometric properties of the proof mass and thus affect the first two terms in equation (3.26), which are expressed in terms of these mode shapes. Likewise, as other terms in the governing equations of motions in Section 2.2, such as effective stiffness (\mathbf{K}), coupling ($\mathbf{\Theta}$), and capacitive matrices (\mathbf{C}_p), depend on the mode shapes, the variation of the mode shape will alternate the values for these effective terms when there is a proof mass. Previously, the forcing function, \mathbf{B}_f , has been defined to account for the inertial loading of the device due to base excitation. Since not only a beam/plate but also a proof mass at the tip contributes to the inertial loading of the device, the forcing vector must be modified so that the displacement and the rotation of the tip mass are taken into account. The last two additional terms modify the forcing vector:

$$\mathbf{B}_f = \int_0^L m(\boldsymbol{\psi}_r(x_a))^t dx_a + M_0(\boldsymbol{\psi}_r(L))^t + S_0(\boldsymbol{\psi}'_r(L))^t \quad (3.27)$$

The matrices \mathbf{M} , \mathbf{K} , $\mathbf{\Theta}$, and \mathbf{C}_p in equations (2.10) to (2.15), and (3.26) represent square matrices, while \mathbf{B}_f in equations (2.16) and (3.27) represents a column matrix. Additionally, the mass and stiffness matrices, \mathbf{M} and \mathbf{K} , are diagonal matrices because of the orthogonality conditions that exist between any two modes, ψ_i and ψ_j . Since each mode satisfies the differential equation (3.16) and the boundary conditions equations (3.14) to (3.17), one can readily show the orthogonality conditions to result in:

$$M_{ij} = \delta_{ij}M_{ii} \quad (3.28)$$

$$K_{ij} = \delta_{ij}M_{ii}\omega_i^2 \quad (3.29)$$

where δ_{ij} represents the Kronecker delta. The fact that the mass and stiffness matrices, \mathbf{M} and \mathbf{K} , are diagonal is important in that it allows each vibration mode, ri , in the governing equation (2.10) to be uncoupled structurally from one another (orthogonal vibration modes) in the governing system of equations (2.10) and (2.11). This allows for easier computation of the governing equations in the multi-degree-of-freedom (MDOF) treatment of the system.

Modified coefficients above, M and B_f , can be expressed in the single mode governing equations as below while the same expressions for other coefficients in the governing equations can be employed as described in Section 2.2:

$$M = \int_0^L m \psi_r^2 dx_a + M_0 (\psi_r(L))^2 + 2S_0 \psi_r(L) \psi_r'(L) + I_0 ((\psi_r'(L))^2) \quad (3.30)$$

$$B_f = \int_0^L m \psi_r dx_a + M_0 \psi_r(L) + S_0 \psi_r'(L) \quad (3.31)$$

An improved treatment of the proof mass is considered here resulting in modification of calculated terms in the prior normalized governing equations that are described in Section 2.2. It is shown that while the addition of the proof mass modifies numerous terms in the governing equations, the normalized results (*e.g.*, equations (2.24) to (2.26)) still hold.

3.3 Exact Treatment of Flexible Proof Mass Using Two-beam Method

In this section, the author develops a more rigorous model that considers a flexible proof mass for a cantilevered harvester, where the proof mass also makes contributions to the bending stiffness of the system. Long, thin, distributed proof masses are quite common in MEMS devices due to the constraints of thin-film processing (*e.g.*, deposition height of proof mass, resolution of lithography, *etc.*). A cantilevered device with a proof mass is modeled as two joined beams with different uniform cross-sections rather than a beam with the simple addition of a proof mass, as illustrated in Figure 3.3. Notations L and L_{PM} represent here the length of the beam without proof mass (beam 1) and the length of a proof mass (beam 2), respectively, whereas L_T is again the total length of the device. The axial beam coordinate is denoted as x_a while x_t indicates the transverse coordinate along which direction bending of a cantilever occurs. A sinusoidal base-excitation induces mechanical vibration of a cantilever beam with a proof mass, where \ddot{w}_B

represents base acceleration. Beam displacement, w , can be defined as displacement relative to the base of the cantilever. Although an under-hanging proof mass is drawn here consistent with the actual experiment (see Chapter 5) in Figure 3.3, it should be noted that both analytical and experimental results are the same for either an over-hanging or under-hanging proof mass. It is assumed here that the neutral axis location of the two beams is made to be continuous near the junction of the two beams, $x_a = L$.

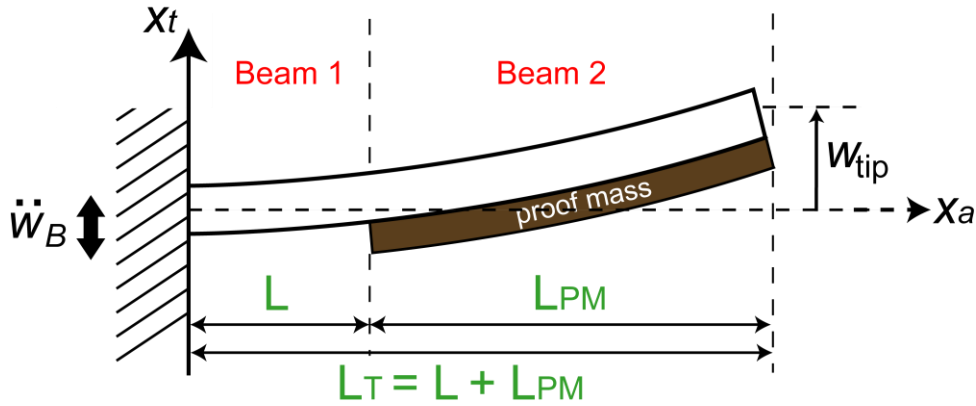


Figure 3.3 Schematic of a cantilever with a long, flexible proof mass. Notations ‘beam 1’ and ‘beam 2’ are used to demonstrate the concept of ‘two-beam method’.

For the vibration analysis, the N^{th} mode of the mechanical mode shape of each beam is expressed as $\psi_{N,1}$ for beam 1 and $\psi_{N,2}$ for beam 2 with an arbitrary set of constants, c, d, e, f and $\bar{c}, \bar{d}, \bar{e}, \bar{f}$, respectively, as shown in equations (3.32) and (3.33):

$$\psi_{N,1} = c \sinh \lambda_{N,1} x_a + d \cosh \lambda_{N,1} x_a + e \sin \lambda_{N,1} x_a + f \cos \lambda_{N,1} x_a \quad (3.32)$$

$$\psi_{N,2} = \bar{c} \sinh \lambda_{N,2} x_a + \bar{d} \cosh \lambda_{N,2} x_a + \bar{e} \sin \lambda_{N,2} x_a + \bar{f} \cos \lambda_{N,2} x_a \quad (3.33)$$

Euler-Bernoulli beam theory enables determination of the mechanical mode shape following the

relations in equations (3.34) and (3.35). \overline{EI} is the effective bending stiffness, which is obtained considering the neutral axis and the properties of the beam multi-layers, while m is mass per length for each beam. \overline{EI} and m can also represents a plate in bending [52]. ω_N represents the N^{th} mode resonance frequencies in units of $[rad/s]$.

$$(\overline{EI})_1 \psi_{N,1}^{IV} - m_1 \omega_N^2 \psi_{N,1} = 0 \quad 0 \leq x_a \leq L \quad (3.34)$$

$$(\overline{EI})_2 \psi_{N,2}^{IV} - m_2 \omega_N^2 \psi_{N,2} = 0 \quad L \leq x_a \leq L_T \quad (3.35)$$

Boundary conditions at the fixed end, free end, and the junction between beam 1 and beam 2 are established, considering the clamping (equation (3.36)), bending moment and shear force at the tip (equation (3.37)), and continuity condition for displacement, slope, bending moment and shear force at the junction, $x_a = L$ (equations (3.38) and (3.39)):

$$\text{At } x_a = 0, \psi_{N,1} = 0 \text{ and } \psi'_{N,1} = 0 \quad (3.36)$$

$$\text{At } x_a = L_T, (\overline{EI})_2 \psi''_{N,2} = 0 \text{ and } (\overline{EI})_2 \psi'''_{N,2} = 0 \quad (3.37)$$

$$\text{At } x_a = L, \psi_{N,1} = \psi_{N,2} \text{ and } \psi'_{N,1} = \psi'_{N,2} \quad (3.38)$$

$$\text{At } x_a = L, (\overline{EI})_1 \psi''_{N,1} = (\overline{EI})_2 \psi''_{N,2} \text{ and } (\overline{EI})_1 \psi'''_{N,1} = (\overline{EI})_2 \psi'''_{N,2} \quad (3.39)$$

where $(\)' = \partial / \partial x_a$. It is convenient to define the parameters, $\lambda_{N,1} = \sqrt[4]{\frac{m_1 \omega_N^2}{(\overline{EI})_1}}$,

$\lambda_{N,2} = \sqrt[4]{\frac{m_2 \omega_N^2}{(\overline{EI})_2}} = \sqrt[4]{\frac{m_2}{m_1} \frac{(\overline{EI})_1}{(\overline{EI})_2}} \lambda_{N,1}$. These boundary conditions give eight equations which can be

reduced to an 8×8 matrix as written in equation (3.40), where $\alpha = \frac{(\overline{EI})_2}{(EI)_1}$,

$$\beta = \frac{\lambda_{N,2}}{\lambda_{N,1}} = \sqrt[4]{\frac{m_2 (\overline{EI})_1}{m_1 (EI)_2}}, \text{ are defined for simplicity. For convenience, all terms above are}$$

nondimensionalized such that $\bar{\lambda}_N = \lambda_{N,1} L_T$. We solve for $\bar{\lambda}_N$ which makes the determinant

$|A| = 0$ as before and thus obtain successive values of $\bar{\lambda}_N$, from which both mode shape and

the resonance frequency for the N^{th} mode are readily obtainable through the relation,

$$\bar{\lambda}_N^4 = (\lambda_{N,1})^4 L_T^4 = m_1 \omega_N^2 L_T^4 / (\overline{EI})_1:$$

$$[A] = \begin{bmatrix} 1 & 0 & 1 & 0 & 0 & 0 & 0 & 0 \\ 0 & 1 & 0 & 1 & 0 & 0 & 0 & 0 \\ \sinh \lambda_{N,1} L & \cosh \lambda_{N,1} L & \sin \lambda_{N,1} L & \cos \lambda_{N,1} L & -\sinh \lambda_{N,2} L & -\cosh \lambda_{N,2} L & -\sin \lambda_{N,2} L & -\cos \lambda_{N,2} L \\ \cosh \lambda_{N,1} L & \sinh \lambda_{N,1} L & \cos \lambda_{N,1} L & -\sin \lambda_{N,1} L & -\beta \cosh \lambda_{N,2} L & -\beta \sinh \lambda_{N,2} L & -\beta \cos \lambda_{N,2} L & \beta \sin \lambda_{N,2} L \\ \sinh \lambda_{N,1} L & \cosh \lambda_{N,1} L & -\sin \lambda_{N,1} L & -\cos \lambda_{N,1} L & -\alpha \beta^2 \sinh \lambda_{N,2} L & -\alpha \beta^2 \cosh \lambda_{N,2} L & \alpha \beta^2 \sin \lambda_{N,2} L & \alpha \beta^2 \cos \lambda_{N,2} L \\ \cosh \lambda_{N,1} L & \sinh \lambda_{N,1} L & -\cos \lambda_{N,1} L & \sin \lambda_{N,1} L & -\alpha \beta^3 \cosh \lambda_{N,2} L & -\alpha \beta^3 \sinh \lambda_{N,2} L & \alpha \beta^3 \cos \lambda_{N,2} L & -\alpha \beta^3 \sin \lambda_{N,2} L \\ 0 & 0 & 0 & 0 & \sinh \lambda_{N,2} L_T & \cosh \lambda_{N,2} L_T & -\sin \lambda_{N,2} L_T & -\cos \lambda_{N,2} L_T \\ 0 & 0 & 0 & 0 & \cosh \lambda_{N,2} L_T & \sinh \lambda_{N,2} L_T & -\cos \lambda_{N,2} L_T & \sin \lambda_{N,2} L_T \end{bmatrix} \begin{bmatrix} c \\ d \\ e \\ f \\ \bar{c} \\ \bar{d} \\ \bar{e} \\ \bar{f} \end{bmatrix} = 0 \quad (3.40)$$

The first resonance frequency, for example, is given by equations (3.41) and (3.42) in units of [rad/s] and [Hz], respectively:

$$\omega_1 = (\bar{\lambda}_1)^2 \sqrt{\frac{(\overline{EI})_1}{m_1 L_T^4}} \quad [\text{rad/s}] \quad (3.41)$$

$$f_1 = \frac{1}{2\pi} \omega_1 \quad [\text{Hz}] \quad (3.42)$$

The general bending mode shape of a clamped-free (simple cantilever) beam/plate with a proof

mass at the tip will be given as follows:

$$\psi_{rN,1} = c \sinh \bar{\lambda}_N \xi + d \cos \bar{\lambda}_N \xi + e \sin \bar{\lambda}_N \xi + f \cos \bar{\lambda}_N \xi \quad (3.43)$$

$$\psi_{rN,2} = \bar{c} \sinh \beta \bar{\lambda}_N \xi + \bar{d} \cos \beta \bar{\lambda}_N \xi + \bar{e} \sin \beta \bar{\lambda}_N \xi + \bar{f} \cos \beta \bar{\lambda}_N \xi \quad (3.44)$$

Parameter, ξ is introduced such that $\lambda_N x_a = \bar{\lambda}_N \frac{x_a}{L_T} = \bar{\lambda}_N \xi$. For practical use, we normalize the mode shape to $\psi_N(L_T) = 2$ at the tip as is common practice in beam dynamics [69]. Based on this modal analysis, we can predict mechanical performance of a cantilever such as resonant frequencies, mechanical mode shape, and strain distribution along the beam depending on various sizes of flexible proof masses once we input material property constants and geometric dimensions.

The flexible proof mass analysis presented in this section enables thorough investigation of the mechanical behavior of micro-scale single crystal silicon cantilevers with a distributed, flexible proof mass and furthermore, establishment of the effect of proof mass on the performance of MEMS-PVEHs. When analyzing a cantilevered piezoelectric energy harvesting device with a flexible, long proof mass, mechanical mode shapes obtained from the two-beam method can be used directly in the key parameter equations (2.12)-(2.31) and (3.26)-(3.34). As a result, prediction of key performance metrics such as mechanical displacement, voltage and power is possible.

3.4 Summary of Key Effects of Proof Mass Modeling Treatments

Extended analytical models for a cantilevered PVEH focusing on the addition of a proof mass are presented throughout this chapter. Significance of appropriate treatment of proof mass in PVEH device design for enhanced power generation is highlighted by modeling detailed proof mass effects on PVEH performance at three different levels of accuracy: simple approximation for concentrated proof mass, improved treatment of rigid proof mass with rotation, and exact

treatment of a flexible proof mass using a two-beam method.

Damping ratio, ζ_m , is one of key parameters that can significantly affect device performance. In the following, a generalized treatment for the determination of mechanical damping ratios based on simple measurement of actual tip and base displacements originated in du Toit *et al.* [30, 74] is presented. When the governing equations of motion are derived, mechanical damping is incorporated through addition of a viscous damping term, C , which is related to mechanical damping ratio, ζ_m , via $C = 2\zeta_m\omega_1M$ in the case of a single mode. Mechanical damping is assumed to encompass all non-electrical damping that influences the system response. Accurate characterization of mechanical damping is essential for device performance prediction. As an alternative to the log-decrement method (described for energy harvesters in detail in [30]), another measurement scheme can be developed to obtain ζ_m through convenient dynamic tests of the harvester. Previously, du Toit *et al* [29, 30, 73, 74] presented a generalized treatment for the determination of mechanical damping ratios based on simple measurement of tip and base displacements. While the derivation procedure for the expression of mechanical damping ratio is reasonable there, some of the detailed terms should be corrected such that these expressions can be applied to the system regardless of whether there is a proof mass or not. The relative displacement is expressed as a function of dimensionless time constant, α , as in equation (2.24). At short-circuit ($\alpha = 0$) where electrical damping is zero, and at resonance ($\Omega = 1$), equation (2.24) can be rewritten:

$$\left| \frac{r}{B_f \ddot{w}_B} \right| = \frac{1}{K} \frac{1}{2\zeta_m} \quad (3.45)$$

With an input harmonic base excitation given by $\ddot{w}_B = -\omega_1^2 w_B$, where w_B is amplitude of base excitation and ω_1 denotes the first resonant frequency of the vibration. In addition to the base acceleration, $w_{tip} = \psi_{tip} r$ and $K = M\omega_1^2$ can be substituted into equation (3.45) to derive an expression for the mechanical damping ratio, ζ_m , given easily measurable displacement amplitudes:

$$\zeta_m = \frac{B_f}{M} \frac{\psi_{r,tip}}{2} \left| \frac{w_B}{w_{tip}} \right| = \frac{B_f}{M} \frac{\psi_r(L+L_{PM})}{2} \left| \frac{w_B}{w_{tip}} \right| \quad (3.46)$$

Absolute tip displacement, w_{tip} , and absolute base displacement, w_B , should be experimentally measured at resonance and short-circuit conditions by aligning the input frequency with the resonant frequency of the device and letting the electrical resistance, R_l be zero. Other values such as forcing function, B_f , and effective mass, M , in the equation can be obtained from model implementation for specific devices. When a proof mass is attached at the end, the mechanical mode shape at the tip, $\psi_{r,tip}$ is equal to $\psi_r(L+L_{PM})$ instead of simply $\psi_r(L) = 2$, as mentioned earlier, following equation (3.25). For the energy harvester system without a proof mass, where L_{PM} is zero, the mechanical mode shape at the tip reduces to 2 through $\psi_r(L) = 2$:

$$\zeta_m \approx \frac{B_f}{M} \left| \frac{w_B}{w_{tip}} \right| \quad (3.47)$$

Equation (3.47) coincides with the form that was developed in prior work by du Toit *et al* [74] for the case of no proof mass, where the experimental results agreed well with simulated results. Note that in both cases, the mechanical damping has dependence on effective mass, M , and forcing function, B_f , that are represented in terms of mechanical mode shape and its derivatives, as shown previously. As the mechanical mode shape varies according to change in proof mass properties, these terms change accordingly and thus, it is also necessary to evaluate the mechanical damping ratio that is appropriate to each proof mass (*i.e.*, device). As damping is typically measured at the device natural frequency, which is fixed, the damping dependence on frequency is not considered here. However, if the damping ratios are not the same at the resonance and anti-resonance frequencies, the dependence of the mechanical damping ratios on frequencies should be examined. The scheme to obtain the mechanical damping ratio from modeling and experiments presented here is used in Chapter 4, where it is found that analysis of damping ratios contributes to accurate prediction of device performance.

In Chapter 4, the rigid proof mass model developed in Section 3.2 is experimentally verified through a detailed set of experiments (with various proof mass geometries). Chapter 5

follows with the results from newly designed experiments that are performed not only for experimental verification of the flexible proof mass modeling but also for comparison of three different-level modeling approaches of proof mass effects that have been described in this chapter. The mechanical behavior of a flexible, distributed proof mass in terms of its resonant frequency and mode shapes as a function of proof mass size is considered, followed by model-experiment correlation based on AFM and FIB lithography of Si microcantilevers. Modeling is an indispensable element in predicting and analyzing the characteristics of PVEHs. Therefore, the exact analysis presented here for PVEHs with a proof mass is an essential step in realizing MEMS devices for future applications.

Chapter 4

Experiment-Model Correlation for Macro-scale PVEHs with a Proof Mass

Analytical models for a cantilevered PVEH focusing on the addition of a proof mass are presented in Chapter 3. In this chapter, the analytical model of rigid proof mass with rotation developed in Section 3.2 is experimentally verified using a macroscale, symmetric, bimorph, cantilevered PZT bimorph device operating in {3-1}-mode with and without a proof mass. The proof mass in the experiments are large and effectively rigid in bending relative to the PVEH cantilever. Experimental tests undertaken on the energy harvesting device with different geometry proof masses demonstrate that the properties of the proof mass affect the resulting performance of the energy harvester device beyond simply reducing the natural frequency. It is also shown that the rigid proof mass model accurately captures all aspects of the measured response, including the location of peak-power operating points at resonance and anti-resonance, and trends such as the dependence of maximal power harvested versus frequency. As a summary, the last section concludes with a demonstration of energy harvesting system behavior under various operating conditions (*e.g.*, driving input frequencies, electrical resistance, and damping), based on the analytical model developed for PVEH devices in Chapters 2-4. Experiments were performed by Mathias Hoegen [118], and the author undertook the model implementation and model-experiment comparison study.

4.1 Model Implementation for Cantilevered Bimorph Piezoelectric Energy Harvesters

A symmetric, bimorph cantilevered PZT ‘bender’ is chosen and tested with various sizes of proof mass as well as without a proof mass. The harvester is a cantilevered plate consisting of two piezoelectric layers (bimorph), one structural layer, and electrodes (see Figure 4.1). The test device is operated in {3-1} mode of operation with series connection between active elements, which requires two piezoelectric elements to be oppositely poled. In order to implement the electromechanically-coupled model based on an improved modal analysis of rigid proof mass that can accommodate the specific test device configurations and interconnection of the piezoelectric elements, it is necessary to evaluate the relevant coefficients. In this section, we obtain appropriate scalar equations for the experimental device with a single mechanical mode.

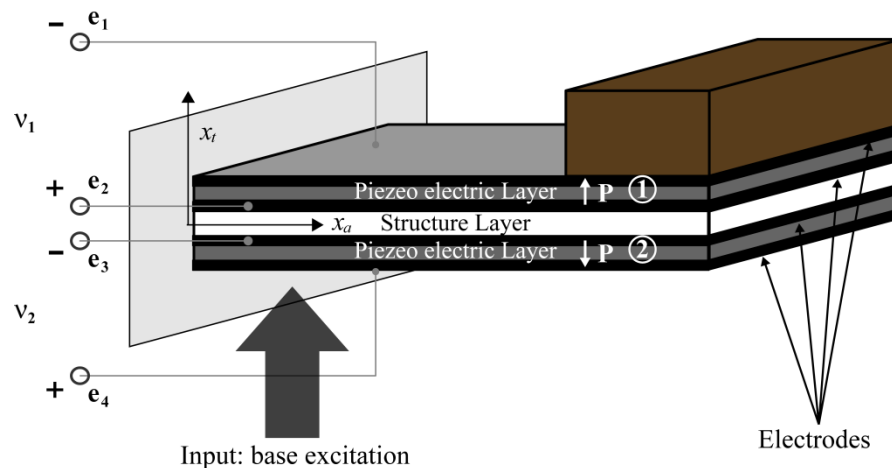


Figure 4.1 Illustration of symmetric, bimorph energy harvester with a tip proof mass. The active elements are electrically connected in series.

Since there are two piezoelectric elements, each layer can be denoted with subscripts 1 and 2, to treat the two active layers in the bimorph configuration. Considering these two layers for the bimorph configuration, we use equations (2.10) and (2.11) to write equations (4.1) and (4.2)

as:

$$M\ddot{r} + C\dot{r} + Kr - (\theta_1 v_1 + \theta_2 v_2) = -B_f \ddot{w}_B \quad (4.1)$$

$$\begin{Bmatrix} \theta_1 \\ \theta_2 \end{Bmatrix} r + \begin{bmatrix} C_{p1} & 0 \\ 0 & C_{p2} \end{bmatrix} \begin{Bmatrix} v_1 \\ v_2 \end{Bmatrix} = -\begin{Bmatrix} q_1 \\ q_2 \end{Bmatrix} \quad (4.2)$$

Equations (4.2) are summed to obtain a form similar to the scalar equation (2.18), and effective constants derived:

$$(\theta_1 + \theta_2)r + (C_{p1}v_1 + C_{p2}v_2) = -(q_1 + q_2) \quad (4.3)$$

For the symmetric bimorph configuration, $\theta_1 = \theta_2$, $C_{p1} = C_{p2}$, $v_1 = v_2 = \frac{1}{2}v$, and $q_1 = q_2$.

Next, the coefficients for one of the piezoelectric elements (here 1 is chosen) need to be considered so that they can be applied in the governing equations. For bimorph cantilevered energy harvesters, there are two ways to interconnect the piezoelectric elements: parallel or series connection. As the test device in this work is connected in series, the poling directions of each piezoelectric layer should be opposite. Please refer to [30, 74, 83] for detailed information of the effect of poling direction and corresponding electrical connection. The in-series connection, as illustrated in Figure 4.1, has the device connected to the electrical load by shorting the two center electrodes (e_2 and e_3), and connecting the top (e_1) and bottom electrodes (e_4) across the electrical load. Based on this, relations of voltage and charge are achieved such that $v_1 + v_2 = v$, and $q_1 = q_2$, giving:

$$M\ddot{r} + C\dot{r} + Kr - \theta_1 v = -B_f \ddot{w}_B \quad (4.4)$$

$$\theta_1 \dot{r} + \frac{1}{2}C_{p1}\dot{v} + \frac{1}{R_l}v = 0 \quad (4.5)$$

Based on the comparison between the above expressions (4.4) and (4.5) and the governing equations (2.17) and (2.18) for the general single mechanical mode harvester, it is recognized that the coupling term, θ , and the capacitance term, C_p in the general expression can be rewritten using coupling and capacitance values for one piezoelectric layer through $\theta = \theta_1$, and $C_p = \frac{1}{2}C_{p1}$ for the energy harvester with bimorph configuration that is electrically connected in series. This result is intuitive in that two piezoelectric layers are regarded as simple capacitors and that the effective capacitance of two identical simple capacitors wired in series is half of the capacitance of one capacitor.

As a next step, it is necessary to examine the appropriate expression for electrical potential that corresponds to the symmetric, bimorph configuration in {3-1} mode of operation in order to evaluate coupling and capacitance more specifically. In this work, electric potential distribution is taken to give a constant electric field through the thickness of the piezoelectric element. The potential varies from 0 at the top electrode to +1 of at the bottom electrode in Figure 4.1. The electric potential for the bimorph structure in {3-1} mode operation is then expressed employing the thicknesses of the piezoelectric layer (t_p) and structural layer (t_s) as given by:

$$\psi_v = \begin{cases} \frac{(t_p + \frac{t_s}{2}) - x_t}{t_p} & x_t > 0 \\ \frac{-\frac{t_s}{2} - x_t}{t_p} & x_t < 0 \end{cases} \quad \text{for} \quad (4.6)$$

If the device is of unimorph configuration or in {3-3} mode of operation, electric potential will vary according to each case (see Section 8.1). Now it is possible to determine the final expression for coupling term, θ , and the capacitance term, C_p , by substituting the electric potential expression shown in equation (4.6) into equations (2.21) and (2.22). The resulting expressions are:

$$\theta = \theta_1 = (e_{31}^*) \left(\frac{t_p + t_s}{2} \right) b \psi_r'(L) \quad (4.7)$$

$$C_p = \frac{1}{2} C_{p1} = \frac{1}{2} \frac{b(L + L_{PM})}{t_p} \epsilon_{33}^{S*} \quad (4.8)$$

Concerning the calculation of capacitance, the entire beam/plate length, $L+L_{PM}$, is employed because of the test device structure. Thus, the model is implemented for the test device, that is, a symmetric, bimorph configuration in {3-1} mode of operation, connected electrically in series. Based on this, mechanical and electrical performance of the system is simulated and compared with the experimental results, as presented in Section 4.4.

4.2 Experimental Procedures for Device Characterization of Macro-scale Energy Harvesters

4.2.1 Experimental Setup and Device Performance Measurements

A macroscale, cantilevered plate is used as a test device. The schematic of a bimorph device with addition of a proof mass at the end of the device along with electrical connection is shown in Figure 4.1. A brass-reinforced bending actuator (Piezo Systems Inc., T226-A4-503X) is composed of seven layers: two piezoelectric (active) layers, each of which is sandwiched by two electrode layers (four layers of electrodes in total) and one structural (inactive) layer made of brass. Two piezoelectric layers (PZT-5A) are poled in opposite directions so that opposite strains in each layer generate electric fields in the same directions. For the bimorph configuration, there are two ways to interconnect active layers: series and parallel connections. Series connection is chosen to match the poling direction in use. Further details on poling direction and relevant coordinate systems are described in [29, 30, 73]. The {3-1} operation mode is employed where the strain develops in the direction perpendicular to the electric field. Proof masses are added at the free end of the PVEH using superglue and insulating tape. In order to mount the PVEH device on an electrostatic shaker for input base excitation, a simple aluminum clamp is adopted, which is shown in Figure 4.2.

Absolute tip displacement as well as the base displacement in transverse direction is measured to obtain the relative mechanical displacement using a laser Doppler vibrometer (Polytec PSV 300-H). As illustrated in Figure 4.1, a simple circuit that consists of purely resistive electrical load in conjunction with a bimorph device electrically connected in series is established to achieve electrical responses of the device. A purely resistive electrical load is helpful not only to simplify the calculation but also to measure the power generated. The measured voltage is root-mean-square voltage, v_{rms} , and is converted to v_{max} by multiplying by $\sqrt{2}$. Power is evaluated from the measured voltage and applied electrical resistance, R_l , through the relation, $P_{\text{max}} = v_{\text{max}}^2 / R_l$. Voltage and power calculated from equations (2.25) and (2.26) correspond to experimental v_{max} and P_{max} , respectively. To determine the operating points, it is important to assess both resonant and anti-resonant frequencies, which is accomplished by sweeping a range of frequencies using a laser vibrometer either at short-circuit conditions or at open-circuit conditions. The resonant frequency is defined as the natural frequency when the device is in the short-circuit condition while the anti-resonant frequency is the natural frequency in open-circuit condition. Anti-resonant frequency, in particular, is an important measure of electromechanical coupling and thus, from the information of anti-resonance frequency, it is possible to assess the extent of electromechanical coupling in the system. Once resonant and anti-resonant frequencies are found, both mechanical and electrical tests are performed at resonances, near resonances, and away from resonances with varying electrical loading conditions. The results are graphically presented in the next section in comparison with simulated results from analytical modeling.

4.2.2 Test-device Dimensions and Material Properties

Geometric parameters of the devices and material properties used in model implementation are listed in Table 4.1. Depending on availability, values are adopted from publications, measured, or calculated. It is necessary to differentiate energy harvester length, L_{EH} , from actual cantilevered energy harvester length, L_T , which describes the length of the energy harvester plate excluding the length occupied by the clamping device. As the thickness of the nickel electrode is about 1 μm , it is regarded as negligible considering the entire macroscale

device thickness of 0.675 mm. Regarding material properties, several values such as density, elastic stiffness, piezoelectric constant, and the absolute permittivity at constant stress of piezoelectric layer (PZT-5A) are taken from available literature. The density of the structural layer and proof masses are calculated from the known values of mass and volume. The elastic stiffness of the structural layer is found to be 100 GPa (inferred from device resonant frequency, as it was not directly measured). While piezoelectric strain constant, d_{31} , is available as -190×10^{-12} [C/m], the stress constant, e_{31}^* , is computed using its relation with the coupling coefficient, θ . Refer to [30] for more detailed description of measurement methods for each property. For plate structures, the absolute permittivity at constant strain, ϵ_{33}^{S*} , is related to the absolute permittivity at constant stress, ϵ_{33}^T , through $\epsilon_{33}^{S*} = \epsilon_{33}^T - 2d_{31}e_{31}^*$ (see Appendix A), and thus, the absolute permittivity at constant strain is evaluated based on the known information of ϵ_{33}^T . Masses, lengths, thicknesses of two different sizes of proof masses are presented in Table 4.2 together with input base accelerations at which the energy harvester device with a proof mass is excited.

In general, all the parameters needed to implement the model presented in Chapter 2, equations (2.24)-(2.26), can be calculated from basic physical and electrical data, except for the mechanical damping ratio, ζ_m . This ζ_m can only be obtained from experiments on the particular device tested.

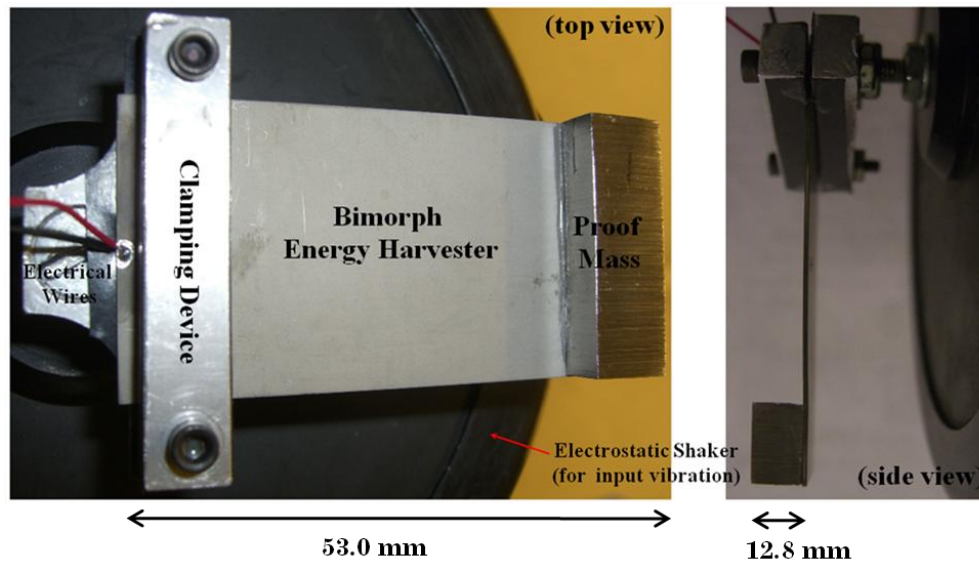


Figure 4.2 Connection between the electrostatic shaker (as the part that moves the system), the clamping device, and the energy harvester device with Proof Mass I. Energy harvester device is electrically wired through electrical leads in order to obtain electrical data as shown in the left image.

Table 4.1 Geometric and material properties of the tested macroscale bimorph energy harvesters.

	Value	Comment
<i>Device dimensions</i>		
Energy harvester length L_{EH} / [mm]	63.7	Measured
Cantilevered energy harvester length L_T / [mm]	53.0	Measured
Energy harvester width b / [mm]	31.7	Measured
Energy harvester thickness t / [mm]	0.675	Measured
Energy harvester mass M_{EH} / [g]	10.5	Measured
Piezoelectric layer thickness t_p / [mm]	0.275	Measured
Structural layer thickness t_s / [mm]	0.126	Measured
<i>Material properties used</i>		
Piezoelectric layer density ρ_p / [kg/m ³]	7750	Ref.[86]
Structural layer density ρ_s / [kg/m ³]	7630	Calculated
Proof mass density ρ_0 / [kg/m ³]	7751	Calculated
Piezoelectric layer stiffness c_{11}^E * / [Gpa]	61	Ref.[86]
Structural layer stiffness c_s * / [Gpa]	100	Calculated
Absolute permittivity ϵ_{33}^T / [F/m]	1800 ϵ_0	Ref.[87]
Absolute permittivity ϵ_{33}^S * / [F/m]	1551 ϵ_0	Calculated
Vacuum permittivity ϵ_0 / [F/m]	8.854 x 10 ⁻¹²	Ref.[88]
Strain constant d_{31} / 10 ⁻¹² [C/m]	-190	Ref.[87]
Strain constant e_{31} * / [C/m]	-14.2	Calculated

Note on *: asterisk (*) is used to indicate material property constants specified for a plate structure when needed (refer to Appendix A).

Table 4.2 Geometric dimensions of device proof masses and input base accelerations.

	Mass, M_{PM} [g]	Active plate length, L [mm]	Proof mass length, L_{PM} [mm]	L_T ($=L+L_{PM}$) [mm]	Proof mass thickness, h_{PM} [mm]	Base acceleration [m/s ²]
No Proof Mass	0	53.0	0	53.0	0	2.5
Proof Mass I	16.7	42.7	10.4	53.1	6.61	0.5
Proof Mass II	34.7	31.6	21.6	53.2	6.66	0.2

4.3 Experiment-Model Correlation and Discussion of Proof Mass Effects on Harvesting Performance

4.3.1 Model Implementation

Model simulations in Section 3.3 are run on the macroscale PVEH without a proof mass (No PM), with Proof Mass I (PM I), and with Proof Mass II (PM II), followed by experimental performance tests for the purpose of model verification. It is beneficial to test the device without a proof mass as the experimental results can be compared with prior work by du Toit *et al* [74], where the same type of device was tested without a proof mass.

Key effective parameters such as mass, stiffness, capacitance etc. that appear in the governing equations for model implementation are listed in Table 4.3. Overall, all effective parameters in the governing equations (2.17) and (2.18) vary depending on whether a proof mass is added or not as well as geometric specifics of the proof mass. Consistent with expectations, the effective mass, M , increases as the size and the mass of a proof mass increases and that effective stiffness, K increases as the active beam/plate length is reduced the longer the proof mass becomes. Other parameters such as coupling, θ , capacitance, C_p , and system coupling, κ^2 , are found not to change significantly with proof masses as they are affected by coupling constant and electrical mode shapes, not mechanical or geometric factors and thus have a weak dependence on a proof mass.

Mechanical damping ratio is also obtained following the procedure stated in Section 3.4 previously, where mechanical responses measured at short-circuit condition are required along with theoretical values of effective mass, M , forcing function, B_f , and mechanical mode shape at the tip of the device, $\psi_{r,tip}$. It should be noted that the mechanical mode shape at the tip, $\psi_{r,tip}$, as well as effective mass, M , and forcing function, B_f , increase significantly as proof mass becomes larger and heavier. It is important to note that the mechanical damping ratios are derived from the equation of mechanical displacement at short-circuit conditions and resonance and thus must be computed using the data measured at short-circuit condition and resonance. As it is also possible to evaluate the mechanical damping ratio utilizing the equations and measured data at open-circuit conditions and anti-resonance as well, they are also computed to confirm that damping has little dependence on frequency in that range. Although detailed damping analysis at open-circuit condition and anti-resonance is not presented here, the key result from comparison is that there is little difference in the values of mechanical damping ratios analyzed either at short-circuit and resonance, or at open-circuit and anti-resonance. Determination of damping is critical and the scheme suggested and utilized in this work is effective, as small changes in values of mechanical damping ratios cause large changes in device response, especially at the resonances. This implies the importance of considering the geometric and material properties of a proof mass when a device incorporates a proof mass in order to get exact treatment of device dynamics (*e.g.*, damping ratio analysis) instead of using a point-mass assumption.

Key resulting performance equations are used to gain mechanical tip displacement histories as well as electrical responses as a function of electrical loading, R_l , which are plotted together with experimental results in Figures 4.4 through 4.12.

Table 4.3 Key device parameters for model implementation.

	M [kg]	K [N/m]	Θ [N/V]	C_p [F]	B_f	κ^2	$\psi_{r,tip}$	ζ_m
No PM	0.00878	4150	0.00469	4.12×10^{-8}	0.00687	0.126	2.00	0.0182
PM I	0.114	7760	0.00665	4.20×10^{-8}	0.0496	0.137	2.77	0.0154
PM II	0.414	19900	0.00961	4.21×10^{-8}	0.126	0.111	4.30	0.0146

4.3.2 Mechanical Mode Shapes for the Proof Masses

Mechanical mode shape, ψ_r , plays a major role in describing the structural dynamics of the beam/plate harvester. In this investigation, the first vibration mode would generally give the greatest power, and the subsequent experiment targets the first vibration mode as the frequency of interest for these energy harvesters, *i.e.*, the input energy at higher modes will be less than at the first mode as it is a design choice. Importantly, axial strain, (see equation (2.8)) is written in terms of the second derivative of mechanical mode shapes.

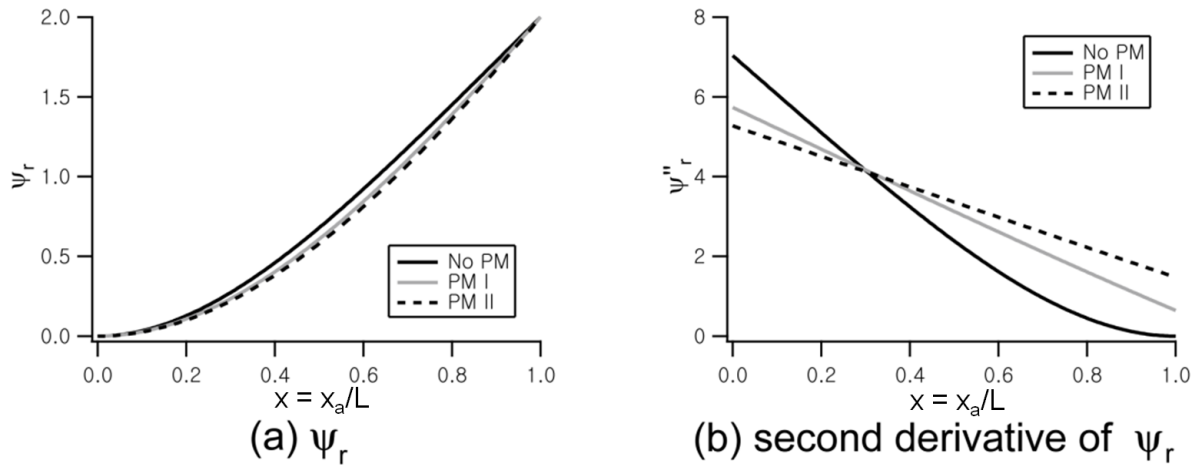


Figure 4.3 Variation of mechanical mode shapes and second derivatives (strain is proportional to the second derivative) in the axial direction from the clamp ($x=0$) to the proof mass junction ($x=1$). Here, x represents an axial position of normalized length of the device plate.

In Figure 4.3, the effect of proof mass on the mechanical mode shape and the second derivatives of mode shapes are presented. The horizontal axis represent x , an axial position of normalized length of the device plate, where the 1.0 indicates the junction point between the device plate and the proof mass. Figure 4.3 (a) clearly shows that the mechanical mode shape is normalized to 2 consistently for all cases at the junction where the proof mass begins. The plot in Figure 4.3 (a) reveals that the mechanical mode shapes change slightly, depending on whether there is a proof mass or not (No PM vs. PM I or II), as well as on the size of the proof masses.

When the second derivatives of mechanical mode shapes are compared with one another, the difference along the plate length is more apparent. Considering Figure 4.3 (b), in addition to managing resonant frequency, adding a proof mass has an additional positive effect: average strain is increased due to non-zero strain at the proof mass (device end).

4.3.3 Performance of Piezoelectric Vibration Energy Harvesters

4.3.3.1 Resonant and Anti-resonant Frequencies

The models in Chapters 2 and 3 allow one to predict resonant and anti-resonant frequencies, which are compared with experimental results. As shown in Table 4.2, the dimensions of PM I and PM II are distinct particularly in that PM II is longer in the axial direction, therefore having more distributed mass over the energy harvester than PM I. As they have similar thickness, this geometric sequence is quite beneficial to investigate the influence of mass distribution as well as the geometric variation.

Table 4.4 summarizes resonant frequencies and anti-resonant frequencies obtained from simulation and measurement for all proof mass cases. Overall, measured values and simulated values of both resonant frequencies ($f_{l,r}$) and anti-resonant frequencies ($f_{l,ar}$) are in good agreement for all cases. Considering the fact that an accuracy of down to 0.125 Hz is possible to obtain experimentally, the difference between the measured frequencies and calculated ones correspond quite accurately. An important point is that the resonant frequency is greatly reduced when a proof mass is introduced. For example, the natural frequency at short-circuit condition of the device without a proof mass is measured as 109.5 Hz, which is decreased by more than half to 41.63 Hz by adding PM I at the end of the device. Although the proof mass length of PM II is roughly twice longer than that of PM I, the resonant frequency of PM II (34.75 Hz) is not lower by half than that of PM I (41.63 Hz). The same trends are seen in not only resonance frequencies but also anti-resonance frequencies, both empirically and theoretically. The results shown in Table 4.4 suggest that the model is capable of predicting both resonance and anti-resonance frequencies both with and without a proof mass.

Table 4.4 Summary of frequencies, dimensionless time constants and electrical load at short-circuit and open-circuit conditions.

Case	Measured	Calculated	Measured	Calculated	Calculated		Calculated	
	$f_{l,r}$ [Hz]	$f_{l,r}$ [Hz]	$f_{l,ar}$ [Hz]	$f_{l,ar}$ [Hz]	$\alpha_{r,opt}$	$\alpha_{ar,opt}$	$R_{r,opt}$	$R_{ar,opt}$
							[k Ω]	
No PM	109.5	109.45	115.25	116.15	0.278	3.21	9.62	111.5
PM I	41.63	41.44	44.5	44.16	0.222	3.98	20.3	364.0
PM II	34.75	34.85	37.0	36.73	0.255	3.55	27.6	384.6

4.3.3.2 Model-Experiment Comparison of Overall Energy Harvester Response

Mechanical and electrical device responses are compared here. For each case (No PM, PM I, and PM II) depending on proof masses, mechanical tip displacement is measured at various discrete electrical resistances ranging from 0 k Ω to 100 k Ω with varying operating frequencies. Operating frequencies are selected to be two frequencies below resonance, at resonant and anti-resonant frequency, and two frequencies above anti-resonance for comparison, so that both off-resonant operation and resonant operation are systematically analyzed. For the PM II case, considering the narrow range of frequencies, one below resonance and one above anti-resonance are chosen as off-resonant operating frequencies instead of two points for each. At the same conditions, electrical performance is obtained by measuring the voltage generated across the electrical resistive loads and calculating the extracted power using measured voltage. All experimental results are graphically demonstrated in Figures 4.4 through 4.12 using dots while predicted results from modeling are represented by lines on the same plots. In addition to the data points from 0-100 k Ω , the measured points at open-circuit (where electrical loading, R_l , goes to infinity) are included at each input frequency in the plots of mechanical tip displacements (Figures 4.4, 4.7, and 4.10) and voltages (Figures 4.6, 4.8, and 4.11) versus electrical resistance, R_l . Empty squares in red color are used to distinguish these points from other measured points. As power goes to zero under open- or short-circuit conditions, these points are not considered in

power-resistance plots.

Tip displacements are shown in Figures 4.4, 4.7, and 4.10, and compare the experimentally obtained tip displacements, w_{tip} , with predicted tip displacement from modeling for No PM, PM I and PM II, respectively. On the whole, the simulation is in good agreement with experimental results at various electrical loadings and multiple operating frequencies. Particularly, at off-resonant operations, for example, at 75 Hz or 160 Hz in Figure 4.4 (a) and (f), respectively, the model accurately predicts the magnitudes and trends of mechanical tip displacement. It is also shown that further away from resonance or anti-resonances, the model becomes closer to the experimental results. Regardless of whether there is an attachment of a proof mass or not, similar trends in tip displacement histories result. At frequencies below resonance, tip displacements decrease slightly as the electrical loading increases (*e.g.*, Figure 4.4 (a), (b), Figure 4.7 (a), (b) and Figure 4.10 (a)). As the operating frequency gets closer to resonance, the extent of decrease becomes larger although it does not decrease proportionally to resistance. For frequencies at the point of anti-resonance and above anti-resonance, the trends of tip displacements are different in that they increase with increasing resistance. It should be noted that the maximum tip displacements are obtained at resonance for the short-circuit condition ($R_l = 0$), and at anti-resonance for the open-circuit condition ($R_l \rightarrow \infty$). These displacements are approximately equal, and represent the two points where no energy is harvested.

Voltages generated are plotted against resistance from 0 k Ω to 100 k Ω at various operating frequencies. Overall, experimental voltages agree well with the simulations for all cases as shown in Figures 4.5, 4.8, and 4.11, respectively. In a similar fashion to the mechanical relative tip displacements, when further away from resonances or anti-resonances, the more precise the predicted values are when compared with experimental results. In general, the voltage increases along with increase of resistance for both on- and off-resonance operation. The maximum voltages are obtained at anti-resonance, not at resonances. For example, within the resistance range of experimental measurements used here (0 k Ω -100 k Ω), the highest voltage of 6.9 V appears at anti-resonance among all other operating frequencies in case of a device without a proof mass (Figure 4.5 (d)). However, the data point of 11.1 V measured at the open-circuit condition ($R_l \rightarrow \infty$) suggests that the voltage would keep increasing as the electrical resistance increases until it reaches this value, if the measurements were taken at an extended range of

electrical load beyond 100 k Ω . This trend appears prominently at anti-resonance for all cases (Figures 4.5 (d), 4.8 (d), and 4.11 (c)). Unfortunately, the range of electrical resistance for experimental measurements was limited here to 0-100 k Ω , but the experimental trends are indicated by the open-circuit data points. On the other hand, at resonances (Figures 4.5 (c), 4.8 (c), and 4.11 (b)), it is observed that the voltages measured at 100 k Ω are already close to the values measured at open-circuit condition ($R_l \rightarrow \infty$), which is quite in contrast to the trends at anti-resonances where a large numerical difference is present between resistance data at 100 k Ω and infinity.

In Section 2.2, optimal electrical loading conditions for maximum power at both resonance and anti-resonance are derived and given in equations (2.28) and (2.29). Optimal electrical resistances as well as corresponding dimensionless time constant, α_{opt} at resonance and anti-resonance for all three proof mass cases are computed and listed in Table 4.4. As shown in Table 4.4, optimal electrical loading conditions at resonances are within the range of 0-100 k Ω , while optimal electrical resistances appear well above 100 k Ω at anti-resonances. For example, 384.6 k Ω and 364.0 k Ω are calculated for PM I and PM II, respectively, as optimal electrical resistances where maximum power can be obtained. This is related to the different behavior at open-circuit condition between resonance and anti-resonance. If the voltage were measured near the optimal points, like 400 k Ω , for instance, at anti-resonance, the measured points at these points would approach the values measured at $R_l \rightarrow \infty$. The empirical results of device responses at open-circuit conditions ($R_l \rightarrow \infty$) help predict the tendency of voltage behavior against electrical loading that are beyond the range of measurement undertaken in this work. Also, this tendency corresponds well with the trends of simulated results. Not only voltages but also tip displacements measured at open-circuit conditions ($R_l \rightarrow \infty$) do exhibit the similar behavior in that the values at open-circuit conditions ($R_l \rightarrow \infty$) represent the device responses at extended electrical loading conditions as in Figures 4.4, 4.5, 4.7, 4.8, 4.10, and 4.11.

One other point to notice in these voltage-resistance figures is the large difference in voltage between resonance and anti-resonance. This change is reflected in the voltage equation (2.25) yielding:

$$\frac{v_{ar}}{v_r} = \frac{\kappa^2}{2\zeta_m} \sqrt{1 + \kappa^2} \quad (4.9)$$

where v_{ar} and v_r represent the voltages at anti-resonance and resonance, respectively. In fact, from equation (2.25), the largest voltage in the system for a constant base acceleration, \ddot{w}_B , is obtained at open-circuit conditions ($R_l \rightarrow \infty$). This corresponds with the maximum tip displacement for open-circuit conditions mentioned earlier, and together they serve to identify the anti-resonance frequency, ω_{ar} . Also from equations (2.24)-(2.26), a check can be made on the electrical coupling parameter, κ^2 , by comparing the resonance and anti-resonance frequencies, ω_r and ω_{ar} , using the relation,

$$\kappa^2 = \left(\frac{\omega_{ar}}{\omega_r}\right)^2 - 1 \quad (4.10)$$

Power extracted from a test PVEH is acquired using the relation, $P_{\max} = v_{\max}^2 / R_l$ and are presented in Figures 4.6, 4.9, and 4.12 together with the simulated lines obtained from modeling. The unit of power here is micro-Watts. Again, the model captures accurately the trend of power across varying electrical loading conditions at various input frequencies. In a prior work by du Toit *et al* [29, 30, 73, 74], it was theoretically shown that there are two optimum operating points in terms of power maximization and that those two points correspond to resonance and anti-resonance, giving equal values of maximum power when $2\zeta_m/\kappa^2 \ll 1$. The optimal points of electrical loadings for maximum power at resonance ($R_{r,opt}$) and anti-resonance ($R_{ar,opt}$) are calculated using equations (2.28) and (2.29), respectively, with the results summarized in Table 4.4.

As the optimal electrical resistances particularly at anti-resonances exceeds the experimental performance test range (100 k Ω), simulated powers are re-plotted against a more extended range of electrical resistances from 0 k Ω to 400 k Ω at resonances and at anti-resonance for all cases of No PM, PM I and PM II, and presented in Figure 4.13. For example, for the case of PM I, the maximum power, 166.9 μ W, takes place at around 20.3 k Ω at resonant operation

whereas the power is maximized as 164.5 μW at about 364 $\text{k}\Omega$ at anti-resonance. For No PM case, 335.2 μW at 9.62 $\text{k}\Omega$ is obtained at resonance while 327.5 μW is computed at its optimal resistance of 111.5 $\text{k}\Omega$ at anti-resonant operation. Power in PM II case is maximal at 60.5 μW at resonance, and 59.3 μW is obtained at anti-resonance at their optimal electrical resistances of 27.6 $\text{k}\Omega$ and 384.6 $\text{k}\Omega$, respectively. It is quite significant that almost equal maximum power can be achieved at distinct electrical loading conditions, depending on whether a device is operated at resonance or anti-resonance. This also implies the frequency shift according to electrical loading, which is consistent with the discussion by du Toit *et al* [74], using power-frequency ratio plots at various electrical resistances. The slight numerical difference between the maximum power at resonance and anti-resonance suggests that system coupling, κ^2 , is not large enough compared to the mechanical damping ratio, ζ_m , to satisfy the approximation that $2\zeta_m/\kappa^2 \ll 1$. As already shown in voltage-resistance plots, the maximum voltage appears at anti-resonance rather than resonance. Therefore, anti-resonant operation is advantageous when high voltage is required with high electrical resistance while resonant operation is beneficial for the applications that require high current. This explains why not only resonant frequency but also anti-resonant frequency should be considered for optimal design.

There are two aspects that should be mentioned regarding the operation at resonances. First of all, the advantages of resonant (or anti-resonant) operation for energy harvesting are clearly observable when the resonant operation is compared with the off-resonant operation. Both mechanical and electrical performance of the system is greatly amplified at resonance compared to the off-resonant operation. Small deviations from resonance or anti-resonance condition will cause the device to perform with much diminished effectiveness. In terms of voltage, the maximum value is seen to be achievable at anti-resonance conditions. Thus, depending on the application, it should be determined whether the system will be operated at resonance or anti-resonance (*i.e.*, if high current or voltage is desired, respectively). Also, adjusting the input conditions such that they are as close to the resonance or anti-resonance is another substantial point when considering the device operations. Secondly, although predicted and measured performance results are well correlated both mechanically and electrically at off-resonant operations, it is observed that a consistent discrepancy exists at the resonances and anti-resonances between the simulation and the measurement. When prediction deviates from

experimental measurement for voltage, the extent of discrepancy for power is more pronounced because the power is obtained through using the value of voltage squared, as shown in the power plots of Figures 4.6, 4.9, and 4.12. The deviation that occurs at resonance and anti-resonance is attributed to the nonlinearity in piezoelectric coupling that is not incorporated in the modeling. The model here is based on a linear constitutive relation of piezoelectricity. However, the piezoelectric constants are known to be nonlinear even at moderate levels of strain (*e.g.*, 100 μ -strain). Accordingly, a moderate discrepancy takes place at resonant and anti-resonant conditions due to the nonlinearity and this is consistent with modeling of the nonlinearity by others [89-92]. Although there are small quantitative differences between measurement and simulation at the resonances, the general trends of the tip displacement, voltage, and power at resonance as well as at away from resonance are predicted accurately.

Lastly, the relation between the electrical damping ratio, ζ_e and mechanical damping ratio, ζ_m can be analyzed using tip displacement vs. electrical loading result. As stated earlier, the electrical damping ratio is known to be equal to mechanical damping ratio when the power is maximized at optimal electrical loadings. As electrical resistance is zero at short-circuit condition, no electrical damping exists at this point. However, when electrical resistance is introduced, more and more electrical damping affects the device responses. This is observed in the measurement results of tip displacement against electrical loading especially at resonance. For PM I case, the maximum power in measurement occurs at 20 k Ω at resonant operation (41.625 Hz) as in Figure 4.9 (c). If we compare the tip displacement at 20 k Ω , where the maximum power takes place, with the tip displacement at short-circuit conditions ($R_l = 0$ k Ω), the former comes as 138.3 μ m, which is about a half of the latter, 280.3 μ m. It can be easily derived from equation (2.24) that the tip displacement at resonance is inversely proportional to mechanical damping ratio, ζ_m at short-circuit conditions ($R_l = 0$ k Ω). Since the electrical damping ratio becomes equal to the mechanical damping ratio at the point where the power reaches maximum, the total damping at the point of maximum power will be twice the total damping at short-circuit condition where only mechanical damping is involved. This coincides with the observation on the decrease in experimentally measured tip displacements by about a half when the value at short-circuit condition is compared with the data measured at the point where power is maximum.

The electromechanically coupled energy harvester model predicts quite accurately both

mechanical and electrical device responses overall, especially at off-resonant operations both below and above resonance or anti-resonance. The model has a capability of not only capturing the general trend of system response but also estimating quite precisely values of magnitude for resonance frequencies, mechanical performances, and electrical device responses. The governing equations of the system (equations (4.4) and (4.5)) are almost identical to those used by Erturk *et al* [76], but use of mass-normalized modes and complex quantities obscure the meaning of the resulting calculations; although the proof mass was not rigorously treated, the behavior in that work does indicate (undiscussed) resonant and anti-resonant behavior.

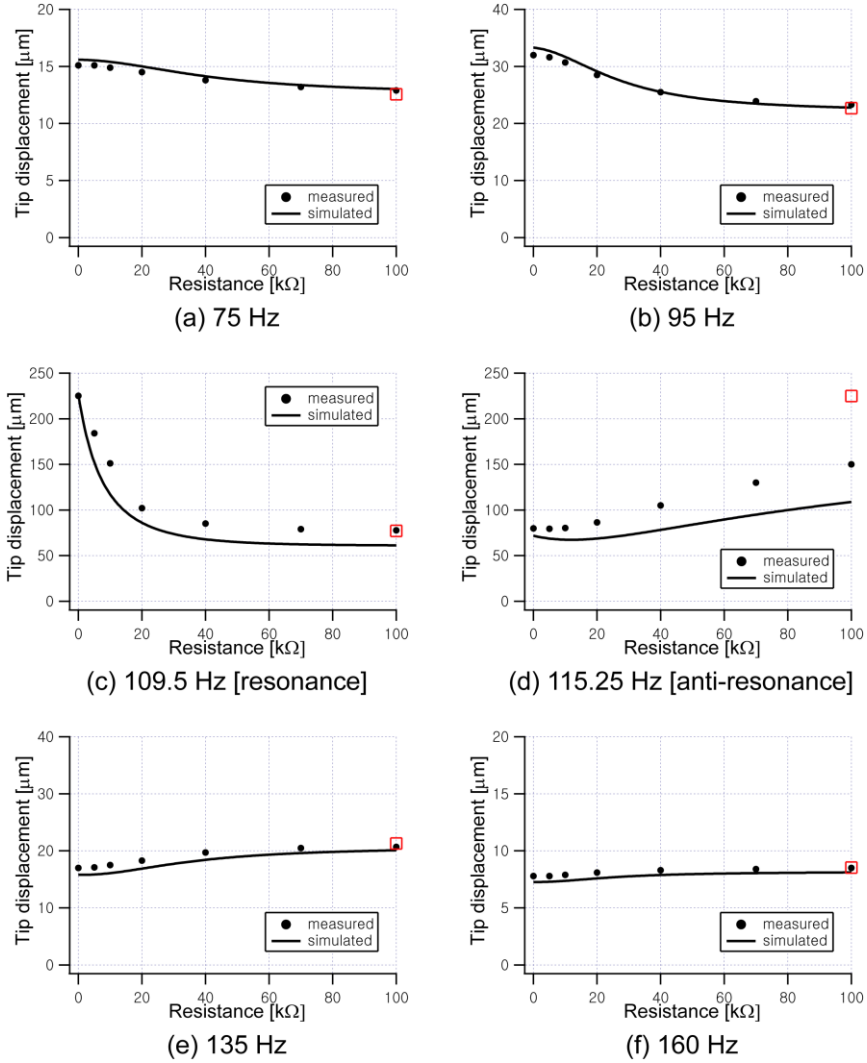


Figure 4.4 No Proof Mass (No PM): predicted vs. measured response: tip displacement plotted against the electrical load at various input frequencies. Base acceleration is held constant at 2.5 m/s^2 . Empty squares in red color indicate the tip displacements measured at open-circuit condition ($R_l \rightarrow \infty$).

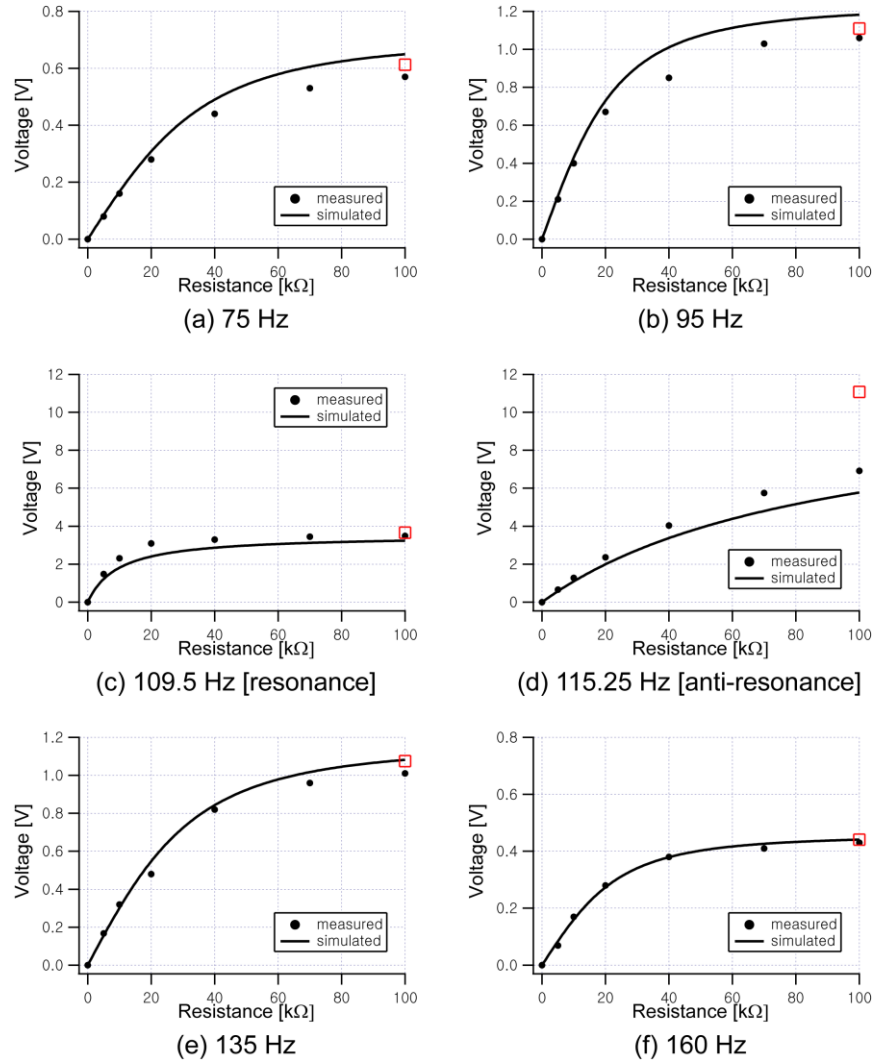


Figure 4.5 No Proof Mass (No PM): predicted vs. measured response: voltage developed, plotted against the electrical load at various input frequencies. Base acceleration is held constant at 2.5 m/s^2 . Empty squares in red color indicate the voltages measured at open-circuit condition ($R_l \rightarrow \infty$).

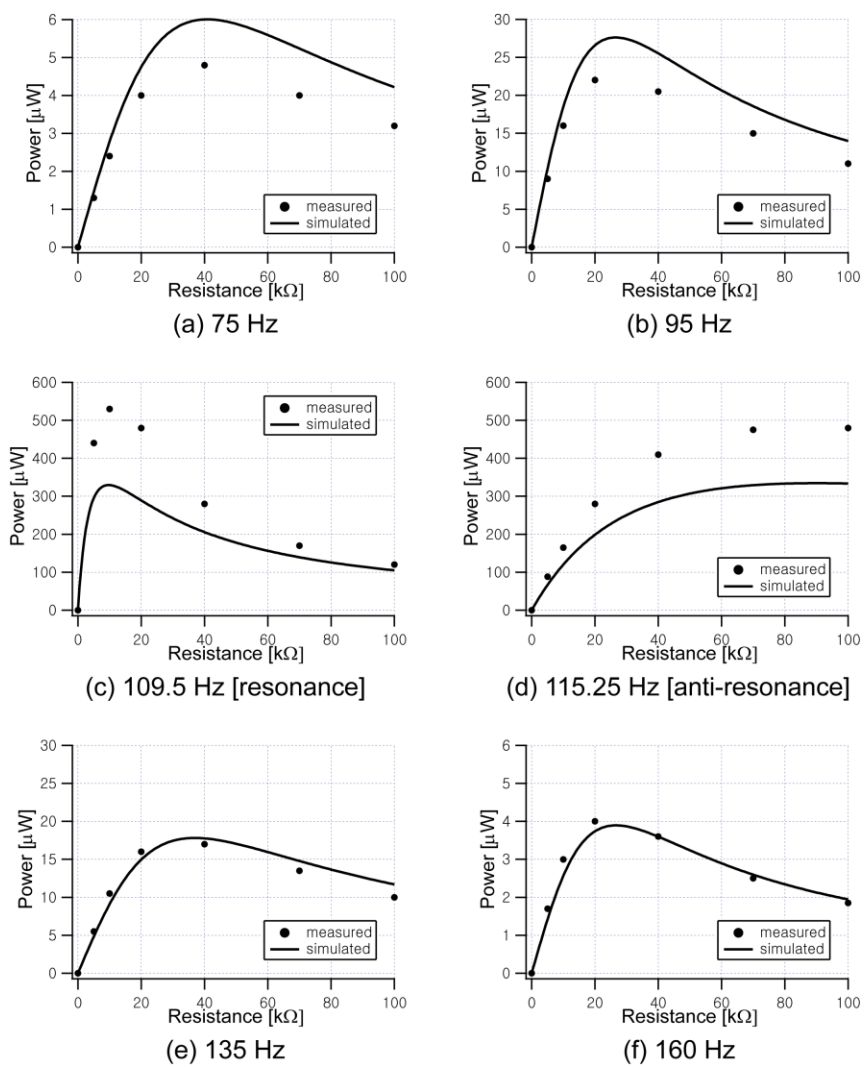


Figure 4.6 No Proof Mass (No PM): predicted vs. measured response: extracted power plotted against the electrical load at various input frequencies. Base acceleration is held constant at 2.5 m/s^2 .

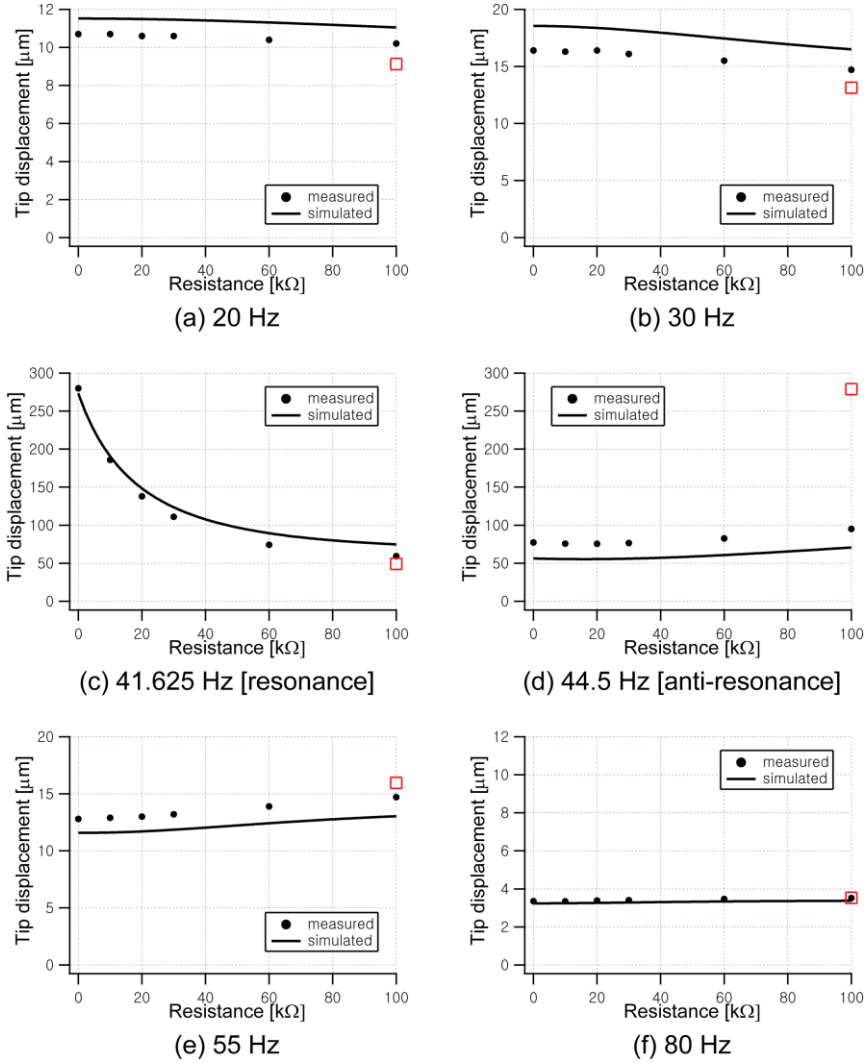


Figure 4.7 Proof Mass I (PM I): predicted vs. measured response: tip displacement plotted against the electrical load at various input frequencies. Base acceleration is held constant at 0.5 m/s^2 . Empty squares in red color indicate the tip displacements measured at open-circuit condition ($R_T \rightarrow \infty$).

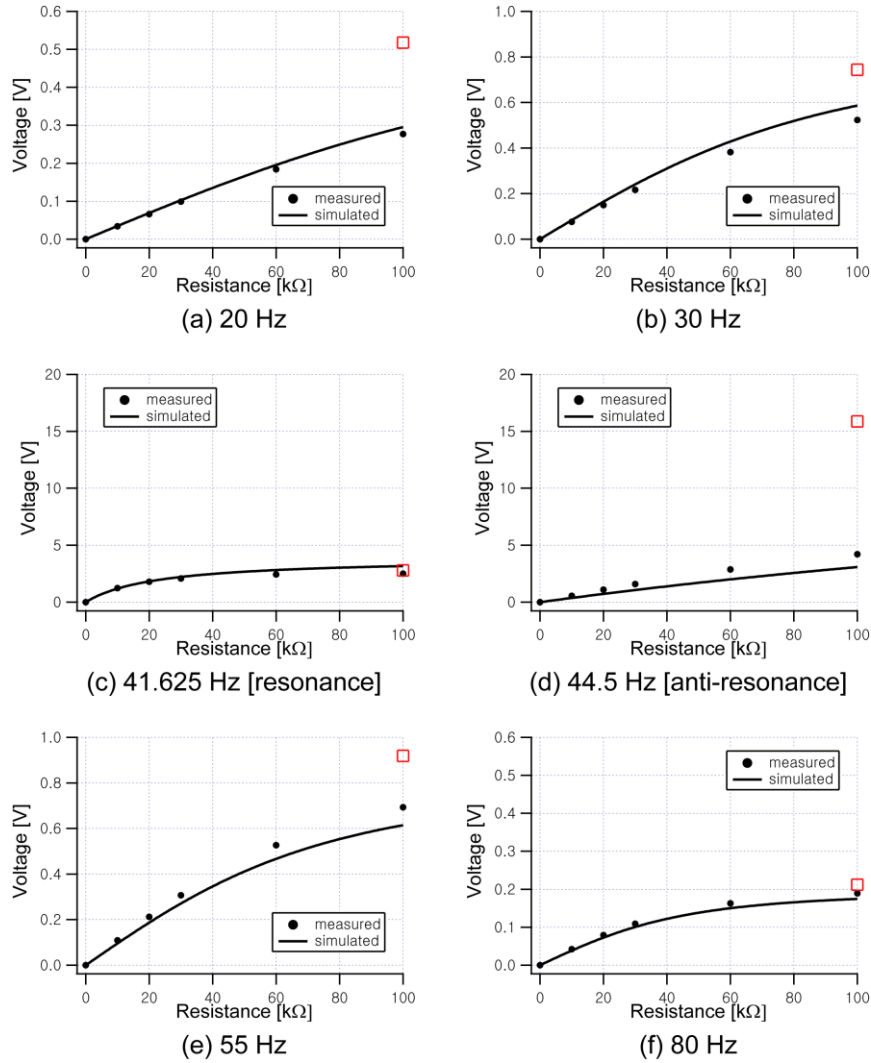


Figure 4.8 Proof Mass I (PM I): predicted vs. measured response: voltage developed, plotted against the electrical load at various input frequencies. Base acceleration is held constant at 0.5 m/s^2 . Empty squares in red color indicate the voltages measured at open-circuit condition ($R_l \rightarrow \infty$).

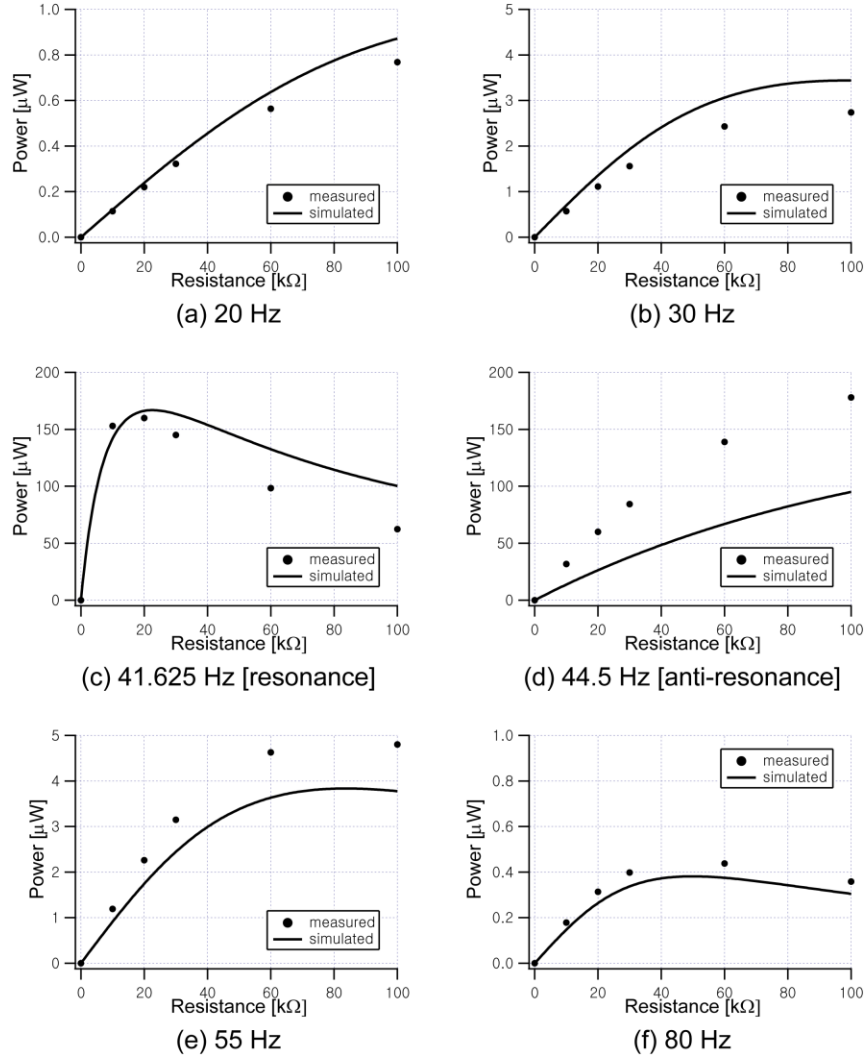


Figure 4.9 Proof Mass I (PM I): predicted vs. measured response: extracted power plotted against the electrical load at various input frequencies. Base acceleration is held constant at 0.5 m/s^2 .

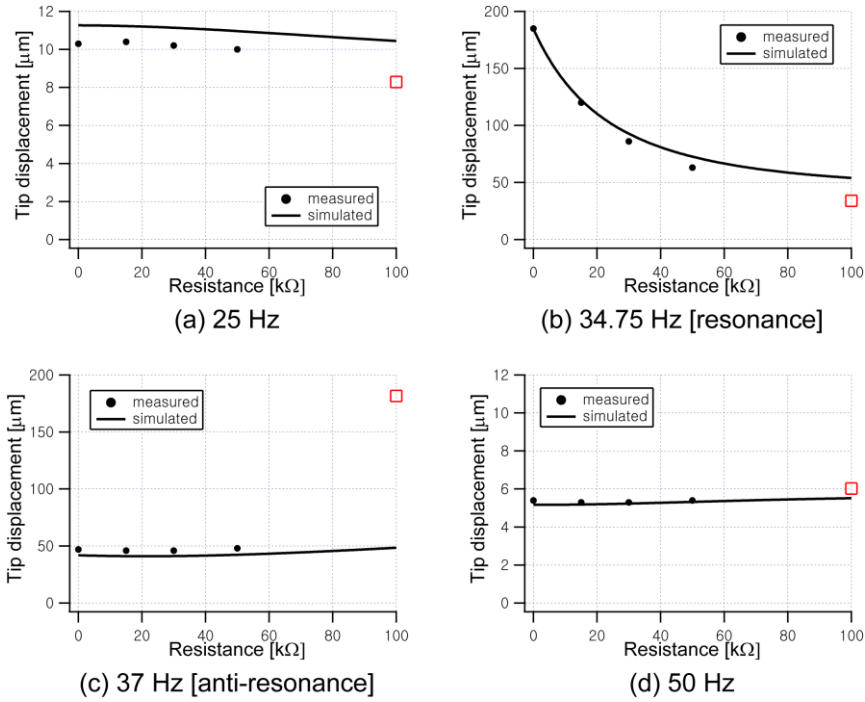


Figure 4.10 Proof Mass II (PM II): predicted vs. measured response: tip displacement plotted against the electrical load at various input frequencies. Base acceleration is held constant at 0.2 m/s^2 . Empty squares in red color indicate the tip displacements measured at open-circuit condition ($R_l \rightarrow \infty$).

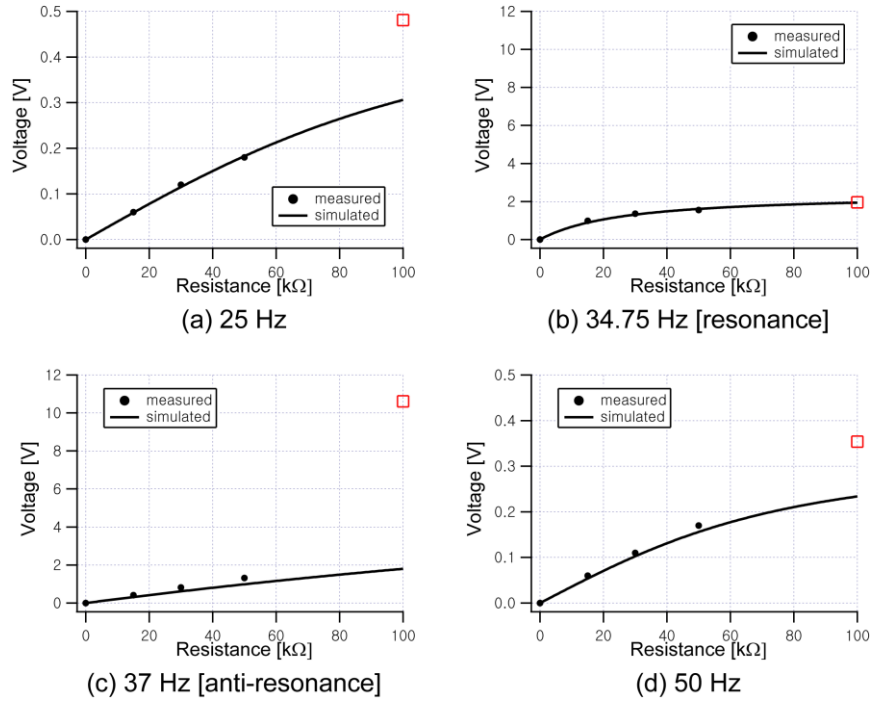


Figure 4.11 Proof Mass II (PM II): predicted vs. measured response: voltage developed, plotted against the electrical load at various input frequencies. Base acceleration is held constant at 0.2 m/s^2 . Empty squares in red color indicate the voltages measured at open-circuit condition ($R_l \rightarrow \infty$).

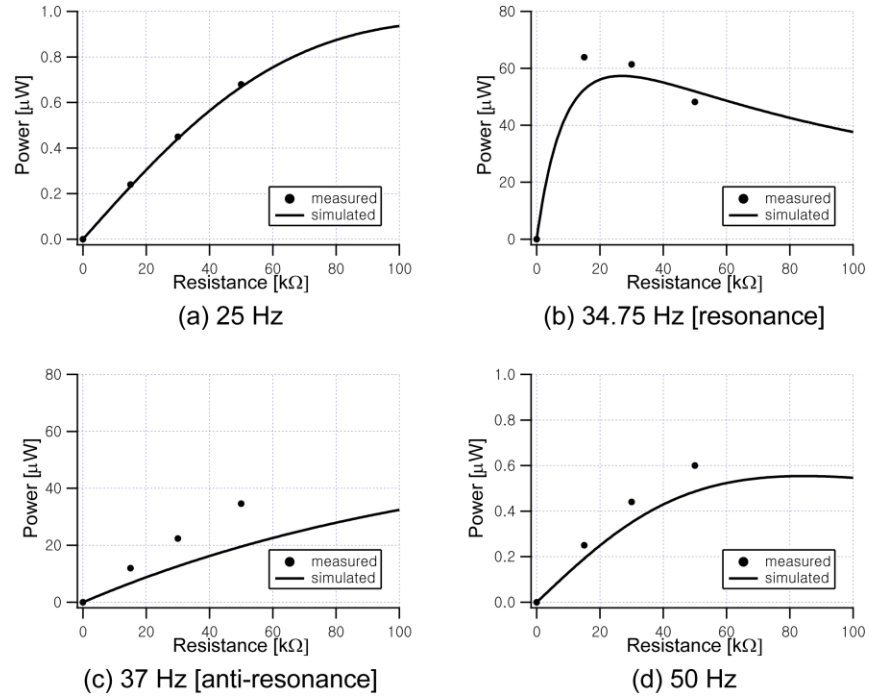


Figure 4.12 Proof Mass II (PM II): predicted vs. measured response: extracted power plotted against the electrical load at various input frequencies. Base acceleration is held constant at 0.2 m/s^2 .

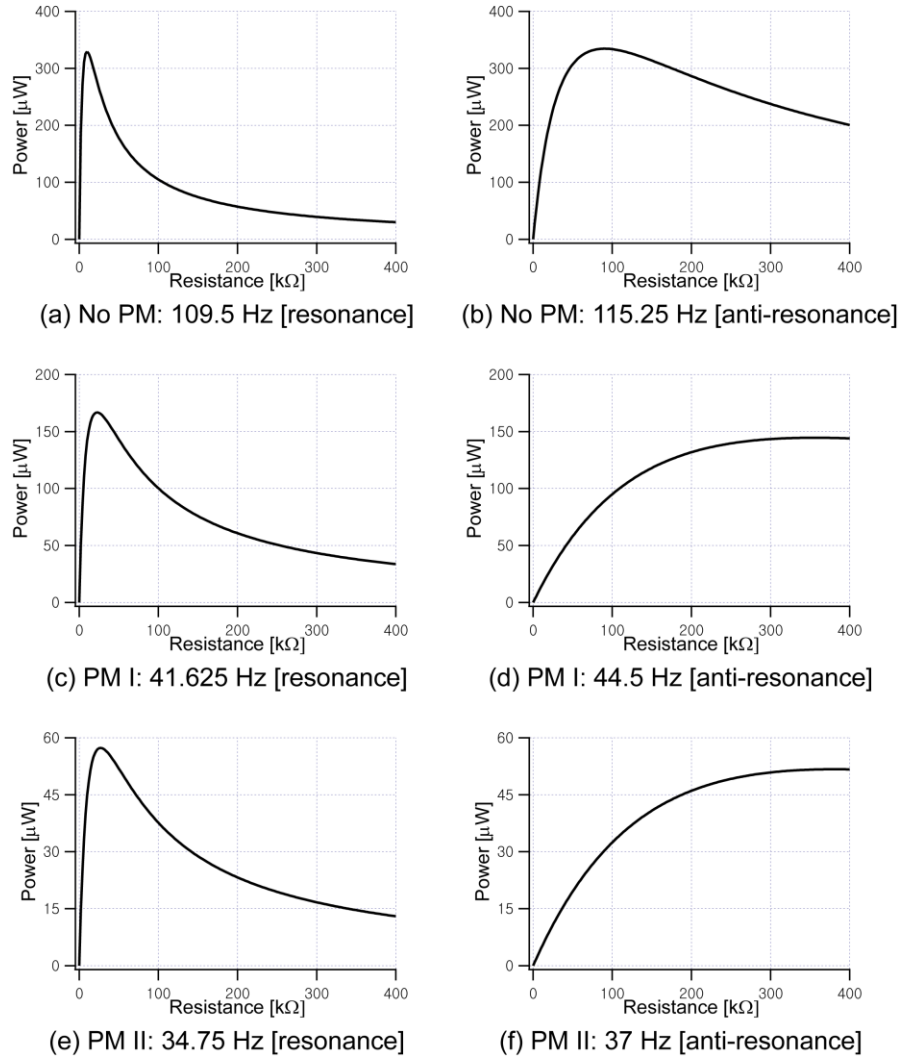


Figure 4.13 Dual-power optimization at resonance and anti-resonance for each proof mass case.

4.3.3.3 System Behavior under Various Operating Conditions

Performance of PVEH devices is dependent upon several operating parameters including operating frequencies, electrical impedance (resistance used throughout here), and damping conditions. The trends and magnitudes of mechanical displacement, developed voltage and output power across varying electrical resistances at various operating frequency conditions are observed both experimentally and analytically for macroscopic, bimorph PVEH devices in series connection with and without a proof mass in this chapter. In Chapter 6, output power of the same device is plotted against operating frequencies at various electrical resistances to study the system-level optimization. All these works lead to the following key conclusions: 1) there are dual optimal points for maximum power generation at resonance and anti-resonance, and 2) electrical resistances can be used to tune the optima for power. So far, output power is plotted against either electrical resistance or input operating frequencies in two-dimensional spaces. As a summary for the power behavior under various operating conditions, output power is plotted in three-dimensional space in Figure 4.14 while varying electrical resistance and input operating frequencies (here, normalized frequency, Ω is used) simultaneously for the macroscopic device with proof mass I (PM I) that is used in this chapter. The peak ($\Omega = 1$ at $R_l \rightarrow 0$ and $\Omega = \sqrt{1 + \kappa^2}$ at $R_l \rightarrow \infty$) represents the optimum for power, and the largest frequency shift from resonance to anti-resonance occurs when electrical resistance increases, which are clearly shown in Figure 4.14. It is also interesting to see how flat the peak power is between resonance and anti-resonance frequencies, suggesting that the electrical resistance gives us a tailorable bandwidth for vibration energy harvesting.

To see the damping effect briefly on the power behavior, particularly at resonance, multiple plots of output power of the same device (PM I case) versus electrical resistance at various quality factors (Q) are given in Figure 4.15. Mechanical damping ratio, ζ_m , is frequently used throughout this thesis but quality factor is also a commonly used notation as a measure of the damping condition. These two parameters are related via $Q = \frac{1}{2\zeta_m}$. Observation of the plots in Figure 4.15 indicate that as the quality factor gets higher (*i.e.*, less damping is involved), the power peaks tends to have a narrower bandwidth with increased magnitude of power. While the

measured power values are in good agreement with the simulated power for the test-specific (macroscopic energy harvester device) quality factor of 32.4, quality factors higher than 10,000 are typically expected in MEMS-scale PVEH devices.

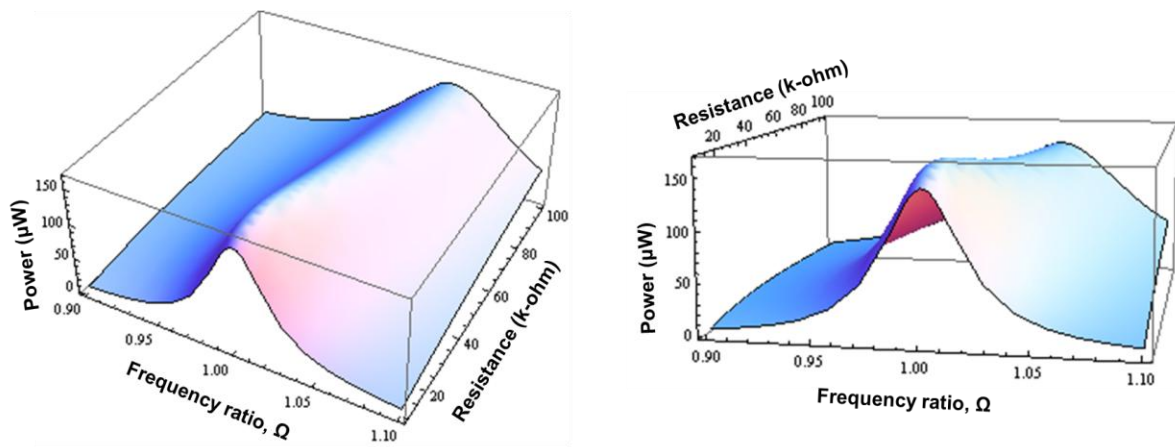


Figure 4.14 3-D plot (2 views) of output power against normalized frequency and electrical resistance. The model simulation is run on the experimentally verified macroscopic energy harvester with PM I.

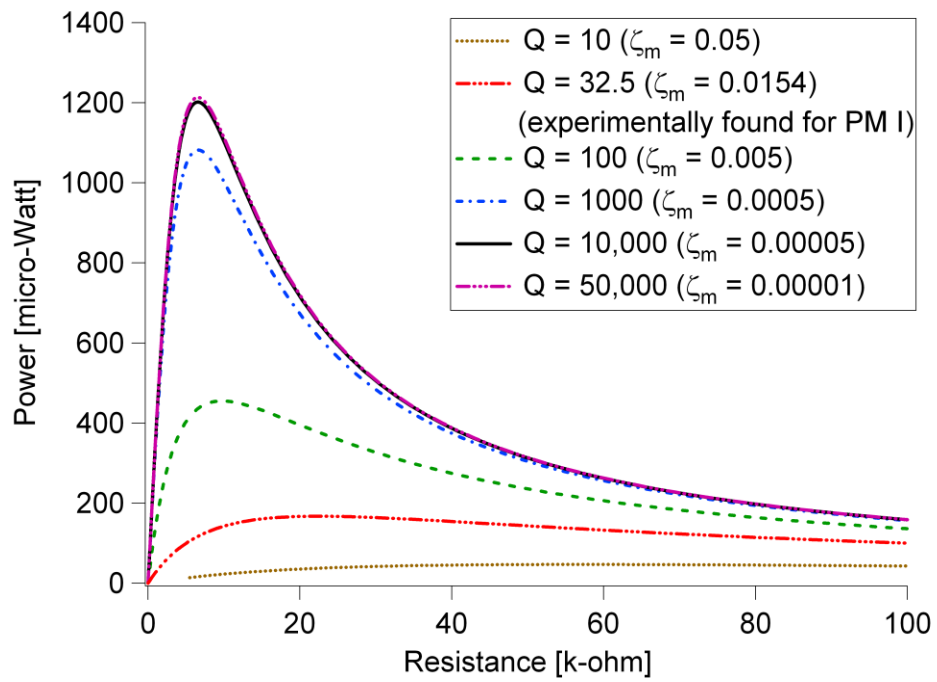


Figure 4.15 Power versus electrical resistance at various damping conditions. The model simulation is run on the experimentally verified macroscopic energy harvester with PM I.

Chapter 5

Experiment-Model Correlation for MEMS-scale Cantilevers with a Flexible Proof Mass

A thorough investigation of the mechanical behavior of micro-scale single crystal silicon cantilever with a distributed, flexible proof mass is presented in this chapter. This includes not only the experimental verification of the model developed for a flexible proof mass in Section 3.3 based on the two-beam method, but also the study of the implication of proof mass effects on the performance of PVEHs particularly at MEMS-scale. A set of new experiments are designed that include fabrication of novel MEMS-scale proof masses with various lengths using focused ion beam milling (FIB), and testing of MEMS-scale cantilevers using atomic force microscopy (AFM).

The basic operating principles of AFM served as inspiration for using a cantilever probe from AFM for the study of mechanical performance of MEMS cantilevers. As illustrated in Figure 5.1, AFM consists of three main parts: i) AFM head that includes piezoactuator (high frequency actuator and Z-axis positioner), holder for cantilever probes, and laser beam bouncing detection unit (laser and split photo diode), ii) sample stage for sample holding and x-y positioning of the sample, and iii) controller box. The primary function of AFM is to map the surface topography of target samples by monitoring the cantilever deflection induced by the Van der Waals force between a probe tip and the sample. Before topography acquisition in non-

contact mode where the cantilever probe is oscillating near its resonance frequency, preliminary characterization of cantilever probes is required, which includes the measurement of mechanical characteristics such as resonant frequencies, deflections, and quality factors of the AFM cantilever probe. Careful examination of these processes reveals that the characterization of cantilever probes in AFM has components very similar to the analysis of base-excited cantilevered PVEH structures. First of all, cantilevers at micron-scale provide the size and geometric shape of interest for the analysis of MEMS-scale cantilevered PVEH devices. Secondly, the piezoactuator can serve as mechanical shaker to vibrate the cantilevered structures at or near resonance. Lastly, the preliminary probe characterization process can be used to characterize the mechanical behavior of micron-scale cantilevered structures vibrated particularly at or near resonances by providing the experimental data for resonance frequency, deflection along the beam, and quality factors, as explained earlier. The deflection is measured using a laser spot reflected from the top surface of the cantilever into an array of photodiodes. While laser beam spot is fixed on one point of the cantilever in typical experiments using AFM, it is also possible to vary the position of the laser beam spot, allowing acquisition of mechanical responses at different locations along the cantilever length [93].

Consideration of all these factors discussed above gave a novel idea to utilize AFM probe cantilevers as “the sample” to test, instead of using it as a tool for the topography measurement of materials samples, in order to verify the model for a flexible proof mass as well as to investigate the mechanical behavior of micro-scale cantilevers with a distributed, flexible proof mass. Furthermore, this AFM-based test method is a newly designed experiment especially in the research area of energy harvesting and thus, the application of the recipes used in this experiment may open up other possibilities of using AFM in diverse fields of research.

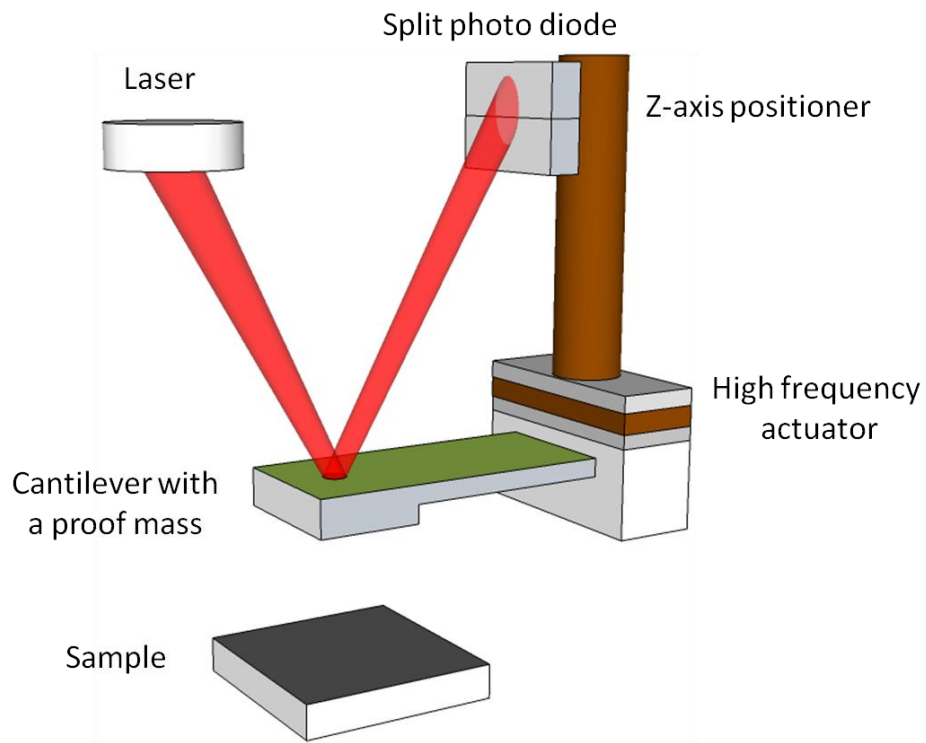


Figure 5.1 Schematic of AFM equipped with a cantilever (with a proof mass).

5.1 Fabrication of Proof Masses Using Focused Ion Beam

An AFM probe typically consists of a micro-scale cantilever with a sharp tip at its end that is used to scan the specimen surface. For the purposes here, however, a tip-less cantilever is more suitable as modification of its structure is easier to have proof masses of various lengths using FIB. Figure 5.2 contains SEM images of the as-purchased tip-less single-crystal silicon cantilever probe (Nanosensor, TL-FM 20) before any FIB processing. FIB is a time-efficient tool for custom-shaped geometries. FIB (Zeiss NVision 40 at the Electron Microscopy Center, Argonne National Laboratory) was used to micro-machine the cantilever probe to have various sizes of proof masses by sequential subtraction of material (single-crystal Si). This FIB instrument provides a well-focused Ga-ion beam with a high probe current necessary for the efficient removal of relatively large volumes of material (for FIB-SEM). In this instrument, the ion gun is oriented at an angle of 54° from the electron gun. Thus, a sample (cantilever probe) should be tilted to this angle from the electron gun and toward the ion gun under normal FIB-SEM working conditions. However, the sample should be tilted by 36° from the electron gun and 90° from the ion gun in edge-on milling where we use the relatively low energy component of the ion beam to etch (see Figure 5.3). Edge-on milling for accurate dimension control [94] was carried out at 30 kV with a probe current of 13 nA for initial trimming of a tip-less cantilever and 700 pA for sequential subtraction to vary the length of proof mass. SEM images were collected at each stage to provide detailed dimensions of each cantilever with distributed proof mass.

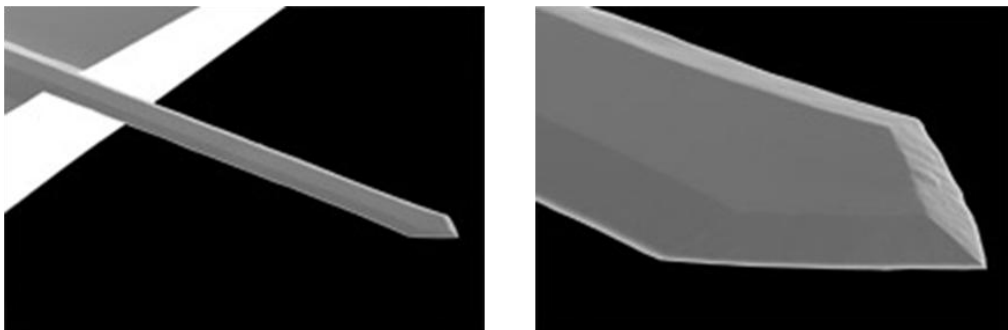


Figure 5.2 SEM images of the as-purchased tip-less single-crystal silicon cantilever probe
(Source: <http://www.asylumresearch.com/Probe/TL-FM,Nanosensors>).

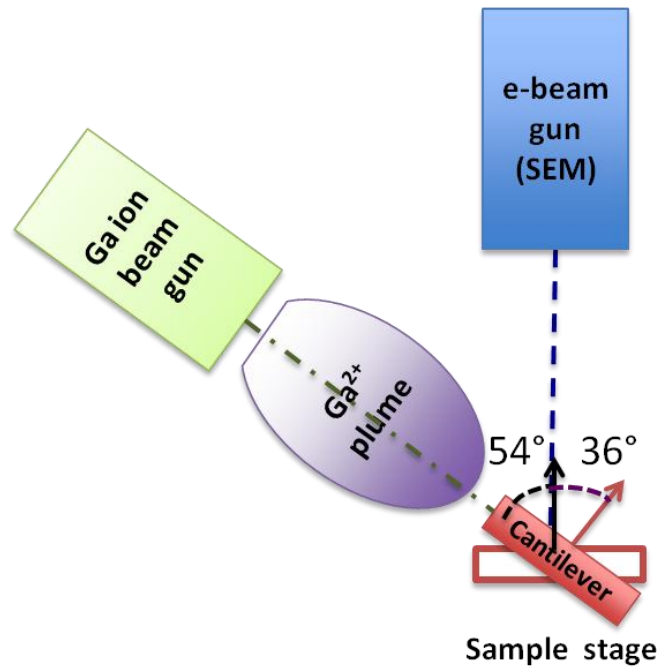


Figure 5.3 Schematic of dual-beam FIB apparatus and sample configuration for edge-on milling.

In Figure 5.4, we illustrate a cantilever with a relatively thin, distributed proof mass of different lengths (dashed and solid lines) together with SEM images of one proof mass case ($L_{PM} = 28.5 \mu\text{m}$) from different perspectives. Starting from a uniform beam where total length of the beam, L_T , is $220.7 \mu\text{m}$ and the total thickness is $3.07 \mu\text{m}$, we milled out sequentially 20, 20, 40, 40, 30, and 30 μm s in length from the clamped end, yielding a set of cantilevers with proof mass lengths of 200, 181.3, 140.3, 99.7, 59.2, 28.5 μm , and lastly a cantilever with no proof mass ($1.94 \mu\text{m}$ in average thickness of the beam). The width of the cantilever was measured to be $20.7 \mu\text{m}$ on average. There are two aspects noteworthy in the SEM images of Figure 5.4. First, a step-like trace remained visible for each segment that was milled away as it is hard to control the milling thickness and orientation of the sample perfectly to match with the previous segment. Therefore, when we implement our model to calculate resonant frequency, the average beam thickness of $1.13 \mu\text{m}$ was used as the thickness of the proof mass, thus giving a total thickness of $3.07 \mu\text{m}$ for the beam plus proof mass. Second, it is quite notable that no bending was observed even after the full milling process, implying that little residual stress is induced even when

significantly etched by Ga ions. More SEM images are available in Appendix D.

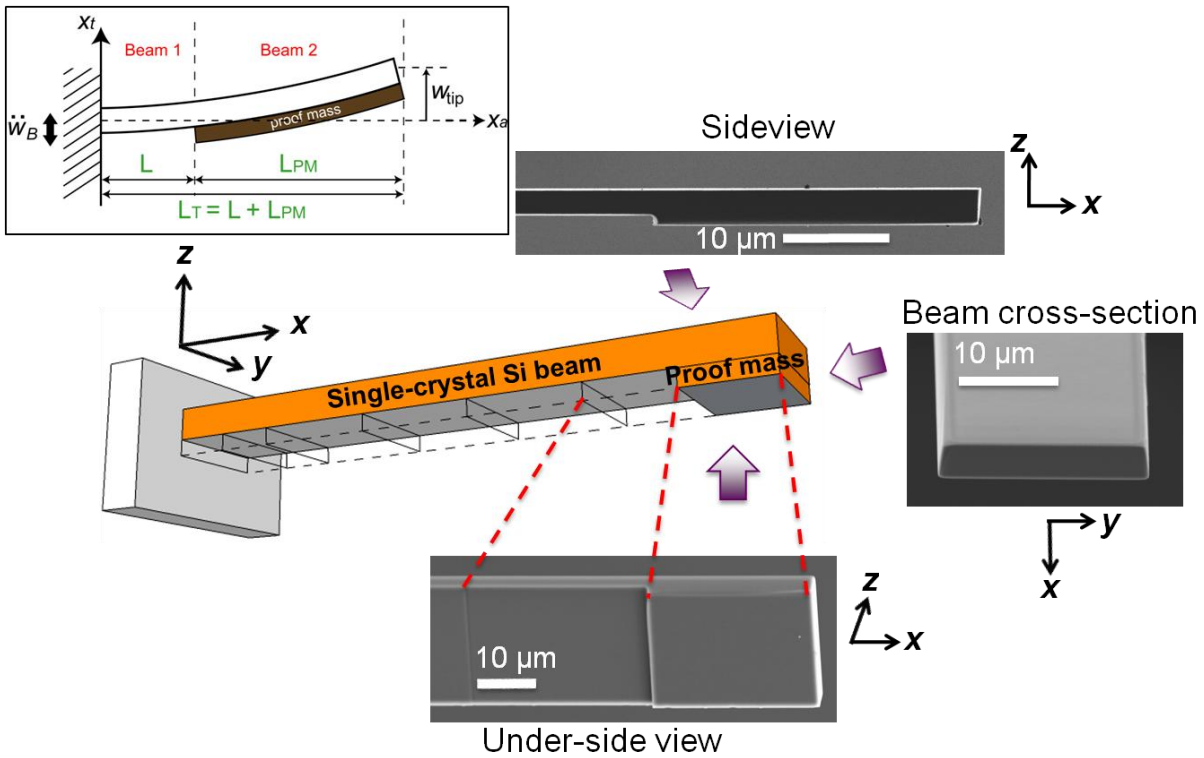


Figure 5.4 3-D schematic and SEM images of a single-crystal silicon cantilever with a flexible, distributed, thin proof mass fabricated by FIB lithography. Inset shows 2-D schematic of base-excited cantilevered beam with a proof mass at the tip with model parameters.

5.2 Characterization of MEMS-scale Cantilevers Using Atomic Force Microscopy

The micro-machined Si cantilever probe with a proof mass was mounted in an AFM (MFP-3-D, Asylum Research) to characterize its mechanical behavior, most importantly the resonant frequencies depending on the lengths of proof mass. Following is the experimental 5-step sequence devised for this work, based upon the typical AFM probe characterization process:

1) Laser beam positioning and dimension measurement

Performance parameters were measured at six different positions with equi-distances ($\sim 20 \mu\text{m}$) along the beam length, which allows acquisition of each parameter as a function of x_a (where x_a is the distance from the fixed end of the cantilever). The interval between the positions of measurement was determined considering the size of the laser beam spot ($\sim 40 \mu\text{m}$ in diameter) and the cantilever. The laser beam spot was positioned onto the point of interest on the cantilever using the real-time images of the beam spot and cantilevers captured by CCD camera. The same images were also used to estimate the geometric dimensions, particularly the distance between the fixed end of cantilever and the laser spot (the point of measurement). Dimensions obtained here are compared with the dimensions estimated from SEM images for accuracy.

2) Quantification of photo-diode signal in units of nano-meters

In AFM characterization, amplitude (deflection) of the vibrating cantilever probe is measured using a photo-diode signal and thus the data is obtained in units of [V], which needs to be converted into a length unit. For this, so called “inverse optical lever sensitivity (OLS)” should be measured, which is defined as the inverse of the output voltage from the photo diode when the cantilever is bent by the movement of the piezoactuator by 1nm. Inverse OLS in units of [V/nm] is obtained from the force-distance curve by assessing the ratio of the distance [nm] that the given probe tip moves to the output voltage [V] of the photo-diode signal. Contact mode is used where the cantilever probe tip is in touch with the sample surface and thus, a standard stainless steel substrate was chosen and used as a sample in this case due to its rigidity and low stiction characteristics.

3) Measurement of stiffness, K [N/m]

After the measurement of inverse OLS, the mode is switched to AC mode and thermal measurements are undertaken. Thermal analysis is the measurement of mechanical behavior of a cantilever probe when agitated only by thermal energy at room temperature without any external

application of other driving forces. From this analysis, we obtain stiffness, K [N/m] and thermal quality factor.

4) Measurement of resonant frequency, deflection, and quality factor

The function “auto-tuning” in AFM (MFP-3-D, Asylum Research) permits measurement of vibration amplitude as a function of input driving frequency under the condition of constant photo-diode signal at resonance. This provides information on mechanical characteristics such as resonant frequency of a given cantilever probe [Hz], amplitude at the laser beam targeted position [V], and mechanical quality factor. Then, the same measurement is repeated but at constant drive amplitude to analyze the mechanical behavior of the cantilever at constant excitation.

5) Data analysis and model-experiment comparison

Below is the list of key performance parameters from the experimental procedure described above.

- Resonant frequency, f_I , as a function of proof mass size (L_{PM}/L_T where L_{PM} and L_T are the lengths of proof mass and the total beam, respectively.)
- Stiffness, K , as a function of position, x_a , along the beam length
- Quality factor, Q , both as a function of proof mass size and of position along the beam length
- Mechanical deflection along the beam length at various base excitations

Future work will incorporate the size effect of proof mass on mechanical damping and deflection in MEMS-scale cantilevered systems both theoretically and experimentally, based on the data acquired from the set of experiments described above.

5.3 Mechanical Behavior of Micron-scale Cantilevers With a Proof Mass

Measured first-mode resonant frequencies are compared with simulated results from three different modeling approaches on the single-crystal silicon cantilever probe with proof masses of various lengths. The three different modeling approaches include simple concentrated proof mass approximation, improved treatment of rigid proof mass with rotation, and exact treatment of flexible proof mass using the two-beam method (see Section 3.3). The results are shown in Figure 5.5 where resonant frequencies are plotted against normalized length of proof mass (*i.e.*, ratios of length of proof masses (L_{PM}) to the total length of the system (L_T)). From a perspective of FIB fabrication, the proof mass size becomes smaller as more milling is carried out. Density and elastic modulus are required as modeling inputs. $2,329 \text{ kg/m}^3$ is used as the density of single-crystal Si [69]. Elastic modulus of single-crystal silicon in [001] direction is estimated by using the 1st resonant frequency that is experimentally obtained at both end points where we can apply a well-established beam theory of bending vibration of a free-end cantilever without a proof mass. 88.6 kHz is obtained at the right ending point ($L_{PM} = 220.7 \text{ }\mu\text{m}$) while 49.6 kHz is recorded at the left ending point ($L_{PM} = 0.0 \text{ }\mu\text{m}$), each providing elastic modulus of 176.0 GPa and 138.4 GPa, respectively, which are in the range of the reported values for single-crystal Si of this orientation, 125 GPa-179 GPa [95]. The reason for the change in elastic properties between these ending points can be explained by the effect of Ga ions during FIB lithography. Therefore, we take 138.4 GPa for the elastic modulus of the beam (beam 1) where Ga ions cause the material property to change, while we use 176.0 GPa for the second beam (proof mass region) which is unaffected by FIB milling.

There are two important aspects that should be noted in Figure 5.5. First of all, comparison of three different modeling results from each model with the experimentally measured values suggest that each model has good predictive capability of resonant frequencies up to the point when the size of proof mass occupies about 60% of the total cantilever length, despite the significant approximations in those models, which is beneficial for simplicity of engineering design perspective. However, a discrepancy between the modeling results and the measured

values becomes prominent once the proof mass gets longer and more distributed than 60% of the total length. For instance, the resonant frequency predicted by the flexible proof mass analysis is in much better agreement with the measured frequency (1% difference vs. 26% by concentrated proof mass analysis, and 17% by rigid proof mass analysis when normalized proof mass length is 0.82). From the perspective of predicting dynamics (*e.g.*, estimation of resonant frequencies), Figure 5.5 would seem to indicate that a refined 'two-beam' dynamic model as presented here is of little value except when very long and thin proof masses are considered [11, 96]. However, this is not true because prominent difference occurs when it comes to prediction of strains (and therefore energy harvested in the case of, *e.g.*, a PVEH) depending on the choice of model as discussed next.

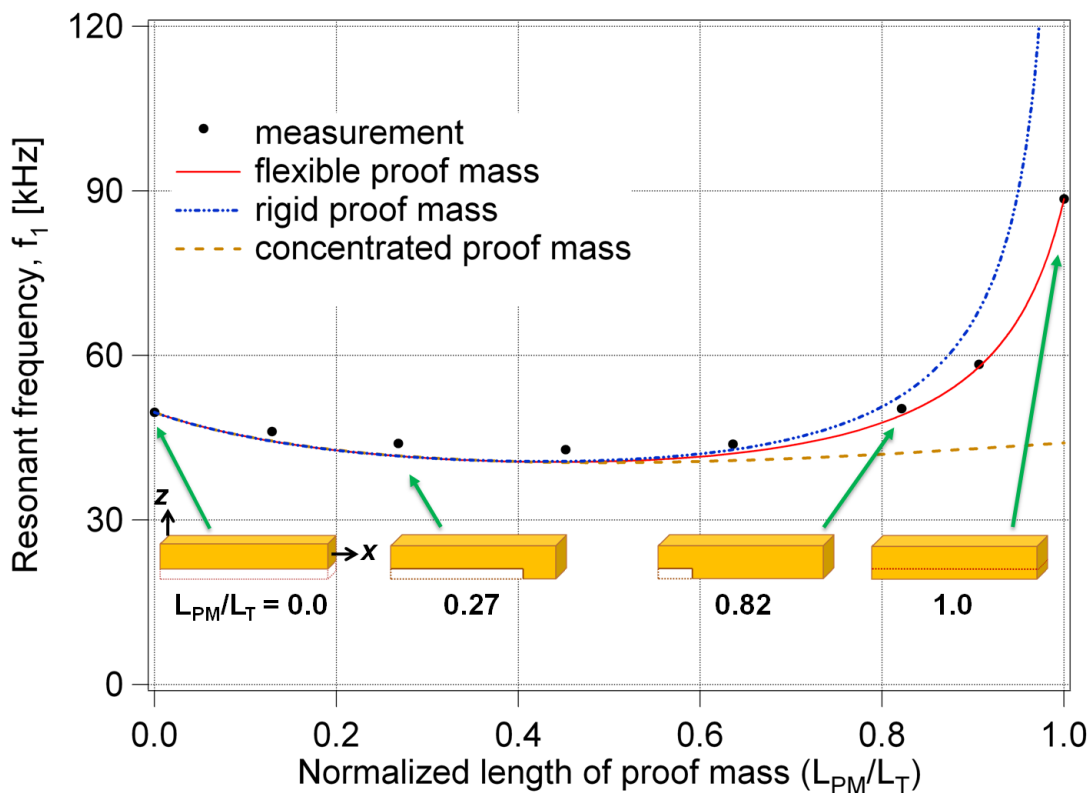


Figure 5.5 Resonant frequency vs. normalized proof mass length (simulated vs. experiments).

Secondly, observation on the extent of resonant frequency reduction with increasing proof mass size provides an important insight into the design and fabrication of proof mass configuration for MEMS-scale PVEHs. From the right-hand side of Figure 5.5, it is shown that when we subtract a portion of 20% of a total beam length, then the cantilever would have a proof mass of 80% of total beam length, decreasing the resonant frequency of the system by 46.2 %. In contrast, if we add a proof mass of 20% size of the total beam length, the resonant frequency can be reduced by 13.9%, as presented in the left-hand side of Figure 5.5. Conventionally, addition of a proof mass that occupies a portion of a cantilever is thought of when a proof mass is required. Here, we can see that another way to effectively adjust resonant frequency is to etch out a small portion of a beam layer, which results in a long and distributed proof mass, particularly at this MEMS-scale.

In Figure 5.6, mechanical mode shapes that are obtained from three different proof mass analyses are drawn against x_a , axial position of normalized length of the entire cantilever, where 0.0 and 1.0 indicate the clamped (fixed end) and the very end of the beam (or end of proof mass), respectively, at various lengths of proof masses. Mechanical mode shape, ψ_r , plays a major role in describing not only the structural dynamics of the cantilever system but also the device performance of PVEHs [52]. The longer a proof mass becomes, the greater the difference in mechanical mode shapes predicted by the different modeling approaches. The difference among modeling methods becomes even more distinct in the prediction of beam curvature (2nd derivative of mechanical mode shapes) which is directly related to axial strain, when the length of the proof mass increases [52]. Discontinuities in Figure 5.7 indicate the junction between proof mass and active beam. Accurate estimate of strain is very significant not only because it helps control fatigue and therefore design against structural failure during vibrating operation, but moreover, more power can be extracted by PVEHs at larger strains as power scales with strain squared [52]. Comparison of the absolute magnitudes of strain in Figures 5.7 (a), (b), and (c) suggests that the longer and more distributed proof mass induces more strain, implying increased power generation of PVEHs. The flexible proof mass analysis using the two-beam method accounts for the strain distribution in detail over the entire cantilever including the proof mass region. In contrast, neither the concentrated proof mass nor the rigid proof mass analysis can capture the elastic nature of the proof mass and, accordingly, the strain distribution under the

proof mass area. It is also seen in Figure 5.7 that when normalized proof mass length is 0.82, the predicted maximum strain at the clamped end of a cantilever can differ by up to 40% depending on the analytical approach for proof mass, underscoring the importance of appropriate treatment of flexible proof mass in MEMS-scale systems.

One last thing to note is that no experimental data on strain is available here, only measured deflection data along the beam length using AFM can be used to perform model-comparison analysis on mode shapes. As mentioned earlier in this chapter, future work will address the size effect of proof mass on the deflection, and thus mode shapes, in more detail.

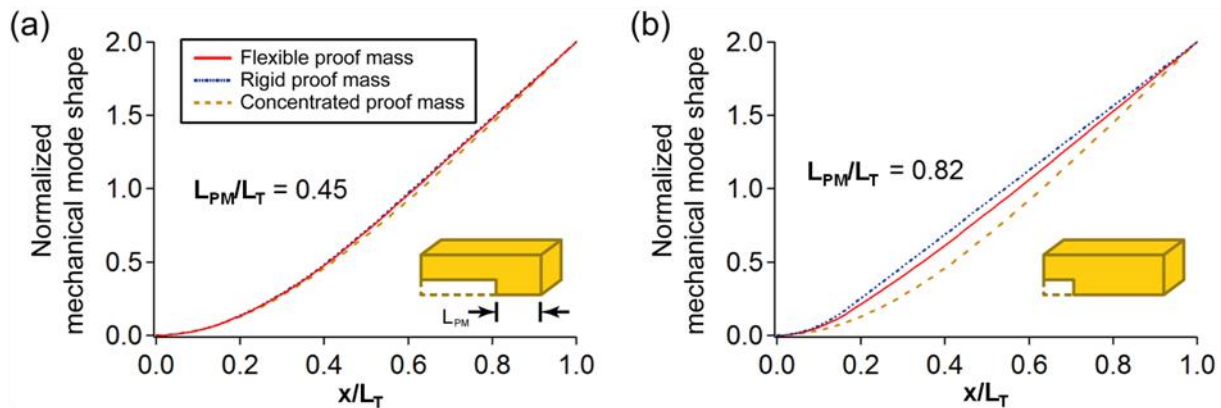


Figure 5.6 Normalized mechanical mode shape along the beam length (x) for various sizes of proof mass.

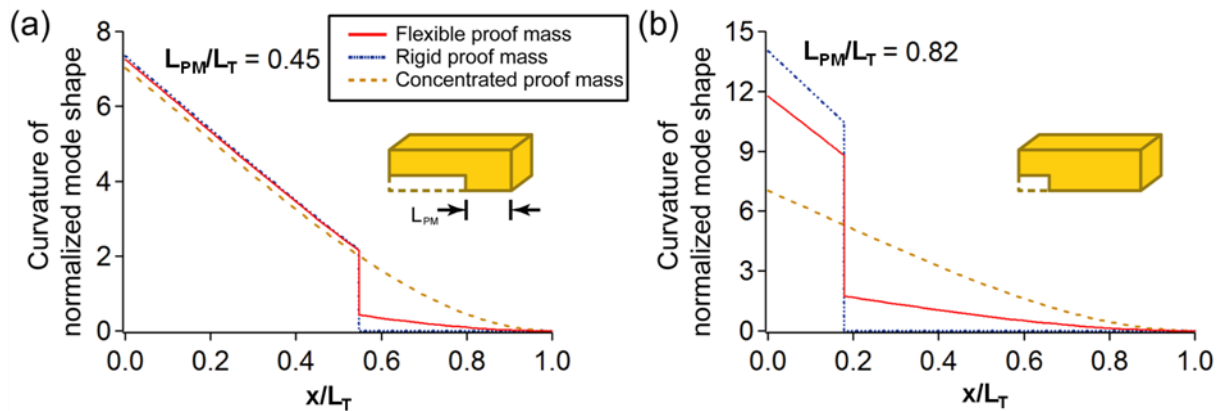


Figure 5.7 Curvature of normalized mode shape along the beam length (x) for various sizes of proof mass.

5.4 Implications for Performance of Piezoelectric Energy Harvesters

The mechanical behavior of a cantilever with a flexible, distributed proof mass is rigorously modeled in terms of its resonant frequency and mode shapes as a function of proof mass size, based on the ‘two-beam’ method developed in Section 3.3. For the experimental verification of this flexible proof mass model, newly designed experiments are performed based on AFM and FIB lithography. Comparison of three different analytical modeling results for the proof mass with measured data leads to a conclusion that flexible proof mass analysis based on a ‘two-beam’ method has the most accurate predictive capability over the range of proof mass sizes in terms of both resonant frequencies and modal analysis. Although the experimental work shown in this chapter highlights the proof mass effects only on the mechanical characteristics of MEMS-scale cantilevered structures, marked differences in the prediction of strain distribution resulting from different modeling approaches suggests a considerable significance in selecting appropriate modeling approaches for studying and designing PVEH devices.

Chapter 6

Model-derived Piezoelectric Materials Design in Energy Harvesting

The biggest challenge in utilizing PVEHs has been their insufficient power generation for practical applications, which necessitates creative and disruptive materials and structure design at various scales. To date, research in piezoelectric energy harvesting has focused on the development of more power efficient devices through the system optimization both in design level and fabrication. In this chapter, special emphasis is placed on the design and selection of optimal piezoelectric materials in terms of power generation. Using a macroscopically verified analytical electromechanical coupled beam model (see Chapters 2-5), sensitivity of device performance to material properties of the piezoelectric element such as elastic stiffness, dielectric constants, and piezoelectric coupling coefficients, is investigated. Notable is the observation that piezoelectric constant dominantly influences harvested power at off-resonance as widely noted, but that at the resonances an optimal value for a given device exists. This is intriguing because it is in contrast with the widely-held perception that higher piezoelectric coupling yields increased power generation. By showing how this optimization scheme can be applied to a PVEH, materials design and selection for power-optimized devices is presented along with physical interpretation of optimal piezoelectric coupling as it relates to tunable device parameters such as system impedance.

6.1 Piezoelectric Materials and Material Constants

As to the matter of the design and selection of optimal piezoelectric materials in terms of more power generation, two key questions are of primary interest especially to materials scientists: 1) “what are the important material properties when we design PVEH devices?” and 2) “then, how do we design and select piezoelectric materials”? To answer the first question, it is useful to take a look at the constitutive equations of piezoelectric materials, which describe the relation between mechanical behavior (stress and strain) and electrical behavior (electrical displacement and electrical field). Equation (6.1) is one way to express the linear constitutive relations in tensor form. (Please note that there are multiple ways to write the constitutive relations with different associated material property constants depending on convenience; see IEEE standard [35].)

$$\begin{Bmatrix} \mathbf{T} \\ \mathbf{D} \end{Bmatrix} = \begin{bmatrix} \mathbf{c}^E & -\mathbf{e}^t \\ \mathbf{e} & \boldsymbol{\varepsilon}^S \end{bmatrix} \begin{Bmatrix} \mathbf{S} \\ \mathbf{E} \end{Bmatrix} \quad (6.1)$$

From the above, we consider three main relevant materials properties of piezoelectric materials: elastic stiffness at constant electric field (\mathbf{E}), \mathbf{c}^E in units of [GPa], piezoelectric constant, \mathbf{e} in units of [C/m²] relating charge density and strain or stress and electric field [N/V·m] and dielectric constant at constant strain (\mathbf{S}), $\boldsymbol{\varepsilon}^S$ in units of [F/m]. Superscript, t , indicates the transpose of the matrix. Piezoelectric materials typically exhibit anisotropic characteristics, thus, the properties of the material differ depending upon the direction of stress etc. and orientation of the polarization and electrodes. In equation (6.1), these material properties are written in tensor form that consists of a number of elements for each property constants. In the general anisotropic stiffness case, for example, one needs to know 21 independent constants for \mathbf{c}^E [119]. Measuring and analyzing all of these parameters is not generally practical, especially for thin films in MEMS. Fortunately, the fact that poled ferroelectrics exhibit symmetries [97] allows a reduced form with fewer elements (*e.g.*, equation (A.1)). These three-dimensional linear elastic constitutive relations can be easily simplified for {3-1} and {3-3} modes of operation, of which

detailed derivation procedure is available in Appendix A. Equation (6.2) represents the simplified expression for {3-1} mode of operation for a plate where the asterisk (*) is employed for distinction from the 3-D constant:

$$\begin{Bmatrix} T_1 \\ D_3 \end{Bmatrix} = \begin{bmatrix} c_{11}^E * & -e_{31} * \\ e_{31} * & \epsilon_{33}^S * \end{bmatrix} \begin{Bmatrix} S_1 \\ E_3 \end{Bmatrix} \quad (6.2)$$

Hence, elastic stiffness, $c_{11}^E *$, piezoelectric constant, $e_{31} *$, and permittivity, $\epsilon_{33}^S *$ are the key material properties of interest in this work to analyze the their effects on the output performance of PVEH devices, particularly based on a poled ferroelectric material such as lead zirconate titanate (PZT) [97]. While piezoelectric stress constant, $e_{31} *$, is of the focus in this case, there are a series of piezoelectric constants to define the level of piezoelectric activity of a material. One of the most frequently used piezoelectric constants is the piezoelectric stain constant, d_{ij} , defined as the strain developed per applied field in units of [m/V] or short-circuit charge density per applied stress in units of [C/N]. Another piezoelectric constant of common use is the voltage constant, g_{ij} , defined as electrical field generated per unit of mechanical stress, or the strain developed for an applied charge density in units of [V·m/N] or [m²/C]. Electromechanical coupling factor, k_{ij} , is also frequently used as an indicator of the effectiveness with which a piezoelectric material converts electrical energy into mechanical energy or vice versa. These piezoelectric constants have close relation with one another through such mechanical or electrical parameters as permittivity and compliance. For a more complete description of the constants, the reader is referred to the IEEE standards [35]. Piezoelectric and dielectric constants for common materials like lead zirconate titanate (PZT) in bulk and thin films, zinc oxide (ZnO), aluminum nitrides (AlN) and polyvinylidene fluoride (PVDF) are given in Table 6.1 for comparison. Note that while larger values for these materials properties keep being reported, the values in Table 6.1 give a general sense of relative magnitudes.

The next question is “what are the criteria to design and select piezoelectric materials for the realization of PVEH devices with optimal output performance?”. To date, researchers have spent considerable effort to fabricate piezoelectric materials that exhibit as high piezoelectric

coupling constants as possible to generate more power through PVEH devices. A good example of this is the intensive focus on the fabrication and integration of PZT at the morphotropic phase boundary (MPB) into PVEH devices because the highest achievable piezoelectric coupling coefficient of PZT is observed at this composition [33, 34]. However, conclusions from the model-based study undertaken in this chapter find that higher piezoelectric coupling does not necessarily lead to increased power generation from PVEH devices despite this widely-held “intuitive” perception. The following chapters include an analysis on material property effects on PVEH device performance based on the experimentally verified analytical model and furthermore, their implications into the device design of PVEHs, providing device design guidelines particularly from a perspective of materials selection.

Table 6.1 Comparison of material properties of commonly used piezoelectric materials.

Material Properties	PZT Bulk [33]	PZT (111) 45/55 film [33]	PZT (100) 53/47 Film [33]	ZnO [34]	AlN [34]	PVDF [98, 99]
e_{31}^* [C/m ²]	-14.7	-8.5	-12	-1.0	-1.05	-0.13
$\epsilon_{33}^S / \epsilon_0$	300 ~ 1300			10.9	10.5	12

6.2 Sensitivity Analysis of Device Performance to Material Properties

The model developed for a base-excited piezoelectric cantilever system (Chapters 2 and 3) is adopted as a useful analysis tool as it proved to have conservative predictive capability through experimental verification ([74], Chapters 4 and 5). Modeling yields prediction of harvesting device responses as outputs when accepting such input parameters as materials properties, geometric configuration, and external operating conditions. Thus, it is possible to observe the trends of device output performances as a function of material properties on a device of given geometric configuration using the analytical model. The previous test device used in

Chapter 4 is considered, a macroscopic, bimorph PVEH device with proof mass I (PM I) because this is the device that the model is experimentally verified on. It should be noted that whether there is a proof mass or not is irrelevant in terms of this topic (*i.e.* relation of piezoelectric material properties and device performance) and the same results would hold for the no proof mass case. The same geometric dimensions and materials properties listed in Table 4.1 are employed.

To see the sensitivity of output power to the relevant material properties, output power is plotted against piezoelectric coupling constants, e_{31}^* , and dielectric constant, ϵ_{33}^S , in Figures 6.1 (a) and (b), respectively, under given constant external operating conditions. The external operating conditions here include not only input driving frequency that is determined from the vibration environment where device operation takes place, but also the electrical load (resistance, R_l), an adjustable parameter externally that we apply to the harvesting device through an electric circuit. In this case, electrical resistance is set to be constant at 20 k Ω and the device is assumed to operate at its theoretical resonance ($\Omega = 1$ or $f_l = 41.4$ Hz). Note that the range of each material property constant as indicated along the x -axis of both Figures 6.1 (a) and (b) covers sufficiently those of the existing piezoelectric materials that are commonly used and reported. Consistent with the material properties listed in Table 4.2, when piezoelectric constant, e_{31}^* , varies as in Figure 6.1, dielectric constant, ϵ_{33}^S , is fixed to be 1.373×10^{-8} , while -14.2 C/m² is used for a fixed value of e_{31}^* when dielectric constant, ϵ_{33}^S , becomes a variable as shown in Figure 6.1 (b).

The results in Figure 6.1 lead to two key conclusions. First, comparison of power behavior across varying piezoelectric constant, e_{31}^* , and dielectric constant, ϵ_{33}^S , implies that piezoelectric constant, e_{31}^* , dominantly affects the power output over dielectric constant, ϵ_{33}^S . In other words, when electrical resistance, R_l , is not tuned to optimum but fixed to a certain value, here 20 k Ω , the magnitude of output power is not as sensitive to the change in the values of dielectric constants as to the changes in piezoelectric constants. Second, as piezoelectric constants increase, the output power goes up and then down, showing that there exists an optimal point of piezoelectric constant for maximum power generation under the given condition (*i.e.* at resonance and a fixed electrical resistance, 20 k Ω). This local maximum takes place when

piezoelectric constant, e_{31}^* , corresponds to -14.7 C/m^2 while generating $165.0 \text{ } \mu\text{W}$ of output power.

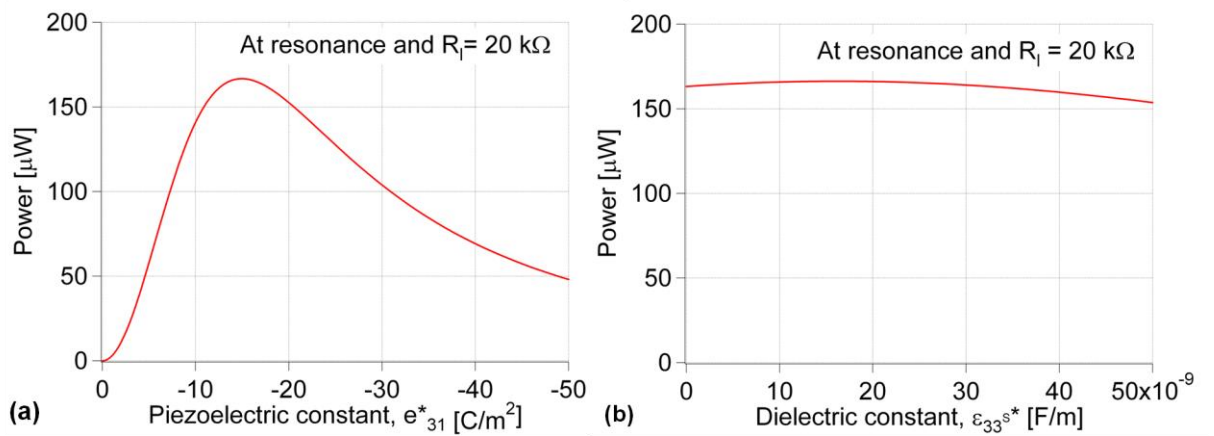


Figure 6.1 Sensitivity of output power of a PVEH device to materials properties: (a) output power versus piezoelectric constant, e_{31}^* , and (b) output power versus dielectric constant, ϵ_{33}^s , at resonance and $20 \text{ k}\Omega$ for the device (PM I) of Chapter 4.

In Figure 6.2 (a), output power, P_{out} , is plotted against normalized frequency, Ω , at various values of piezoelectric constant, e_{31}^* , for further in-depth analysis on the effect of piezoelectric constant, e_{31}^* , on the output power performance. The external operating condition is the same as the previous such that operation occurs at resonance and electrical resistance, R_l , is kept at $20 \text{ k}\Omega$. Several distinctive aspects are noticeable in Figure 6.2 (a). At off-resonance (when the input driving frequency moves away from resonant frequency ($\Omega = 1$), either below ($\Omega < 1$), or above ($\Omega > 1$)), power increases as piezoelectric constant, e_{31}^* , increases. In contrast to the “expected” behavior at off-resonance, output power at or near resonance exhibits a counter-intuitive trend. Since there is an optimal point that maximizes power harvesting from a given device, decreased power is achieved even when piezoelectric constant, e_{31}^* , increases at or near resonance. This is the opposite result to the general thought on the relation of piezoelectric coupling constants and power generation. For better demonstration of this trend, maximum output power at each

peak is plotted against distinct piezoelectric constants in Figure 6.2 (b) using the same symbol (blue ribbon) as in Figure 6.2 (a). In Figure 6.2 (b), maximum power appears when the piezoelectric constant is close to -15 C/m^2 , which corresponds to the result in Figure 6.1 (a).

In addition to contrasting behavior at resonance and off-resonance, shift in resonant frequencies at peak power depending on piezoelectric constant, e_{31}^* , is noteworthy. In Figure 6.2 (a), the normalized frequency (Ω) shifts upon the increase of piezoelectric constant, which is re-illustrated in Figure 6.2 (c). In the previous chapters, it is already mentioned several times that the resonant frequency (f_r) is the natural frequency at short-circuit condition ($R_l \rightarrow 0$) while the anti-resonant frequency (f_{ar}) is the natural frequency at open-circuit conditions ($R_l \rightarrow \infty$). Thus, the peak-power frequency shifts from resonance toward anti-resonance when electrical resistance becomes larger [52, 74, and chapter 4]. The increasing trends of peak-power frequencies with higher piezoelectric constants that appear in Figures 6.2 (a) and (c) have a close similarity to the frequency shift from resonance to anti-resonance due to increasing electrical resistance. This suggests that it could be possible to interpret the effect of materials' piezoelectric coupling and externally applied electrical resistances on the output power performance of PVEH devices in the same scheme. The following section presents a physical interpretation (damping) of this optimum piezoelectric coupling behavior at resonance by deriving appropriate analytical expressions, which also account for the similar effect of electrical resistances and piezoelectric coupling on the power performance observed in Figures 6.2 (a) and (c).

One more aspect to note in Figure 6.2 (a) is widening of peaks with higher piezoelectric coupling constants. As piezoelectric constant, e_{31}^* , increases, the broader the peak becomes. The similar kind of peak-widening phenomenon is observed when we plot amplitude versus normalized frequencies for typical resonant-operating devices represented by mass-spring-damper system [69] and increase the mechanical damping ratio (*or* decrease the quality factor). In addition to the frequency shift at the peaks, the analytical expressions derived in the following section also help explain this peak-widening with increased piezoelectric coupling constants in relation to mechanical damping effects on the device operated at resonance.

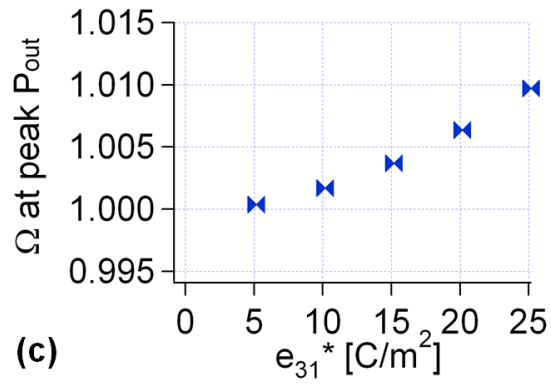
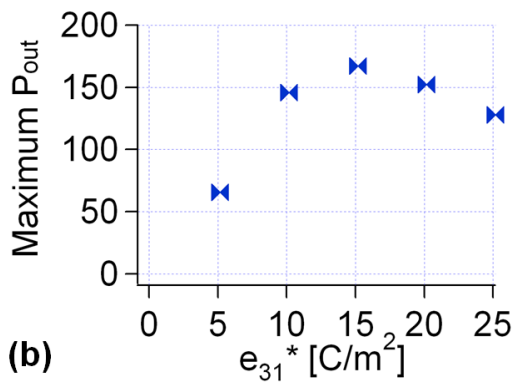
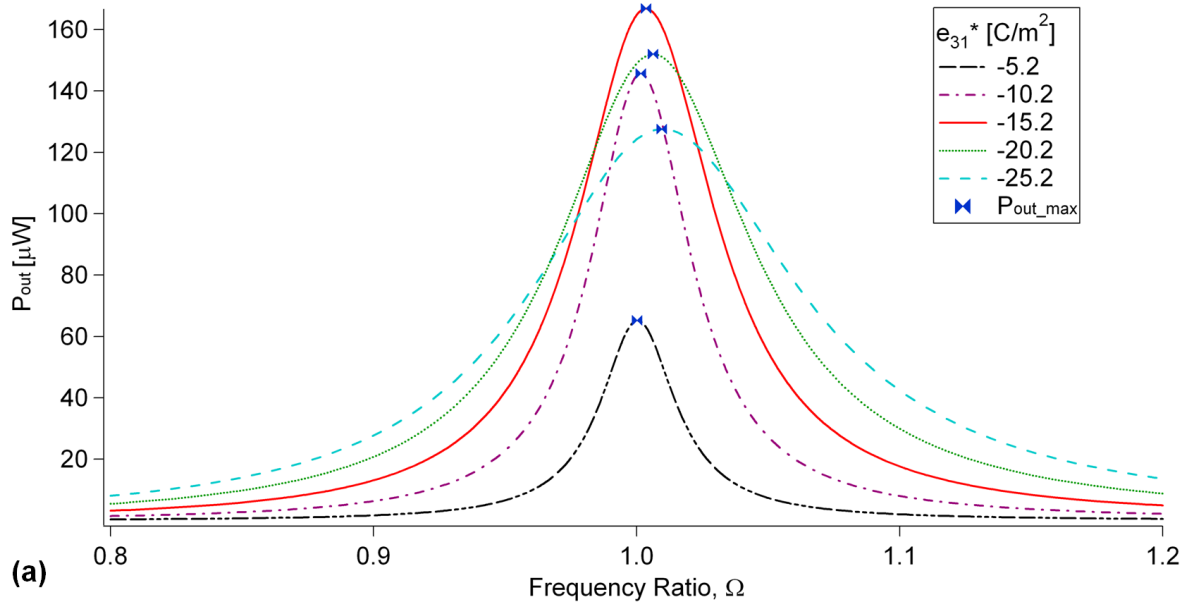


Figure 6.2 Device performance trends with e_{31}^* : (a) Output power versus normalized frequency (Ω) at various piezoelectric constants, e_{31}^* , under given operating conditions (at resonance and at 20 k Ω), (b) maximum output power vs. piezoelectric constant, (c) peak-power frequency ratio vs. piezoelectric constant, e_{31}^* .

6.3 Damping Analysis and Its Relation to Piezoelectric Coupling in Energy Harvesting

In sensitivity analysis, we've seen that the magnitude and width of power at the peaks vary as electrical resistance and/or piezoelectric coupling constant, e_{31}^* , change, in addition to the peak-power frequency shift. Also, there is an optimum point of e_{31}^* that generates the maximum power, leading to an important conclusion that larger piezoelectric coupling is not necessarily required for more power extraction. To interpret such interesting behaviors of output power at resonance depending on piezoelectric coupling constants, it is useful to introduce the concept of *equivalent mechanical damping* in a PVEH system and use its analogy to a pure mechanical system consisting of a mass-damper-spring system [30]. This is possible through the derivation and study of associated analytical expressions for “equivalent” mechanical damping terms from the governing equations previously developed for PVEH devices. In order to find an “effective” mechanical damping term, rearrangement of the two governing equations (2.17) and (2.18) for PVEHs is required such that the system can be described as a force-driven damped harmonic oscillation in a mechanical mass-spring-damper system. For convenience, these scalar governing equations are reproduced in equations (6.3) and (6.4), where C_m represents the mechanical damping term in the PVEH system:

$$M\ddot{r} + C_m\dot{r} + Kr - \theta v = -B_f \ddot{w}_B \quad (6.3)$$

$$\theta\dot{r} + C_p\dot{v} + \frac{v}{R_l} = 0 \quad (6.4)$$

In Chapter 2, these equations were solved using harmonic oscillations for r , v , and \ddot{w}_B in both equations, and this resulted in the harmonic expressions given by equations (2.24)-(2.26). This solution contains the resonance and anti-resonance phenomena and the natural transition between the two phenomena.

A simple approximate way to explore the effects at the resonant frequency, $\Omega = 1$, is to

retain the simple second-order system behavior of equations (6.3) and (6.4) in the time domain, but to modify its behavior by the voltage term, θv . Assumption of harmonic oscillation of generated voltage, v , allows us to have the voltage expression in terms of the frequency-time domain as well as to express the time-derivative of voltage in terms of driving frequency (ω) and voltage. These are written in equations (6.5) and (6.6), respectively:

$$v = v_0 e^{i\omega t} \quad (6.5)$$

$$\dot{v} = i\omega v_0 e^{i\omega t} = i\omega v \quad (6.6)$$

where v_0 is voltage amplitude and ω represents the input frequency as before. Substitution of equation (6.6) into the sensing equation (6.4) results in the voltage expression with respect to velocity (\dot{r}) term:

$$\theta \dot{r} + iC_p \omega v + \frac{v}{R_l} = 0 \quad (6.7)$$

$$v = \frac{-\theta}{\left(\frac{1}{R_l} + iC_p \omega\right)} \dot{r} \quad (6.8)$$

Then, using the relation in equation (6.8), it is now possible to eliminate the voltage term in the governing equation (6.3), as shown in equations (6.9) and (6.10):

$$M\ddot{r} + C_m \dot{r} + Kr - \theta \left[\frac{-\theta}{\left(iC_p \omega + \frac{1}{R_l}\right)} \dot{r} \right] = -B_f \ddot{w}_B \quad (6.9)$$

$$M\ddot{r} + \left(C_m + \frac{\theta^2}{\left(\frac{1}{R_l} + iC_p \omega\right)} \right) \dot{r} + Kr = -B_f \ddot{w}_B \quad (6.10)$$

A general mathematical expression for forced harmonic oscillators with external force, $F(t)$ [69], is:

$$M\ddot{r} + C_{effective}\dot{r} + Kx = F(t) \quad (6.11)$$

where $C_{effective}$ represents the total or “*effective*” mechanical damping of a purely mechanical system with no electrical or piezoelectric element. Comparison of equations (6.10) and (6.11) suggests that *equivalent* “*effective*” mechanical damping constant, $C_{effective}$, in a PVEH system consists of the pure mechanical damping constant (C_m) and equivalent electrical damping effect due to piezoelectric coupling (θ^2) and electrical resistance (R_l), as expressed below in terms of electrical and mechanical damping ratios:

$$C_{effective} = C_m + \frac{\theta^2}{\left(\frac{1}{R_l} + iC_p\omega\right)} = C_m + C_e = 2M(\zeta_m + \zeta_e)\omega_N \quad (6.12)$$

Equation (6.12) shows how electromechanical coupling in a PVEH system contributes to the mechanical damping to the system “*effectively*”. If we focus on the *equivalent* electrical damping constant, C_e , as in equation (6.13), piezoelectric coupling (θ^2), capacitance (C_p), driving frequency (ω) and electrical resistance (R_l), comprise the equivalent electrical damping:

$$C_e = \frac{\theta^2}{\left(\frac{1}{R_l} + iC_p\omega\right)} = 2M\zeta_e\omega_N \quad (6.13)$$

As previously, we know $M = \frac{K}{\omega_N^2}$ and can define non-dimensional terms such as system

coupling, $\kappa^2 = \frac{\theta^2}{KC_p}$, time constant, $\alpha = \omega_N R_l C_p$ (and frequency ratio, $\Omega = \frac{\omega}{\omega_N}$).

Rearrangement of the expression in equation (6.13) enables us to derive an expression for electrical damping ratio in terms of non-dimensional terms as below:

$$\zeta_e = \frac{\kappa^2 \alpha}{2(1 + i\alpha\Omega)} \quad (6.14)$$

As the expression above is in complex form, the magnitude of electrical damping ratio, ζ_e , should be evaluated through the relation $|\zeta_e| = \sqrt{\zeta_e \zeta_e^*}$ (where superscript * indicates conjugate complex number) in order to obtain a physically meaningful quantity. Then, the final expression for electrical damping ratio is written as in equation (6.15) below:

$$\zeta_e = \frac{\kappa^2 \alpha}{2\sqrt{1 + (\alpha\Omega)^2}} \quad (6.15)$$

At resonance ($\Omega=1$), this becomes:

$$\zeta_e = \frac{\kappa^2 \alpha}{2\sqrt{1 + \alpha^2}} \quad (6.16)$$

Equation (6.16) is exactly consistent with the expression for equivalent electrical damping ratio, ζ_e , that du Toit *et al.* derived in [74]. This was obtained there using the complete solutions, equations (2.24)-(2.26), with the mechanical damping, $\zeta_m = 0$, and expressing the resonance-peak at $\Omega_r = 1$ in terms of an equivalent electrical damping, ζ_e . A similar type expressions was also obtained at the anti-resonance peak, $\Omega_{ar} = \sqrt{1 + \kappa^2}$.

Analytical expressions derived above are useful to interpret several intriguing behaviors of output power at resonance when piezoelectric constant, e_{31}^* , increases as discussed earlier, in terms of equivalent mechanical damping effect on the system due to piezoelectric and electrical parameters. First of all, the concept of equivalent mechanical damping effect due to piezoelectric

and electrical terms helps explain the existence of the optimum piezoelectric constant, e_{31}^* , for maximum power in terms of competitive mechanisms between more power generation and more damping. Examination of equation (6.12) reveals that the more the system is piezoelectrically coupled through θ , which is proportional to piezoelectric constant, e_{31}^* , the greater the effective mechanical damping. This implies that when we integrate piezoelectric materials with higher piezoelectric coupling into a PVEH system, it contributes to generating more power through piezoelectric coupling while it has an increasing equivalent damping effect on the system, thus decreasing the amount of generated power. Combining more damping of the system and more harvester power through higher piezoelectric coupling constant explains the appearance of the optimal point (see Figure 6.2). The same logic can be used to account for the reason why there exists an optimal electrical resistance with a peak that maximizes power at resonance in a similar way to piezoelectric coupling (see Figures 4.13 (a), (c), and (e)). As electrical resistance, R_l , increases, more damping is expected to occur from the relation in equation (6.12). While electrical resistance is an essential element to extract the harvested power from the system, it entails more damping effect to the system and as a result, there is an optimum point of electrical resistance for maximum power extraction as noted earlier in this thesis and by earlier work [74]. The similar effect that electrical resistance, R_l , and piezoelectric coupling exhibit on the output power performance particularly at resonance provides a reasonable explanation of the peak-power frequency shift observed in both cases as well. The analogy of PVEH system to a purely mechanical mass-spring damper system at resonance can also be applied to the interpretation of the peak-widening phenomenon at higher piezoelectric coupling. In a typical damped harmonic oscillation system, quality factor is known to determine the width of the peak when amplitude is plotted against driving frequencies (as in Figure 6.2 (a)) [69]. Quality factor, Q , is a commonly used parameter to parameterize damping and has a relation with damping ratio, ζ , through $Q = \frac{1}{2\zeta}$. This implies that the mechanical damping term expressed in equation (6.12) determines the peak-width of the resulting performance governed by equation (6.10), which represents the equivalent expression for the PVEH system to that of a common damped harmonic oscillation system. Thus, when more damping is involved through higher piezoelectric coupling, peaks are expected to broaden, as observed in Figure 6.2 (a).

In summary, the governing equations for PVEH systems are rewritten in an analogous form to the typical resonant mechanical system comprised of mass, damper, and spring for the purpose of finding the relation of piezoelectric coupling in PVEH systems with damping effect on the system. This analysis scheme enables explanation of those output power behaviors observed in the previous section using a simple mathematical analogy: optimal power harvesting point, shift in peak-power frequency, and peak widening upon the increase of piezoelectric coupling. This proposes a possibility to optimize the PVEH devices based on different piezoelectric materials through tuning of externally adjustable condition, that is, electrical resistance in this case. Details on this topic are discussed in the following section, providing a device design rationale for power-optimized PVEH devices.

6.4 Energy Harvesting Device Implications

In Section 6.2, a sensitivity analysis on which material property constants affect the output performance of PVEH devices under constant external operating conditions was presented. Piezoelectric constant, e_{31}^* , is found to be the dominant property with an optimal value for maximum power when compared to the dielectric constant, ϵ_{33}^S , that does not significantly influence the magnitude of power generated at resonance with fixed electrical resistance. To consider voltage in addition to power, both are plotted against normalized frequency at various electrical resistances for the same macroscopic PVEH device with proof mass I (PM I) in Figures 6.3 and 6.4. The solid lines in red color of these figures are of most importance as they represent possible maximum power and corresponding voltage at any given input frequency relative to resonance and anti-resonance by adjusting the electrical resistances to optimal values that give the maximum output power. When electrical load resistance defines the optima, power increases up to the maximum point at the peak when input frequency reaches the resonant frequency. Then, a decrease in power is observed down to the local minimum between resonance and anti-resonance. The power increases again after this point and reaches another maximum at anti-resonance with the same magnitude as the first maximum at resonance. It is quite noticeable that one can harness maximum output power with equal magnitude not only at the resonance but also

at the anti-resonance by changing electrical load resistances [74]. The fact that both peaks at resonance and anti-resonance are closely spaced gives us a potential advantage to design a device within a small range of target driving frequency, which could be used for both low and high voltage applications. For example, plots in Figures 6.3 and 6.4 yield resonant and anti-resonant frequencies of this device at 41.4 Hz and 44.2 Hz, respectively. The optimal electrical resistances that maximize power generation at these two closely-spaced frequencies correspond to 20.3 k Ω and 364.0 k Ω , respectively, having quite a gap between the values of electrical resistances. As power is equal to current times voltage ($P = IV$), if equal power can be generated at two distinctive electrical resistance conditions, this entails a current-voltage trade at these two operating points. While high voltage and low current are predicted at anti-resonance, low voltage and high current are expected at resonance, as shown in Figure 6.4. This is significant in engineering PVEH devices as one can choose the operating point, either resonance or anti-resonance, depending on the application of specific desire while satisfying the maximum power generation at or near targeted input frequencies [29, 30]. Note that du Toit *et al.* performed the same analysis on optimal power and voltage for a 1-dimensional PVEH system and drew the same conclusions for PVEH device design considerations as discussed here [29, 30].

Analytical expressions for optimal power and corresponding voltage (at resonance) when electrical resistance is tuned to optimum are derived in Section 2.2 and previously by du Toit *et al.* [30] and rewritten here in equations (6.17) and (6.18). Equation (6.19) describes the optimal resistance at resonance, $R_{l,opt,r}$:

$$|P_{out}|_{opt,r} \text{ or } |P_{out}|_{opt,ar} \approx \frac{B_f^2}{\sqrt{KM}} \frac{\ddot{w}_B^2}{8\zeta_m} \quad (6.17)$$

$$|v_{out}|_{opt,r} \approx \frac{1}{2|\theta|} B_f \ddot{w}_B \quad (6.18)$$

$$R_{l,opt,r} = \frac{1}{\omega_1 C_p} \sqrt{\frac{4\zeta_m^2}{4\zeta_m^2 + \kappa^4}} \quad (6.19)$$

Note that subscript, *opt*, refers to power optimization in the above expressions. A conspicuous finding here is that optimum power either at resonance or anti-resonance is independent of piezoelectric coupling constant of material, which is quite non-intuitive. This suggests that if electrical resistances vary to optimal values, the same magnitude of power is achievable regardless of the choice of piezoelectric materials for a given PVEH device. Then, what important implications does this intriguing result address especially on design and selection of piezoelectric materials to realize power-optimized PVEH devices? Although extraction of equal power is possible using any piezoelectric material if the resistance is tuned to keep power-optimal, the voltage developed does have a dependence on piezoelectric coupling through the coupling term, θ , satisfying intuition to some extent, as shown in equation (6.18). So does the power-optimal resistance, $R_{l,opt,r}$, as it has the system coupling term, κ^2 in its expression of equation (6.19). Both piezoelectric coupling term, θ , and system coupling term, κ^2 , are direct functions of piezoelectric constant, e_{31}^* , and thus both voltage and electrical resistance at optimal power condition are a function of piezoelectric coupling constant, e_{31}^* . While power is the primary objective to optimize in piezoelectric energy harvesting, the independence of power and dependence of voltage on the piezoelectric coupling constant, present output voltage as a secondary objective. This can be demonstrated by considering the effect of piezoelectric constant on the device performance of PVEH system relative to the real case. The same macroscopic bimorph PVEH device with PM I is considered as in Chapter 4. Taking all other parameters (*i.e.* both geometric and material) constant and varying the piezoelectric constant, e_{31}^* , then according to equation (6.17), equal power of 166.9 μW is predicted regardless of the kind of piezoelectric material used from a given system (PVEH device with PM I) when the device is operated at resonance and its optimal electrical resistance that is estimated from equation (6.19) is employed. Then, the corresponding voltage can be plotted as a function piezoelectric constant, e_{31}^* , in Figure 6.5, where an optimum point develops. Among the given commonly used piezoelectric materials, lead zirconate titanate (PZT) thin film at the composition of 45/55 (Zr/Ti) in (111) orientation offers the closest value of e_{31}^* (-8.5 C/m^2) to the optimal piezoelectric constant at which maximum voltage is generated as indicated in Figure 6.5. This is a remarkable finding as even when voltage is considered as a secondary objective to optimize, the optimal

piezoelectric material that maximizes both voltage and power is not necessarily the piezoelectric material with the highest piezoelectric constant. The key point of considerable significance here is that it is not absolutely true that one always desires to choose a piezoelectric material with the highest piezoelectric coupling constant for maximum power generation. Tuning of electrical resistance enables extraction of equal power from a given system regardless of piezoelectric material selection. The design point for power does not depend on piezoelectric coupling at optimal operating conditions, contrary to intuition. Furthermore, the secondary variable of voltage is *not* maximized by increasing the piezoelectric coupling constant. Results in Figure 6.5 suggest that the optimal piezoelectric constant for maximum voltage is modest, not of PZT thin film at morphotropic phase boundary (MPB) and much less than bulk or single crystal PZT.

Here is the summary of the piezoelectric material design guidelines for power-optimized PVEH devices that are learnt from model-based material property analysis in this chapter. First of all, if there is no restriction on external operating conditions, devices should be operated at resonance or anti-resonance by aligning input driving frequency with either resonant or anti-resonant frequency. If high voltage and low current are desirable for the targeted application, anti-resonant operation is appropriate while low voltage and high current requires resonant operations. At equal power, consideration of voltage as a secondary objective gives the criteria to select piezoelectric material that exhibit optimal piezoelectric constant to maximize the voltage. Then, electrical resistance should be tuned to the power-optimized value using equation (6.19). There can be a case where restriction is posed on the external operating conditions such as electrical resistance. For example, if optimal electrical resistance is too large to apply to the system or implausible, application of a practically available value for electrical resistances is required. Then, under such given constant operating conditions (*e.g.*, resonance and fixed electrical resistance), the knowledge from materials-level optimization enters. As piezoelectric constant, e_{31}^* , dominantly affects the output power over dielectric constant, ϵ_{33} , with an optimum value particularly at resonance, it is wise to choose the piezoelectric material that possesses piezoelectric constant close to that optimal point. If a PVEH device is operated away from resonance and a non-optimized electrical resistance, then, the highest piezoelectric coupling constant will yield the most power consistent with intuition. These materials design and selection guidelines are an extremely useful product of the model-based analysis developed in this thesis.

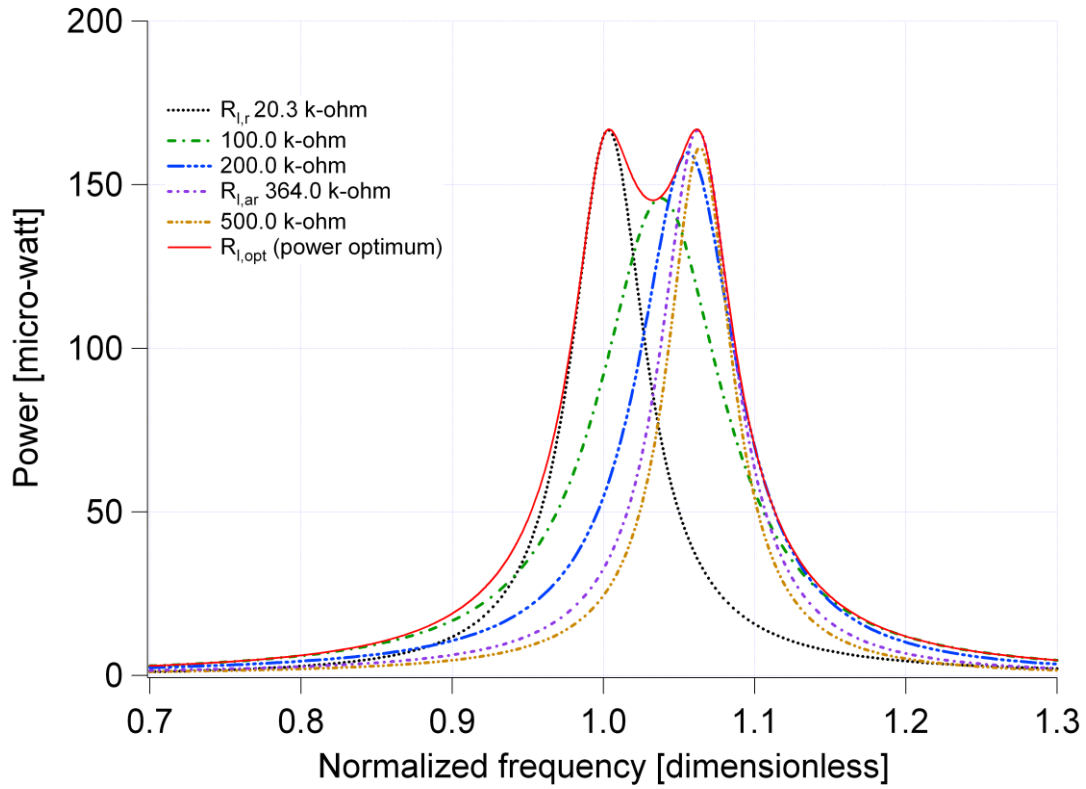


Figure 6.3 Power output versus normalized frequency at various electrical resistances for macroscopic energy harvester with PM I. Base acceleration is held at 0.5 m/s^2 . R_l is the electrical load resistance, $R_{l,r}$ and $R_{l,ar}$ are the power optimized electrical loads at resonance and anti-resonance, respectively. The solid line in red color is the optimized power (optimal electrical load, $R_{l,opt}$, at all frequencies).

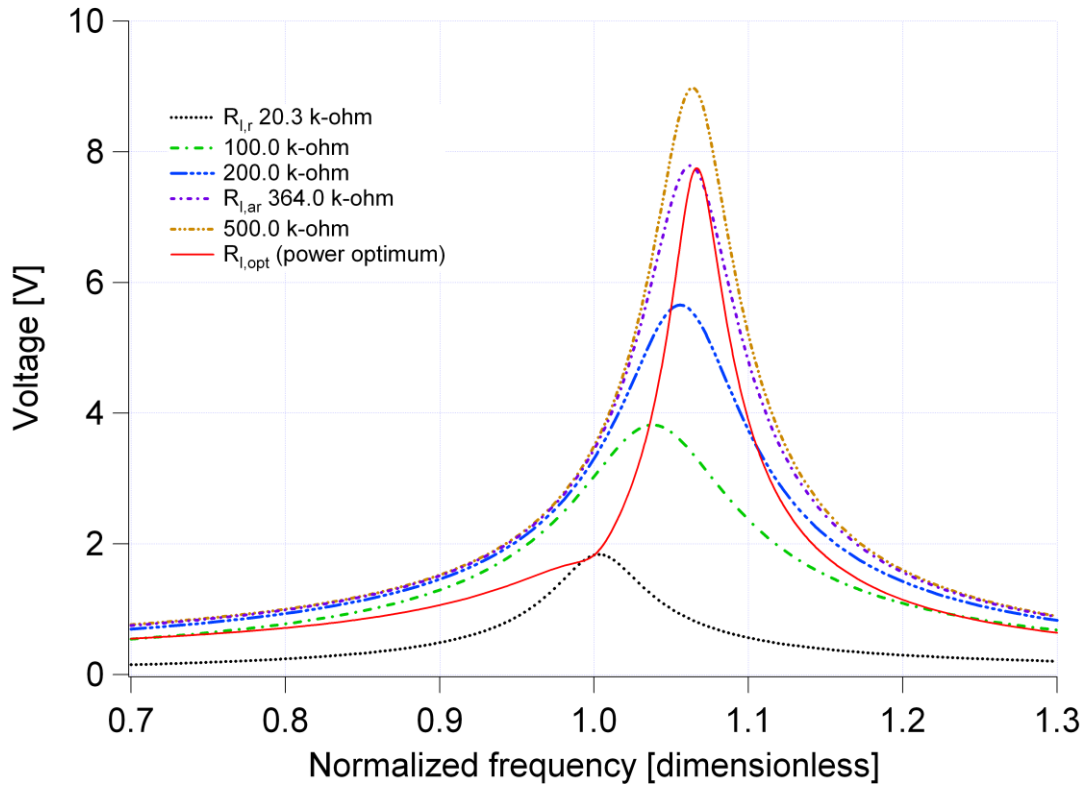


Figure 6.4 Voltage versus normalized frequency at various electrical resistances for macroscopic energy harvester with PM I. Base acceleration is held at 0.5 m/s^2 . R_l is the electrical load resistance, $R_{l,r}$ and $R_{l,ar}$ are the power-optimized electrical loads at resonance and anti-resonance, respectively. The solid line in red color is the optimized power (optimal electrical load, $R_{l,opt}$, at all frequencies).

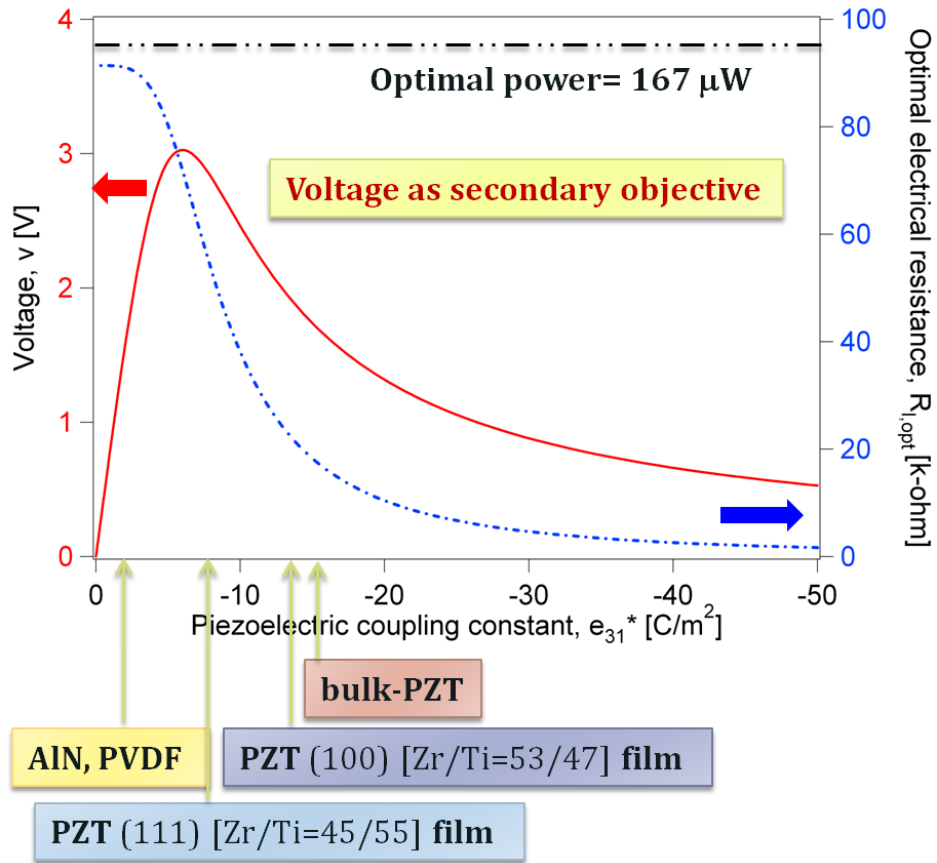


Figure 6.5 Power-optimized voltage (solid line in red color) and electrical resistance (dotted line in blue color) at resonance versus piezoelectric constant, e_{31}^* , with indication of commonly used piezoelectric materials: $e_{31}^* = -1.0$ for AlN and PVDF, -8.5 for PZT(111) [Zr/Ti =45/55] film, -12 for PZT(100) [Zr/Ti =53/47] film, and -14.7 for bulk-PZT. At all piezoelectric constants (*i.e.*, regardless of the choice of piezoelectric materials), a given PVEH system is predicted to generate equal power, $167 \mu\text{W}$.

Chapter 7

Model-based Optimization Framework and Performance Quantification of Piezoelectric Energy Harvesting Devices

This chapter introduces another use for the verified model – an enhanced method for analysis of PVEH device performance and design of optimal PVEHs. The contents consist of the following: first, standardization of key performance metrics in Section 7.1, which includes identification of key performance parameters (Section 7.1.1), definition and exploration of device efficiency (Section 7.1.2), and comparison of different optimal conditions for each performance parameter such as power, voltage, and efficiency (Section 7.1.3), and second, extraction of useful information on both materials and system properties of PVEH devices via two different model-based approaches, in Section 7.2.

7.1 Standardization of Key Performance Metrics for Energy Harvesters

Throughout the open literature, metrics for comparing different PVEH devices have not

been clearly defined. Standardization of comparison metrics is significant because it can provide needed figures of merit, enabling fair comparison of PVEH devices with different specifications (*e.g.*, dimension, geometry, and input operating conditions) as well as full characterization of PVEH device performance. To date, description of the PVEH devices in the reported literature has focused on emphasizing their maximum power output without mentioning input power or dimensions. Or, when volume or area is considered to calculate power density (power per unit volume or area), those dimension parameters are of static devices, which results in exaggerated power production. While recent attempts to identify key parameters for PVEHs can be found in [79, 100, 101], they are either limited to resonant devices or based on oversimplifications. Thus, the main purpose of the following section is to suggest proper PVEH output performance metrics and show the usefulness of model in calculating them.

7.1.1 Identification of Key Performance Parameters

In the basic flow of modeling, key parameters for a PVEH system can be classified into two categories: input and output parameters. Following is the list of relevant input parameters for PVEH devices, which can be categorized either by device intrinsic properties or by extrinsic operating conditions:

- ◆ ***Inputs***

- 1) Intrinsic properties of device constituents

- Geometric dimensions (beam/plate & proof mass): length, width, thickness.
- Material properties: density and structural elastic constants of each layer that constitutes the cantilever and proof mass. For a piezoelectric layer, piezoelectric and dielectric constants are required in addition to density and structural elastic constants.
- Device configurations: geometry, modes of operation ($\{3-1\}$ or $\{3-3\}$), inter-element connection of piezoelectric layers (in case of bimorph, series or parallel connection).

2) Extrinsic operating conditions

- Input vibrations from base excitation: base accelerations (w_B) and operating frequencies (ω_{in} or Ω_{in}).
- Mechanical damping ratio (ζ_m) or quality factor Q , ($Q = 1/(2\zeta_m)$).

Note that damping could do have some intrinsic contributions, as from material damping. Key output performance metrics for PVEH devices are listed in Table 7.1 together with their commonly used symbols and units. Analytical modeling can predict values for these performance parameters based upon the information of relevant input parameters described as above. Using models (*e.g.*, governing equations (2.17) and (2.18)) and the solutions, it is possible to measure system parameters such as M , K , θ , C_p and then compute optimal points for objective performance objectives (see Section 7.1.3). This so called “model-parameter estimation” is discussed in more detail in Section 7.2, where descriptions of two different approaches, bottom-up and top-down approaches, to measure materials and system properties of PVEH systems are available.

Resonant frequency (f_r) is the natural frequency of a given energy harvesting structure at short-circuit condition ($R_l \rightarrow 0$) while anti-resonant frequency (f_{ar}) is the natural frequency of the same system at open-circuit conditions ($R_l \rightarrow \infty$). Compared to the resonant frequency, which is determined purely by the mechanical properties of the system, the anti-resonant frequency is a function of piezoelectric parameters as well. As written in equation (7.1), anti-resonant frequency is a measure of system electromechanical coupling factor (κ^2).

$$f_{ar} = f_r \sqrt{1 + \kappa^2} \quad (7.1)$$

Previously, in Chapter 4, it is shown that electrical resistance applied to the piezoelectric system affects the natural frequency of the system and that a frequency shift occurs from resonant frequency toward anti-resonant frequency upon the increase of electrical resistances.

Table 7.1 Key metrics for energy harvesting device comparison.

Performance parameter	Symbol	SI Units
Resonant frequency	ω_r or f_r	[rad/s] or [Hz]
Anti-resonant frequency	ω_{ar} or f_{ar}	[rad/s] or [Hz]
Mechanical displacement	w	[μm]
Device output voltage	v_{out}	[V]
Current	I_{out}	[A]
Device output power	P_{out}	[μW]
Operating power density	P_{op}	[$\mu\text{W}/\text{cm}^3$]
Static power density	P_{st}	[$\mu\text{W}/\text{cm}^3$]
Specific power	P_{sp}	[$\mu\text{W}/\text{kg}$]
Input power	P_{in}	[μW]
Device efficiency	η	P_{out}/P_{in}

The voltage expression in equation (2.25) allows calculation of not only the device output voltage (v_{out}), but also the device output power through the relation $P_{out} = v_{out}^2/R_l$. Output voltage itself is an important performance metric for two reasons. First of all, one can determine the operating point of PVEHs depending on the voltage required for the targeted application while generating the same magnitude of power as discussed in Chapter 6 (see Figures 6.4 and 6.5). If the application requires high voltage/low current, the anti-resonant frequency operating point is more advantageous, whereas driving frequency should be tuned to the resonant frequency for low voltage/high current applications. Secondly, voltage becomes a valuable performance metric in piezoelectric materials design and selection. When a PVEH device is operated at the optimal points (resonance or anti-resonance) and optimal electrical loading conditions, it generates the same magnitude of power regardless of the piezoelectric constant values (see Section 6.4). As a result, output voltage becomes a definite criterion of materials design.

The next discussion is on power. When the targeted application has no constraints on size or mass, device output power calculated or measured in Watt [W] or micro-Watt [μW] is of interest to optimize. One can simply use equation (2.26) to compute the device output power.

However, if the application of interest is either weight-constrained or the operational space is limited, other performance metrics such as specific power or power density (power per volume) should enter into consideration. Specific power is defined as power per device mass with SI units of [$\mu\text{W}/\text{kg}$] and this metric becomes a primary objective for weight-constrained applications. Power density is defined as power per volume and has SI units of [$\mu\text{W}/\text{cm}^3$]. While static power density ($P_{st} = P_{out} / V_{st}$) is given more commonly in the literature because of its simplicity, operating power density ($P_{op} = P_{out} / V_{op}$) should be the most telling metric. This is because the operating volume is the actual volume occupied by the device while in operation and thus required for device implementation into a structure or organism, as Mracek pointed out [79]. For a cantilever structure with a proof mass, as in Figures 3.2 or 4.1, the operating volume, V_{op} , is the space swept by the tip displacement of a structure while static volume, V_{st} , is simply the volume of a device when not in any motion. Analytical expressions of these volume parameters are available in equations (7.2) and (7.3) where the definition of symbols used is indicated in Figure 3.2:

$$V_{st} = (L + L_{PM}) * (b_{PM}) * (h + h_{PM}) \quad (7.2)$$

$$V_{op} = (L + L_{PM}) * (b_{PM}) * [2w(L) + 2L_{PM} \frac{\partial w(L)}{\partial x_a} + (h + h_{PM})] \quad (7.3)$$

When each of these various power performance metrics is optimized as a primary objective, it results in different optimum device configurations. This will be discussed in Section 8.3.

One more significant performance metric is harvesting efficiency (η), defined as the ratio of device output power (P_{out}) to mechanical input power (P_{in}). Harvesting efficiency is an essential standard to compare PVEH devices operating in different environments. Available input vibration sources vary in different environments (ranging from a few Hertz to a several thousand Hertz) and the amount of input mechanical power achievable from various input vibration sources varies accordingly. In the following Section 7.1.2, analytical expressions for mechanical input power and harvesting efficiency are thoroughly derived.

7.1.2 Definition and Exploration of Harvesting Efficiency

Harvesting efficiency (η) indicates how much a given PVEH device can convert input mechanical power (P_{in}), from a given vibration source, into output electrical power (P_{out}). This performance metric is a useful criterion that enables the performance of different devices to be compared. Previously, Richards *et al.* [102] derived a formula to evaluate the power conversion efficiency for a device that contains a piezoelectric component (see Figure 7.1). Roundy *et al.* [103] defined the term “effectiveness” to compare conversion efficiency of different transduction mechanisms (*e.g.*, electrostatic, electromagnetic, and piezoelectric conversion) based on a simple and general vibration conversion model and equivalent circuit model. Although these models could provide some insight into the parameters that affect efficiency, such as quality factor and electromechanical coupling factor, these models only permit analysis of the devices at resonant-operation.

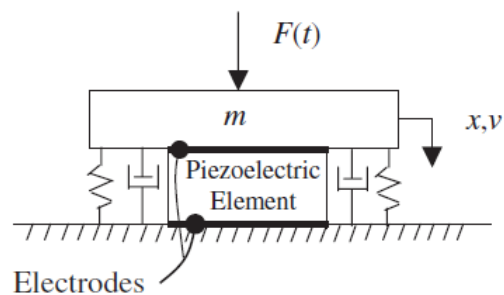


Figure 7.1 Schematic of a simple, 1-dimensional piezoelectric energy conversion device modeled by Richards *et al.* [102].

Here, an analytical expression for harvesting efficiency (η) is derived for a cantilevered PVEH device. This is used to gain insight into the design of PVEH devices by identifying the factors that affect the device efficiency.

Harvesting efficiency is defined based on power as:

$$\eta = \frac{P_{out}}{P_{in}} \quad (7.4)$$

where P_{in} comes from mechanical vibration due to base excitation while P_{out} is the generated electrical power through electrical impedance (here, resistance, R_l). The expression for electrical output power (P_{out}) in PVEH devices is already obtained in Chapter 2 and repeated here for convenience:

$$\left| \frac{P_{out}}{(B_f \ddot{w}_B)^2} \right| = \frac{\omega_1}{K} \frac{\alpha \kappa^2 \Omega^2}{[(1 - \Omega^2) - 2\zeta_m \alpha \Omega^2]^2 + [(1 + \kappa^2) - \Omega^2] \alpha \Omega + 2\zeta_m \Omega^2} \quad (7.5)$$

It is convenient to define a dimensionless forcing term, F_{EP} , and rewrite the above expression as follows:

$$|P_{out}| = F_{EP} \frac{\omega_1}{K} (B_f \ddot{w}_B)^2 \quad (7.6)$$

$$\text{where } F_{EP} = \frac{\alpha \kappa^2 \Omega^2}{[(1 - \Omega^2) - 2\zeta_m \alpha \Omega^2]^2 + [(1 + \kappa^2) - \Omega^2] \alpha \Omega + 2\zeta_m \Omega^2} \quad (7.7)$$

It is noteworthy that the term, $B_f \ddot{w}_B$ or $(B_f \ddot{w}_B)^2$, in equation (7.6) represents an inertia force exerted on a PVEH system due to the base excitations.

The next step to derive the expression for harvesting efficiency is to define the mechanical input power, which is the power that the device absorbs from mechanical vibration parameterized by a base excitation force, F_B , acting at the base, as shown in Figure 7.2. The system here now has three degrees of freedom, beam displacement, $w = \psi_r(x)r(t)$, absolute base displacement, $w_B(t)$, and voltage, $v(t)$, and it is excited by a force $F_B(t)$. After introducing the additional external work term $\delta W = F_B(t)\delta w_B$ from equation (2.5) into the energy expressions, the three basic equations for r , w_B , and v become:

$$M\ddot{r} + B_f\ddot{w}_B + C\dot{r} + Kr - \theta v = 0 \quad (7.8)$$

$$B_f\ddot{r} + M_T\ddot{w}_B = F_B(t) \quad (7.9)$$

$$\theta\dot{r} + C_P\dot{v} + \frac{1}{R_l}v = 0 \quad (7.10)$$

where total mass, M_T is the sum of base mass, M_B , and the beam mass, mL , and can be written as $M_T = M_B + mL$ (see Figure 7.2). Equation (7.8), with $B_f\ddot{w}_B$ transferred to the right-hand side and equation (7.10) are the same as the earlier equations (2.17) and (2.18). These two equations can be solved as before for a given base motion, \ddot{w}_B , as the input, and equation (7.9) then gives the force, $F_B(t)$, associated with this base motion, \ddot{w}_B . Then from this force, $F_B(t)$, the input power can be determined. Note that the results will hold regardless of whether there is a proof mass or not although addition of a proof mass is not illustrated in Figure 7.2.

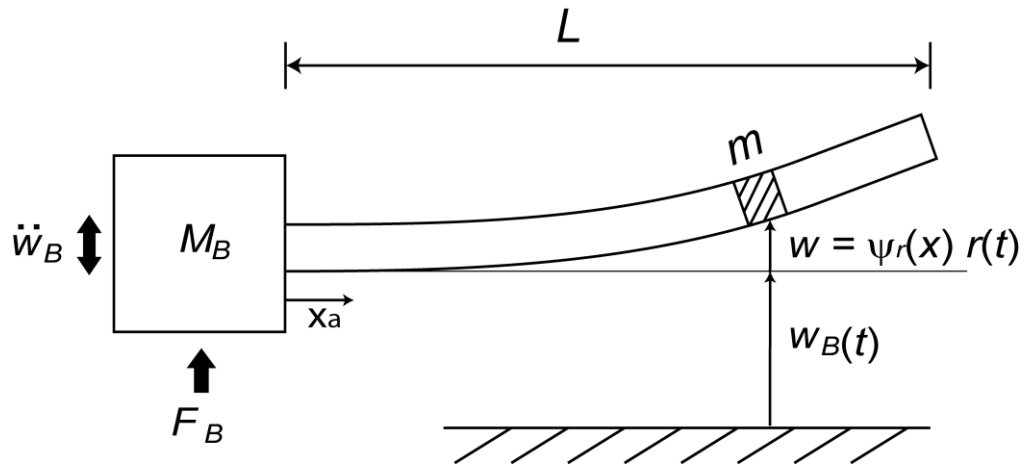


Figure 7.2 Schematic of a base-excited cantilevered beam/plate with indication of parameters defined for efficiency.

Making the assumption of harmonic motions allows development of general exponential expressions for base motion (w_B), relative displacement (r), voltage (v), and input force (F_B):

$$w_B = \bar{w}_B e^{i\alpha t} = w_{B0} e^{i\alpha t} \quad (7.11)$$

$$r = \bar{r} e^{i\alpha t} \quad (7.12)$$

$$v = \bar{v} e^{i\alpha t} \quad (7.13)$$

$$F_B = \bar{F}_B e^{i\alpha t} \quad (7.14)$$

In the above, the \bar{r} , \bar{v} , and \bar{F}_B are complex quantities, but the control variable $\bar{w}_B = w_{B0}$ is set to be real. Here, base motion $w_B(t)$ is specified as input and the force $F_B(t)$ that is associated with it is calculated. Substitution of these expressions into the governing equations (7.8) and (7.10) and use of the prior definition of $\frac{K}{M} = \omega_1^2$, $C = 2\zeta_m \omega_1 M$, $\Omega = \frac{\omega}{\omega_1}$, $\alpha = \omega_1 R_I C_p$, and

$\kappa^2 = \frac{\theta^2}{KC_p}$ result in a solution for amplitude of r and v as follows:

$$\frac{\bar{r}}{w_{B0}} = \frac{B_f}{M} \frac{\Omega^2 [(A_R + \alpha \Omega A_I) - i(A_I - \alpha \Omega A_R)]}{[A_R^2 + A_I^2]} \quad (7.15)$$

$$\left| \frac{\bar{v}}{w_{B0}} \right| = B_f \omega^2 \frac{\Omega \alpha \kappa^2}{|\theta| \sqrt{A_R^2 + A_I^2}} \quad (7.16)$$

$$\text{where } A_R = [(1 - \Omega^2) + 2\zeta_m \Omega^2 \alpha] \quad (7.17)$$

$$A_I = [(1 + \kappa^2) - \Omega^2] \Omega \alpha + 2\zeta_m \Omega \quad (7.18)$$

Equation (7.15) for the amplitude of displacement \bar{r} , and the harmonic oscillation assumption for base motion and input force in equations (7.11) and (7.14), are inserted into the second governing equation (7.9) to give the expression for \bar{F}_B :

$$\bar{F}_B = B_f (G_R + iG_I)(-\omega^2 w_{B0}) \quad (7.19)$$

$$\text{where } G_R = \frac{M_T}{B_f} + \frac{B_f}{M} \frac{\Omega^2[(1-\Omega^2) + (\alpha\Omega)^2(\{1+\kappa^2\} - \Omega^2)]}{[(1-\Omega^2) - 2\zeta_m\alpha\Omega^2]^2 + [(\{1+\kappa^2\} - \Omega^2)\alpha\Omega + 2\zeta_m\Omega]^2} \quad (7.20)$$

$$G_I = -\frac{B_f}{M} \frac{\Omega^2[2\zeta_m\Omega + \kappa^2\alpha\Omega + 2\zeta_m\Omega(\alpha\Omega)^2]}{[(1-\Omega^2) - 2\zeta_m\alpha\Omega^2]^2 + [(\{1+\kappa^2\} - \Omega^2)\alpha\Omega + 2\zeta_m\Omega]^2} \quad (7.21)$$

Returning to the time domain $w_B(t)$ and $F_B(t)$ by using equations (7.11), (7.14), and (7.19), one obtains:

$$w_B(t) = \text{Re}\{w_{B0}e^{i\omega t}\} = w_{B0} \cos \omega t \quad (7.22)$$

$$F_B(t) = \text{Re}\{\bar{F}_B e^{i\omega t}\} = B_f G_R(-\omega^2 w_{B0}) \cos \omega t - B_f G_I(-\omega^2 w_{B0}) \sin \omega t \quad (7.23)$$

where $\text{Re}\{ \}$ is used to indicate the real part in a complex number. Input power, P_{in} , is calculated through the relation *force* \times *velocity* and thus can be written as in equation (7.24) here:

$$P_{in} = F_B \dot{w}_B \quad (7.24)$$

Then, the detailed expression for input power over one cycle can be presented as follows by substituting equations (7.22) and (7.23) into equation (7.24):

$$|P_{in}| = F_{MP} \frac{\omega_1}{K} (B_f \ddot{w}_B)^2 \quad (7.25)$$

$$\text{where } F_{MP} = \frac{\Omega[2\zeta_m\Omega + \kappa^2\alpha\Omega + 2\zeta_m\Omega(\alpha\Omega)^2]}{[(1-\Omega^2) - 2\zeta_m\alpha\Omega^2]^2 + [(1+\kappa^2) - \Omega^2]\alpha\Omega + 2\zeta_m\Omega^2} \quad (7.26)$$

Note that the G_R portion of $F_B(t)$ in equation (7.23) does not contribute to the power over one cycle in equation (7.24). It is also noteworthy that P_{in} is written in terms of a dimensionless forcing parameter, F_{MP} , for a concise expression, as was P_{out} with F_{EP} in equation (7.6). Now it is possible to obtain an analytical expression for harvesting efficiency:

$$\eta = \frac{P_{out}}{P_{in}} = \frac{F_{EP}}{F_{MP}} = \frac{\alpha\kappa^2}{[2\zeta_m + \kappa^2\alpha + 2\zeta_m(\alpha\Omega)^2]} \quad (7.27)$$

In the above equation (7.25), mechanical input power for PVEHs is shown to have a similar analytical expression to electrical output power (see equation (7.6)). Although mechanical input power originates from pure mechanical vibration through the base motion, equations (7.25) and (7.26) suggest that even mechanical input power is not a function of pure mechanical terms anymore, but a function of mechanical, electrical and electromechanical parameters. This includes a very interesting implication that when mechanical vibration energy goes into the PVEH system, the amount of mechanical power available to the system depends not only on the vibration environment but also on device specifics such as piezoelectric coupling.

In prior work by Richards *et al.* [102], efficiency achieved by a given piezoelectric device (see Figure 7.1) is evaluated as a function of the relative magnitude of the electromechanical coupling factor (k^2 in their notation, and κ^2 here) and quality factor only, thus not reflecting the effect of electrical resistance (R_l) on the harvesting efficiency. Furthermore, their evaluation of efficiency is possible only at resonance, not capturing the case when input driving frequency does not align with the resonant frequency of a given PVEH system.

As an example case study, values for the mechanical input power, electrical output power, and harvesting efficiency of a macroscopic, bimorph PVEH with no proof mass (No PM) that was used for experimental verification earlier in this thesis (Chapter 4) are computed at varying electrical resistances and at several input frequency conditions, which are plotted in Figures 7.3-

7.5. In terms of input driving frequencies, both input and output power at resonance (109.5 Hz) and anti-resonance (115.25 Hz) are prominently amplified in comparison with power at off-resonance (at 75 Hz and 160 Hz), as shown in Figures 7.3 and 7.4. In contrast to power, harvesting efficiency, η , in Figure 7.5 shows similar trends within a similar range of magnitudes regardless of whether it is at resonance (anti-resonance) or off-resonance. Overall, when the normalized frequencies (= input frequency/resonant frequency) go up, efficiency decreases. This can be explained by a close examination of equation (7.27). Normalized frequency ratio, Ω , appears only in the denominator of equation (7.27).

Another noticeable aspect in Figure 7.5 is that efficiency values at resonance and anti-resonance have little difference over the entire range of electrical resistances. This underscores the significance of resonance and anti-resonance as optimal operating points as they can offer equal maximum power generation with similar efficiencies. When electrical resistance varies, optimum points are observed not only in output power at resonance and anti-resonance, but also for efficiency similarly. One key observation of engineering importance is that the optimal electrical resistance for maximum power differs from that for maximum efficiency. For example, in the case of a PVEH device with no proof mass (No PM), shown in the plots of Figures 7.4 and 7.5, at resonance (109.5 Hz), the optimal resistance is 9.6 k Ω and generates a maximum power of 335.2 μ W with an efficiency of 37%, while 34.7 k Ω of electrical resistance is required to achieve the maximum harvesting efficiency (63%) but results in less power output (223.8 μ W). Depending on the desired objective, which could be either power or efficiency (single-objective function), or both (multi-objective functions), one can determine the optimal electrical resistances that should be applied to the PVEH system by using the model as an analytical tool. In Section 7.1.3, analytical expressions of different optimal electrical resistance conditions that maximize output power (P_{out}) and efficiency (η) are presented.

Examination of the expression for harvesting efficiency in equation (7.27) also reveals that damping conditions affect the harvesting efficiency by the term of mechanical damping ratio (ζ_m). Referring to equation (7.27), harvesting efficiency is expected to increase when the mechanical damping ratio (ζ_m) becomes smaller (*i.e.* higher quality factor, Q). To see how harvesting efficiency behaves depending on damping graphically, plots of harvesting efficiency vs. varying electrical resistance (R_l) at various values of quality factor (Q) are drawn for the macroscopic

PVEH device with no proof mass (No PM) in Figure 7.6. The input driving frequency here is fixed at the device resonant frequency (109.5 Hz). Consistent with the expectation from the analytical expression, one can observe the increasing tendency of harvesting efficiency with increasing quality factor (thus, less damping) in the plots shown in Figure 7.6. Another aspect to note in Figure 7.6 is that efficiency tends to have little dependence on electrical resistance when the quality factor exceeds 1000. Thus, when a PVEH device is operated in the environment where quality factor exceeds a certain value (here, 1000), it would be more beneficial to find an optimal value of electrical resistance that can maximize other key performance such as power output, rather than focusing on the harvesting efficiency.

7.1.3 Optimal Design for Different Key Performance Metrics

The model-derived design study for piezoelectric materials in Chapter 6 includes sensitivity analyses of device performance to material properties for materials-level optimization and system-level optimization for output power, producing detailed design guidelines focusing on optimal piezoelectric material selection. Throughout the analysis, the focus is on maximization of output power. The analytical expressions for maximum power and corresponding optimal dimensionless time constant, α_{opt} , can be obtained by differentiation of output power equation (2.26) and setting it equal to zero with respect to dimensionless time constant, α . The resulting expression for the optimal dimensionless time constant, α_{opt} for power shows its dependence on electromechanical coupling factor (κ^2), normalized frequency (Ω), and mechanical damping ratio (ζ_m), as written in equation (2.27).

Expressions for the maximum harvesting efficiency, η_{max} , can be achieved by optimizing equation (7.25) with respect to α as $\frac{\partial \eta}{\partial \alpha} = 0$, which results in:

$$\alpha_{opt} = \frac{1}{\Omega} \quad (7.28)$$

In Figure 7.5, it is observed that optimal electrical resistance that yields maximum efficiency (*i.e.*,

peak points of each plot) decreases upon increasing operating frequency and this can be explained analytically by equation (7.28). Substitution of equation (7.28) into equation (7.27), then, gives maximum harvesting efficiency, η_{max} (or η_{opt}):

$$\eta_{opt} = \frac{\kappa^2}{[4\zeta_m\Omega + \kappa^2]} \quad (7.29)$$

Examination of equation (7.29) reveals that optimal efficiency, η_{opt} , is inversely proportional to mechanical damping ratio, ζ_m , which exists only in the denominator of the expression. This explains on the increase of optimal efficiencies when quality factor increases in Figure 7.6 as quality factor, Q , has a reciprocal relation to mechanical damping ratio, ζ_m , via $Q = 1/(2\zeta_m)$.

It should be noted that optimum harvesting efficiency has dependence not only on the electromechanical coupling factor (κ^2) and mechanical damping ratio (ζ_m), but also on the normalized frequency (Ω). From a perspective of maximizing harvesting efficiency, resonance and anti-resonance are not necessarily the optimal operating points as observed in Figure 7.5, unlike the case of power optimization. Another distinction in the optimal α for maximum efficiency in equation (7.28) is that it has no dependence on piezoelectric coupling, unlike optimal α for maximum power in equation (2.27). Input frequency is the only parameter that determines the optimal electrical loading condition for maximum efficiency. At resonance ($\Omega = 1$), equation (7.29) becomes:

$$\eta_{opt,r} = \frac{\kappa^2}{[4\zeta + \kappa^2]} \quad (7.30)$$

If the mechanical damping ratio is really low (or quality factor is really high) such that $4\zeta_m \ll \kappa^2$, the optimized efficiency at resonance in equation (7.30) approaches one. This implies that all the mechanical input power absorbed by a given PVEH device is converted to electrical power through the piezoelectric transduction mechanism at extremely low damping conditions and resonance. Thus, it would be more advantageous to tune electrical resistance to an optimal value that can maximize other key performance such as power output, rather than focusing on the

harvesting efficiency, as efficiency is close to its maximum value (100 %) at such conditions ($4\zeta_m \ll \kappa^2$).

As described above with power and efficiency as example performance objectives, choice of the objective function determines optimal electrical or operating conditions. Electrical resistances that generate maximum power appear different from the point where we can maximize harvesting efficiency. Thus, it is required to consider appropriate analytical expressions for optimal points depending on the performance of primary interest for system-level optimization.

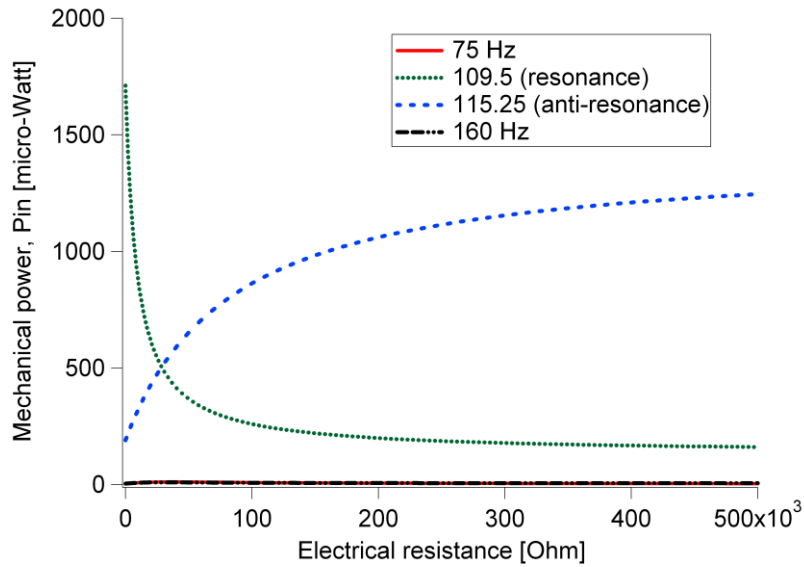


Figure 7.3 Mechanical input power vs. electrical resistance at various operating frequencies for a macroscopic, bimorph energy harvester in {3-1} mode of operation with no proof mass (No PM).

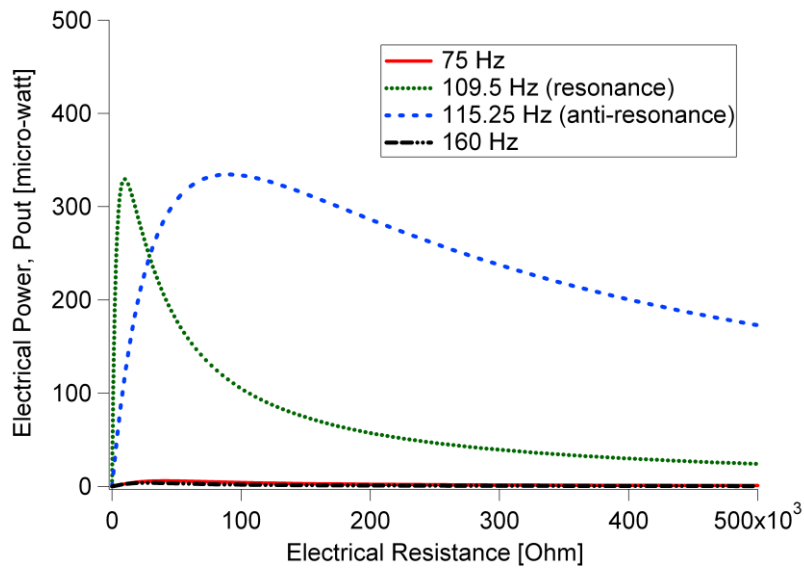


Figure 7.4 Electrical output power vs. electrical resistance at various operating frequencies for a macroscopic, bimorph energy harvester in {3-1} mode of operation with no proof mass (No PM).

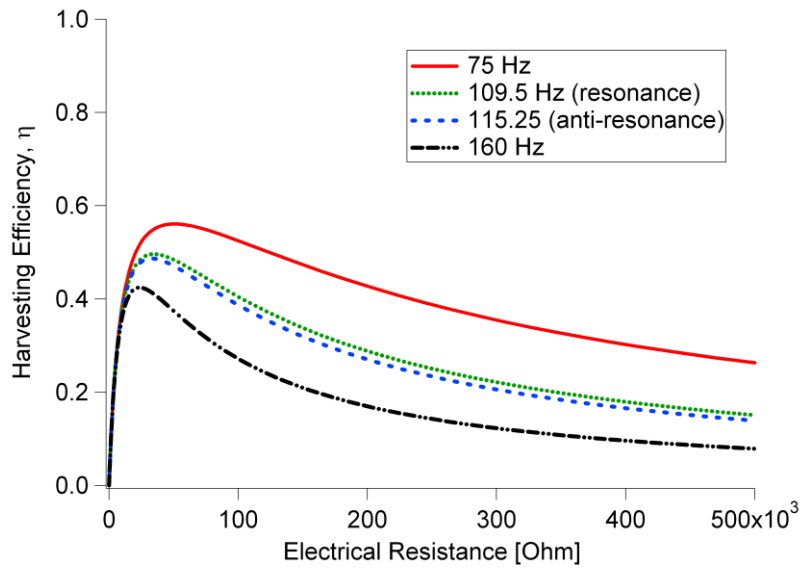


Figure 7.5 Harvesting efficiency vs. electrical resistance at various operating frequencies for a macroscopic, bimorph energy harvester in {3-1} mode of operation with no proof mass (No PM).

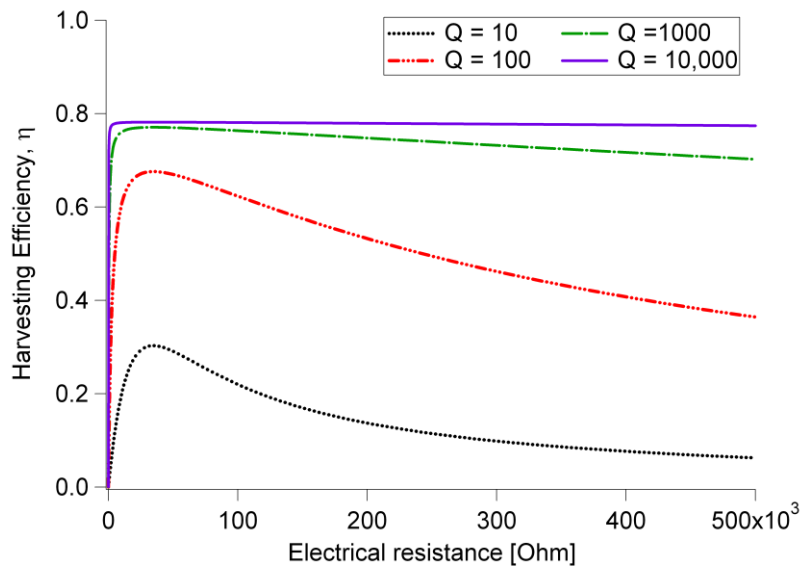


Figure 7.6 Harvesting efficiency at resonance (109.5 Hz) vs. electrical resistance at various damping conditions for a macroscopic, bimorph energy harvester in {3-1} mode of operation with no proof mass (No PM).

7.2 Direct Estimation of Materials and System Properties

Using the model, it is also possible to estimate materials and system properties. In the following, two different model-based approaches are introduced to assess materials and system properties: bottom-up and top-down approaches.

7.2.1 Bottom-up Approach

In the basic flow of modeling, key parameters can be classified into two categories: input and output parameters. When input parameters are known either from measurement or literature, calculation and prediction of performance parameters are straightforward via the analytical expressions derived so far. This is referred to as the “bottom-up” approach because input parameters (“bottom”) are fed into the model to calculate the output parameters (“top”). The usefulness of this approach is the fact that we can predict maximum performance of a given device even before conducting the actual experiment for device fabrication or characterization. For example, equation (2.30) is derived through power optimization with respect to electrical resistance for the maximum power that a given PVEH device can generate.

Another good example is the assessment of maximum voltage for a given PVEH system. From the plots of voltage versus electrical resistance at various operating frequencies, demonstrated in Chapter 4, it is observed that saturation of voltage toward a certain maximum value takes place as electrical resistance increases and that the maximum voltage appears at anti-resonance and open-circuit condition ($R_l \rightarrow \infty$). Reduction of the voltage, equation (2.25), to these specific conditions yields equation (7.31), which is a function of input parameters:

$$\left| \frac{v}{B_f \ddot{w}_B} \right|_{\text{Anti-res}, R_l \rightarrow \infty} = \frac{1}{|\theta|} \frac{1}{\frac{2\zeta_m}{\kappa^2} \sqrt{1 + \kappa^2}} \quad (7.31)$$

Thus, it is possible to estimate the engineering limit of voltage that can be developed from a given PVEH device. This capability has the potential to have considerable impact on device

design.

7.2.2 Top-down Approach

The goal of the top-down approach is to deduce the input or system parameters based on measured data of output performance. This top-down method is required when evaluation of certain material properties is time- or cost-prohibitive or unavailable, but measurement of device performance is possible. In [29, 74], du Toit *et al.* present a procedure to calculate the elastic stiffness of a structural layer in a macro-scale PVEH using measured data of resonant frequency at short-circuit condition in combination with model-derived analytical expressions. They also inferred values for the piezoelectric constants of their device using voltage values measured at resonance and power-optimized electrical resistance. Such a top-down approach for the estimation of materials and system properties becomes significantly advantageous when it comes to MEMS-scale PVEH devices. In most studies, use of the materials properties measured in thin-film form as the input parameters for the prediction of device performance is quite common, based on the assumption that such materials properties remain the same after integration into devices. However, it is hard to regard that those material properties in thin-film stacks remain the same at the final device level due to the effect of thin-film fabrication processing such as etching. In addition, it is difficult to probe the material properties of each layer embedded in the device. Even measurement of material properties in thin-films poses a great challenge. Hence, a necessity for a method to accurately evaluate the properties of materials when they are integrated into certain device configurations arises, and the model-based top-down approach can be one such solution.

First of all, equation (7.32) for the resonant frequency is derived in Chapter 3 and this can be used to deduce elastic modulus of a constituent material of a device. If geometric dimensions, density of materials, and elastic moduli of other materials than the material of interest are known and resonant frequency at short-circuit condition is measured, for instance, the unknown parameters in equation (7.32a) are the effective bending stiffness, \overline{EI} , and normalized eigenvalue, $\overline{\lambda}_1$, which are a function of geometric dimensions and elastic moduli. Then, the elastic modulus of the material of interest can be inferred by solving for the unknown:

$$\omega_1 = (\bar{\lambda}_1)^2 \sqrt{\frac{EI}{mL^4}} \quad [\text{rad/s}] \quad (7.32a)$$

$$f_1 = \frac{1}{2\pi} \omega_1 \quad [\text{Hz}] \quad (7.32b)$$

Another use of the top-down model as a standardized tool to predict material properties is to estimate the piezoelectric constant (e_{31}^*) by measuring the voltage at resonance with open-circuit condition. The voltage expression in equation (2.25) can be reduced to equation (7.33) at resonance ($\Omega_r = 1$) and open-circuit condition ($R_l \rightarrow \infty$):

$$|\theta| \approx \left| \frac{B_f \ddot{w}_B}{v} \right|_{r, R_l \rightarrow \infty} \quad (7.33)$$

In Chapter 4, the expression for coupling term, θ , for a bimorph PVEH device in {3-1} mode of operation and series connection is given by equation (7.34):

$$\theta = (e_{31}^*) \left(\frac{t_p + t_s}{2} \right) b \psi'_r(L) \quad (7.34)$$

Given the geometric dimensions and other input parameters, evaluation of the piezoelectric constant, e_{31}^* , becomes possible when measured data of voltage at resonance and open-circuit condition is available by using equations (7.33) and (7.34). Also, one can get another estimate of θ using equation (7.31) at anti-resonance where the voltage is much higher, but ζ_m and κ^2 enter the picture as well.

The electromechanical coupling factor, κ^2 , is a useful system property as a measure of system coupling in PVEHs and this can be extracted from the measurement of resonant frequency and anti-resonant frequency through relation (7.35):

$$\kappa^2 = (\omega_{ar} / \omega_r)^2 - 1 \quad (7.35)$$

Anti-resonant frequency has an importance as it is an optimal point where maximum power can be generated at high voltage, whereas resonant frequency, which is another optimal point for maximum power generation, generates low voltage. Despite its significance for power, anti-resonant frequency has not received sufficient attention and has been overlooked in device characterization. For a full characterization of a fabricated PVEH device, it is crucial to measure not only resonant frequency (system frequency at short-circuit condition) but also anti-resonant frequency (system frequency at open-circuit condition) so that both optimal operating points for maximum power generation can be identified. By doing so, the dimensionless system coupling parameter, κ^2 , can be estimated as well through equation (7.35).

One last example is to analyze mechanical damping ratio (ζ_m). In Section 3.4, the scheme is already presented to estimate the mechanical damping ratio from the measurement of absolute tip and base displacement, given that other input parameters such as material properties and device dimensions are known.

This top-down method to predict materials and system properties from the measurement of device performance can find further useful applications, particularly in studying fatigue phenomenon of PVEH devices. Fatigue is an important issue related to the reliability of energy harvesting devices in operation. Two kinds of fatigue can occur during piezoelectric vibration energy harvesting: piezoelectric and mechanical degradation [129]. One example of top-down approaches presented in this chapter was estimation of the piezoelectric constant using the measured data of voltage. Based on the relation of the voltage and piezoelectric constant, if voltage is measured as a function of time during PVEH device operation, the piezoelectric constants can be expressed as a function of time as well, from which one can see piezoelectric degradation trend during vibration operation. The advantage of this method is it does not require the device to stop its operation or be separated from the system to measure the piezoelectric characteristics of the embedded piezoelectric layers. In addition, measurement of resonant frequency or mechanical displacement as a function of operating time can provide a measure of mechanical degradation of the device as it is directly related to the structural properties of the constituent materials in PVEH devices. Investigation of fatigue phenomena in

PVEH systems based on these top-down approaches will be addressed in future work as listed in Section 11.2.

Chapter 8

Design of Unimorph MEMS Piezoelectric Energy Harvesters in {3-1} and {3-3} Modes of Operation

This chapter consists of three topics: analytical modeling for different electrode configurations in PVEH devices (Section 8.1), experimental characterization of MEMS-scale PVEHs and model-experiment comparison study (Section 8.2), and development of a multi-variable tool for the optimization of MEMS-PVEH devices (Section 8.3).

8.1 Analytical Modeling for Microfabricated Unimorph Piezoelectric Cantilever with Different Electrode Configurations

Use of two different modes is common to operate PVEH devices: {3-1} mode of operation and {3-3} mode of operation. In {3-1} mode, the voltage (and therefore, electric field) acts in the “3” direction while the mechanical strain is applied in the “1” direction. In {3-3} mode, both strain and voltage occur in the same direction, “3”. Index “1” and “3” come from Cartesian coordinate directions. For simplicity of analysis in the {3-3} mode of operation, x_1 coincides

with the beam thickness coordinate (x_t) while x_3 corresponds to general beam structure axial coordinate (x_a) (see Figure 8.1). The definition of this coordinate system is closely related to the poling directions, of which details are found elsewhere [30]. Conventionally, the poling direction is always in the “3” direction and thus this coincides with the direction of electric field induced upon applied mechanical strain. Choice of electrode configuration is dependent upon the modes of operations. Standard capacitor type electrodes are employed for {3-1} modes of operation while interdigitated electrodes (IDTEs) are commonly used to implement {3-3} modes of operation (see Figures 1.4 and 1.5). {3-3} mode of operation is advantageous in that the voltage developed can be controlled. While the electrode spacing is determined by the thickness of the piezoelectric layer in {3-1} mode, the electrode spacing determines the voltage produced in {3-3} mode configuration and can therefore be varied in design. In microsystems, there is a limitation in the thickness of piezoelectric layer that can be deposited due to the microfabrication processing, and thus, the voltage that can be obtained from {3-1} mode will be limited as well. However, once we have a series of PVEHs on a single die as a final system, it is possible to control the electrical output of the entire system by controlling the interconnections of individual devices [30]. Therefore, it implies that both modes of operations are potentially attractive for practical applications.

While models for standard capacitor type electrodes – either approximated or detailed- are not hard to find in the open literature, only a few modeling approaches have been attempted on IDTE configurations in PVEH devices. Jeon *et al.* demonstrated a MEMS-scale, {3-3} mode, piezoelectric micro power generator with IDTEs in [51] where their calculation of output voltage and power is based only on a very simple approximation. Other prior modeling includes theoretical analysis by Mo *et al.* where they developed a model for unimorph piezoelectric benders with IDTEs and performed both numerical and parametric studies on energy, charge, and voltage developed [104]. Their model encompasses only static considerations and it does not consider electrode spacing. This presents a need to develop a dynamic model of the PVEH with IDTEs and refine the model to include electrode spacing. In this section, a model for a unimorph PVEH device in {3-3} mode of operation with IDTEs is developed and briefly compared with {3-1} mode with standard electrodes especially in terms of expressions for electrical parameters such as electrical potential, capacitance, and piezoelectric coupling. A model for a bimorph

piezoelectric cantilever in {3-1} mode of operation was already presented in Section 4.1. All these models incorporate dynamic motion of piezoelectric energy harvesting cantilever as well as parameters that define the electrode structures.

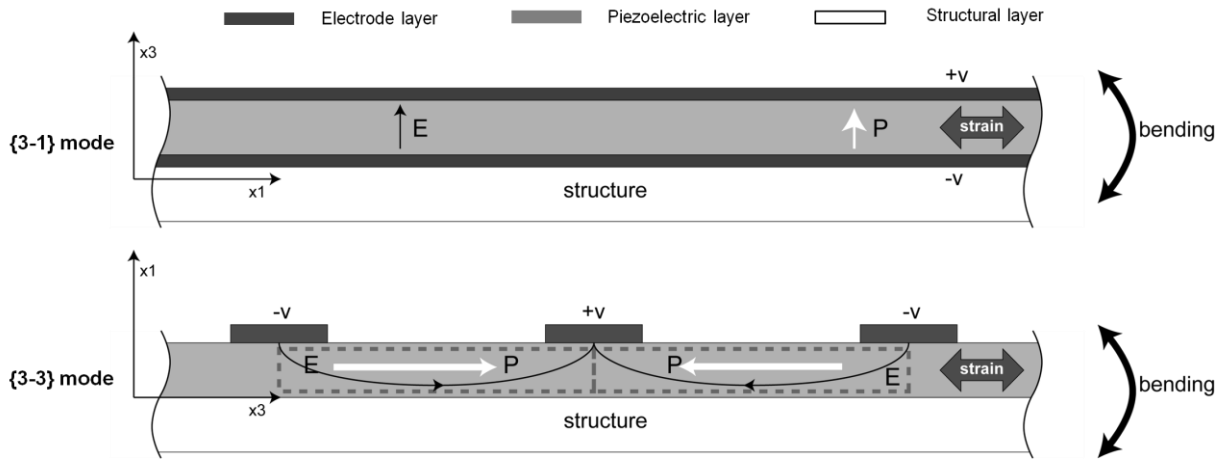


Figure 8.1 {3-1} and {3-3} mode unimorph PVEH configurations: side-view elements of (top) a cantilevered PVEH in {3-1} mode of operation with standard electrodes, and (bottom) a cantilevered PVEH in {3-3} mode of operation with IDTEs.

In {3-3} mode, the directions of the strain and the electric field are parallel to each other in the 3-direction. As demonstrated in Figures 1.5 and 8.1, IDTEs on top of a single layer of piezoelectric element are employed in {3-3} mode, eliminating the need for a bottom electrode, compared to {3-1} mode where top and bottom electrode layers are required. In the IDTE configuration, three dimensions are required: the thickness of the piezoelectric layer, t_p , the width of the electrodes, a , and the spacing between the centers of the electrodes (or called pitch), p . These are shown in Figure 8.2. For the IDTE configuration, it is helpful to introduce several approximations for simplicity. First of all, a full {3-3} effect through coupling is assumed in the section of piezoelectric element between the electrodes. Additionally, it is assumed that the region of the piezoelectric element under the electrode is electrically inactive. Although the electric field is not completely axial through the thickness of the piezoelectric element, nor is the region entirely inactive in practice, these effects are expected to compensate for each other to some extent. The geometry of this approximate model is illustrated in Figure 8.2 (right). Then, as

in {3-1} mode, proper expressions for electrical potential that varies from +1 at the electrode (left-side) to 0 to the other electrode (right-side) gives a constant electric field between the electrodes.

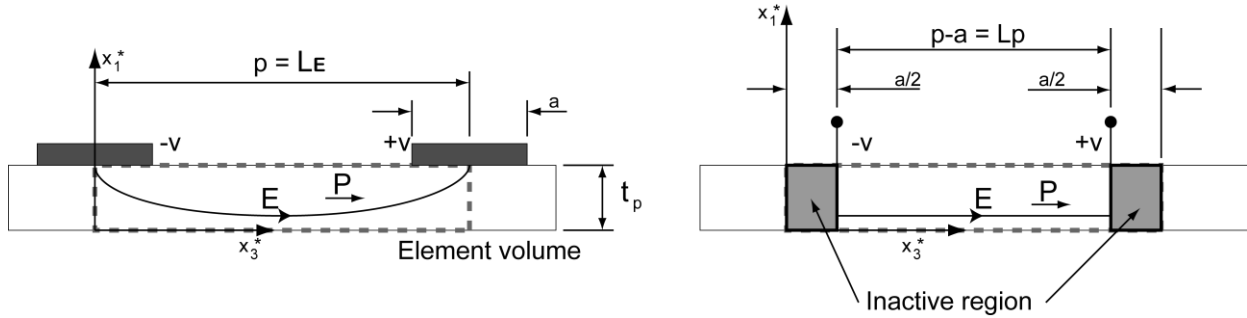


Figure 8.2 Side-view of piezoelectric layer in a unimorph, cantilevered PVEH in {3-3} mode of operation: {3-3} mode of operation (left) and approximate model (right) of electric field (E) between interdigitated electrodes. p is the pitch of the electrodes and a is the width of the electrodes. x_1^* and x_3^* are the element local coordinates. P denotes polarization.

For the energy, the internal mechanical potential, U , and electrical energy, W_e , can be placed together into a combined potential energy expressions, $\bar{U} = U - W_e$, namely:

$$\bar{U} = \frac{1}{2} \int_{V_s} \mathbf{S}' \mathbf{T} dV_s + \frac{1}{2} \int_{V_p} \mathbf{S}' \mathbf{T} dV_p - \frac{1}{2} \int_{V_p} \mathbf{E}' \mathbf{D} dV_p \quad (8.1)$$

These quantities were all described and defined by equations (2.1) to (2.5) in Section 2.2. Upon introducing the previous matrix relation equation (2.7) (repeated here in equation (8.2) for convenience):

$$\begin{Bmatrix} \mathbf{T} \\ \mathbf{D} \end{Bmatrix} = \begin{bmatrix} \mathbf{c}^E & -\mathbf{e}' \\ \mathbf{e} & \boldsymbol{\varepsilon}^S \end{bmatrix} \begin{Bmatrix} \mathbf{S} \\ \mathbf{E} \end{Bmatrix} \quad (8.2)$$

into the general expressions for \bar{U} in equation (8.1) above, one obtains:

$$\bar{U} = \frac{1}{2} \left[\int_{V_s} \mathbf{S}' \mathbf{c}_s \mathbf{S} dV_s + \int_{V_p} \mathbf{S}' \mathbf{c}^E \mathbf{S} dV_p - \int_{V_p} \mathbf{S}' \mathbf{e}' \mathbf{E} dV_p - \int_{V_p} \mathbf{E}' \mathbf{e} \mathbf{S} dV_p - \int_{V_p} \mathbf{E}' \boldsymbol{\varepsilon}^S \mathbf{E} dV_p \right] \quad (8.3)$$

This same potential energy expression for combined mechanical potential energy and electrical energy was given by Sodano *et al.* [72]. The three-dimensional linear elastic equation (8.2) can be readily reduced for simple beam theory and this {3-3} mode of operation, to:

$$\begin{Bmatrix} T_3 \\ D_3 \end{Bmatrix} = \begin{bmatrix} c_{33}^E * & -e_{33} * \\ e_{33} * & \varepsilon_{33}^S * \end{bmatrix} \begin{Bmatrix} S_3 \\ E_3 \end{Bmatrix} \quad (8.4)$$

, as shown in Appendix A. The reduction for plates as well is shown there.

Development of analytical modeling for IDTEs begins with consideration of the piezoelectric layer over a single element between one pair of electrode fingers, where element length L_E is defined as equal to pitch, p , *i.e.*, $L_E = p$, and the length of piezoelectric layer not under the electrodes, L_p , is defined as $L_p = p - a$, and t_p is the thickness of the piezoelectric layer. Then, the combined internal potential energy (\bar{U}_E) over the single element, L_E , can be written as:

$$\bar{U}_E = \frac{1}{2} \left[\int_{V_s} c_s S_3^2 dV_s + \int_{V_p} (c_{33}^E *) S_3^2 dV_p \right] - \int_{V_p} (e_{33} *) E_3 S_3 dV_p - \frac{1}{2} \int_{V_p} (\varepsilon_{33}^S *) E_3^2 dV_p \quad (8.5)$$

All parameters above follow the same definitions used in Section 2.2 and Appendix A. Expressions for strain, S_3 , and electrical field, E_3 , in equations (8.6) and (8.7) allow us to rewrite equation (8.5) into (8.8):

$$S_3 = -zw'' \quad (\text{where } z \text{ is distance measured from neutral axis}) \quad (8.6)$$

$$E_3 = -\frac{v}{L_p} \quad (\text{where } v \text{ is voltage developed}) \quad (8.7)$$

$$\bar{U}_E = \frac{1}{2} [c_s I_s (w'')^2 L_E + (c_{33}^{E*}) I_p (w'')^2 L_E] - (e_{33}^{S*}) S_p v w'' - \frac{1}{2} (\varepsilon_{33}^{S*}) \frac{v^2}{L_p} A_p \quad (8.8)$$

$$\text{where } I_s = \int_s b z^2 dz, \quad I_p = \int_p b z^2 dz, \quad S_p = \int_p b z dz, \quad A_p = \int_p b dz \quad \text{and } w'' = (w'')_{avg}$$

In the above expressions, z is the vertical distance measured from the neutral axis of the combined structural and piezoelectric beam, and $w'' = \partial^2 w / \partial x_3^2$. Also, $A_p = b t_p$, and S_p is the moment of the area, A_p , about the neutral axis. w_{avg} is the average value of w at the center of element, L_E .

If we also rewrite the expressions for kinetic energy (T_k) and external work (W) in equations (2.2) and (2.5) over the single element, L_E , in a similar way to internal potential energy (\bar{U}_E) in equation (8.8), and place them into Lagrange's equations, we find as before (equations (2.17) and (2.18)):

$$M\ddot{r} + C\dot{r} + Kr - \theta_p v = -B_f \ddot{w}_B \quad (8.9)$$

$$\theta\dot{r} + C_p \dot{v} + \frac{1}{R_l} v = 0 \quad (8.10)$$

where again time differentiation has been done on equation (8.10) and Ohm's law, $v = R_l \frac{dq}{dt}$, has been introduced. Each key parameter in the equations (8.9) and (8.10) above is defined as in equations (8.11) to (8.15):

$$M = (m_p + m_s) \psi_r^2 L_E \quad (8.11)$$

$$K = c_s I_s (\psi_r'')^2 L_E + (c_{33}^{E*}) I_p (\psi_r'')^2 L_E \quad (8.12)$$

$$\theta_p = (e_{33}^*)S_p\psi_r'' \quad (8.13)$$

$$C_p = \frac{(\varepsilon_{33}^S)^*A_p}{L_p} \quad (8.14)$$

$$B_f = -(m_s + m_p)\psi_r L_E \quad (8.15)$$

where I_s , I_p , S_p , and A_p are geometric properties, ψ_r'' is the mechanical mode shape at the center of the element (L_E), and v represents the voltage on the electrodes. Mass per length is denoted as m_p and m_s where subscripts p and s represent piezoelectric layer and structural layer, respectively.

For modeling of the entire cantilever with length, $L=nL_E$, summation or integration of each parameter (M , K , θ_p , C_p , and B_f) in equations (8.11)-(8.15), over the entire length, L , is required. These integrated terms, in turn, can be substituted into the governing equations to predict device performances of the whole cantilever system such as mechanical displacement, voltage, and power using equations (2.24)-(2.26). The total beam M , K , and B_f terms now include the piezoelectric mass, m_p , and stiffness, c_{33}^E *, which are readily combined with the basic structure terms, m_s and c_s , appearing in the basic integrals of equations (2.19), (2.20) and (2.23). The total beam piezoelectric terms, θ_p and C_p , are summed up as:

$$\theta_p = \sum_{i=1}^n (e_{33}^*)S_p \frac{d^2\psi_r}{dx_3^2} \approx \frac{(e_{33}^*)S_p}{L_E} \frac{d\psi}{dx_3}(L) \quad (8.16)$$

$$C_p = \sum_{i=1}^n \frac{(\varepsilon_{33}^S)^*A_p}{L_p} = \frac{L}{L_E} \frac{(\varepsilon_{33}^S)^*A_p}{L_p} \quad (8.17)$$

where $n = L/L_E$, and the approximate numerical integration relation below was introduced into equation (8.16), namely:

$$\int_0^L \frac{d^2\psi}{dx_3^2} dx = \left[\frac{d^2\psi(1)}{dx_3^2} + \frac{d^2\psi(2)}{dx_3^2} + \dots \right] \Delta x_3 = \frac{d\psi(L)}{dx_3} - \frac{d\psi(0)}{dx_3} \quad (8.18)$$

In the above, $\frac{d\psi(0)}{dx_3} = 0$ because of the cantilever boundary condition, and also $\Delta x_3 = L_E$.

Note that piezoelectric constant for longitudinal piezoelectric effect, e_{33}^* , is used in equation (8.12) for modeling of {3-3} mode PVEH devices, whereas piezoelectric constant for transverse piezoelectric effect, e_{31}^* , is suitable for modeling of {3-1} mode PVEH devices (see Section 4.1). Equations (8.16) and (8.17) describe the coupling term (θ_p) and capacitance (C_p) over the entire cantilever that are obtained from the summing equations (8.13) and (8.14) over the cantilever length, L . Direct substitution of these expressions into the governing equations for PVEH devices enables modeling of a unimorph cantilevered PVEH device in {3-3} mode of operation with IDTEs.

When modeling PVEH devices in {3-1} mode of operation with the standard electrode configuration, the induced electric field is regarded as constant through the thickness of the piezoelectric layer. Since there is only one pair of electrodes in standard electrodes (top and bottom), there is no need to use integration or summation of each element in {3-1} mode PVEHs. If the piezoelectric layer between the electrodes is regarded as a simple capacitor, the device in {3-1} mode consists of only one capacitor over the entire length (L) while the device in {3-3} mode can be thought of as a collection of multiple small capacitors. In comparison with {3-3} mode of operation, corresponding expressions to describe the coupling term (θ_p) and capacitance (C_p) of a unimorph, {3-1} mode, PVEH device with standard electrode configuration are as follows in equations (8.19) and (8.20):

$$\theta_p = (e_{31}^*) \frac{bz_N}{L} \frac{d\psi}{d\xi}(L) = \frac{(e_{31}^*)S_p}{t_p} \frac{d\psi}{dx_1}(L) \quad (8.19)$$

$$C_p = \frac{(\epsilon_{33}^S) bL}{t_p} = \frac{(\epsilon_{33}^S) A_p}{t_p} \frac{L}{t_p} \quad (8.20)$$

where ξ is non-dimensional length coordinate ($= x_1/L$), and z_N represents the distance between the centroid of area A_p and the neutral axis of the combined beam. These equations (8.19) and (8.20) give coupling and capacitance for the entire beam, not just over one element, and these equations for {3-1} mode are directly comparable to equations (8.16) and (8.17) for {3-3} mode, with no need to integrate when it is a uniform beam in cross-section. Again, it should be noted that the piezoelectric constant, e_{31}^* , is used in {3-1} mode while e_{33}^* is used for {3-3} mode, as well as different physical lengths. For application to a bimorph, {3-1} mode PVEH device, see the discussion about θ_p and C_p in Chapter 4.

In the following section, analytical models developed for different configurations described above are implemented to analyze fabricated MEMS-PVEH devices, and the simulated results are compared with measured data.

8.2 Experimental Evaluation and Correlation with Modeling

For applications in microsystems, several studies have focused on developing MEMS-PVEHs using established piezoelectric film processing [26, 59, 60, 105]. In macro-scale, a number of devices have been successfully developed, tested, and even available commercially (*e.g.*, the test device plate used in Chapter 4 to make a cantilever with proof mass). While fabrication of MEMS-PVEH devices is an area of many research groups' interest, not many microscopic prototype devices have yet been documented. In terms of materials, lead zirconium titanate, PZT, receives the most focus and its corresponding multi-layer structure is typically deposited on a Si substrate. In general, SiO_2 and/or SiN_x are deposited first as a supporting layer to enhance the mechanical strength of the structure by compensating for the internal stress between the Si substrate and other layers. ZrO_2 is often used as a diffusion barrier/buffer layer to prevent electrical charge diffusion from the piezoelectric layer (PZT). Pt and Ti comprise the electrode layers and Ti has the role of improving adhesion between PZT and Pt. For {3-1} mode, the bottom electrode Pt and interlayer Ti are deposited before the PZT layer, followed by a liftoff process for the top electrode. In comparison with {3-1} mode, there are only top IDTEs consisting of Pt/Ti that are deposited after the deposition of PZT layer in {3-3} mode. There is

one thing to note on materials selection for PVEH devices. Although poled ferroelectric materials such as PZT are preferred due to higher piezoelectric coupling constants than non-ferroelectric materials such as AlN and ZnO, those perovskite-type piezoceramics such as PZT require a poling process to create ceramic materials with strong piezoelectric coupling while non-ferroelectric materials don't need this poling process. Furthermore, as discussed earlier in Chapter 6, materials with the highest piezoelectric coupling constants are not necessarily the optimal piezoelectric materials one can choose in terms of power maximization. Thus, use of non-ferroelectrics can be more beneficial than poled ferroelectrics depending on the application of interest for the realization of power-optimized PVEH devices, which is in contrast with the pervasive notion in current PVEH research.

For this work, MEMS-scale unimorph PZT-based energy harvester cantilevers, both in {3-1} mode and {3-3} mode using standard electrodes and IDTEs, have been fabricated and tested by collaborators. Fabrication of MEMS-scale cantilevered PVEH devices were undertaken by the groups at Auburn and Brown Universities. The research group at Auburn University, particularly, has already presented their work on fabrication and evaluation of MEMS devices in several publications [75, 105, 106]. One of their recent studies includes the micromachined PZT cantilever based on SOI (silicon on insulator) structure with integrated Si proof mass for low frequency vibration energy harvesting [106]. Compared to their previous PVEH devices based on a Si substrate, use of SOI makes possible more precise control of the device dimensions, especially in thickness, resulting in much less discrepancy between calculation (design) and measurement of resonant frequency. A schematic of a piezoelectric energy harvesting cantilever based on a SOI wafer is given in Figure 8.3. The detailed fabrication process is beyond the scope of this thesis and can be found in [106]. Both {3-1} mode and {3-3} mode PZT-based devices are poled under the same condition at 200 KV/cm AC and at room temperature. One thing to note here is that an under-hang Si proof mass as shown in Figures 8.3 and 8.4 is integrated through bulk etching of the Si wafer. Figure 8.4 contains images of fabricated prototype energy harvester devices in {3-1} and {3-3} modes of operation. These devices are designed to target low frequencies (60-200 Hz) and their geometric dimensions are provided in Tables 8.1 and 8.2.

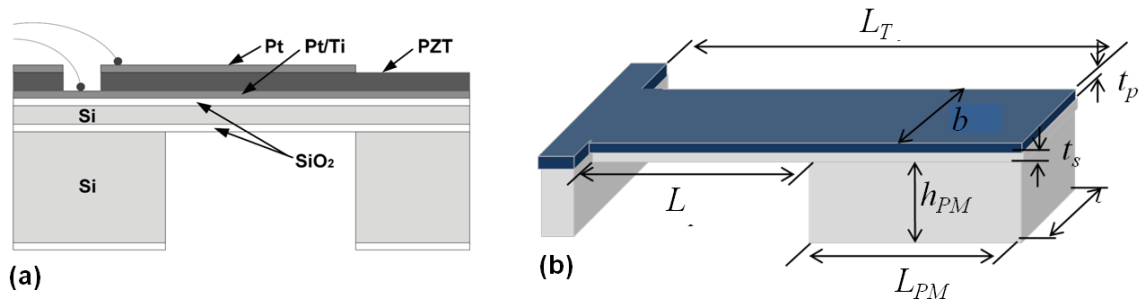


Figure 8.3 A unimorph, MEMS-scale PVEH: (a) schematic of the side view of piezoelectric energy harvesting cantilever based on SOI wafer, (b) cantilever structure with indication of dimension parameters. Reprinted with permission from [105, 106].

Table 8.1 Dimension for a unimorph thin film PZT cantilever.

Parameter	L_T	L	L_{PM}	b	b_{PM}	h_{PM}
Dimension [mm]	7	4	3	2	2	0.5

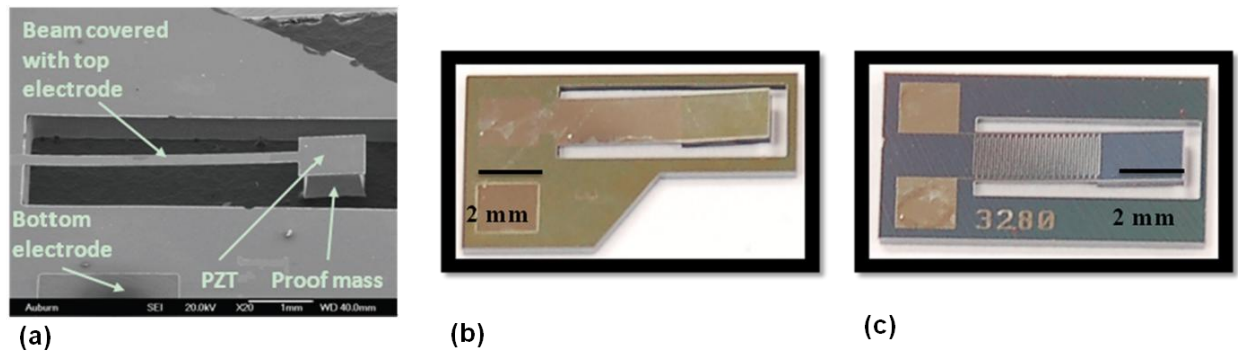


Figure 8.4 Fabricated, unimorph, MEMS-scale PVEH: (a) SEM image and (b) optical image of a MEMS-scale PZT cantilever in {3-1} mode with a proof mass, (c) optical image of a MEMS-scale PZT cantilever with a proof mass in {3-3} mode with IDTEs. (a) Reprinted with permission from [106]. (b), (c) courtesy of Dr. Jung-Hyun Park.

Table 8.2 Layers in micro-scale, unimorph, PZT-based energy harvester devices in {3-1} and {3-3} modes of operation.

	Layer	Thickness		Layer	Thickness
		[μm]			[μm]
{3-1} mode of operation	Pt	0.12	{3-3} mode of operation	Pt	0.2 (IDTE)
	PZT	1.0		PZT	1.0
	Pt/Ti	0.12/0.01		ZrO ₂	0.12
	SiO ₂	0.5		SiO ₂	0.5
	Si	20.0		Si	20.0
	SiO ₂	0.5		SiO ₂	0.5
	Total	21.75 μm		Total	22.12 μm

The properties of piezoelectric materials are critical to the quality and the reliability of the devices, especially in micro-electromechanical systems. While both mechanical and piezoelectric properties are well characterized in bulk piezoelectric ceramics, the material properties of thin films are not, unfortunately. This is due to the unique geometry and small displacements of thin films and thus requires different measurement methods from bulk cases when considering material properties of piezoelectric thin films [33, 34, 107]. In this work, as these material constants are primary inputs in analytical modeling, it can be said that the prediction capability of the modeling is highly dependent upon the extent of accuracy of the material properties of PZT thin films. The material properties of PZT thin films vary substantially depending on quite a number of factors such as composition, film orientation (texture), processing technique, thickness, etc. Therefore, evaluation of mechanical and dielectric constants as well as piezoelectric coefficients in PZT thin films of specific use is essential in order to predict the performance of PVEH devices. This study is also undertaken in collaboration with Prof. Dong-Joo Kim's group at Auburn University and Prof. Angus' group at Brown University.

First of all, PZT thin film is deposited on a substrate in a stack structure that is the same as the final PVEH devices. Although the specific order, or material, of these layers can vary for device improvement purposes, PZT thin films are typically fabricated on Pt (111) /Ti /SiO₂/Si substrates. As we fabricate the final PVEH device on top of a SOI structure, then PZT thin films

are characterized with the same structural substrate (SOI wafer). As mentioned, since film orientation (texture), composition, fabrication technique, thickness all impact the piezoelectric coefficients of PZT thin films, it is necessary to define the specific conditions for the PZT thin film of interest. In this work, we focus on the following PZT thin films both for material evaluation and PVEH devices:

- ◆ Composition: Zr0.52/ Ti0.48 (Pb(Zr_{0.52}Ti_{0.48})O₃), morphotropic phase boundary (MPB)
- ◆ Processing technique: sol-gel (multiple) coating method
- ◆ Thickness of PZT thin film: ~ 1 μm

Appropriate composition selection is required according to applications. When compared with other film compositions (*e.g.*, 30/70 or 70/30), MPB (52/48) is known to exhibit high piezoelectric coefficients, low coercive voltage, and high dielectric constant, thus considered optimal for PVEH devices [108]. Crystalline texture (*e.g.*, {111} preferred) and microstructure (*e.g.*, columnar) are also factors that should be considered.

Secondly, multiple tests were undertaken to check the characteristics of fabricated PZT thin films. To determine the crystalline texture and phase of the PZT thin films, X-ray diffraction is used (Figure 8.5 (a)). Polarization as a function of applied voltage (P-V hysteresis loops) is obtained and used to see if the PZT thin films retain sufficient ferroelectric properties after processing (Figure 8.5 (b)). Piezoelectric coefficients are of our major interest. In order to obtain the piezoelectric coefficients of PZT thin films, several evaluation techniques [33-35, 107-109] have been reported including normal loading method, impulse method, wafer flexure technique, interferometer method, and atomic force microscopy. (For bulk PZT, Berlincourt method and resonance method are widely utilized, which are not usually applicable for piezoelectric thin films.) In this work, the transverse mode piezoelectric coefficient of thin films, e_{31f} , is determined by 4-point bending measurement (aixACT aix 4PB, <http://www.aixacct.com>) while pneumatic loading method [130] is utilized for longitudinal coefficient, d_{33f} . The piezoelectric stress constant, e_{31f} , is found to be - 11.1 C/m² while d_{31f} is -104.3 pm/V by 4-point bending method. As stated in previous chapters, explicit knowledge of mechanical properties, particularly elastic moduli, are also required to implement the simulation for PVEH devices. For example,

published values for elastic moduli of PZT thin film are known to range from 37 to 400 GPa [109], which tells us that the disparities among piezoelectric coefficient values reported in the literature could result from use of different elastic moduli in calculation. It was determined for simulation purpose to rely on published values of PZT thin films of which specifics are as close as to the PZT thin films that we use. Liu *et al.* [110] presented the effects of the substrate and crystalline orientations on the mechanical properties of sol-gel processed $\text{Pb}(\text{Zr}_{0.52}\text{Ti}_{0.48})\text{O}_3$ thin films on Si/SiO₂ substrate, which is very similar to the PZT thin films here. From here, 140 GPa is adopted for model implementation. The dielectric constant is also required to implement the model. Dielectric data was collected using a HP 4292A impedance analyzer and the resulting dielectric constant as a function of dc biased voltage is shown in Figure 8.6, giving $1550\epsilon_0$ for the dielectric constant, ϵ_{33f}^S .

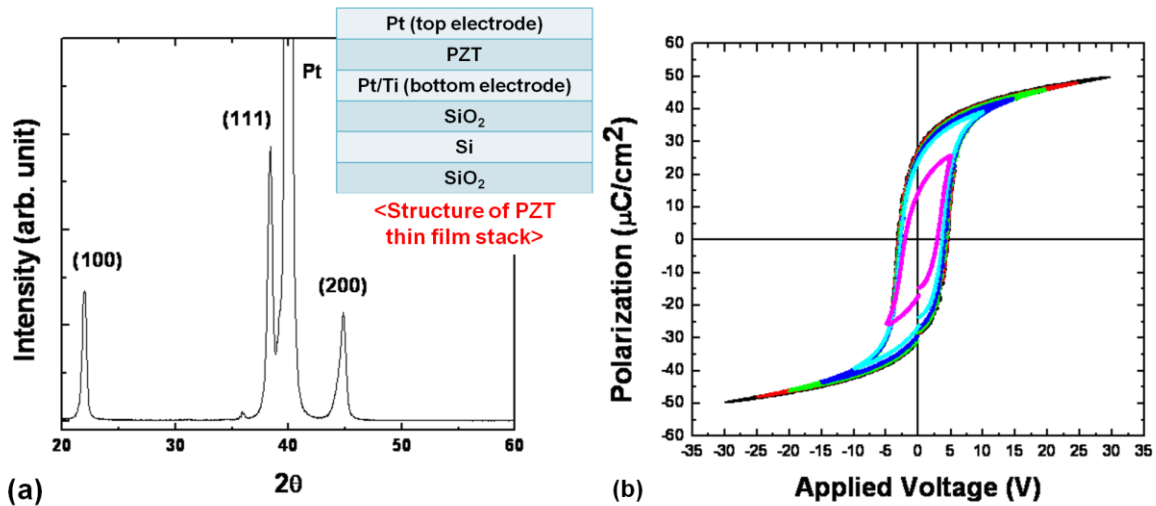


Figure 8.5 Characteristics of fabricated PZT thin films: (a) X-Ray Diffraction and (b) polarization-voltage hysteresis loop for polycrystalline PZT thin films.

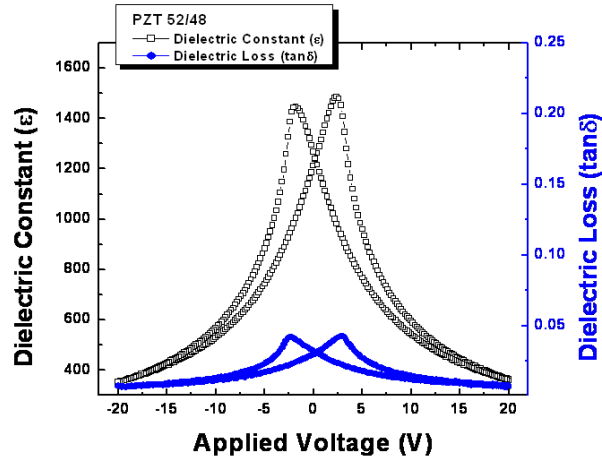


Figure 8.6 Dielectric constant-voltage curves.

Models are implemented on the fabricated unimorph MEMS-PVEH devices both in {3-1} and {3-3} modes of which geometric dimensions are available in Tables in 8.1 and 8.2. Material properties of each layer in both {3-1} and {3-3} mode devices are listed in Table 8.3. First of all, key effective parameters such as mass, stiffness, capacitance, and system coupling that appear in the governing equations (8.9) and (8.10) are computed, as listed in Table 8.4. It is noticeable that the key parameters of MEMS-scale PVEHs are much smaller order than those for macroscopic bimorph PVEHs in Table 4.3, due to their distinct difference in scale. Comparison of the calculated results for {3-1} mode and {3-3} mode devices in Table 8.4 suggests that electrical and electromechanical terms differ depending on the type of electrode configurations, as expected. Those terms related to geometric dimensions and mechanical properties such as mass (M), stiffness (K), and forcing function (B_f) have similar values as these two devices are fabricated with similar dimensions (see Tables 8.1 and 8.2).

Table 8.3 Material properties of layers in MEMS unimorph energy harvester device [30, 79].

Layer material	Density ^a [kg/m ³]	Modulus ^a [GPa]	Poisson's ratio ^a ν	Plate modulus ^c [GPa]
Pt	21440	170.0	0.39	200.5
Ti	4510	110.0	0.34	124.4
PZT (thin film)	7750	140.0	-	140.0
ZrO ₂	6000	244.0	0.27	263.2
SiO ₂	2300	69.0	0.15	70.6
Si	2329	129.5	0.28	140.5

^a Measured^b Literature values^c Computed as $E/(1-\nu^2)$ **Table 8.4** Key device parameters for model implementation on MEMS unimorph energy harvester devices in {3-1} and {3-3} modes (see Tables 8.1-8.3).

	M [kg]	K [N/m]	θ_p [N/V]	C_p [F]	B_f	κ^2
{3-1} mode	8.35×10^{-5}	48.5	-1.98×10^{-4}	1.60×10^{-6}	2.44×10^{-5}	0.00995
{3-3} mode	8.32×10^{-5}	44.4	-3.07×10^{-6}	2.15×10^{-11}	2.44×10^{-5}	0.00509

Model simulation permits prediction of both resonant and anti-resonant frequencies of MEMS-scale unimorph PVEH devices in both modes of operation. For the unimorph, {3-1} mode device, 121.3 Hz is calculated as resonant frequency while 121.6 Hz is estimated as anti-resonant frequency. For the unimorph, {3-3} mode device with similar dimensions, 116.2 Hz and 116.8 Hz are obtained as resonant and anti-resonant frequencies, respectively. Several aspects are noteworthy here. First of all, the difference in resonant and anti-resonant frequencies between {3-1} and {3-3} devices with similar dimensions arises because of the different constituent layers such as ZrO₂ in {3-3} mode device and different electrode configurations. Particularly, in {3-3} mode devices with IDTE configuration, contributions of the electrode layers to the mass and stiffness of the entire system affect the resonant frequencies. As electrode layers don't cover the entire area of the cantilever, the ratio of the area covered by the fingered electrodes in IDTEs

to the entire area is useful to estimate the partial contribution of these electrode layers to the mass and stiffness of the system, and thus resonant frequencies. The mass and stiffness of IDTE layer materials (Pt, here) are thus multiplied by the area ratio (0.31, here) and then used to calculate the resonant frequency of the entire systems.

Another aspect to note here is the low value of system coupling, κ^2 . In contrast with system couplings for macroscopic PVEH devices shown in Chapter 4 (Table 4.3) with values around 0.1, the system coupling for the MEMS-scale PVEH devices considered here are in the range of 0.005~0.009 as shown in Table 8.4. The low value of system coupling, κ^2 , here results in the small difference between the resonant frequencies and anti-resonance frequencies (*e.g.*, 121.3 Hz and 121.6 Hz, respectively for {3-1} mode device) of these MEMS-scale systems treated here, as anti-resonant frequencies of PVEH devices differ from their resonant frequencies depending on the magnitude of system coupling (κ^2). The low κ^2 here is likely due to lack of any systematic design for optimal PVEH devices – the design of these devices was driven mostly by what can be fabricated in the lab. When model-based design for optimal devices is implemented (see Section 8.3), it is possible to achieve MEMS-PVEH devices with much higher values of system coupling κ^2 . In Section 8.3, for example, it is shown that optimal device dimensions for operating power density (*e.g.* beam length, $L = 0.10$ mm & proof mass length, $L_{PM} = 0.68$ mm) gives 0.06 for system coupling, κ^2 , given the same materials properties and structures as those in Table 8.3. This highlights a considerable significance of model-derived optimal device design in order to realize PVEH devices with optimal materials and system parameters. Thus, future work will include further optimal device design studies to determine dimensions such as layer thickness, beam length, and proof mass length to enable fabrication of optimized PVEH devices.

At Auburn University, “resonant frequencies” were experimentally measured on these devices by finding the frequency points where highest voltage appears from the voltage vs. frequency plots at certain electrical resistances (11 k Ω and 4 M Ω). 128.3 Hz is obtained experimentally for the {3-1} mode device while 118.1 Hz is measured for the {3-3} device, which shows 5.8% and 1.6% difference from theoretically predicted values. However, the frequencies at which the peak voltages occur at certain electrical loading conditions do not necessarily correspond with either resonant or anti-resonant frequencies (refer to Figure 6.4). As part of a full characterization of energy harvester performance, measurement of natural

frequency of a system both at short circuit condition (resonance) and open-circuit condition (anti-resonance) is recommended using the appropriate equipment such as a laser vibrometer.

Electrical device responses, voltage and power, of the fabricated MEMS-scale device in {3-1} mode of operation were measured at the experimental “resonance” condition while keeping the base acceleration constant at 0.25 g ($g = 9.8 \text{ m/s}^2$). In Figure 8.7, measured electrical performance is plotted against electrical resistances ranging from 0 k Ω to 100 k Ω (dots) along with the simulated results (lines) for voltage and power at various damping conditions. In contrast with the experiments on macroscopic system presented in Chapter 4, it was not possible to estimate the mechanical damping ratios for these MEMS-scale systems according to the scheme presented in Section 3.1 due to the lack of measured data for mechanical performance. Thus, here, several reasonable values were chosen for mechanical damping ratio or quality factor to best fit the experimental electrical results. Model-informed experiments should be performed in the future. Model-experiment comparison shows that trends of electrical behavior are well predicted regardless of quality factors. In terms of magnitudes, simulated voltage and power match well with the experimental results when the quality factor (Q) is close to 250. Predicted power results reveal that the values of maximum power at the peaks and peak positions vary depending on the magnitudes of quality factor, implying the significance of operating environment, especially, damping conditions of the MEMS-scale system. Maximum power and corresponding optimal electrical resistances are of significance. According to the analytical modeling results, maximum power of 3.1 μW can be generated at $Q = 250$ when electrical resistance of 5.1 k Ω is applied at resonance ($\Omega_r = 1$) and 13.2 k Ω is applied at anti-resonance condition ($\Omega_{ar} = \sqrt{1 + \kappa^2}$). Experimentally, power of 3.0 μW was extracted at around 11 k Ω and experimental resonant frequency (128.3 Hz), as shown in Figure 8.7 (b).

In Figure 8.8, simulated results of electrical performance for the unimorph, {3-3} mode device are also graphically demonstrated at a damping condition of $Q = 250$. For {3-3} mode case, measured data are not available due to lacking test parameters and challenges in poling of devices with IDTEs [128]. It should be mentioned that fewer input parameters, particularly, thin film PZT material properties were available for {3-3} mode device than {3-1} mode device for simulation. Therefore, considering the fact that material properties in thin films are typically smaller than in bulk, material constants for PZT-5A in bulk used in Chapter 4 were considered to

undertake a rough estimation for the {3-3} mode, unimorph, MEMS-PVEH. Simulation results reveal that generating maximum power of $3.5 \mu\text{W}$ is possible from the {3-3} mode unimorph energy harvester device when operated either at $23.8 \text{ M}\Omega$ and resonance ($\Omega_r = 1$) or $170 \text{ M}\Omega$ and anti-resonance ($\Omega_{ar} = 1$). Comparison of PVEHs of similar size but operating in different modes ({3-1} and {3-3}), is possible using the results shown in Figures 8.7 and 8.8. While both mode devices are expected to produce similar maximum power of around $3.0 \sim 3.1 \mu\text{W}$, much higher voltage ($\sim 14 \text{ V}$) and required electrical resistance ($\sim 20 \text{ M}\Omega$) are observed for the {3-3} mode device when compared to the {3-1} mode device where maximum voltage is around 0.4 V and optimal electrical resistance is $13 \text{ k}\Omega$.

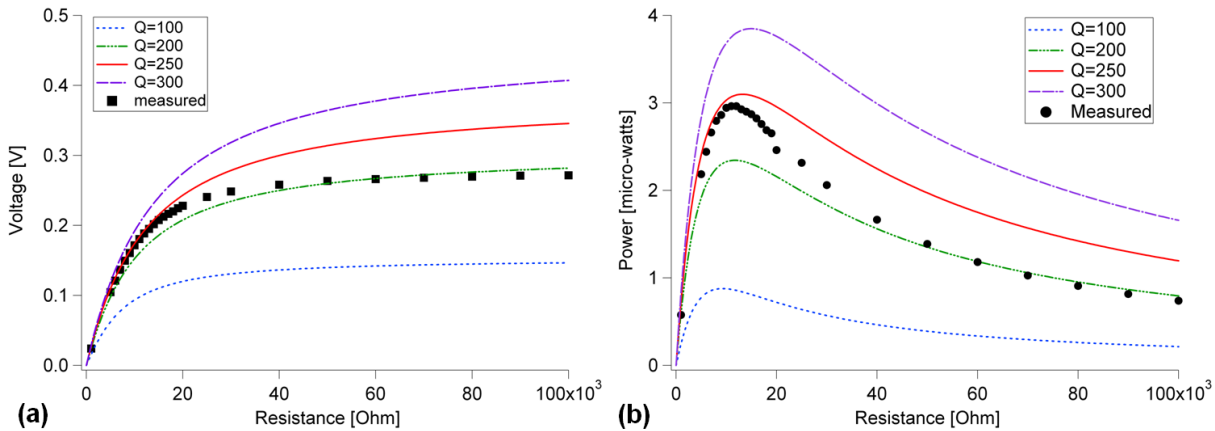


Figure 8.7 Model-experiment comparisons for a MEMS-scale unimorph energy harvesting PZT cantilever with a proof mass in {3-1} mode: (a) voltage versus electrical resistance and (b) power versus electrical resistance at resonances and various damping conditions. Q indicates the quality factor.

In summary, the developed model for PVEH devices exhibits conservative predictive capability not only on macroscopic devices but also on MEMS-scale PVEHs. PVEH device in {3-3} mode operation needs further study and details of future work are addressed in Chapter 11.

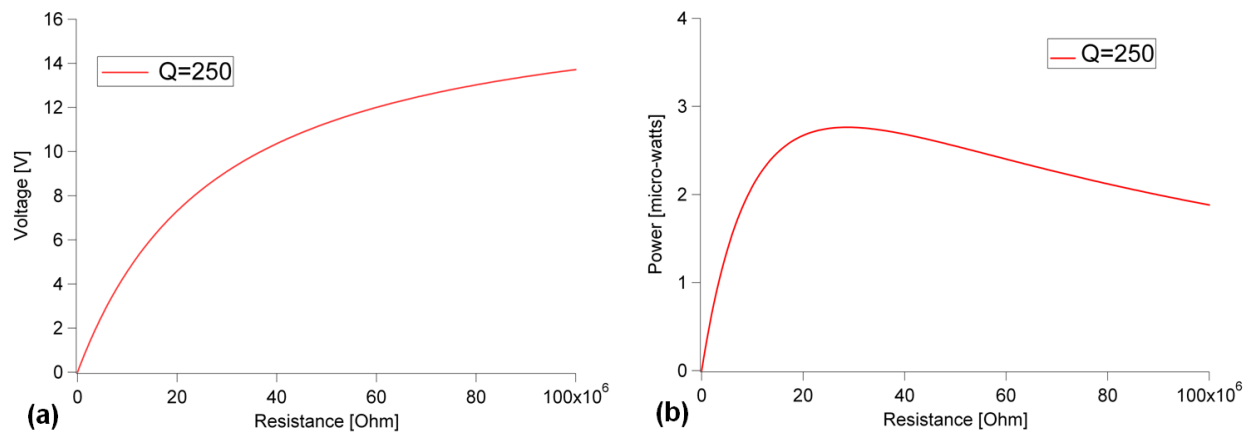


Figure 8.8 MEMS-scale unimorph energy harvesting PZT cantilever with a proof mass in {3-3} mode with IDTEs: predicted (a) voltage versus electrical resistance and (b) power versus electrical resistance at resonances and $Q = 250$. No measured data available.

8.3 Design of MEMS Piezoelectric Energy Vibration Energy Harvesters for Different Objectives

Throughout this thesis, a rigorous analytical model for PVEH devices has been developed and experimentally verified on both macro- and micro-scale devices. Chapters 6 and 7 include demonstration of several ways to utilize the model, particularly in materials design and performance standardization for the realization of optimal PVEH devices. Device design optimization study is another useful application of the model. In this section, a multi-variable design tool is developed and implemented with special focus on the optimization of MEMS-PVEH devices for embeddable structural health monitoring (SHM) sensor applications.

8.3.1 Design Constraints for Aerostructural Sensor Applications

Advances in the technology of microelectronics have made possible the miniaturization of sensor components and thus realization of distributed, embedded or implanted devices using these sensor nodes. Among all the sensor applications where PVEHs can be useful, of particular

interest in this work is wireless structural health monitoring (SHM). According to Boller [111], approximately 70 % of the damage discovered on aircraft components after inspection is due to fatigue cracking. However, predicting these cracks accurately is quite difficult, resulting in an increase of inspection costs due to the complexity, weight and expense of wire cables to connect damage sensor nodes. Thus, development of a self-powered SHM sensor node that can be integrated into the airframe would pave the way for significant savings throughout an aircraft's life as well as increased safety. In order to build wireless self-powered sensor nodes for aircraft health management, micro-scale PVEH devices should be pursued. Therefore, using a verified analytical modal model, the author focuses on the optimal design of the most common cantilevered-type of PVEHs.

An optimization scheme begins with consideration of the vibration environment of aircraft to obtain the design point. As our interest lies in the SHM of aircraft primary structures, in order to find an operating frequency and acceleration, it is necessary to investigate the vibration environment of aircraft. Using the data found in the Military Standard 810F, Annex C, Method 514.5 [112], it is possible to calculate the vibration exposure on the aircraft's empennage, where the highest life-cycle cost occurs, and thus obtain an operating frequency point of 1000 Hz at 3.89 m/s^2 (nearly $0.5g$'s). Thus, 1 kHz is selected as the input excitation frequency at a given acceleration of 3.89 m/s^2 for this work. While it is the upper bound of vibration level that a component on the aircraft must be able to withstand, given that only aerodynamic vibration, not including engine vibration, is considered here, this vibration level of 3.89 m/s^2 at 1 kHz can be regarded as conservative for the purposes of predicting device output.

8.3.2 Multi-variable Design Optimization for Various Performance Metrics

After quantifying the targeted vibration environment (*e.g.*, aircraft), design optimization extends to the investigation of geometric configurations, modes of operation, and fabrication constraints of PVEH devices. In terms of geometric configuration, a cantilevered PVEH is chosen due to its compliant structure that can produce large strain and thus high power as well as its compatibility with MEMS fabrication processes. Depending on the number of piezoelectric layers, devices can be defined either as unimorph (one piezoelectric layer) or bimorph (two

piezoelectric layers) devices. As stated earlier in this chapter, the biggest difference between {3-1} and {3-3} modes of operation takes place in terms of voltage control. In the case of {3-1} mode of operation, the magnitude of voltage generated is determined by the thickness of piezoelectric layers. In contrast with this, the voltage can be adjusted by controlling the spacing between the IDTEs for {3-3} mode of operation. In microsystems of our interest, since it is challenging to deposit thick ($>1 \mu\text{m}$) layers of piezoelectric material (*e.g.*, PZT) with consistent reproducibility, unimorph IDTE PVEH devices with {3-3} mode of operation are found to be most suitable. Also, a proof mass is added at the tip of the cantilevered energy harvester structure in order to adjust the natural frequency to the operating point of interest [52].

Several significant factors in micro-fabrication (such as mask image resolution, obtainable layer thicknesses, inter-layer adhesion, and residual stress management) are also taken into account in order to propose an optimized design approach. For the micro-scale unimorph, {3-3} mode PVEH device with a proof mass and IDTEs, (see Figure 1.5), the device is typically comprised of one piezoelectric layer (PZT), a structural layer consisting of silicon nitride (SiN_x), silicon dioxide (SiO_2), and zirconia (ZrO_2) layers, the IDTEs composed of titanium (Ti) and platinum (Pt), and the proof mass. The thickness of each layer is often limited by the manufacturing processes in microsystems and thus should be considered in the design process. For example, it has been known that depositing a thick layer of PZT exceeding $1 \mu\text{m}$ usually causes serious film cracking. Platinum is chosen as a proof mass material because of its high density and the height of the platinum proof mass is restricted to $3 \mu\text{m}$ by the current e-beam deposition techniques. The obtainable resolution of mask image is another factor to limit the size and the spacing of the electrodes. Taking all these factors into account, including fabrication experience, numerical values are determined for thicknesses of all layers as in Table 8.5. The beam width is set to be 1mm , considering the feasible size of the entire system for embeddable sensor nodes. It should be noted that as these values for thicknesses can vary within the constraint factors in microfabrication processes, and the optimum for the device can be improved further by expanding the optimization to include layer thicknesses.

For {3-3} mode device, IDTE patterns shown in Figures 1.5 and 8.2 are used and consideration of the constraints in lithography and poling condition yield a pitch, p , of $16 \mu\text{m}$ and a “finger” width, a , of $4 \mu\text{m}$ [113]. The electrodes were assumed to cover 50 % of the top

surface of the device for stiffness calculations.

Table 8.5 Example device dimensions for a unimorph, {3-3} mode energy harvester, given microfabrication constraints.

Material	Pt	Ti	PZT	ZrO ₂	SiO ₂	SiN _x
Thickness [μm]	0.20	0.02	0.5	0.05	0.10	0.40

If all material properties of use are known either by measurement or from the open literature, the remaining variables for the unimorph, {3-3} mode, energy harvester device are active beam length (L) and proof mass length (L_{PM}). Thus, the objective will be a function of two variables. Depending on the particular applications of interest, objective functions can be set differently. For instance, pure power output (units in [μW]) can be obtained as a function of two variables (L and L_{PM}) and optimization results can be graphically demonstrated as presented in the following section. It should be noted that optimal resistance is used at every design point. Since the total package size and mass are important for final design of energy harvester system, the volume and the mass should be taken into account. For this, power should be normalized by operating volume, static volume, or mass, resulting in operating power density, static power density, or specific power density, respectively. Once the objective functions or combinations are selected according to specific application of the devices, a plot can be obtained that provides a visual optimal design as well as sensitivity of the results, as examined via example in the next section.

8.3.3 Optimization Results for an Example Prototype MEMS Harvesting Device

Following the optimization schemes presented up to now, an example design for a unimorph, {3-3} mode, PVEH device with a proof mass at the tip is achieved. In terms of modeling for proof mass effects, improved treatment of rigid proof mass with rotation in Section 3.2 is used. For the given example device design, three-dimensional plots of operating power density (power normalized by operating volume), P_{op} , and output power, P_{out} , as a function of

active beam length (L) and proof mass length (L_{PM}) are graphically demonstrated in Figures 8.9 (a) and (b), respectively. Emphasis should be put on the fact that optimal resistance is used at every design point of device performance. Comparison between the optimization results for output power and for operating power density reveals that optimal design of the device varies depending on which objective function is considered. While the given PVEH device structure is advantageous in terms of operating power density and expected to generate up to $\sim 70 \mu\text{W}/\text{cm}^3$, the predicted power output is quite small for practical applications, implying further optimization should be performed for other parameters such as thickness of each layer to provide more optimal geometry and design of PVEH devices. The reason why different points are obtained in terms of maximum power extraction for the case of operating power density can be explained using tip displacements. Large tip displacement occurs at resonance and this increases the operating volume, the entire space where the device vibrates. Therefore, the optimum point is found at the point where the benefit of high power and the penalty of large tip displacements at resonance are traded. Although the static power density and the specific power density are not presented here, different optimal device dimensions, especially the lengths, will be obtained for the same device depending on the chosen objective function. In Figure 8.10, the operating power density is plotted as a function of proof mass length (L_{PM}) when the active beam length (L) is fixed at $100 \mu\text{m}$. The system coupling factor, κ^2 , for this given device with these dimensions is around 0.06, which is one magnitude larger than that of both Si-based MEMS-PVEHs analyzed in Section 8.2. There are two optimal points exhibiting maximum P_{op} of similar magnitude as observed in Figure 8.10. These two points exactly correspond to resonant and anti-resonant operating points, which is consistent with the modeling results as mentioned before. In this case, the value for operating power density is $70 \mu\text{W}/\text{cm}^3$ with optimal proof mass length of $680 \mu\text{m}$ at resonance when the beam length is $100 \mu\text{m}$, requiring a long, distributed proof mass. One thing to note here is that sharp peaks in Figure 8.9 are attributed to the collection of discrete data points during simulation and do not represent the real phenomenon. Smooth curve shown in Figure 8.10 is the expected result of multi-variable optimization.

In this work, an optimization technique is presented that allows one to design MEMS piezoelectric mechanical energy harvesters targeting the operating frequency and acceleration of aircraft vibration for structural health monitoring (SHM) applications. This optimization scheme

is based on the electromechanically coupled modal model of cantilevered structured energy harvesters, which has been experimentally verified in earlier chapters. Geometric configurations including a proof mass, modes of operations, as well as factors in microfabrication are considered. Design of a unimorph, {3-3} mode, PVEH device with a proof mass with detailed dimensions is discussed. Depending on the application of interest, four different objective functions such as power output, operating power density, static power density, and specific power density, can be obtained as a plot in 3-dimensional space with two variables of active beam length and proof mass length. When objective functions vary, the resulting device dimension will come out differently through the optimization procedures. A single example device design is shown in this work, and following the optimization scheme presented here, this optimization technique can be expanded to various device configurations depending on the specific applications of interest.

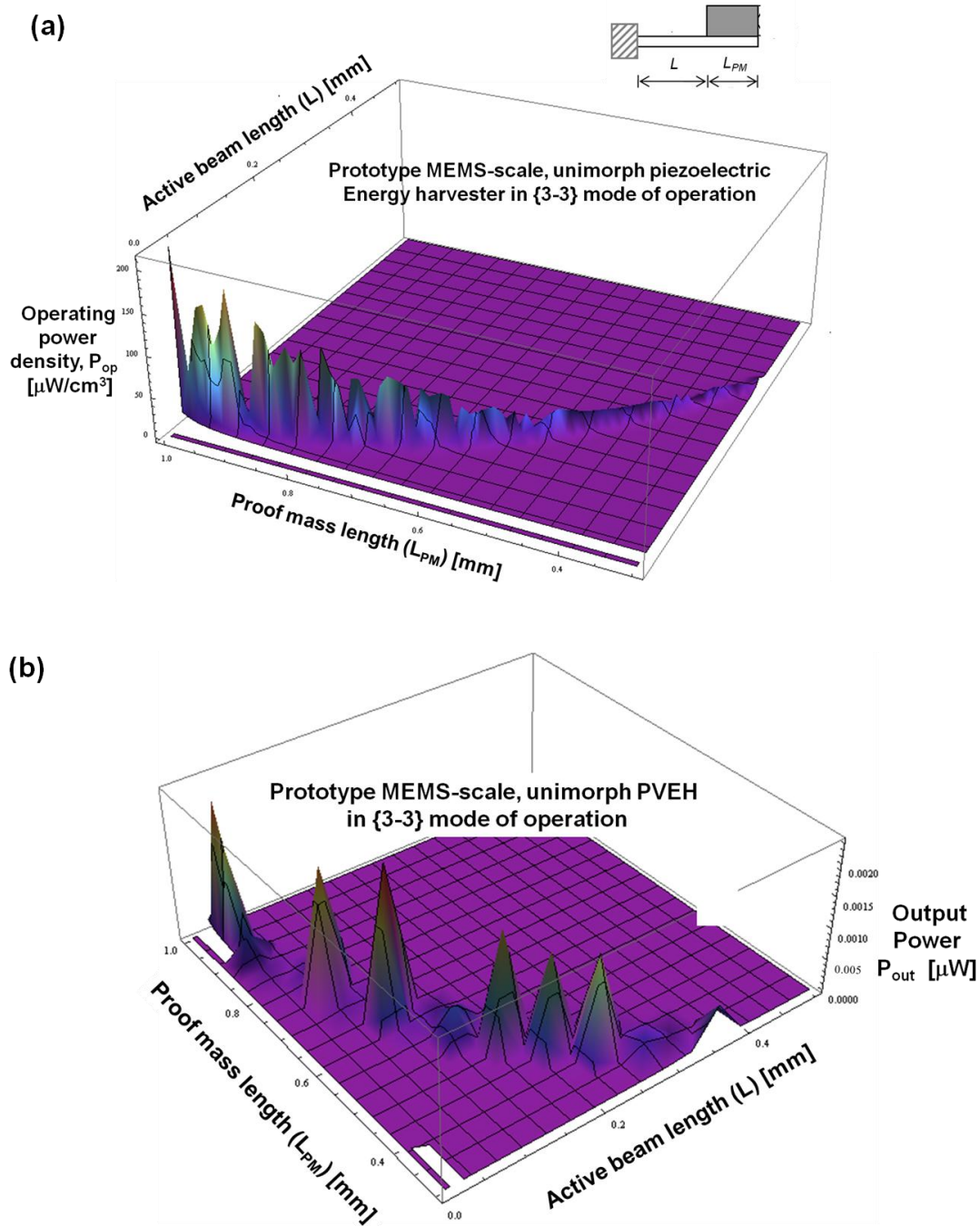


Figure 8.9 3-D plots of two-variable optimal design exercise for {3-3} SHM MEMS-PVEHs: (a) operating power density optimal designs and (b) power output optimal designs, both as a function of active beam length (L) and proof mass (L_{PM}). Both are at $Q = 100$ ($\zeta_m = 0.005$). Sharp peaks in the above plots are due to the collection of discrete data points during simulation and do not represent the real phenomenon.

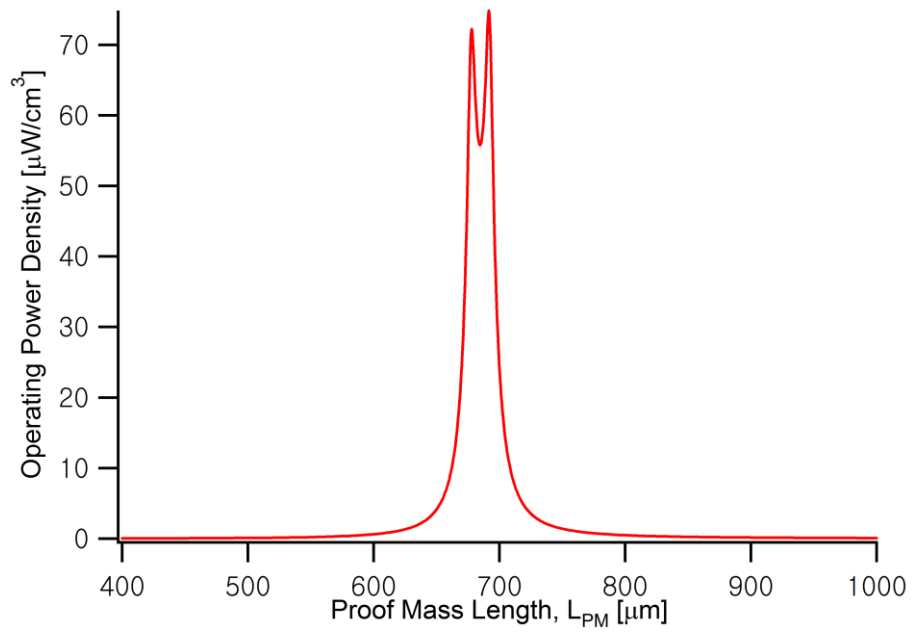


Figure 8.10 1-D plot of operating power density as a function of proof mass length (L_{PM}) when the active beam length (L) is fixed at 100 μm and P_{op} is optimized.

Chapter 9

Device Design Study: MEMS Piezoelectric Energy Harvesters with Novel Structural Layer Materials

The modeling and optimization schemes developed so far are useful in designing MEMS-PVEHs with novel structural layer materials. This chapter focuses on model-based device and processing design of power-optimized PZT/ultrananocrystalline diamond (UNCD) PVEH cantilevers.

9.1 Introduction & Motivation

For the realization of PVEHs, Si-based MEMS devices have been extensively explored due to the fact that they can be fabricated using well-established processes developed for the fabrication of microelectronic devices. However, the development of Si-based MEMS-PVEH devices has been impeded due to the challenges in precise dimension control as well as residual stress developed during fabrication [54]. Ultrananocrystalline diamond (UNCD), developed at Argonne National Laboratory (ANL), exhibits superior mechanical (*e.g.*, hardness, flexural

strength) and tribological (*e.g.*, coefficient of friction, stiction, wear) properties combined with a much smoother surface morphology (4–7 nm rms roughness as shown in Figure 9.1 (a)) [114–117]. Another advantageous aspect of UNCD is the lowest diamond deposition temperature (400 °C), compared with single crystal diamond, microcrystalline diamond, nanocrystalline diamond (NCD), and diamond-like films [117]. These properties of UNCD enable the production of reliable MEMS devices, especially for many critical technologies, such as MEMS resonators, which require high Young’s modulus, or MEMS optical switches, which require extensive surface contact among the MEMS components.

Replacement of Si with UNCD offers a way to circumvent the challenges in Si-based PVEHs. Successful integration of high-quality $\text{Pb}(\text{Zr,Ti})\text{O}_3$ (PZT) thin films on UNCD in a cantilever structure has been demonstrated at ANL, supporting the feasibility of MEMS-PVEHs based on UNCD [114–117]. PZT/UNCD cantilevers (see Figure 9.1 (b)) were fabricated and actuated at 3 V and up to 1 billion cycles without failure, demonstrating the robustness of the PZT/UNCD system as a platform for high performance MEMS devices [117]. The breakthrough came from the idea of using TiAl layer as the diffusion barrier of oxygen that would otherwise decompose the UNCD layer when depositing the PZT film at high temperature and oxygen-rich environment.

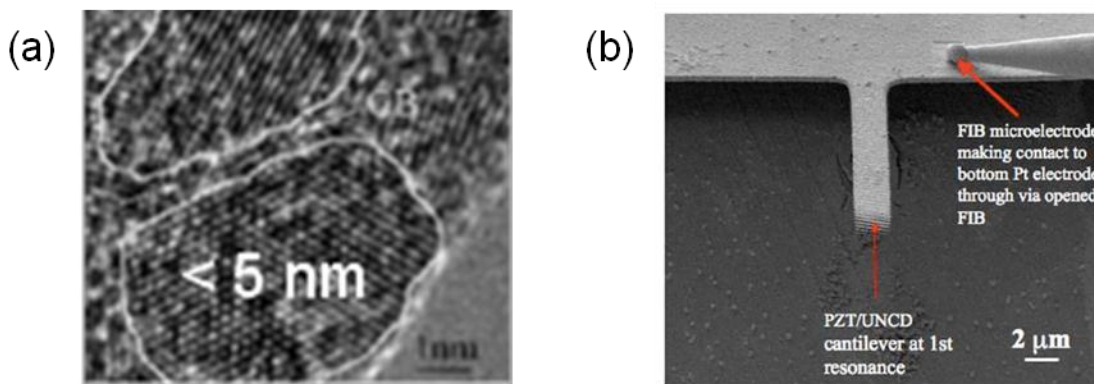


Figure 9.1 PZT/UNCD characteristics for MEMS-PVEHs: (a) TEM image of nano-size grains in UNCD, and (b) SEM image of PZT/UNCD cantilever [117].

Electromechanically coupled models developed in this thesis enable calculation of

maximum power with corresponding operating conditions, which is inversely proportional to “effective” stiffness of the system as shown in equations (2.30) and (2.31). Strong mechanical properties and achievable thin layers of the UNCD structural layer decreases the effective stiffness, resulting in higher power generation at lower system resonant frequencies, which is a key factor in realizing practical MEMS-PVEHs. Calculation results presented in Section 9.2 show that about 37 times higher power can be extracted from UNCD-based PVEH compared to the Si-based case at resonance and corresponding optimal electrical conditions, given the same material properties of PZT thin film layer, geometric dimensions of a cantilever (except for the thickness of each layer) and a proof mass, and input operating conditions. All these experimental and theoretical results strongly suggest that UNCD-based PVEHs can replace Si-based systems due to higher maximum output power of the UNCD-based PVEH and absence of fabrication issues related to Si-based processing.

9.2 Modeling and Prototype Design of Power-optimized PZT/Ultrananocrystalline Diamond (UNCD) Energy Harvesting Cantilevers

A research project has been set up to fabricate optimally-designed UNCD-based cantilevered PVEHs with a proof mass, based on the collaboration with researchers at ANL. The overall project focuses on the development of a {3-1} mode PVEH device (*i.e.*, d_{31} mode of operation) in a cantilever configuration consisting of a Pt/PZT/Pt/TiAl/UNCD multi-layer. The project is divided into four parts as outlined below.

- i) A power-optimized device is designed using the multi-variable tool based upon the model developed in this thesis, and also considering micro-fabrication constraints from previous fabrication experience.
- ii) Fabrication of hybrid PZT/UNCD-MEMS-PVEH films is performed with varying thickness of PZT (70 nm ~ 1 μ m) and UNCD (0.5 ~ 1 μ m) layers, followed by material

property evaluation.

- iii) Once the cantilever is defined and a proof mass is integrated, the PVEHs will be wired for performance characterization including atomic force microscopy (AFM) at ANL.
- iv) Comparison of the experimental results on device output to simulation results will provide significant insights into the size and geometry that are optimum for realization of efficient/reliable hybrid PZT/UNCD MEMS-PVEHs with useful power generation for sensors.

Among the tasks described above, part 1 and some of part 2 are covered in this thesis, in Sections 9.2 and 9.3, respectively.

As a preliminary work, a cantilevered PVEH device based on PZT/UNCD is modeled and compared with the Si-based PVEH device in terms of device performance such as resonant frequency and optimal power. Previously in Chapter 8, fabrication and characterization studies of Si-based, unimorph, MEMS-PVEH devices in {3-1} and {3-3} modes of operation were presented, validating the predictive capability of the model for MEMS-scale PVEHs. For comparison, the geometric dimensions including beam length, beam width, proof mass length, and PZT layer thickness of PZT/UNCD-based devices are set to be the same as the previous Si-based devices shown in Figures 8.5 and 8.6. Detailed dimensions are available in Tables 8.1-8.3. Silicon is assumed to be the proof mass material for both PZT/UNCD-based PVEH devices and Si-based PVEH devices. The piezoelectric layer, PZT, is set to have 1 μm in thickness. Relevant material properties such as density and modulus are listed in Table 9.1 as well as in Table 8.3. In the modeling, the same input operating conditions are applied to both Si- and UNCD-based energy harvester devices: mechanical damping ratio, $\zeta_m = 0.002$ ($Q = 250$) and base acceleration is 1g ($g=9.81 \text{ m/s}^2$). Previously in Figure 8.7, it is found that simulated voltage and power for MEMS Si-based PVEH devices are in good agreement with measured data when quality factor is close to 250. Base acceleration, 1g is chosen in order to consider general ambient vibration conditions, as described in Section 1.2 (refer to Table 1.1). These operating conditions can vary depending on the specific application of interest.

Table 9.1 Material properties of layers in UNCD/PZT-based MEMS energy harvester device [30, 79, 124, 125].

Layer material	Density, ρ [kg/m ³]	Modulus, E [GPa]	Poisson's ratio ν	Plate modulus [GPa]
Pt	21440	170.0	0.39	200.5
PZT (thin film)	7750	140.0	-	140.0
TiAl*	3603	93.0	0.34	140.0
UNCD	3520	980.0	0.2	1225

* As the relevant properties of TiAl are not fully known, averaged values of Ti and Al material properties are employed.

Constituent layers that comprise UNCD-based and Si-based PVEHs in the left and right columns, respectively, are given in Table 9.2. For the Si-based PVEH device, layer materials and associated thicknesses are adopted from the specifications of the actual devices fabricated by the group at Auburn University (see Section 8.2). For the UNCD-based piezoelectric cantilevers, material layers and their thicknesses are determined from the experimental data published by Auciello *et al.* at ANL [117] and also based on personal discussion with researchers at ANL.

Resonant and anti-resonant frequencies and optimal power at such resonances of both UNCD- and Si-based PVEH devices are simulated from modeling and summarized in Table 9.3. Here, as described earlier, the same material properties of PZT thin film layers, geometric dimensions of the cantilever and proof mass, and input operating conditions are used for both UNCD- and Si-based PVEH devices but with different constituent structural layers with their optimal thicknesses from fabrication perspectives. If all the counterpart layers in UNCD- and Si-based devices are assumed to have the same thicknesses (*e.g.*, UNCD and Si have the same thickness, 20.0 μm), maximum power either at resonance or anti-resonance that can be generated by UNCD-based PVEH devices would be smaller than Si-based PVEH devices due to the higher stiffness of UNCD according to equations (2.30) and (2.31). However, UNCD-based PVEHs benefit from the fact that it is possible to integrate PZT onto UNCD film with much thinner layers than Si, resulting in much lower effective (bending) stiffness of the system, and thus more power generation at much lower resonant frequencies, as shown in Table 9.3. Given the same

cantilever dimensions but with thinner layer deposition of the structural layer, PZT/UNCD based PVEH devices exhibit resonant frequencies around 3.1 Hz, a very low resonant frequency for a MEMS device. Considering the fact that heartbeat has a frequency of 1.6 Hz [126] and UNCD is a proven bio-compatible substrate [127] with its chemical inertness, UNCD-based PVEHs have considerable potential for bio-applications. Above all, maximum power that can be obtained with the prototype UNCD-based PVEH is expected to exceed 2 mW at its optimal conditions, as shown in Table 9.3 and this value meets the current power requirement of small electronics [6, 9]. The difference between optimal power values at resonance and anti-resonance occurs due to the fact that system coupling factor, κ^2 , calculated here is not large enough to satisfy the approximation condition, $2\zeta_m/\kappa^2 \ll 1$ (see equations (2.30) and (2.31)). Note that higher system coupling can be obtained than the values shown in Table 9.3 when dimensions are optimized through model-based design (see Section 8.3) in future work. As both input mechanical power, P_{in} , and harvesting efficiency, η , have dependence on system coupling factor, κ^2 , these differ in UNCD- and Si-based PVEHs (see Section 7.1.2). Efficiency of 49% is predicted for the UNCD-based PVEH both at resonance and anti-resonance while lower efficiency of 36% is expected for the Si-based PVEH at resonance and anti-resonance, as shown in Table 9.3.

Table 9.2 Layers and each thickness of PZT/UNCD based energy harvester and Si-based energy harvester in {3-1} mode of operation.

	Layer	Thickness [μm]		Layer	Thickness [μm]
PZT/UNCD based energy harvester	Pt	0.10	PZT/Si based energy harvester	Pt	0.12
	PZT	1.0		PZT	1.0
	Pt	0.10		Pt/Ti	0.12/0.01
	TiAl	0.15		SiO ₂	0.5
	UNCD	0.5		Si	20.0
	(W) ^a	(0.5~0.10)		SiO ₂	0.5
	total	2.35~2.85		total	22.3

^a Tungsten (W) layer is often needed as a seeding layer to deposit UNCD.

Table 9.3 Predicted results of device performance for the PZT/UNCD and Si-based energy harvesters.

Device performance	UNCD-based PVEH	PZT/Si-based PVEH
Resonant frequency	3.1 Hz	121.3 Hz
Anti-resonant frequency	3.1 Hz	121.6 Hz
Optimal power & corresponding voltage at resonance	2,074 μ W & 11.7 V at 65.9 k Ω	56.4 μ W & 0.5 V at 5.1 k Ω
Optimal power & corresponding voltage at anti-resonance	2,051 μ W & 55.9 V at 1.5 M Ω	27.8 μ W & 0.8V at 13.2 k Ω
System coupling factor, κ^2	0.019	0.005
$2\zeta_m/\kappa^2$	0.2	0.8
Efficiency, η [%]	49 %	36 %

9.3 Processing Design of Piezoelectric MEMS Energy Harvesters based on Piezoelectric/Ultrananocrystalline Diamond Thin Film Heterostructures

The model enables one to design power-optimized PZT/UNCD-based MEMS-PVEH devices, considering targeted application environment and microfabrication factors. This can provide various sets of optimal dimensions for a cantilever and a proof mass depending on objective function and target application, which will be reflected during the mask fabrication for lithography. Fabrication process will begin with the growth of UNCD films on Si substrates (5~10 wafers) using the extensive database existing at the Center for Nanoscale Materials (CNM) at ANL, to produce UNCD layers with optimum performance for the proposed MEMS-PVEHs. Then, TiAl or TaAl layers, oxygen diffusion barriers for efficient integration of oxide PZT films with carbon-based UNCD layers, without etching the UNCD layer, will be deposited using the magnetron sputter-deposition system. In order to have a capacitor-type device, growth of Pt or SrRuO₃ (SRO) bottom and top electrode layers sandwiching the PZT layer will be

performed using the magnetron system. A PZT layer (70 nm ~ 1 μ m thick) will be integrated on top of the bottom electrode/TiAl or TaAl/UNCD layers, providing an electroded piezoelectric structure (Pt or SRO/PZT/Pt or SRO). Several processing techniques have been explored to deposit PZT thin films of good quality: sol-gel processing, metal-organic chemical vapor deposition (MOCVD), and sputter deposition. A proof mass will be added to the structure either by depositing an additional layer on the top electrode and patterned by optical lithography or using part of the silicon substrate via a backside reactive ion etching process. After optimizing the deposition processes for Pt/PZT/Pt/TiAl/UNCD layers, the film stacks will be etched, using optical lithography and reactive ion etching (RIE), to define the shape of the cantilevers and form the metal pads that connect to the top and bottom electrode layers. We will release the cantilevers with or without proof mass using deep RIE process. Etching processes will be developed to create a dry etch process to selectively etch layers against other layers. Additionally, wet etches will be required for the removal of layers and resists. Dry plasma etching processes will be performed to remove resists as well. After these steps are performed, there will be several iterations to further optimize the film stacks, the MEMS-PVEH geometry and dimensions, layouts and the processing steps to fabricate the MEMS-PVEHs. Output behavior of fabricated MEMS-PVEHs based on UNCD will be evaluated using the test setups based on atomic force microscopy (AFM) and/or laser vibrometry. Full characterization of the MEMS-PVEH devices will be conducted with help of the model from this thesis (see Chapter 7). Extensive analysis on the correlation of experimental data and modeling results will help to improve both model and fabrication parameters for better PVEH performance.

Overall, this chapter shows how the developed model and model-based design process can be integrated into the current research project and make contributions by bridging the existing state-of-the-art technology (*e.g.*, UNCD thin film growth and PZT/UNCD integration with good quality) and targeted applications (*e.g.*, PVEHs, here). Such a systematic approach based on modeling, fabrication and characterization will accelerate the development of MEMS-PVEHs based on PZT/UNCD thin film heterostructures for practical applications such as bio-sensors.

Chapter 10

Application of Electromechanical Modeling to Other Systems

So far, the focus of this thesis has been put on model development, experimental verification of the developed model, and various useful applications of the model for PVEH systems. In this chapter, a broader application of the developed electromechanical model to other systems such as piezoelectric actuators (Section 10.1) and MEMS resonators based on electrostatically-driven actuation (Section 10.2) is presented.

10.1 Modeling of Piezoelectric Actuator System

When subject to mechanical strain, electrical field is induced in piezoelectric materials, offering a basis for PVEHs. The reverse effect also exists that piezoelectric materials deform when an electrical field is applied across them. These aspects of piezoelectric materials make them attractive and well suited as actuators. PVEHs and piezoelectric actuators are both electromechanically coupled systems through the piezoelectric effect. Their difference lies in the input source: PVEHs are mechanically excited to generate electricity whereas controlled voltage is applied as input to drive piezoelectric actuators mechanically. Two governing equations were derived for PVEHs in Chapter 2 and scalar versions of those equations are repeated in equations

(10.1) and (10.2) for convenience. Equation (10.1) is an actuator equation that represents the mechanical domain of the PVEH system. In contrast, equation (10.2) is a sensor equation that represents the electrical domain of the same system. The actuator equation is typically used to analyze structural dynamics of the piezoelectric system while the sensor equation is used to find the voltage appearing due to the piezoelectric when the structure is deformed. These two equations are coupled through the electromechanical coupling term, θ :

$$M\ddot{r} + C\dot{r} + Kr - \theta v = -B_f \ddot{w}_B \quad (10.1)$$

$$\theta \dot{r} + C_p \dot{v} + \frac{1}{R_l} v = 0 \quad (10.2)$$

The input source of PVEHs is mechanical excitation at the base and this is expressed by the absolute base displacement, $w_B(t)$, or base acceleration, \ddot{w}_B , as shown in the right-hand side of equation (10.1). The output device responses include absolute mechanical displacement (w) and electrical performance such as voltage (v) and power (P_{out}), and their analytical expressions were obtained by solving the two above governing equations, as written in equations (2.24)-(2.26).

The governing equation derived for PVEHs also enables derivation of the equation of motion for a piezoelectric actuator driven by a voltage source. For piezoelectric actuators, controlled voltage, $v = v(t)$, is input and the base displacement is zero ($w_B = 0$) because no mechanical input exists. Thus, the governing equation of motion for voltage-driven piezoelectric actuators can be written as follows:

$$M\ddot{r} + C\dot{r} + Kr = \theta v \quad (10.3)$$

When compared with equation (10.1) for PVEHs where mechanical input is expressed in the right-hand side of the equation as $-B_f \ddot{w}_B$, the input voltage at the electrodes of piezoelectric actuators is described by the term θv in the right-hand side of equation (10.3). Voltage, v , is a function of time as $v = v(t)$ and consists of both direct-current (DC) voltage ($v_{dc} = v_0$) and

alternative-current (AC) voltage (v_{ac}) in equation (10.4):

$$v = v_{dc} + v_{ac} = v_0 + v e^{j\omega t} \quad (10.4)$$

The output device response of a piezoelectric actuator system is mechanical displacement and this can be obtained by the analytical expressions of relative displacement, r , or absolute displacement, w . It should be noted that the DC voltage determines static zero position (r_{static}) while AC voltage gives the oscillating displacement ($r_{dynamic}$) as in a PVEH system. The detailed resulting expression for the relative displacement, r , is the summation of r_{static} and $r_{dynamic}$ as written in equation (10.5):

$$r = r_{static} + r_{dynamic} \quad (10.5)$$

where $r_{static} = \frac{\theta}{K} v_0$, $r_{dynamic}$ is as in as equation (2.24). It is quite beneficial that all the key parameters such as mass (M), stiffness (K), and electromechanical coupling (θ) in the governing equation in (10.3) for piezoelectric actuators, particularly cantilevered systems, can be easily calculated using the same expressions derived for PVEHs in earlier chapters. Furthermore, the detailed proof mass analyses (Chapters 3, 4, and 5) that were performed on the energy harvester system is also applicable to the actuator system.

10.2 Design of High-Frequency Si-based MEMS Resonators

This section contains a description of design and fabrication of high-frequency (> MHz) Si-based MEMS resonators useful in electronic devices for clocking operations. Such a technology could replace current quartz-based bulk resonators with an on-chip MEMS element to go alongside other circuitry and functions. There is commercial activity towards this end, notably technology being commercialized by a company called SiTime and others. There still exist potential challenges in fatigue for silicon beams during resonating operation. Thus, in this work, cantilevered silicon resonators driven by electrostatic actuation are modeled, and

consideration of the simulation results and fabrication factors results in the design of optimized low-strain fatigue-resistant MEMS resonators.

A closed-form design of capacitively-driven (low-voltage, very advantageous) Si resonators with very low strain levels, and methods of MEMS fabrication, are described next. It may be possible to use solely complementary metal-semiconductor-oxide (CMOS) processing, but this has not been explored. Furthermore, a proof mass analysis allows simple (from a fabrication perspective) tuning of natural frequency, as well as allows design of high-strain Si test devices to explore fatigue properties of the Si-based resonators as future work. As MEMS resonators here are based on micro-scale beams, electrostatic actuation, and mechanical vibration, this work is another application of an electromechanically coupled beam model developed earlier in this thesis but without a piezoelectric element.

10.2.1 Device Design Considerations

Single crystal silicon (SCS) is chosen for the MEMS resonator material. Quartz is currently the most widely used resonator material. However, their relatively bulky size limits the possibilities for reduction in circuit volume and requires high manufacturing cost. Silicon-based MEMS resonators are attractive alternatives to replace quartz-based resonators for several reasons. Silicon not only has potential for reduced size, cost and power consumption but also is advantageous in terms of integration with circuitry on the same wafer. In modeling, 129.5 GPa is adopted for the Young's modulus of SCS with crystal orientation [100] while 2320 kg/m³ is used as the density of SCS, ρ_{Si} , from [58].

SCS-based resonators optimized for mega-hertz (MHz) operating frequencies are the main target application. Conservative analysis demonstrates that a 25 MHz-device is achievable and 10 MHz-device is very easy to obtain. Thus, two different frequencies, 25 MHz as a desirable target and 10 MHz, are considered. It should be noted that higher-order coupled beam models can expand the design space significantly although this work focuses on the fundamental mode of beam vibrations only. The driving force to operate Si-based MEMS resonators considered here is the electrostatically-driven (or in-plane) mode using electrostatic actuation. Electrostatic parallel-plate actuators are a common way of actuating micromechanical systems [122]. More

details on parallel-plate electrostatic actuation are discussed in the following section.

In terms of geometry, both singly-clamped beams (cantilever) and doubly-clamped beams are of interest and these are illustrated in Figure 10.1 with defined dimension parameters. A cantilever beam structure is chosen for its simplicity in analysis and geometric compatibility with MEMS fabrication processes. Doubly-clamped beams are advantageous in terms of reaching higher natural frequencies [69]. Preliminary simulation results also demonstrate that given the same dimension, it is much easier to obtain high aspect ratio ($b, h \ll L$) with doubly-clamped beams than with singly-clamped beams. L is the length of the beam while b, h are thickness and width of the beam, respectively, as indicated in Figure 10.1. (Note that the notations follow the conventions in vibration engineering. *E.g.*, the dimension in the vibration direction is denoted as h .) In terms of pull-in voltage, *i.e.* the maximum voltage that can be applied to the system, doubly-clamped beams permit 8 times larger pull-in voltages than singly-clamped beams, thus providing a broader range of operation. From a perspective of stiffness, according to simple beam theory, doubly-clamped beams are expected to have 64 times higher stiffness than the singly-clamped beams (linear bending comparison only). As each structure has its own advantages, both singly- and doubly-clamped beams are considered.

The following are desirable conditions for geometric dimensions of considered beams:

- ◆ $L \gg h, b$
- ◆ $L > 10h$ (high-aspect ratio)
- ◆ $b > h$ ($h \sim 1/2 b$, or $2/3 b$)

Considering the limitation in the resolution of lithography, $1 \mu\text{m}$ or larger is a good value for the initial gap size, g_0 , between the electrodes and the beams. To satisfy the assumption of parallel-plate capacitor and point-loading condition in the analysis presented in Section 10.2.2, the beam is required to be much longer (L : beam length) than the length of the electrode, c , such that $L \gg c$.

For the realization of practical applications, 5 V or less would be desirable as an applied voltage, v_{app} . In addition, v_{app} should satisfy the condition that $v_{min} < v_{app} < v_{pi}$ where v_{min} is the minimum voltage required to initiate the beam vibration and v_{pi} is the pull-in voltage at which

the beam would deviate from the stable range and might stick to the electrode. In order to prevent stiction or pull-in, beam deflection should not exceed the gap for pull-in condition at anytime during operation, which is $1/3 g_0$ (static) or $1/2 g_0$ (dynamic) where g_0 is the initial gap size between the beam and the electrodes at rest. All the factors described above are considered in device design of optimal Si-based MEMS resonators and presented in Sections 10.2.2-10.2.4.

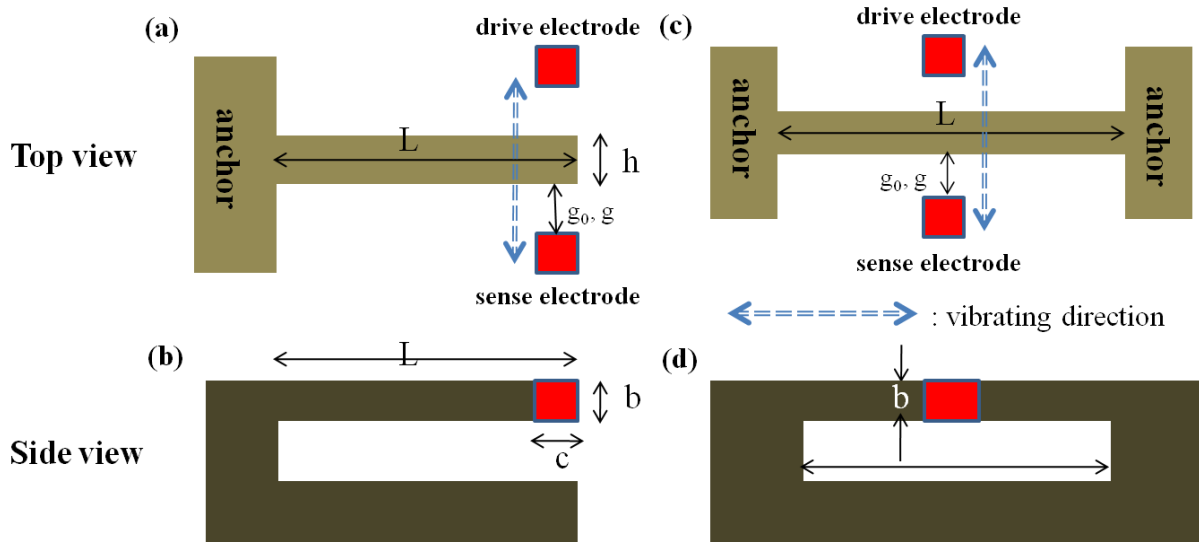


Figure 10.1 Schematics of beam resonators driven by electrostatic actuation with indication of dimensions, drive and sense electrodes, and the vibration direction: (a) top-view of singly-clamped beam, (b) side-view of singly-clamped beam, (c) top-view of doubly-clamped beam, and (d) side-view of doubly-clamped beam.

10.2.2 Modeling of Electrostatically-driven Beam Resonators

Modeling of beam resonators driven by parallel-plate electrostatic actuation benefits from the understanding of a one-dimensional damped, force oscillation model represented by a mass-spring-damper, simple beam theory [69], and the principle of parallel-plate electrostatic actuation. The schematic of a basic electrostatic actuator illustrated in Figure 10.2 (a) is useful to understand the concept of a voltage-controlled parallel-plate capacitor with one movable plate. It is convenient to define the capacitor as having plate area, A_{el} , and a gap, g . When the plates are

charged, a charge $+Q$ is generated on one plate and $-Q$ on the other plate and because of the opposite charges on the two plates, there is a force of attraction between the plates (electrostatic force). Addition of a spring between the moveable plate and a fixed support creates an upward force on the moveable plate if the plate moves down from its rest position (*i.e.*, $z = 0$ or $g = g_0$ in Figure 10.2 (a)). The net force exerted on the moveable plate is thus the summation of electrostatic force and spring force, each in opposite directions.

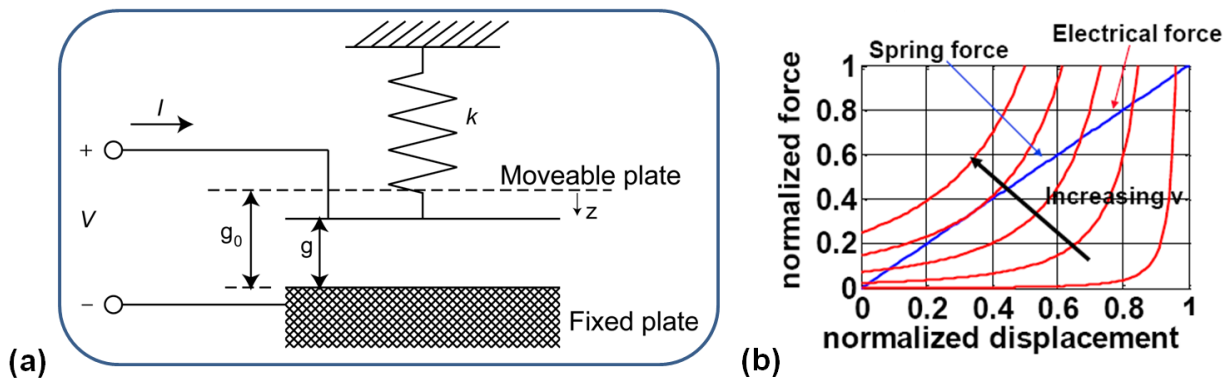


Figure 10.2 A parallel-plate electrostatic actuator: (a) schematic of the basic electrostatic actuator with the moveable plate attached to a spring, and (b) electrical (electrostatic) force and spring forces for voltage controlled parallel-plate electrostatic actuators [121].

The characteristic of the spring requires that the displacement of the end of the spring, z , be given by Hooke's law:

$$F_{spring} = kz \quad (10.6)$$

where F_{spring} indicates spring force while k and z represent stiffness of the spring and displacement of the end of the spring, respectively. Electrostatic force, $F_{electrostatic}$, is determined by the voltage, which stretches the spring, thus determining the change in gap:

$$F_{electrostatic} = \frac{\epsilon A_{el} v_{app}^2}{2g^2} \quad (10.7)$$

where g denotes the distance between the plates when moving and ε is the permittivity of the material between the gap, presumed to be air, thus, $\varepsilon \sim \varepsilon_0$, the permittivity of free space. Then, at equilibrium, setting $F_{spring} = F_{electrostatic}$ and introducing the relation, $g = g_0 - z$, into equation (10.6), enables determination of the change in gap:

$$g = g_0 - \frac{\varepsilon A_{el} v_{app}^2}{2kg^2} \quad (10.8)$$

It should be noted that the decrease in gap, g , is an increase in the length of the spring, z . Net force, F_{net} , on the upper plate at voltage, v_{app} , and gap, g , can be expressed as:

$$F_{net} = \frac{-\varepsilon A_{el} v_{app}^2}{2g^2} + k(g_0 - g) \quad (10.9)$$

The voltage-controlled parallel-plate electrostatic actuator exhibits an important behavior called *pull-in*. In Figure 10.2 (b), both spring force and electrical (electrostatic) force are plotted across the normalized displacement, z/g_0 . As one increases the voltage, the gap decreases, with the amount of decrease growing as the gap gets smaller. At some critical voltage, the system becomes unstable, and the gap collapses to zero. This phenomenon is called pull-in or snap-down. At a point of equilibrium, $F_{net} = 0$, such that the plots of spring force and electrical force intersect in Figure 10.2 (b) and equilibrium exists between the electrostatic force pulling plate down and the spring force pulling the spring up. In other words, pull-in voltage is the specific voltage at which the stability of the equilibrium is lost, thus determining the travel range of the moveable plate. It is thus important to pay attention to the pull-in condition (*i.e.*, the gap distance and the voltage at pull-in) in device design so that the designed beam device can actuate without collapsing to the electrodes.

In the design shown in Figure 10.1, the beams act as moveable plates while the electrodes play the role of the fixed plate when compared with the basic electrostatic actuator illustrated in Figure 10.2 (a). Here, it is assumed that the beam deflection has negligible curvature over the

area of the electrodes. In combination with simple beam theory and one-dimensional, damped, forced oscillation for the beam structures, the analytical expressions for the parallel-plate electrostatic actuator described above permit calculation of the displacement, z , at a given voltage and the gap size and the voltage at pull-in, g_{pi} and v_{pi} , respectively.

In static cases [121], displacement, z , can be obtained by solving the cubic equation (10.8) for the gap size, g , since $z = g_0 - g$, once the input voltage, $v_{app} = v_{dc} = 5V$, is known. It can be

easily shown that static pull-in occurs at $g_{pi} = \frac{2}{3} g_0$ and $v_{pi} = \sqrt{\frac{8kg_0^3}{27\epsilon A_{el}}}$.

In the dynamic case [69, 122], it is convenient to regard the beam actuator as a classical mass-spring-damper system that undergoes damped, forced oscillation. Then, derivation of the following expression to represent the dynamics of the electrostatically-driven beam actuators is possible:

$$M\ddot{z} + C\dot{z} + kz = \frac{\epsilon A_{el} v_{app}^2}{2(g_0 - z)^2} \quad (10.10)$$

where the actuation voltage is $v_{app}(t) = v_{ac}(t) + v_{dc}$ and M , C , and k represent mass, damping constant, and the stiffness of the beam, respectively. Solving for z in equation (10.10) at the given actuation voltage for a given mechanical system results in not only the displacement, z , but also the gap size, g . Fargas-Marques *et al.* derived the dynamic pull-in condition in [122] and the analytical expressions for the gap size, g_{dpi} , and voltage at dynamic pull-in, v_{dpi} , are adopted here:

$$g_{dpi} = \frac{1}{2} g_0 \quad (10.11)$$

$$v_{dpi} = \sqrt{\frac{1}{4} \frac{kg_0^3}{\epsilon A_{el}}} \quad (10.12)$$

Compared with the static case, dynamic pull-in allows longer travel range of the moveable

plate but smaller range for applied voltage. In the above, calculation of the stiffness for a given beam structure is required for modeling of the system. Based on the point-loading condition in simple beam theory [69], it is possible to analytically express the stiffnesses of a singly-clamped beam under tip-loading, and doubly-clamped beam at middle-loaded conditions:

$$k_{\text{singly-clamped}} = \frac{Ehb^3}{4L^3} \quad (10.13)$$

$$k_{\text{doubly-clamped}} = \frac{16Ehb^3}{L^3} \quad (10.14)$$

where E , h , b , and L are Young's modulus (of Si, here), thickness of the beam, width of the beam, and length of the beam, respectively. Lastly, in order to find desirable geometric dimensions of the beams that have natural frequencies coinciding with targeted frequencies, it is necessary to know the relation between the properties of the beam and its resonant frequencies. From the governing equation for bending vibration of a beam in equation (10.15), one can derive the resonant frequency for free vibrations of the beam [69]:

$$m \frac{\partial^2 w(x,t)}{\partial t^2} + \frac{\partial^2}{\partial x^2} [EI(x) \frac{\partial^2 w(x,t)}{\partial x^2}] = f(x,t) \quad (10.15)$$

where m is beam mass per length and $w(x,t)$ is beam deflection as a function of position (x) and time (t). E represents Young's modulus and $I(x)$ is cross-sectional area moment of inertia while $f(x,t)$ indicates external force. The first mode resonant frequencies for a singly-clamped beam and a doubly-clamped beam are described in equations (10.16) and (10.17), respectively:

$$f_1 = \frac{1}{2\pi} (1.875)^2 \frac{h}{L^2} \sqrt{\frac{E}{12\rho}} \quad (\text{Singly-clamped beam}) \quad (10.16)$$

$$f_1 = \frac{1}{2\pi} (4.730)^2 \frac{h}{L^2} \sqrt{\frac{E}{12\rho}} \quad (\text{Doubly-clamped beam}) \quad (10.17)$$

In order to validate the analytical expressions for the in-plane capacitive resonators presented above, experimental results reported by No *et al.* in the literature [123] are employed. Figure 10.3 contains the illustration of doubly-clamped beam resonators made of SCS in (a) and also the obtained experimental data of resonant frequency vs. voltage with the beam dimensions in (b). In their analysis, resonant frequency, f_1 , with a value of 505 kHz is obtained experimentally and the pull-in voltage is computed as 56 V for the fabricated doubly-clamped beam resonators driven by electrostatic actuation. Using the expression in equation (10.17), our own results provide the value of 555 kHz for the resonant frequency of the same structure and a calculated pull-in voltage of 64.8 V using equations (10.12), (10.14) and (10.17). Comparison of the values obtained in [123] and here suggests that they have a reasonable correspondence in terms of orders of magnitude, particularly for the resonant frequency and the pull-in condition.

10.2.3 Results of Model-based Device Design for Si MEMS Resonators

The first step in designing high frequency Si MEMS resonators is to determine the geometric dimensions, which not only correspond to the targeted frequencies, 10 and 25 MHz, but are also within a reasonable range in terms of fabrication. With this in mind, sets of length (L) and width (h) are drawn at given values of frequencies, 10 and 25 MHz, in the plot of Figure 10.4 using equations (10.16) and (10.17). Then, the range which satisfies high-aspect ratio ($h \ll L$) is identified as shown in Figure 10.4 using arrows. Within this range, the sets of dimensions for both singly- and doubly-clamped beam resonators (*i.e.* length, width, and thickness), are selected considering fabrication-wise favorable values (see Table 10.1). Considering the fabrication factors again, the initial gap size, which is the distance between the beam and the electrodes, is set to be 1 μ m and the length of the electrode, c , is set to be 1 μ m. Device design with reasonable dimensions based upon simulation results and fabrication-level constraints demonstrates that the development of high-performance silicon-based MEMS resonators is

possible.

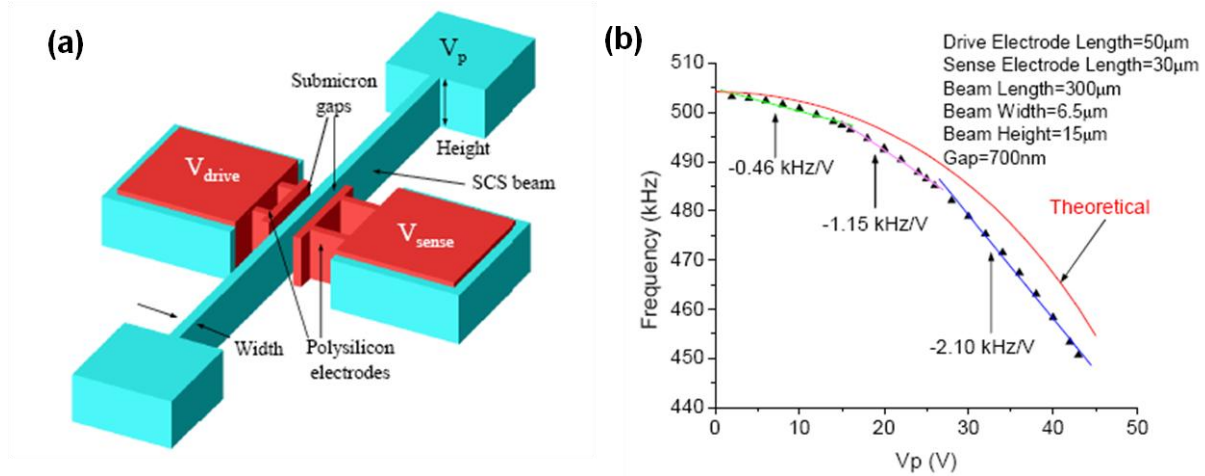


Figure 10.3 Schematic and measured data for a single-crystal silicon capacitive resonator from [123]: (a) doubly-clamped beam single crystal silicon resonator and (b) plot of the resonance frequency vs. polarization voltage for a 300µm long, 6.5µm wide beam resonator.

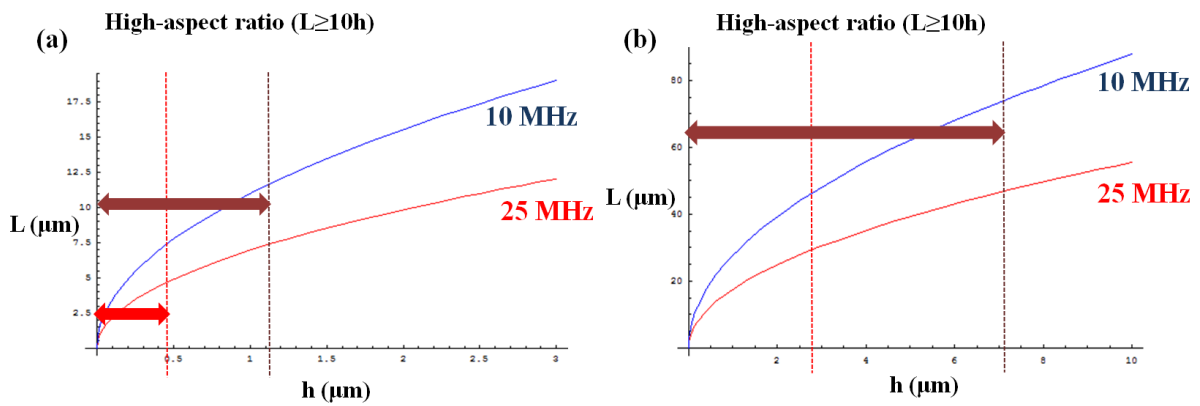


Figure 10.4 Model-derived design space for (a) singly-clamped beam resonators and (b) doubly-clamped beam resonators. Both are targeted to operate at 10 MHz and 25 MHz.

Table 10.1 Beam dimensions for the fabrication of high-frequency Si beam resonators.

	Resonant frequency, f_i	h [μm]	L [μm]	$b (= 2h)$ [μm]	Aspect ratio, L/h
Singly-clamped	25 MHz	2.0	10	4.0	4.9
Singly-clamped	10 MHz	2.0	15	4.0	7.5
Doubly-clamped	25 MHz	2.0	24	4.0	12.0
Doubly-clamped	10 MHz	2.0	38	4.0	18.9

For the given dimensions of four different beam resonators in Table 10.1, prediction of key parameters such as stiffness, k , pull-in voltage, v_{pi} , and maximum static deflection, z_{max} , is possible by using equations (10.6)~(10.14) and the calculated results are listed in Table 10.2. As discussed earlier, the input actuation voltage, v_{app} is set to be 5V as a desirable value in operation and this is much lower than the pull-in voltage listed in Table 10.2. Predicted maximum static deflection, z_{max} , is also much smaller than the deflection at pull-in, z_{pi} , for the given device dimensions and thus, ensures conservative device design of Si beam resonators driven by electrostatic actuation. Maximum dynamic deflections of a singly-clamped, 10 MHz device are also computed at various damping conditions by varying the value of quality factor, Q . As seen in Table 10.3, even for the dynamic case with very high Q values, maximum amplitudes do not exceed the pull-in limit, satisfying the design requirements.

Table 10.2 Predicted key parameters from modeling of singly-clamped, 25 MHz (S. 25 MHz), singly-clamped, 10 MHz (S. 10 MHz), doubly-clamped, 25 MHz (D. 25 MHz), doubly-clamped, 10 MHz (D. 10 MHz) beam resonators.

	Stiffness, k [N/m]	v_{pi} (static) [V]	Static deflection, z_{max} [\AA]	z_{pi} (static) [μm]
S. 25 MHz	1090	3030	0.00404	0.5
S. 10 MHz	309	1610	0.0143	0.5
D. 25 MHz	4860	6380	0.000911	0.5
D. 10 MHz	1230	3210	0.00360	0.5

Expected values for maximum stresses and strains are calculated and indicated in Table 10.4. Considering the typical values of 300MPa (0.3 GPa) or larger and 2000 μ ~4000 μ -strain as applied stresses and strains for dynamic fatigue of SCS, the designed beam resonator devices here are predicted to have extremely low stress and strain according to the simulation results. Therefore, the design presented here will provide low-strain fatigue-resistant MEMS resonators.

Table 10.3 Maximum dynamic deflection and dynamic pull-in conditions of a singly-clamped, 10 MHz beam at various damping conditions.

Quality factor, Q	Damping ratio, ζ_m	Maximum dynamic deflection, z_{max} [\AA]	z_{dpi} (dynamic) [μm]
27.8	0.018	0.397	0.67
100	0.005	1.43	0.67
500	0.001	7.15	0.67
1000	0.005	14.3	0.67

Table 10.4 Maximum stress and strain at quality factor, $Q = 1000$.

Device	Maximum stress at the clamping [MPa]	Maximum strain at the clamping [μ -strain]
S. 25 MHz	1.91	14.7
S. 10 MHz	6.77	52.1
D. 25 MHz	3.45	26.6
D. 10 MHz	13.6	104

10.2.4 Proposed MEMS Fabrication Sequence for Si Resonators

The proposed fabrication scheme for the designed MEMS-scale SCS beam resonators is described below. Use of silicon-on-insulator (SOI) wafers as substrates is recommended for accurate dimension control and the fabrication scheme presented below is based on SOI wafers. The total number of masks required for the entire process is three. Figure 10.5 includes a graphical illustration of the process steps, which is associated with the description of the process

below. One thing to note here is that the description of the proposed fabrication scheme below is based on the facilities available at the Microsystems Technology Laboratories (MTL) at MIT but that the scheme itself can be implemented by replacing the listed facilities by the equivalent facilities available elsewhere and is therefore *not* optimized.

1. Begin with clean out of box 4" SOI wafers.
2. Lithography for deep reactive ion etching (DRIE) (Mask 1)
 - A. Coat resist NR7 (TRL coater)
 - B. Pre-bake
 - C. Expose (EV1)
 - D. Develop (TRL photo-wet)
2. DRIE to define beam geometry (TRL STS1)
3. Remove the residual photoresist (TRL Asher)
4. Clean the residual photoresist with piranha (TRL)
5. Pt electrodes lithography for Lift-off (Mask 2)
 - A. Coat resist AZ5214 (TRL coater)
 - B. Expose (EV1)
 - C. Pre-bake
 - D. Second expose (EV1)
 - E. Develop (TRL photo-wet)
6. Pt (top) /Ti (bottom) deposition (TRL E-beamAu)
7. Lift-off of photoresist with acetone soak
8. Lithography for wet-etch (Mask 3)
 - A. Coat resist AZ4620 (TRL coater)
 - B. Pre-bake
 - C. Expose (EV1)
 - D. Develop (TRL photo-wet)
9. Die-saw and package (ICL diesaw)
10. Lift-off of photoresist with acetone soak
11. Wet-Etch (dilute HF) to release cantilever beam

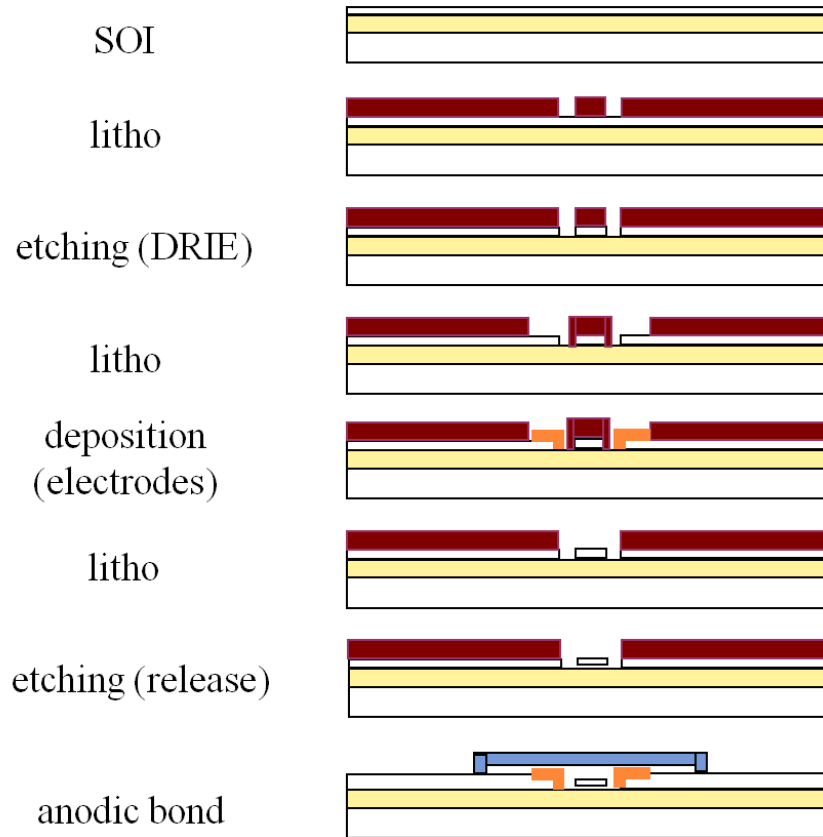


Figure 10.5 Fabrication process for silicon beam resonators – side view.

In summary, throughout this chapter, a closed-form design of capacitively-driven Si resonators with very low strain levels consistent with MEMS fabrication is discussed. Together with the model developed for electrostatically-driven resonators, a detailed proof mass analysis presented in earlier chapters permits not only the tuning of natural frequency of these resonator devices but also design of fatigue test devices for high-strain singly-crystal silicon thin films as future work. The fabrication process proposed here is also applicable to the fabrication of high-strain Si fatigue test devices that are based on parallel-plate electrostatic actuation.

Chapter 11

Conclusions and Recommendations

Throughout this thesis, a verified electromechanically coupled model is developed, including incorporating the detailed proof mass effects and different electrode configurations, to predict the output performance of PVEHs. Then, the model is utilized to guide design of both optimum piezoelectric materials and energy harvesting devices, followed by a device design exercise for a MEMS-PVEH with novel structural layers. Overall, this thesis contributes not only to providing an optimal device design scheme for power improvement along with optimum operating conditions, but also to a better understanding of PVEH performance at both materials- and systems-levels.

11.1 Contributions of This Work

1. Significance of an appropriate treatment of the proof mass in PVEH device design for enhanced power generation is highlighted by modeling detailed proof mass effects on PVEH performance at three different levels of accuracy: simple approximation for concentrated proof mass, improved treatment of rigid proof mass with rotation, and exact treatment of flexible proof mass using a two-beam method. Even a small change in proof mass geometry results in a substantial change in device performance due not only

to the frequency shift, but also to the effect on the piezoelectric layer strain distribution along the device length.

2. A developed model for a piezoelectric cantilever with and without a proof mass is experimentally verified by analyzing the experimental results from a detailed test matrix that captures both mechanical and electrical performance of macroscopic PVEH devices at various operating conditions, not only demonstrating the conservative predictive capability of the model, but also providing benchmark data to verify other modeling efforts.
3. Mechanical behavior of a micro-scale single crystal silicon cantilever with a distributed, flexible proof mass is thoroughly investigated not only to verify the newly-developed flexible proof mass model, but also to study proof mass effects on the performance of MEMS-PVEHs. Newly designed experiments are performed at Argonne National Laboratory that include fabrication of novel MEMS-scale cantilevers with proof masses of various lengths using focused ion beam milling, and testing of these MEMS-scale cantilevers using atomic force microscopy.
4. The effects of piezoelectric materials properties on PVEH device performance by model-based sensitivity analysis are studied, which provides insight into design and selection of optimal piezoelectric materials in terms of power generation. An intriguing finding is that the piezoelectric constant dominates harvester power at off-resonance as widely noted, but that an optimal value (not maximizing piezoelectric coupling) exists for power at the resonances. Two important design considerations are suggested: i) higher piezoelectric coupling doesn't necessarily yield increased power and/or voltage, and ii) materials with relatively low piezoelectric coupling constants can generate the same maximum power by tuning electrical impedance.
5. As another way to utilize the model, key performance metrics for PVEHs are standardized to provide needed figures of merit and to enable full characterization of

PVEH performance. Estimation of materials and useful system parameters using model-based bottom-up and top-down approaches is introduced. This also enables analysis of PVEH system behavior under various operating conditions and prediction of engineering limits in device performance, which is essential for realizing power-optimized PVEH devices.

6. Detailed analytical models for different electrode configurations in PVEHs are developed: standard capacitor type electrodes for {3-1} mode of operation and interdigitated electrodes (IDTEs) for {3-3} mode of operation. Expressions that describe the coupling term (θ_p) and capacitance (C_p) for both electrode configurations are presented in detail. Direct substitution of these expressions into the governing equations for PVEH devices enables modeling and comparison of cantilevered PVEH devices in {3-1} and {3-3} modes of operation. In particular, the refined model for the cantilevered PVEHs with IDTEs in this thesis allows one to consider the detailed effect of electrode dimensions (*e.g.*, spacing) on device performance.
7. The model is also implemented and compared with the experimental test results of a MEMS-PVEH device fabricated by collaborators in order to evaluate the validity of the model experimentally. Model-experiment comparison shows that trends of electrical behavior are well predicted regardless of quality factors. In terms of magnitudes, simulated voltage and power match well with the experimental results when the quality factor, Q , is close to 250 for the MEMS-PVEH in {3-1} mode. Predicted results of power at various damping conditions reveal that the values of maximum power and corresponding electrical resistances vary depending on the magnitudes of quality factor, implying the significance of quantifying the operating environment, especially, damping conditions of the MEMS-scale system.
8. A multi-variable design tool for performance-optimized PVEHs is developed and implemented for prototype MEMS cantilevered devices with IDTEs that can be integrated in wireless structural health monitoring sensor applications for aircraft. Optimization results give very different optimum device configurations when the

objective function (output power, power per mass, power per static or operating volume, etc.) is changed.

9. The model-based optimization studies are then applied to novel structural layer materials (heterostructure piezoelectric/ultrananocrystalline diamond, UNCD, thin films) to design MEMS-PVEHs that will be fabricated and characterized at Argonne National Laboratory (ANL).
10. The models are modified and used to design low-strain fatigue-resistant MEMS resonators (*e.g.*, device dimension, fabrication scheme, and detailed mask design) by expanding the electromechanically coupled modeling for high frequency Si-based electrostatically-driven MEMS resonators.

11.2 Recommendations for Future Work

1. Model-derived piezoelectric materials design guidelines described in Chapter 6 will be applied to fabricated MEMS-PVEHs with various piezoelectric materials including non-ferroelectric materials such as ZnO, AlN, or ferroelectric polymers including poly(vinylidene fluoride) (PVDF) or poly(vinylidene-trifluoroethylene) (P(VDF-TrFE)). The non-intuitive and notable findings described in Chapter 6 that maximum power at optimal conditions are independent of piezoelectric coupling constant imply that piezoelectric materials having relatively low piezoelectric coupling constants can generate sufficient power, exhibiting a considerable potential use for practical applications. In particular, ferroelectric polymers benefit from low-cost fabrication, light weight, flexibility, and low-voltage operation, but have not been explored significantly due to their relatively low piezoelectric coupling constants. Based on the model-derived guidelines, use of ferroelectric polymers in PVEH devices with enhanced power is possible by finding the optimal electrical loading resistance that allows generation of optimal power for a given device.
2. The effect of proof mass and beam geometry on damping will be analyzed, followed by

the study of damping effects on PVEH device performance. The analytical model developed in this thesis in combination with the experimental data of displacement that was already obtained during AFM characterization of MEMS-scale Si cantilevers (see Chapter 5) will provide the basis for this damping analysis.

3. The experimental data of displacement measured during AFM characterization of MEMS-scale Si cantilevers will also be used to experimentally verify the mode shape models as an extended work of Chapter 5.
4. In Chapter 8, analytical modeling for a {3-3} mode PVEH device is presented. This model incorporates not only the structural dynamics of the given cantilevered structure but also the characteristics of IDTE configurations. Due to insufficient experimental data, the model has not yet been experimentally verified especially in MEMS-scale systems. With continuous collaboration with Prof. Dong-Joo Kim's group at Auburn University, model-experiment comparison studies on {3-3} mode devices will be undertaken. Also, a parametric study will be performed to investigate the effect of IDTE geometric dimensions on power performance of PVEH devices.
5. An ongoing work includes modeling and fabrication of MEMS-PVEHs based on heterostructure piezoelectric/UNCD thin films. UNCD-based PVEH devices are being fabricated at ANL and full materials and device characterization will be followed to optimize the device design for improved power generation.
6. Model-informed experiments should be performed for both Si-based and UNCD-based MEMS-PVEHs for full characterization of PVEH performance. Enhanced figures of merit and the model-based optimization framework presented in Chapter 7 will provide a basis for optimal performance quantification along with multi-variable design optimization discussed in Chapter 8.
7. Reliability is a significant issue to overcome for energy harvester devices as the power supply should operate for a long time (ideally infinitely). During the operation of PVEH

devices, it is necessary to consider two kinds of fatigue, namely mechanical fatigue and piezoelectric fatigue. Piezoelectric fatigue can be defined as the phenomenon where the piezoelectric coefficient decreases as a function of either mechanical stress/strain or electric field cycling. In energy harvesting, the induced voltage by mechanical vibration is much lower than the coercive field of the piezoelectric layer. Therefore, one can assume that once the piezoelectric layer is poled in the direction of interest, there is no significant polarization switching during the cycling. Therefore, in order to understand the decrease in piezoelectric coefficient without polarization switching and find a way to improve the reliability of PVEHs, it is necessary to investigate unipolar piezoelectric fatigue where applied electric field across the piezoelectric layer is much lower than its coercive electric field that can be obtained from piezoelectric hysteresis loop measurements. Thus, analytical modeling and experimental study of both structural and piezoelectric unipolar fatigue phenomenon will provide a basis to understand and improve reliability of PVEH devices. The top-down approach will facilitate investigation of fatigue phenomena since evaluation of piezoelectric and structural degradation as a function of time is possible using measured data of voltage and resonant frequency as a function of operation time, as described in Chapter 7.

8. Fabrication of high-frequency Si-based MEMS resonators can be performed based on the optimal device design and fabrication process proposed in Chapter 10. Also, the model developed for electrostatically-driven resonators can be used to design fatigue test devices for high-strain single-crystal silicon thin films.
9. In this thesis, untapered, cantilevered PVEHs with uniform cross-section with or without a proof mass are explored both analytically and experimentally. Future work can include a simple geometric modification that is easily implemented with MEMS fabrication techniques: tapering of the beam/plate cantilever. By making the width at the tip of the beam/plate section not equal to the width at the root, a more evenly distributed strain profile along the beam/plate is expected as compared to an un-tapered beam [79]. Development of a modified model for tapered, cantilevered PVEHs and fabrication of

such devices are recommended as future work.

References

1. K. A. Cook-Chennault, N. Thambi, and A. M. Sastry Powering MEMS portable devices- a review of non-regenerative and regenerative power supply systems with special emphasis on piezoelectric energy harvesting systems *Smart Mater. Struct.* **17** 043001, 2008.
2. L. C. Rome, L. Flynn, E. M. Goldman, and T. D. Yoo Generating electricity while walking with loads *Science* **309** 1725, 2005.
3. J. M. Donelan, Q. Li, V. Naing, J. A. Hoffer, D. J. Weber, and A. D. Kuo Biomechanical energy harvesting: generating electricity during walking with minimal user effort. *Science* **319** 807, 2008.
4. B. L. Wardle, and S. M. Spearing *Microfabricated Power Generation Devices and Technology*: Chapter 9 Structural Considerations, ed Mitsos A and Barton P I (Weinheim: Wiley-VCH), 2009.
5. J. Rabaye, M. J. Ammer, J. L. da Silva, D. Patel, and S. Roundy Picoradio supports ad hoc ultra-low power wireless networking. *IEEE Comput.* **33** 42-8, 2000.
6. R. Amirtharajah, and A. P. Chandrakasan Self-powered signal processing using vibration-based power generation. *IEEE Journal of Solid-State Circuits* **33** 5 687-695, 1998.
7. S. P. Beeby, M. J. Tudor, and N. M. White Energy harvesting vibration sources for microsystems applications. *Meas. Sci. Technol.* **13** R175-95, 2006.
8. T. Ikeda *Fundamentals of Piezoelectricity* (New York: Oxford University Press), 1996.
9. A. Joseph, Paradiso, and Thad Starner Energy scavenging for mobile and wireless electronics. *IEEE pervasive computing*, 2005.

10. Shashank Priya Advances in energy harvesting using low profile piezoelectric transducers. *J. Electroceram.* **19** 165-182, 2007.
11. Shad Roundy, Paul K. Wright, and Jan Rabeey A study of low level vibrations as a power source for wireless sensor nodes. *Computer Communications* **26** 1131-1144, 2003.
12. R. Venkatasubramanian, E. Siivola, T. Coplitts, and B. O'Quinn Thin-film thermoelectric devices with high room-temperature figures of merit *Nature* **413** 597-602, 2001.
13. M. Chen, S. S. Lu, and B. Liao On the figure of merit of thermoelectric generators. *Trans. ASME J. Energy Resources Technol.* **127** 37-41, 2005.
14. J. C. Chen, J. Z. Yan, and L. Q. Wu The influence of Thomson effect on the maximum power output and maximum efficiency of a thermoelectric generator. *J. Appl. Phys.* **79** 8823-8, 1996.
15. S. B. Riffat and Xiaoli Ma Thermoelectrics: a review of present and potential applications. *Applied Thermal Engineering* **23** 8, 2003.
16. T. Starner Human-powered wearable computing *IBM Systems Journal* **35** (3) 618-629, 1996.
17. T. Starner, and J.A. Paradiso "Human-Generated Power for Mobile Electronics" in Low-Power Electronics Design, C. Piguet, ed. *CRC Press* chapter 45, pp. 1-35, 2004.
18. J. Kymissis, C. Kendall, J. Paradiso, and N. Gershenfeld Parasitic Power Harvesting in Shoes *Proceedings of the 2nd IEEE International Symposium on Wearable Computers* October 19-20, Pittsburg, PA, 132-139, 1998.
19. N. S. Shenck, and J. A. Paradiso Energy Scavenging with shoe-mounted piezoelectrics *IEEE Micro.* 21 30-42, 2001.
20. J. F. Antaki, G. E. Bertocci, E. C. Green, A. Nadeem, T. Rintoul, R. L. Kormos, B. P. Griffith "A Gait-Powered Autologous Battery Charging System for Artificial Organs," *ASAIO J.*, vol. 41, no. 3, pp. M588-M595, 1995.
21. Henry A. Sodano, Daniel J. Inman, and Gyuhae Park A review of power harvesting from vibration using piezoelectric materials *The Shock and Vibration Digest* **36** No. 3 pp.197-

205, 2004.

22. Voltree Power (<http://www.voltreepower.com>).
23. George W. Taylor, Joseph R. Burns, Sean M. Kammann, William B. Powers, and Thomas R. Welsh The Energy Harvesting Eel: A Small Subsurface Ocean/River Power Generator *IEEE JOURNAL OF OCEANIC ENGINEERING* **26** 539, 2001.
24. J. J. Allen and A. J. Smits Energy Harvesting Eel *J. Fluids Struct.* **15** 629-40, 2001.
25. V. H. Schmidt Piezoelectric energy conversion in windmills *IEEE Ultrason. Symp.* pp. 897-904, 1992.
26. R. Myers, M. Vickers, H. Kim and S. Priya Small scale windmill *Appl. Phys. Lett.* **90** 3, 2007.
27. David Chandler “Milliwatts with Mega Impact” November/December 2010 *Technology Review* published by Massachusetts Institute of Technology (<http://www.technologyreview.com/computing/26516/>).
28. Yen Kheng Tan, and Sanjib Kumar Panda “Review of Energy Harvesting Technologies for Sustainable Wireless Sensor Network” in Sustainable Wireless Sensor Networks *edited by* Winston Seah and Yen Kheng Tan *Intech*, 2010.
29. N. E. duToit, B. L. Wardle, and S-G. Kim Design considerations for MEMS-scale piezoelectric mechanical vibration energy harvesters *Integr. Ferroelectr.* **71** 121-60, 2005.
30. N. E. du Toit Modeling and design of a MEMS piezoelectric vibration energy harvester *Master’s thesis* Massachusetts Institute of Technology, 2005.
31. C. B. Williams, and R. B. Yates Analysis of a Micro-Electric Generator for Microsystems *Sensor and Actuators* **52** No. 1-3, 8-11, 1996.
32. P. Basset, D. Galayko, A. Mahmood Paracha, F. Marty, A. Dudka and T. Bourouina A batch-fabricated and electrets-free silicon electrostatic vibration energy harvester *J. Micromech. Microeng.* **19** 115025, 2009.
33. P. Muralt Ferroelectric thin films for micro-sensor and actuators: a review *J. Micromech. Microeng.* **10** 136-146, 2000.

34. S. Trolrier-Mckinstry, and P. Muralt Thin Film Piezoelectric for MEMS *J. Electroceram.* **12**, 7-17, 2004.
35. IEEE 1987 ANSI Standard 176-1987: IEEE Standard on Piezoelectricity.
36. S. Tadigadapa and K. Mateti Piezoelectric MEMS sensors: state-of-the-art and perspectives *Meas. Sci. Technol.* **20** 092001, 2004.
37. Steven R. Anton, and Henry A. Sodano A review of power harvesting using piezoelectric materials (2003-2006) *Smart Mater. Struct.* **16** R1-R21, 2007.
38. T. Funasaka, M. Furuhashi, Y. Hashimoto, and K. Nakamura Piezoelectric generator using a LiNbO₃ plate with an inverted domain *Ultrasonics Symp. (Sendai, 1998)* pp959-62, 1998.
39. N. Setter *et al.* Ferroelectric thin films: review of materials, properties, and applications *J. Appl. Phys.* **100** 051606, 2006.
40. Zhong Lin Wang, and Jinhui Song Piezoelectric nanogenerators based on zinc oxide nanowire arrays *Science* **312** 242, 2006.
41. Chen Xu, Sudong Wang, and Zhong Lin Wang Nanowire Structured Hybrid Cell for Concurrently Scavenging Solar and Mechanical Energies *J. Am. Chem. Soc.* **131** 5866-5872, 2009.
42. imec news – imec, 2008 (http://www2.imec.be/be_en/press/imec-news/imec-reports-record-power-for-micromachined-piezoelectric-energy-harvester.html).
43. A. J. Lovinger Ferroelectric polymers *Science* **220** 1115-21, 1983.
44. H. A. Sodano, G. Park, and D. J. Inman An Investigation into the Performance of Macro-Fiber composites for Sensing and Structural Vibration Applications *Mechanical Systems and Signal Processing* **18** pp. 683-697, 2004.
45. H. A. Sodano, G. Park, D. J. Leo, and D. J. Inman Model of piezoelectric Power Harvesting Beam in *ASME International Mechanical Engineering Congress and Expo*, November 15-21, Washington, DC **40** 2, 2004.

46. Hyunuk Kim *et al.* Chapter 1 Piezoelectric energy harvesting in Energy Harvesting Technologies, S. Priya, D. J. Inman (eds.), Springer Science & Business Media, LLC, 2009.
47. A. Erturk, O. Bilgen, and D. J. Inman Power generation and shunt damping performance of a single crystal lead magnesium niobate-lead zirconate titanate unimorph: Analysis and experiment *Appl. Phys. Lett.* **93** 224102, 2008.
48. R. W. Schwartz, J. Ballato, and G. H. Haertling Piezoelectric and electro-optic ceramics *Ceramics Materials for Electronics* ed R. C. Buchanan (New York: Dekker), 2004.
49. Y. Xu *Ferroelectric Materials and their Applications* (Amsterdam: North-Holland), 1991.
50. W. G. Cady *Piezoelectricity* (New York: McGraw-Hill), 1946.
51. N. Setter Electroceramics-based MEMS: fabrication-technology, and applications *Electronics Materials: Science and Technology* ed H. L. Tuller (New York: Springer), 2005.
52. M. Kim, M. Hoegen, J. Dugundji, and B. L. Wardle Modeling and Experimental Verification of Proof Mass Effects on Vibration Energy Harvester Performance *Smart Mater. Struct.* **19** 045023, 2010.
53. Y. B. Jeon, R. Sood, J-H. Jeong, and S-G. Kim MEMS power generator with transverse mode thin film PZT *Sensors and Actuators A* **122** 16-22, 2005.
54. D. Shen, J-H. Park, J. Ajitsaria, S-Y. Choe, C. W. Howard III, and D-J. Kim The design, fabrication and evaluation of a MEMS PZT cantilever with an integrated Si proof mass for vibration energy harvesting *J. Micromech. Microeng.* **18** 055017 2008.
55. Piezoelectric Energy Converter for Electronic Implants, US patent 3,456,134, Patent and Trademark Office, 1969.
56. Shad Roundy *et al.* Improving power output for vibration-based energy scavengers *IEEE pervasive computing*, 2005.
57. Dibin Zhu, Machael J Tudor, and Stephen P Beeby Topical Review: Strategies for Increasing the Operating Frequency Range of Vibration Energy Harvester *Meas. Sci.*

Technol. **21** 022001, 2010.

58. M. J. Madou *Fundamentals of Microfabrication* (200 N.W. Corporate Blvd., Boca Raton, Florida 33431: CRC Press LLC), 2002.
59. H. B. Fang, J. Q. Liu, Z. Y. Xu, L. Dong, L. Wang, D. Chen, B. C. Cai, and Y. Liu Fabrication and performance of MEMS-based piezoelectric power generator for vibration energy harvesting *Microelectron. J.* **37** 1280-4, 2006.
60. M. Marzencki, B. Charlot, S. Basrour, M. Colin, and L. Valbin Design and fabrication of piezoelectric micro power generators for autonomous Microsystems *DTIP' 05 Symp. Design, Test, Integration & Packaging of MEMS/MOEMS (Montreux, Switzerland)* pp 299-302, 2005.
61. J. G. Smits and W. S. Choi The constituent equations of piezoelectric heterogeneous bimorphs *IEEE Trans. Ultrason. Ferroelectr. Freq. Control* **38** 256-70, 1991.
62. W. S. Hwang, and H. C. Park Finite element modeling of piezoelectric sensors and actuators *AIAA J.* **31** 930-7, 1993.
63. M. Umeda, K. Nakamura, and S. Ueha Analysis of the transformation of mechanical impact energy to electric energy using piezoelectric vibrator *Japan. J. Appl. Phys.* **35** 3267-73, 1996.
64. A. Erturk, and D. J. Inman Issues in Mathematical Modeling of Piezoelectric Energy Harvesters *Smart Mater. Struct.* **17** 065016, 2008.
65. S. Roundy, P. K. Wright A Piezoelectric vibration based generator for wireless electronics *Smart Mater. Struct.* **13** 1131-42, 2004.
66. F. Lu, H. Lee, and S. Lim Modeling and analysis of micropiezoelectric power generators for microelectromechanical-systems applications *Smart Mater. Struct.* **13** 57-63, 2004.
67. S-N. Chen, G-J. Wang, and M-C Chien Analytical modeling of piezoelectric vibration-induced micro power generator *Mechatronics* **16** 379-87, 2006.
68. J. H. Lin, X. M. Wu, T. L. Ren, and L. T. Liu Modeling and simulation of piezoelectric MEMS energy harvesting device *Integr. Ferroelectr.* **95** 128-41, 2007.

69. D. J. Inman *Engineering Vibration* (Upper Saddle River, NJ: Prentice Hall), 1996.
70. J. Soderkvist Dynamic behavior of a piezoelectric beam *Journal of the Acoustic Society of America* **90** 685-92, 1991.
71. N. Hagood, W. Chung, and A. Von Flotow Modelling of piezoelectric actuator dynamics for active structural control *Journal of Intelligent Material Systems and Structures* **1** 327-54, 1990.
72. H. A. Sodano, G. Park, and D. J. Inman Estimation of electric charge output for piezoelectric energy harvesting *Strain* **40** 49-58, 2004.
73. N. E. duToit, and B. L. Wardle Performance of microfabricated piezoelectric vibration energy harvesters *Integr. Ferroelectr.* **83** 13-32, 2006.
74. N. E. duToit, and B. L. Wardle Experimental verification of models for microfabricated piezoelectric vibration energy harvesters *AIAA Journal* **45** 1126-1137, 2007.
75. J. Ajitsaria, S-Y. Cho, D. Shen, and D. J. Kim Modeling and analysis of a bimorph piezoelectric cantilever beam for voltage generation *Smart Mater. Struct.* **16** 447-454, 2007.
76. A. Erturk, and D. J. Inman An experimentally validated bimorph cantilever model for piezoelectric energy harvesting from base excitations *Smart Mater. Struct.* **18** 025009, 2009.
77. A. Erturk, and D. J. Inman On mechanical modeling of cantilevered piezoelectric vibration energy harvesters *J. Intell. Mater. Syst. Struct.* **19** 1311–25, 2008.
78. A. Erturk, and D. J. Inman A distributed parameter electromechanical model for cantilevered piezoelectric energy harvesters *ASME J. Vib. Acoust.* **130** 041002, 2008.
79. A. M. Mracek Towards an Embeddable Structural Health Monitoring Sensor: Design and Optimization of MEMS Piezoelectric Vibration Energy Harvesters *Master's thesis* Massachusetts Institute of Technology, 2004.
80. J. E. Sader, I. Larson, P. Mulvaney, and L. R. White Method for the calibration of atomic force microscope cantilevers *Rev. Sci. Instrum.* **66** 3789, 2004.

81. J. W. Yi, W.Y. Shih, and W.-H. Shih Effect of length, width, and mode on the mass detection sensitivity of piezoelectric unimorph cantilevers *J. Appl. Phys.* **91**, 1680, 2002.
82. T. H. Ng, and W. H. Liao Sensitivity analysis and energy harvesting for a self-powered piezoelectric sensor *J. Intell. Mater. Syst. Struct.* **16** 785–97, 2005.
83. D. J. Inman *Engineering Vibration* (Upper Saddle River, NJ: Prentice Hall), 1996.
84. B. Rama Bhat, and H. Wagner Natural Frequencies of a Uniform Cantilever with a Tip Mass Slender in the Axial Direction *Journal of Sound and Vibration* **45** 304-307, 1976.
85. C. To Vibration of a Cantilevered Beam with a Base Excitation and Tip Mass *Journal of Sound and Vibration* **83** 445-460, 1982.
86. eFunda-engineering Fundamentals, Materials
(http://www.efunda.com/materials/materials_home/materials.cfm).
87. Piezo Systems Inc. Introduction to Piezo Transducers” Piezoelectric Engineering & Manufacturing Catalog #7B, 2007.
88. D. Halliday, R. Resnick, and J. Walker *Fundamentals of Physics 8th edition* (111 River Street Hoboken, NJ 07030-5774: Wiley), 2007.
89. D. D. Quinn, A. F. Vakakis, L. A. Bergman Vibration-based energy harvesting with essential nonlinearities *ASME International Design Engineering Technical Conferences* (Las Vegas, NV), 2007.
90. S. W. Shaw, and B. Balachandran A review of nonlinear dynamics of mechanical systems in year 2008 *Journal of System Design and Dynamics* **2** 611-640, 2008.
91. J. M. Renno, M. F. Daqaq, and D. J. Inman On the optimal energy harvesting from a vibration source *Journal of Sound and Vibration* **320** 386-405, 2009.
92. A. Triplett, and D. D. Quinn The effect of nonlinear piezoelectric coupling on vibration-based energy harvesting *Journal of Intelligent Material Systems and Structures* **20** 1959-1967, 2009.
93. R. Nath, S. Hong, J. A. Klug, A. Imre, M. J. Bedzyk, R. S. Katiyar, and O. Auciello

Effects of cantilever buckling on vector piezoresponse force microscopy imaging of ferroelectric domains in BiFeO₃ nanostructures *Appl. Phys. Lett.* **96** 163101, 2010.

94. J. Mayer, L. A. Giannuzzi, T. Kamino, and J. Michael TEM Sample Preparation and FIB-Induced Damage *MRS Bulletin* **32**, 400-407, 2007.
95. B. Bhushan, and X. Li Mircomechanical and tribological characterization of doped single-crystal silicon and polysilicon films for microelectromechanical systems device *J. Mater. Res.* **12**, 1, 1997.
96. S. Roundy, P. K. Wright, and J. M. Rabaey Energy Scavenging for Wireless Sensor Networks, Kluwer Academic Publishers, Norwell, MA., 2004.
97. Dragan Damjanovic Ferroelectric, dielectric and piezoelectric properties of ferroelectric thin films and ceramics *Rep. Prog. Phys.* **61** 1267, 1998.
98. Kenji Omote, and Hiroji Ohigashi Temperature Dependence of Shear Piezoelectric Properties of Poly(vinylidene fluoride) Studied by Piezoelectric Resonance Method *Jpn. J. Appl. Phys.* **35** 1818-1823, 1996.
99. Mark Parker Ambient Energy Harvesting *Bachelor's thesis* University of Queensland, 2003.
100. A.R. Akande, A. Nechibvute, and P.V.C. Luhanga Characterization of Piezoelectric Energy harvesting devices: need for a standard *From Proceeding* (684) Power and Energy Systems - 2010.
101. Frank Goldschmidtboeing *et al.* Parameter identification for resonant piezoelectric energy harvesters in the low- and high-coupling regimes *J. Micromech. Microeng.* 21 045006, 2011.
102. Cecilia D. Richards, Michael J. Anderson, David F. Bahr, and Robert F. Richards. Efficiency of energy conversion for devices containing a piezoelectric component *J. Micromech. Microeng.* 14 717-721, 2004.
103. Shad Roundy On the effectiveness of Vibration-based Energy Harvesting *Journal of Intelligent Material Systems and Structures* Vol. 16, 2005.
104. Changki Mo, Sunghwan Kim, and William W. Clark Theoretical analysis of energy

- harvesting performance for unimorph piezoelectric benders with interdigitated electrodes *Smart Mater. Struct.* **18** 055017, 2009.
105. Dongna Shen, Jung-Hyun Park, Jyoti Ajitsaria, Song-Yul Choe, Howard C Wikle III and Dong-Joo Kim The design, fabrication and evaluation of a MEMS PZT cantilever with an integrated Si proof mass for vibration energy harvesting *J. Micromech. Microeng.* **18** 055017, 2008.
106. Dongna Shena, Jung-Hyun Park, Joo Hyon Noh, Song-Yul Choe, Seung-Hyun Kim, Howard C. Wikle III and Dong-Joo Kim Micromachined PZT cantilever based on SOI structure for low frequency vibration energy harvesting *Sensors and Actuators A* **154** 103–108, 2009.
107. P. Muralt, R. G. Polcawich, and S. Trolrier-McKinstry Piezoelectric thin films for sensors, actuators, and energy harvesting *Materials Research Society bulletin* **34**, 2009.
108. N. Ledermann, P. Muralt, J. Baborowski, S. Gentil, K. Mukati, M. Cantoni, A. Seifert, and N. Setter {100}-Textured, piezoelectric $\text{Pb}(\text{Zr}_x, \text{Ti}_{1-x})\text{O}_3$ thin films for MEMS: integration, deposition and properties *Sensors and Actuators A* **105** 162-170, 2003.
109. K. Lefki, and M. Dormans Measurement of piezoelectric coefficients of ferroelectric thin films *J. Appl. Phys.* **76** (3) 1, 1994.
110. D. Liu, S. H. Yoon, B. Zhou, B. C. Prorok, and D-J. Kim Investigation of the crystalline orientations and substrates dependence on mechanical properties of PZT thin films by nanoindentation *Mater. Res. Soc. Symp. Proc.* **1129**, 2009.
111. C Boller Ways and options for aircraft structural health management *Smart Materials and Structures*, Vol. 10, 432-440, 2009.
112. MIL-STD-810, 1 January 2000, Annex C, Method 514.5, p514.4C 1-11.
113. R. Sood, Y. B. Jeon, J.-h. Jeong, and S. G. Kim Piezoelectric Micro Power Generation for Energy Harvesting *Proceedings of Hilton Head 2004: A Solid State Sensor, Actuator and Microsystems Workshop*, June 2004.
114. O. Auciello *et al.* Materials Science and Fabrication Processes for a New MEMS Technology Based on Ultrananocrystalline Diamond Thin Films. *J. Phys.: Condens. Matter* **16**, R539-R552, 2004.

115. O. Auciello, and A. Sumant. Status review of the science and technology of ultrananocrystalline diamond (UNCDTM) films and application to multifunctional devices. *Diamond & Related Materials* **19**, 699–718, 2010.
116. A. V. Sumant *et al.* MRS Bulletin **35**, 281-288, 2010.
117. S. Srinivasan, J. Hiller, B. Kabius, and O. Auciello. Piezoelectric/ultrananocrystalline diamond heterostructures for high-performance multifunctional micro/nanoelectromechanical systems. *Applied Physics Letters* **90**, 134101, 2007.
118. Mathias Hoegen Design and Testing of Microfabricated Energy Harvesting Systems *Master's thesis* Technische Universitat Carolo-Wilhelmina Zu Braunschweig 2008.
119. J. F. Nye *Physical Properties of Crystals* Oxford Science Publication 1989.
120. N. Hagood, W. Chung, and A. Von Flotow Modelling of piezoelectric actuator dynamics for active structural control. *Journal of Intelligent Material Systems and Structures* **1** 327-54, 1990.
121. Stephen D. Senturia *Microsystem Design*, Springer New York, 2001.
122. Andreu Fargas-Marques, Jasmina Casals-Terre, and Andrei M. Shkel Resonant Pull-In Condition in Parallel-Plate Electrostatic Actuators, *Journal of Microelectromechanical Systems*, Vol. 16, No. 5, 2007.
123. Seong Yoel No, Akinori Hashimura, Siavash Pourkamali, and Farrokh Ayazi Single-Crystal Silicon HARPSS Capacitive Resonators with Submicron Gap-Spacing *Solid-State Sensor, Actuator and Microsystems Workshop, Hilton Head Island, South Carolina*, June 2-6, 2002.
124. <http://en.wikipedia.org/wiki/Titanium>.
125. <http://en.wikipedia.org/wiki/Aluminium>.
126. S. I. Ivashov, V. V. Razevig, A. P. Sheyko, and I. A. Vasilyev Detection of Human Breathing and Heartbeat by Remote Radar *Progress in Electromagnetic Research Symposium, Pisa, Italy*, March 28-31, 2004.

127. P. Bajaj, D. Akin, A. Gupta, D. Sherman, B. Shi, O. Auciello, and R. Bashir
Ultrananocrystalline diamond film as an optimal cell interface for biomedical applications *Biomed Microdevices* **9**, 787-794, 2007.
128. Jung-Hyun Park Development of MEMS Piezoelectric Energy Harvesters *Ph.D Thesis*
Auburn University, 2010.
129. H. W. Kim, S. Priya, K. Uchino, and R. E. Newnham Piezoelectric Energy Harvesting
under High Pre-Stressed Cyclic Vibrations *Journal of Electroceramics* **15**, 27-34, 2005.

Appendix

- A.** Effective Piezoelectric Materials Constants for Beams, Plates, and Thin Films in {3-1} and {3-3} Modes of Operation
- B.** Supplements for Chapter 5
 - B.1** SEM Images of MEMS-scale Cantilever with Proof Masses of Different Lengths Fabricated Using FIB
 - B.2** Experimental Sequence and Detailed Manual for Characterization Using AFM (MFP-3-D, Asylum Research)

Appendix A. Effective Piezoelectric Materials Constants for Beams, Plates and Thin Films in {3-1} and {3-3} Modes of Operation

One can describe the piezoelectric effect mathematically using linear elastic constitutive equations [8,35]. Assumption of small deformations allows linear forms of the constitutive equations to be used. In Chapter 2, the representative expression for three-dimensional linear elastic constitutive relations where a range of small-signal piezoelectric motion is assumed is introduced in equation (2.7). As the matrices of the elastic compliance, dielectric susceptibility, piezoelectric, electrostrictive and pyroelectric coefficients of poled ferroelectric polycrystalline materials with randomly oriented grains have the same nonzero matrix elements as crystals that belong to point group 6mm [97], it is possible to simplify the three-dimensional linear elastic constitutive relations in equation (2.7) as follows:

$$\begin{Bmatrix} S_1 \\ S_2 \\ S_3 \\ S_4 \\ S_5 \\ S_6 \end{Bmatrix} = \begin{bmatrix} s_{11}^E & s_{12}^E & s_{13}^E & 0 & 0 & 0 \\ s_{12}^E & s_{11}^E & s_{13}^E & 0 & 0 & 0 \\ s_{13}^E & s_{13}^E & s_{33}^E & 0 & 0 & 0 \\ 0 & 0 & 0 & s_{44}^E & 0 & 0 \\ 0 & 0 & 0 & 0 & s_{44}^E & 0 \\ 0 & 0 & 0 & 0 & s_{11}^E & s_{66}^E = \frac{c_{11}^E - c_{12}^E}{2} \end{bmatrix} \begin{Bmatrix} T_1 \\ T_2 \\ T_3 \\ T_4 \\ T_5 \\ T_6 \end{Bmatrix} + \begin{bmatrix} 0 & 0 & d_{31} \\ 0 & 0 & d_{31} \\ 0 & 0 & d_{33} \\ 0 & d_{15} & 0 \\ d_{15} & 0 & 0 \\ 0 & 0 & 0 \end{bmatrix} \begin{Bmatrix} E_1 \\ E_2 \\ E_3 \end{Bmatrix} \quad (\text{A.1})$$

$$\begin{Bmatrix} D_1 \\ D_2 \\ D_3 \end{Bmatrix} = \begin{bmatrix} 0 & 0 & 0 & 0 & d_{15} & 0 \\ 0 & 0 & 0 & d_{15} & 0 & 0 \\ d_{31} & d_{31} & d_{33} & 0 & 0 & 0 \end{bmatrix} \begin{Bmatrix} T_1 \\ T_2 \\ T_3 \\ T_4 \\ T_5 \\ T_6 \end{Bmatrix} + \begin{bmatrix} \epsilon_{11}^T & 0 & 0 \\ 0 & \epsilon_{11}^T & 0 \\ 0 & 0 & \epsilon_{33}^T \end{bmatrix} \begin{Bmatrix} E_1 \\ E_2 \\ E_3 \end{Bmatrix} \quad (\text{A.2})$$

In order to derive the expressions for “*effective*” piezoelectric materials constants for beam and plate configurations both in {3-1} and {3-3} modes of operations (see Figure A.1), it is convenient to take all shear stresses as zero relative to the others, which gives:

$$\begin{Bmatrix} S_1 \\ S_2 \\ S_3 \end{Bmatrix} = \begin{bmatrix} S_{11} & S_{12} & S_{13} \\ S_{21} & S_{11} & S_{13} \\ S_{31} & S_{31} & S_{33} \end{bmatrix} \begin{Bmatrix} T_1 \\ T_2 \\ T_3 \end{Bmatrix} + \begin{bmatrix} 0 & 0 & d_{31} \\ 0 & 0 & d_{31} \\ 0 & 0 & d_{33} \end{bmatrix} \begin{Bmatrix} E_1 \\ E_2 \\ E_3 \end{Bmatrix} \quad (\text{A.3})$$

$$\begin{Bmatrix} D_1 \\ D_2 \\ D_3 \end{Bmatrix} = \begin{bmatrix} 0 & 0 & 0 \\ 0 & 0 & 0 \\ d_{31} & d_{31} & d_{33} \end{bmatrix} \begin{Bmatrix} T_1 \\ T_2 \\ T_3 \end{Bmatrix} + \begin{bmatrix} \varepsilon_{11}^T & 0 & 0 \\ 0 & \varepsilon_{11}^T & 0 \\ 0 & 0 & \varepsilon_{33}^T \end{bmatrix} \begin{Bmatrix} E_1 \\ E_2 \\ E_3 \end{Bmatrix} \quad (\text{A.4})$$

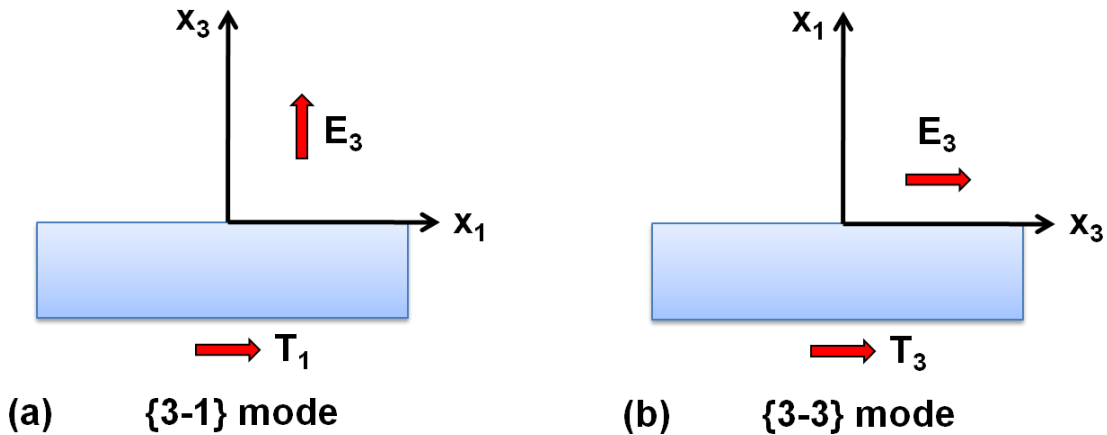


Figure A.1 Schematic of piezoelectric effect for beams and plates in (a) {3-1} mode of operation and (b) {3-3} mode of operation.

For a beam in {3-1} mode of operations, $T_3 = 0$, $T_2 = 0$, and electric field only in the 3 direction (E_3) is in effect, as shown in Figure A.1 (a). Thus, equations (A.3) and (A.4) become:

$$S_1 = s_{11}T_1 + d_{31}E_3 \quad (\text{A.5})$$

$$D_3 = d_{31}T_1 + \varepsilon_{33}^T E_3 \quad (\text{A.6})$$

If we rewrite equation (A.5) in terms of strain (S_1) and electric field (E_3) as in equation (A.7) and then substitute (A.7) into equation (A.6), equation (A.8) is obtained:

$$T_1 = \frac{1}{s_{11}} S_1 - \frac{d_{31}}{s_{11}} E_3 \quad (\text{A.7})$$

$$D_3 = \frac{d_{31}}{s_{11}} S_1 + \left(\varepsilon_{33}^T - \frac{(d_{31})^2}{s_{11}} \right) E_3 \quad (\text{A.8})$$

The three-dimensional linear elastic constitutive relations in equation (2.7) can be easily simplified for {3-1} mode of operation where equation (2.7) is significantly simplified as expressed in equation (A.9):

$$\begin{Bmatrix} T_1 \\ D_3 \end{Bmatrix} = \begin{bmatrix} c_{11}^E * & -e_{31} * \\ e_{31} * & \varepsilon_{33}^S * \end{bmatrix} \begin{Bmatrix} S_1 \\ E_3 \end{Bmatrix} \quad (\text{A.9})$$

It should be noted that these constants, for which asterisk (*) is employed for distinction, are not equal to the fully 3-D constants. Comparison of equation (A.9) with equations (A.7) and (A.8) yields expressions for the physical parameters, $c_{11}^E *$, $e_{31} *$, and $\varepsilon_{33}^S *$ for a beam in {3-1} mode of operation as written below:

$$c_{11}^E * = \frac{1}{s_{11}^E} \quad (\text{A.10})$$

$$e_{31} * = \frac{d_{31}}{s_{11}^E} \quad (\text{A.11})$$

$$\epsilon_{33}^{S*} = \epsilon_{33}^T - \frac{(d_{31})^2}{s_{11}^E} \quad (\text{A.12})$$

The same scheme can be applied to derive expressions of material property constants for a plate in {3-1} mode of operations. For a plate in {3-1} mode of operation, $T_3 = 0$, and electric field only in the 3 direction (E_3) exists. Thus, equations (A.3) and (A.4) become:

$$S_1 = s_{11}T_1 + s_{12}T_2 + d_{31}E_3 \quad (\text{A.13})$$

$$S_2 = s_{12}T_1 + s_{11}T_2 + d_{31}E_3 \quad (\text{A.14})$$

$$S_3 = s_{13}T_1 + s_{13}T_2 + d_{33}E_3 \quad (\text{A.15})$$

$$D_3 = d_{31}T_1 + d_{31}T_2 + \epsilon_{33}^T E_3 \quad (\text{A.16})$$

Note that the terms on the right-hand side of equation (A.15) does not intersect with S_3 in {3-1} mode of operation (see Figure A.1 (a)). One can obtain equations (A.17) to (A.19) by combining equations (A.13) and (A.14) and then, making rearrangements:

$$\begin{Bmatrix} S_1 \\ S_2 \end{Bmatrix} = \begin{bmatrix} s_{11} & s_{12} \\ s_{12} & s_{11} \end{bmatrix} \begin{Bmatrix} T_1 \\ T_2 \end{Bmatrix} + \begin{Bmatrix} d_{31} \\ d_{31} \end{Bmatrix} E_3 \quad (\text{A.17})$$

$$\begin{Bmatrix} T_1 \\ T_2 \end{Bmatrix} = \begin{bmatrix} s_{11} & s_{12} \\ s_{12} & s_{11} \end{bmatrix}^{-1} \begin{Bmatrix} S_1 \\ S_2 \end{Bmatrix} - \begin{bmatrix} s_{11} & s_{12} \\ s_{12} & s_{11} \end{bmatrix}^{-1} \begin{Bmatrix} d_{31} \\ d_{31} \end{Bmatrix} E_3 \quad (\text{A.18})$$

$$\begin{Bmatrix} T_1 \\ T_2 \end{Bmatrix} = \begin{bmatrix} c_{11} & c_{12} \\ c_{12} & c_{11} \end{bmatrix} \begin{Bmatrix} S_1 \\ S_2 \end{Bmatrix} - \begin{bmatrix} c_{11} & c_{12} \\ c_{12} & c_{11} \end{bmatrix} \begin{Bmatrix} d_{31} \\ d_{31} \end{Bmatrix} E_3 \quad (\text{A.19})$$

By noting the plate geometry and typical strain assumption, $S_2 = 0$ as there is no strain in the 2 direction and $L_2 \gg h$. Then, equation (A.19) can be rewritten as:

$$(T_1 + T_2) = (c_{11} + c_{12})S_1 - 2(c_{11} + c_{12})d_{31}E_3 \quad (\text{A.20})$$

Insertion of equation (A.20) into equation (A.16) gives:

$$D_3 = d_{31}(c_{11} + c_{12})S_1 + [\varepsilon_{33}^T - 2(c_{11} + c_{12})(d_{31})^2]E_3 \quad (\text{A.21})$$

The resulting expressions, then, can be written as follows:

$$T_1 = c_{11}S_1 - (c_{11} + c_{12})d_{31}E_3 \quad (\text{A.22})$$

$$D_3 = (c_{11} + c_{12})d_{31}S_1 + [\varepsilon_{33}^T - 2(c_{11} + c_{12})(d_{31})^2]E_3 \quad (\text{A.23})$$

which can be compared with equation (A.9) to find expressions for material property constants for a plate in {3-1} mode of operation:

$$c_{11}^{E*} = \frac{s_{11}^E}{(s_{11}^E)^2 - (s_{12}^E)^2} \quad (\text{A.24})$$

$$e_{31}^{*} = \frac{d_{31}}{s_{11}^E + s_{12}^E} \quad (\text{A.25})$$

$$\varepsilon_{33}^{S*} = \varepsilon_{33}^T - \frac{2d_{31}^2}{s_{11}^E + s_{12}^E} \quad (\text{A.26})$$

For {3-3} mode of operation, simplified expressions of equation (2.7) is:

$$\begin{Bmatrix} T_3 \\ D_3 \end{Bmatrix} = \begin{bmatrix} c_{33}^E * & -e_{33} * \\ e_{33} * & \epsilon_{33}^S * \end{bmatrix} \begin{Bmatrix} S_3 \\ E_3 \end{Bmatrix} \quad (\text{A.27})$$

For a beam in {3-3} mode of operation, $T_1 = T_2 = 0$, with electric field only in the 3 direction (E_3) (see Figure A.1 (b)). Using similar mathematical derivation procedures to {3-1} mode described earlier, one can obtain the expressions for the effective materials property constants for a beam in {3-3} mode of operation as follows:

$$c_{33}^E * = \frac{1}{s_{33}^E} \quad (\text{A.28})$$

$$e_{33} * = \frac{d_{33}}{s_{33}^E} \quad (\text{A.29})$$

$$\epsilon_{33}^S * = \epsilon_{33}^T - \frac{d_{33}^2}{s_{33}^E} \quad (\text{A.30})$$

Also, the condition that $T_l = 0$ and only E_3 exists can be used for a plate in {3-3} mode of operation, which results in the analytical expressions for the effective materials property constants for a plate in {3-3} mode of operations:

$$c_{33}^E * = \frac{s_{11}^E}{s_{11}^E s_{33}^E - (s_{13}^E)^2} \quad (\text{A.31})$$

$$e_{33} * = \frac{s_{11}^E d_{33} - s_{13}^E d_{31}}{s_{11}^E s_{33}^E - (s_{13}^E)^2} \quad (\text{A.32})$$

$$\epsilon_{33}^S * = \epsilon_{33}^T - \frac{(s_{33}^E d_{31}^2 - 2s_{13}^E d_{31} d_{33} + s_{11}^E d_{33}^2)}{s_{11}^E s_{33}^E - (s_{13}^E)^2} \quad (\text{A.33})$$

To sum up, depending on whether the structure is a beam or a plate in {3-1} or {3-3} mode of operation, different expressions should be used to evaluate material property constants: equations (A.10) to (A.12) for a beam in {3-1} mode, equations (A.24) to (A.26) for a plate in {3-1} mode, equations (A.28) to (A.30) for a beam in {3-3} mode, and equations (A.31) to (A.33) for a plate in {3-3} mode.

Piezoelectric thin films behave differently from bulk piezoelectric ceramics as they are fabricated using thin-film processing (microfabrication), which usually entails high residual stress, and different microstructure, when compared to bulk [33, 34, 107]. Their planar geometry and the clamping effect to the substrate, also tells us that the values of material properties measured in piezoelectric thin films and bulk will differ. Therefore, expressions for “effective” piezoelectric coefficients for thin films [109] are derived and expressed in terms of the coefficients for macroscopic systems. Here, the author presents only the resulting expressions for both transverse and longitudinal coefficients as below (equations (A.34) and (A.35)), while readers can refer to [109] for details on derivation:

$$e_{31,f} = \frac{d_{31}}{s_{11}^E + s_{12}^E} = e_{31} - \frac{c_{13}^E}{c_{33}^E} e_{33} \quad (\text{A.34})$$

$$d_{33,f} = d_{33} - \frac{2d_{31}(s_{13}^E + \nu/Y)}{(s_{11}^E + s_{12}^E)} \quad (\text{A.35})$$

Equation (A.34) not only exhibits the relation of effective constant, $e_{31,f}$, for a thin film with real value, e_{31} , but also shows that piezoelectric coefficient, d_{31} , can be obtained when elastic parameters are given. It suggests that $e_{31,f}$ is more practical to apply since the elastic parameters are necessary for the calculation of d_{31} . For longitudinal coefficient, $d_{33,f}$, it should be noted that ν and Y denote Poisson’s ratio and Young’s modulus of the substrate, not of the piezoelectric thin film. As substrates are not always isotropic, values for Young’s modulus should be chosen carefully depending on the orientation of substrate (*e.g.*, Si substrate). As d_{31} , s_{13} , and s_{12} are usually negative and s_{11} is positive and larger than s_{12} , one can expect that transverse coefficient, $d_{31,f}$, will be overestimated while longitudinal coefficient, $d_{33,f}$, will be underestimated in

comparison with real values. It should be emphasized that knowledge of elastic and dielectric properties of piezoelectric thin films is required to determine piezoelectric coefficients of thin film, as shown in the equations (A.34) and (A.35). Note that in modeling MEMS-scale PVEHs in Chapter 8, “effective” piezoelectric coefficients for thin films such as $e_{31,f}$ are used instead of materials constants for beams and plates such as e_{31}^* due to limited availability of data. For more accurate prediction of MEMS-scale PVEH performance, evaluation of material constants in a beam or plate consisting of thin film stacks such as $e_{31,f}^*$ is required, which can be done via top-down approach described in Chapter 7 in future work.

Appendix B. Supplement for Chapter 5

B.1 SEM Images of MEMS-scale Cantilever with Proof Masses of Different Lengths Fabricated Using FIB

Table B.1 Under-, Front-, and Side-view SEM images of tip-less cantilever in the state of as-received, after front trim and after side trim.

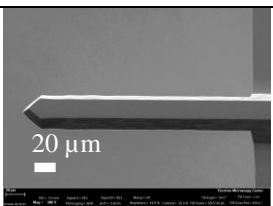
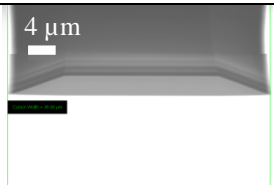
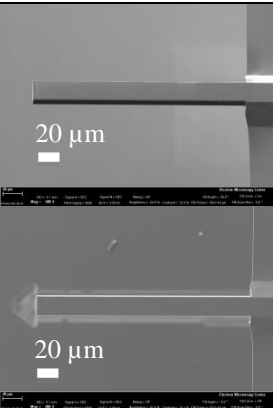
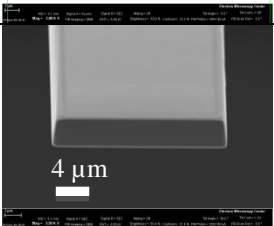
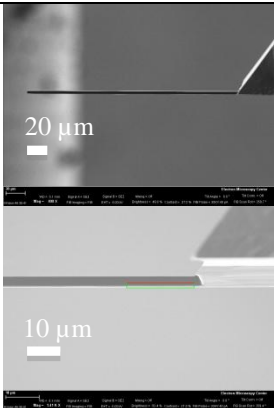
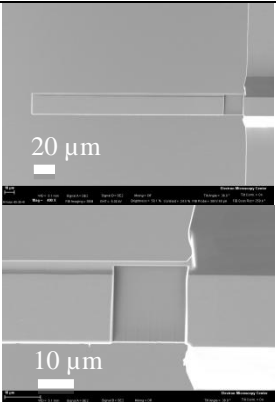
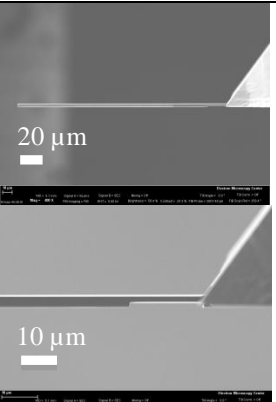
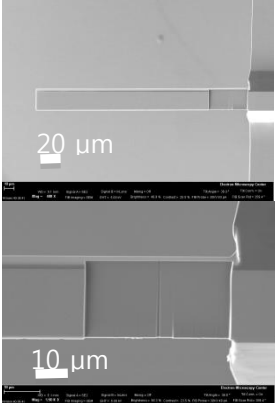



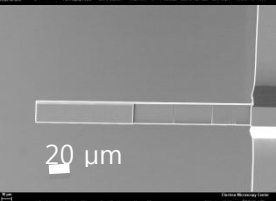
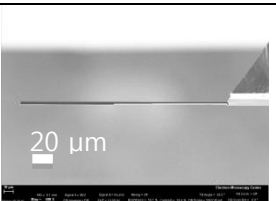
	Under-view	Front-view	Side-view
As-received			
Front trim			
Side trim			

Table B.2 Under- and side-view SEM images of MEMS-scale cantilever with proof masses of different lengths fabricated using FIB

	Under-view	Side-view
1st etch (20 μm)		
2nd etch (40 μm)		
3rd etch (80 μm)		
4th etch (120 μm)		

5th etch (160 μm)		 			
6th etch (190 μm)		 			
7th etch (220 μm)		 			

B.2 Experimental Sequence and Detailed Manual for Characterization Using AFM (MFP-3D, Asylum Research)

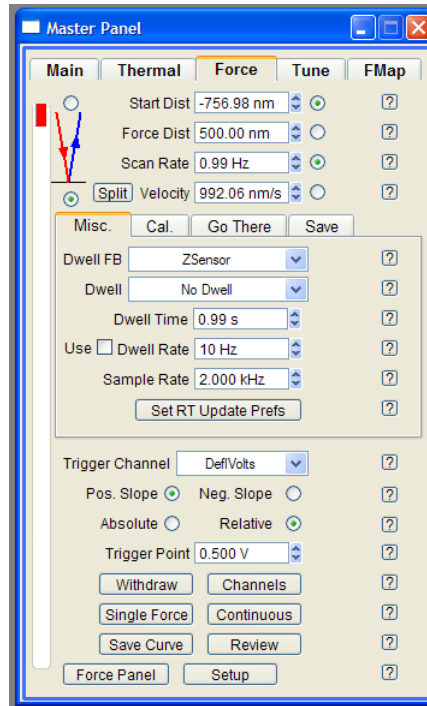
<AFM – Experimental Sequence>

1. Dimension measurement after capturing the image
 - a. Determine the position for laser beam spot on the top side of the cantilever: from the tip, numbering starts from #1, #2, #3, ..., till # 10 with equi-distances (~20 μm). → total 6 points
 - b. Determine # of measurements at each point
 - i. Measure 10 times as initial work.
 - ii. Get standard deviations on the data above.
 - iii. Determine # of measurement at each point → 3 times
 - c. Capture the image (AFM controls → others → video)
2. Force-distance curve measurement
 - a. Sensitivity test (force-distance curve) → Need to look up manual. (AC mode, inverse optical lever sensitivity) → Convert unit of amplitude from [V] into [nm].
3. Thermal measurement: Obtain stiffness K [N/m]. Note: save both in pxx. and csv. formats.
4. Autotune experiment:
 - a. amplitude
 - b. resonant frequency
 - c. quality factor
 - d. phase
5. Acquiring frequency spectrum of cantilever vibration under constant excitation

<Detailed Manual for AFM (MFP-3D, Asylum Research)>

1. S/W open
2. Laser on
3. Unclick 'use Argyle'.
4. When 'ready' is on, close unnecessary windows.
5. [User settings] → In [Mode Master] → click [simple] → enter [AC air topography].
6. Camera on → positioning of laser spot (using a transparent slide)
 - a. (Photo diode) Sum (A+B) signal should be maximized.
 - b. (Photo diode) Deflection (A-B) signal should be as close as possible to zero.
7. Capture the image ([tab] AFM controls → others → video)
 - a. Click 'save 2Mem' and 'Save2 Disk'.
 - b. Click 'capture' and 'display'. (the file is automatically saved w/ file name 'Can#_Pos#.)
8. Measure dimensions, dx (length from clamping to the tip) and dx_1 (to the laser spot)
9. Measure sensitivity from the force-distance curve
 - a. Set imaging mode: contact, Set point for deflection signal: 1V, Set integral gain: 10.0
 - b. Click 'Engage' for approaching the tip to the sample surface → lower the head until the sound "beep" is heard & the sample (stainless) surface is clearly seen.
 - c. Then, check if the deflection is zero, and also if Z voltage is close to 70 V.
 - d. Force tab: drag the red colored bar on the left to the top.
 - e. Set Force distance: 0.5 μm , scan rate: 1 Hz, Trigger channel: Deflvolts, trigger point: 0.5 V (or 1 V)
 - f. Check 'relative'
 - g. Click 'Single force' for measurement.
10. When the plot of force-distance curve pops up, go to [tab] calibration to remove the artifact.
 - a. Set sensitivity: virtual deflection line → Then, close the pop-up window of plot.

11. Click 'single force' again (No touch on the red bar) → slope corrected plot
12. Measure the slope using 'control+I' and setting the sensitivity as Defl invOLS.
 - a. Record Amp invOLS [nm/V] & Deflection invOLS [nm/V].



13. Do Thermal measurement (no driving force, no drive amplitude applied)
 - a. Set Imaging mode: contact → AC mode
 - b. Click 'engage' → (right away) 'withdraw' (this gives a gap of 6 μm between the sample and the cantilever)
 - c. Click 'Do thermal'. When averaging count is over 80, click 'stop thermal'.
 - d. Expand the region of interest. → 'Fit Guess' and 'Try Fit'.
 - e. Record frequency, K (stiffness), and thermal Q.
 - f. Save (.pxp files) using 'Save table copy'.
 - g. Edit -> Save (for csv. files)
14. Go to 'Tune' tab in Master Panel
 - a. Set low frequency limit as 50 kHz
 - b. Set high frequency limit as 400 kHz

- c. Set Target amplitude as 1V (this is the deflection of cantilevers when there is a change of 1V detected by photo diode.)
 - d. Click 'Append phase', 'Both', 'SHO fit', and 'SHO phase'. (SHO: single harmonic oscillation.) → Go to <Auto tune> tab → Click 'Auto tune' → Record the results.
15. After 'Autotune', go to 'Manual Tune' in order to measure deflection under constant driving amplitude.
 - a. Set 'constant' drive amplitude (500 mV and 1 V).
 - b. Click 'One Tune'.
 - c. When done, change 'AC mode' to 'contact mode' not to vibrate.
16. Repeat steps 7 through 15 for all the data points (each beam spot counts as a data point) along the cantilever.